Studies on the Electrodeposition of Calcium Phosphate Coatings for Orthopaedic Applications and the Potential Incorporation of Apatite-Coated Liposomes

Oliver N. F. King
St. Catherine's College

A thesis submitted for the degree of Doctor of Philosophy,
Department of Materials,
University of Oxford

June 2006

Contents

1 Introduction **1**
- 1.0.1 Current problems . . . 2
- 1.0.2 The Host-implant interface . . . 3

1.1 Layout of thesis . . . 5
1.2 Aims . . . 6

2 Literature Review **7**
2.1 Ceramics in Orthopaedics . . . 7
- 2.1.1 Clinical Usage of Calcium Phosphates . . . 8

2.2 Calcium Phosphate Chemistry . . . 11
- 2.2.1 Amorphous Calcium Phosphate (ACP) . . . 11
- 2.2.2 Dicalcium Phosphate Dihydrate (DCPD) . . . 13
- 2.2.3 Tricalcium Phosphate (TCP) . . . 16
- 2.2.4 Octacalcium Phosphate (OCP) . . . 19
- 2.2.5 Hydroxyapatite (HAp) . . . 21

2.3 Comparison of crystallographic properties . . . 26
2.4 Kinetics of precipitation and crystal growth . . . 27
- 2.4.1 Precipitation . . . 27
- 2.4.2 Crystal Growth of Hydroxyapatite (HAp) . . . 31

2.5 Biological Calcium Phosphate . . . 33
- 2.5.1 Biological Apatite . . . 33
- 2.5.2 Composition of Bone . . . 35
- 2.5.3 Structure of Bone . . . 36

2.6 Biological Mineralisation . . . 37
2.7 Coating Methodology . . . 38
- 2.7.1 Current methods . . . 39
- 2.7.2 Biomimetic methods . . . 41
- 2.7.3 Electrodeposition Techniques . . . 43
- 2.7.4 Coating adhesion . . . 52
- 2.7.5 Incorporation of biochemical factors into coatings . . . 53

2.8 Liposomes . . . 59

2.8.1 Structural aspects . . . 59
2.8.2 Manufacture of liposomes . . . 64
2.8.3 Aspects of diffusion . . . 66
2.9 Calcium Phosphate-Liposome Composites . . . 72
2.10 Summary . . . 76

3 Experimental Procedures **78**
3.1 General Methods . . . 78
3.1.1 Measurement and calculation of CaP phase supersaturation . . . 78
3.1.2 Manufacture of stock coating solutions . . . 79
3.2 Electrodeposition coating procedure . . . 80
3.3 Summary of samples prepared . . . 82
3.4 Characterisation techniques . . . 83
3.4.1 X-ray diffraction . . . 83
3.4.2 Transmission electron microscopy (TEM) . . . 84
3.4.3 Electron diffraction . . . 85
3.4.4 Scanning electron microscopy . . . 85
3.4.5 Measurement of mechanical strength (Lap Shear) . . . 85
3.5 The use of different drying methods . . . 88
3.5.1 Air drying . . . 88
3.5.2 Critical point drying (CPD) . . . 88
3.6 Manufacture of thick ($>$ **10** µm) coatings . . . 89
3.6.1 Scale-up of coating process . . . 89
3.7 Effect of coating maturation time . . . 90
3.8 Liposomes . . . 91
3.8.1 Manufacture of multilamellar vesicles (MLVs) . . . 91
3.8.2 Manufacture of stable plurilamellar vesicles (SPLVs) . . . 92
3.8.3 Optical microscopy of liposome suspensions . . . 92
3.8.4 Coating liposomes with calcium phosphate phases . . . 93
3.9 Diffusion studies . . . 93
3.9.1 Utilising calcein for liposome studies . . . 93
3.9.2 Entrapping the antibiotic gentamicin . . . 96
3.10 Manufacture of liposome-CaP composite coatings . . . 99
3.10.1 General procedure . . . 99
3.10.2 Calcein containing liposome-CaP composite coatings . . . 100

4 Results **105**
4.1 Coatings . . . 105
4.1.1 Preliminary Experiments . . . 105
4.1.2 Increasing coating thickness . . . 118

4.1.3 Effects of drying method and maturation time on coating morphology and shear strength . . . 118
4.1.4 SEM investigation of lap-shear fracture surfaces . . . 132
4.1.5 Effect of maturation time on coating crystallinity . . . 136
4.2 Liposomes . . . 139
4.2.1 Preliminary experiments . . . 139
4.2.2 Diffusion studies . . . 142
4.3 Composite coatings . . . 145
4.3.1 Effect of liposomes upon coating solutions . . . 145
4.3.2 Calcein containing liposome-CaP composite coatings . . . 146

5 Discussion **148**
5.1 Coating time and solution concentration . . . 148
5.1.1 Coating time . . . 149
5.1.2 Initial coating solution supersaturation . . . 149
5.1.3 Change in supersaturation . . . 151
5.2 Identification of phases by XRD . . . 153
5.3 Increasing coating thickness . . . 157
5.4 Effects of drying method and maturation time on coating morphology and shear strength . . . 159
5.4.1 Effects upon coating morphology . . . 159
5.4.2 Coating Shear strength . . . 166
5.5 Investigation into Lap shear fracture surfaces using SEM . . . 171
5.5.1 Mechanism of Adhesion . . . 173
5.6 Effect of maturation time on coating crystallinity . . . 174
5.7 Schema for the mechanism of deposition . . . 176
5.8 Liposomes . . . 179
5.8.1 Calcein calibration . . . 180
5.8.2 Method of manufacture . . . 180
5.8.3 Entrapment efficiency . . . 181
5.8.4 Calcein release from coated and uncoated liposomes . . . 182
5.8.5 Studies on gentamicin . . . 184
5.9 Composite coatings . . . 186
5.9.1 Effect of the liposomes upon coating solutions . . . 186
5.9.2 Manufacture of composite coatings . . . 187

6 Conclusions **190**
6.1 Coatings . . . 191
6.1.1 Supersaturation . . . 191
6.1.2 Coating mechanism . . . 191
6.1.3 Characterisation . . . 192

6.2 Liposome studies 193
6.3 Composite coatings 193
6.4 General conclusions 194

7 Further work **195**

Bibliography **198**

Appendices **222**

A Calculation of Supersaturation **222**
A.1 Equilibria 222
A.2 Electroneutrality 223
A.3 Ionic concentration 224
A.4 Solubility Products 226

B Materials Congress 2002 Abstract **227**

List of Figures

1.1 Age specific incidence rates for fractures in men and women. 2
1.2 Representation of events at the bone-implant interface. 3

2.1 Clinical uses of bioceramics 8
2.2 ACP S_6 isomer with a central calcium atom surrounded by six PO_4 groups. 12
2.3 Projection of the structure of dicalcium phosphate dihydrate 14
2.4 Diagram of the bonding between the atoms in one of the corrugated sheets of composition $CaPO_4$ 14
2.5 Dissolution and reprecipitation of DCPD. 15
2.6 A projection of the α-TCP structure on the (001) plane 17
2.7 Unit cell structural diagram of β-TCP 18
2.8 Structural model to show the two different types of column along the c-axis in β-TCP 18
2.9 A view of the unit cell of OCP 20
2.10 The atomic arrangement of hydroxyapatite projected on the $x-y$ plane. . 21
2.11 Schematic representation of the hydroxyapatite crystal projected on the ab plane 22
2.12 Schematic representation of the hierarchy in bone 36
2.13 Schematic of the double layer surrounding a charged particle 45
2.14 Zeta potential of ceramic particles versus pH of suspension 47
2.15 Scheme of nucleation and growth of a calcium phosphate prelayer on a cathodically polarised titanium surface. 50
2.16 The structure of phosphatidylcholine 60
2.17 A space filling model of a phosopholipid bilayer membrane 61
2.18 Diagram showing multilamellar and unilamellar liposomes 64
2.19 Representation of a large unilamellar vesicle (LUV) showing the four regions occupied by the the molecules. 68
2.20 Scheme for passive diffusion for weak acids and bases 69
2.21 Structure of calcein at acidic and neutral pH 72

3.1 Diagram of solution monitoring apparatus. 79

3.2 Diagram of the equipment set-up during coating 81
3.3 Grid coating attachment photograph 84
3.4 Figure showing lap-shear testing procedure 87
3.5 Photograph of the CPD drying apparatus 89
3.6 Laboratory photographs of procedure during manufacture of calcein containing liposome-CaP composite coatings 103

4.1 Example graph of calculated supersaturation against time (6.25 mmol/l Ca^{2+} ions and 3.75mmol/l PO_4^{3-} ions) 106
4.2 Calculated supersaturation against time for OCP at different coating solution starting concentrations 107
4.3 Calculated supersaturation against time for DCPD at different coating solution starting concentrations 107
4.4 Calculated supersaturation against time for HAp at different coating solution starting concentrations 108
4.5 Control: XRD scan of HAp standard reference material 110
4.6 XRD scan of a coating produced by ten repeated electrodeposition cycles . 110
4.7 XRD scan of uncoated 304 stainless steel sample 111
4.8 XRD scan of a coating produced by one coating cycle and no maturation time 112
4.9 XRD scan of a coating produced by one coating cycle and one hour maturation time 113
4.10 XRD scan of a coating produced by one coating cycle and three hours maturation time 113
4.11 XRD scan of a coating produced by one coating cycle and five hours maturation time 114
4.12 XRD scan of a coating produced by one coating cycle and thirteen hours maturation time 114
4.13 XRD scan of a coating produced by five coating cycles 115
4.14 XRD scan of a coating produced by one coating cycle and one hour maturation time followed by four more coating cycles 116
4.15 XRD scan of a coating produced by one coating cycle and three hours maturation time followed by four more coating cycles 116
4.16 Photograph of a thick CaP coating deposited onto TiAl(6%)V(4%) substrate 118
4.17 Control: Scanning electron micrograph of substrate coated in solution containing no Ca^{2+} or PO_4^{3-} ions. 119
4.18 Scanning electron micrographs of samples coated once and then left to stand in solution for various lengths of time before air drying 120
4.19 Scanning electron micrographs of samples coated once, then left to stand in solution for various lengths of time and then coated four more times before air drying 122

4.20 Scanning electron micrographs of samples coated once and then left to stand in solution for various lengths of time before critical point drying . . 124
4.21 Scanning electron micrographs of samples coated once, then left to stand in solution for various lengths of time and then coated four more times before critical point drying 126
4.22 Coating thickness against maturation time for one-coat samples 127
4.23 Coating thickness against maturation time for five-coat samples 128
4.24 Lap-shear strength against maturation time for one coat samples 129
4.25 Lap-shear strength against coating thickness for one coat samples 130
4.26 Lap-shear strength against maturation time for five-coat samples 131
4.27 Lap-shear strength against coating thickness for five-coat samples 132
4.28 Micrographs of the fracture surfaces of blanks used during lap-shear testing of one coat samples. 133
4.29 Diagram explaining views of post-fracture surfaces 134
4.30 Micrographs of the fracture surfaces of blanks used during lap-shear testing of one coat samples. 135
4.31 TEM bright field micrographs and corresponding selected area diffraction patterns of coatings produced by one coating cycle on holey carbon grids. . 137
4.32 Calibration curve for the fluorescence of calcein and calcein with the addition of Ca^{2+} and PO_4^{3-} ions 139
4.33 Optical micrographs of SPLVs containing calcein 141
4.34 Example calcein fluorescence spectra used to calculate entrapment efficiency. 141
4.35 Graph showing the percentage release of calcein over time for CaP-coated and non-coated liposomes at 37℃. 142
4.36 Calibration curves for gentamicin at low and high relative concentrations. . 143
4.37 Example scans of gentamicin fluorescence. 144
4.38 Percentage release of gentamicin from uncoated liposomes at 37 ℃. 144
4.39 Graphs showing supersaturation of CaP phases during electrodeposition of CaP with and without the addition of liposomes. 145

Studies on the Electrodeposition of Calcium Phosphate Coatings for Orthopaedic Applications and the Potential Incorporation of Apatite-Coated Liposomes

Oliver N. F. King, St. Catherine's College.
Submitted for the degree of D.Phil, Trinity Term 2006.

A low temperature electrodeposition technique has been used to coat metal substrates with calcium phosphate (CaP) phases at 37℃ in aqueous solution buffered at *p*H 7.4. Experiments have also been carried out on liposome vesicles, some populations of which were coated in CaP, the final aim being to combine the liposome vesicles with the coating methodology in order to produce composite coatings with a drug delivery capability.

Monitoring of coating solution conditions during deposition allowed calculation of supersaturation (the driving force of precipitation) for the relevant CaP phases. Factors relating to the coating procedure that were altered included: the initial coating solution concentration, the drying method and the time for which the samples were allowed to remain in solution (maturation). The effects upon the coatings were studied using X-ray diffraction (XRD), low voltage-scanning electron microscopy (LV-SEM), transmission electron microscopy (TEM), electron diffraction and measurement of coating shear strengths.

Maturation time was found to influence shear strength, coating thickness and coating crystallinity. LV-SEM revealed that one hour or more of maturation time in solution, after one electrodeposition coating cycle, led to a dramatic change in coating morphology from a thin particulate coating, to one with a coherent structure of interconnected crystallites. TEM and electron diffraction of coatings revealed that the coating crystallinity increased with maturation time. The coating was determined to be hydroxyapatite (HAp) with a preferred orientation of crystallites with their *c*-axis perpendicular to the substrate.

Critical point drying (CPD) appeared to protect the structure of the coatings when compared to air drying. Shear strengths of both CPD and air dried sets of samples were modulated by alterations in maturation time. However penetration of the coating structure by epoxy resin during the testing procedure may have influenced the results.

Lipid vesicles, manufactured from egg phosphatidylcholine (EPC) containing 30 mol % cholesterol and 4 mol % α-tocopherol, were characterised in terms of entrapment efficiency and release of both the marker molecule calcein and the antibiotic gentamicin. A higher percentage release of calcein was measured from CaP-coated liposomes when compared to uncoated vesicles when incubated for periods in excess of 70 h at 37℃, indicating that CaP ultimately increased the permeability of the liposomal membranes.

Addition of CaP-coated liposomes to coating solutions, during the electrodeposition of calcium phosphate, was found to moderate the decrease in HAp and octacalcium phosphate supersaturation that was normally seen in their absence. Composite coatings, incorporating liposomes that contained calcein were also manufactured.

Chapter 1

Introduction

The 2001 census showed that for the first time there are now more people aged over 60 years living in the UK than there are people under the age of 16 (National Statistics Online., 2001). This trend of ageing populations in developed countries has many consequences, including increased pressure on the healthcare system. One area in which this pressure is felt most acutely is in the field of orthopaedics which has to deal with a greatly increased number of fractures (Figure 1.1), which itself is partly due to the the fall in bone density which occurs as part of the ageing process (Currey et al., 1996; Mosekilde, 1990). Statistics from recent years show that osteoporosis alone can be said to cause 70,000 hip fractures per year in the UK (Dolan and Torgerson, 1998) and cost the NHS £1.7 billion to treat in the same time period (Torgerson, 2001).

This study aims to look at a method of producing an economically viable coating for bone implants which may aid rapid healing, ultimately easing some of the pressure on health services.

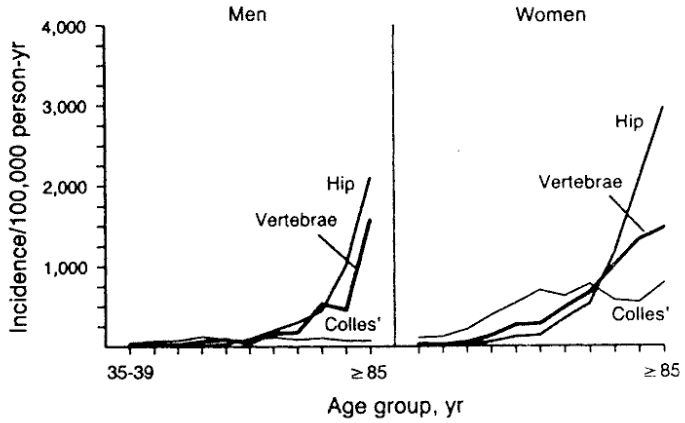

Figure 1.1: Age specific incidence rates for hip, vertebral and distal forearm (Colles') fractures in men and women. Data derived from a population in Minnesota, USA. From Cooper and Melton (1992)

1.0.1 Current problems

Orthopaedic procedures such as total hip replacement (THR) surgery (also known as total hip arthroplasty), which was pioneered by Sir John Charnley in the '50s and '60s (Charnley, 1961), have generally used polymethylmethacrylate (PMMA) grout in order to fix the implant to the surrounding bone tissue. Unfortunately, the use of PMMA has many potential drawbacks, such as the release of heat and toxic monomers into the area surrounding the implant (Lewis, 1997). This kills host tissues at the interface with the prosthesis, providing a great setback to the process of healing. The use of acrylic cement has also been said to increase the quantity of wear-particles produced by the implant during use (Willert et al., 1974), leading to inflammation and subsequent loosening of the implant as immune cells invade and begin to clear up the debris (Willert, 1977).

One method currently used with the possibility of ensuring faster, complication-free incorporation is cementless fixation. In many cases, the metallic portion of the implant has been pre-coated with calcium phosphate (CaP) (Kroon and Freeman, 1992; Lucas et al., 1993; Søballe and Overgaard, 1996; de Groot et al., 1998; Sun et al., 2001; Geesink,

2002). CaP is a popular choice of material because in particular forms, it makes up the main inorganic constituent of the calcified tissues of the human body.

1.0.2 The Host-implant interface

The interface between the host tissue and the implant is incredibly important because it is the site where the events leading to integration of that implant take place. A representation of the specific sequence of events that occur during successful incorporation of orthopaedic devices is displayed in Figure 1.2. The modification of the interface chemistry is likely to be one way to secure a rapid healing, a reduction in chances of contracting an infection and therefore an increased probability of long-term incorporation.

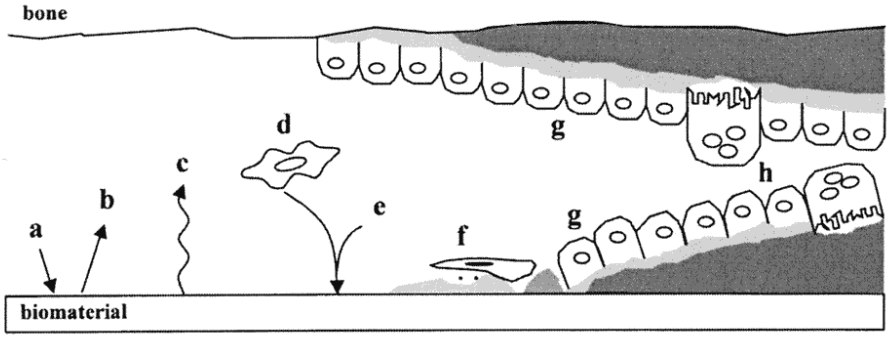

Figure 1.2: Representation of events at the bone-implant interface. (a) Protein adsorption from blood and tissue fluids, (b) protein desorption, (c) surface changes and material release, (d) inflammatory and connective tissue cells approach the implant, (e) possible targeted release of matrix proteins and selected adsorption of proteins, (f) formation of cement lines and adhesion of osteogenic cells, (g) bone deposition on both the exposed bone and implant surfaces, (h) remodelling of newly formed bone. From Puleo and Nanci (1999)

This modification can take a number of forms. Puleo and Nanci (1999) summarise various methods of attempting surface modifications and divide them into three categories:

- Physicochemical, including altering surface energy, surface charge and applying CaP coatings

- Morphological, such as altering surface porosity or morphology such as pits and grooves

- Biochemical, which often involves immobilising proteins or peptides such as the sequence Arginine-Glycine-Aspartate, which has been shown to encourage osteoblasts[1] to adhere to the surface in greater numbers *in vitro* (Dee et al., 1996)

For CaP coated cementless implants, already physicochemically modified, there is now growing interest in incorporating biochemical compounds into the coating itself (Radin et al., 1997; Wen et al., 1999; Liu et al., 2001; Stigter et al., 2002; Liu et al., 2004). These could take the form of antibiotics to prevent infections or bone growth factors which would encourage osteoblasts to build bone tissue in the area surrounding the coating.

Lucas et al. (1989) suggested that if these biochemical factors are to interact with the volume of cells surrounding the implant in an effective manner, they need to be present;

1. for a period long enough to initiate a cellular response (cellular responses to factors such as bone morphogenetic proteins[2] can be seen in time periods of as short as 1 h (Wang et al., 1993) but longer exposure periods have been shown to induce more favourable traits in osteoblast cell populations (Puleo, 1997))

2. at a concentration that is high enough for that response (a concentration of transforming growth factor $\beta 2$ of 10 ng/ml per day has been found to stimulate protein synthesis in cultured osteoblasts (Kim and Valentini, 1997)).

As will be described later (section 2.7), current CaP coating methodology such as plasma spraying has a number of drawbacks especially when considering the incorporation

[1]The cells found in bone tissue which are responsible for building up said tissue.

[2]Multifunctional protein molecules which are members of the the Transforming Growth Factor-β superfamily and cable of singly inducing *de novo* bone formation (Kirker-Head, 2000)

of heat-sensitive biochemical moieties. Impregnation by soaking alone is unlikely to allow the slow, high concentration delivery of these biochemicals in the manner required for an effective cellular response or protection from infection risks.

1.1 Layout of thesis

An outline of the aims of this project (Section 1.2) will be followed by a review of the relevant literature published about calcium phosphate phases, coating methodologies and the manufacture and structure of liposome vesicles (Chapter 2). The experimental protocols used during this study will be detailed in Chapter 3 followed by a description of the results of these experiments in Chapter 4. All of the information from preceding chapters will be brought together in the discussion chapter (Chapter 5) with a summary of the conclusions of the study in Chapter 6. Finally, further areas of work to be explored will be outlined in Chapter 7.

1.2 Aims

This work aims to study some aspects of one way in which calcium phosphate coatings can be made and combined with a drug delivery capability which may aid healing and/or prevent infection.

Along with a review of the current literature, this project will look at three main areas:

1. *The production of CaP coatings using a low temperature deposition technique aided by an electric field.*

   Assessments will be made by looking at the effect of the coating and drying conditions on the microstructure, strength and thickness of the coatings produced.

2. *The production of CaP coated lipid vesicles (liposomes) capable of entrapping chemicals reliably.*

   Quantification of the amount of a chemical that can be entrapped and measuring the release of this chemical from the coated liposomes will be performed.

3. *The combination the CaP-coated liposomes and the CaP coating.*

   Production of a calcium-phosphate-liposome composite coating and the subsequent release of chemicals from it will be studied.

The overall aim is to gain a greater understanding of the steps and factors involved in creating a CaP coating which could improve upon the properties of those in use at present, as well as including the ability to release drugs from the vesicles incorporated within these coatings.

Chapter 2

Literature Review

This literature review will summarise and discuss the current knowledge relating to the use of calcium phosphates (CaP) for coatings to be used on orthopaedic implants, the use of liposome vesicles for drug delivery applications and the combination of both technologies.

After a general introduction, the structure and solution chemistry of the relevant calcium phosphate phases will be reviewed. This will be followed by a section looking at the detail of coating methodology in its current state, research and background information on liposomes and finally, composites of liposomes and CaP phases.

2.1 Ceramics in Orthopaedics

Calcium Phosphates are one subset of a type of ceramic material[1] used in clinical applications (Figure 2.1). These materials are termed 'bioceramics' because of their use in biological environments. However, CaP ceramics differ from other bioceramics, such as alumina (Al_2O_3), because they mimic the inorganic constituents of the calcified tissues

[1]Non-metallic, inorganic materials which exhibit a broad range of composition.

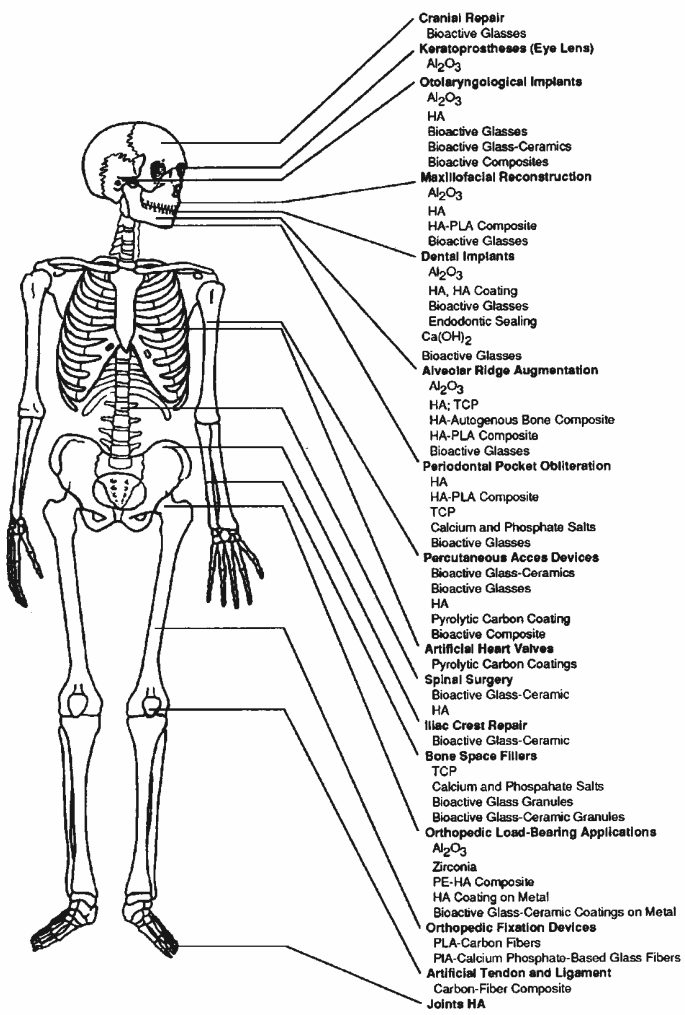

Figure 2.1: Clinical uses of bioceramics (Hench and Wilson, 1993)

found in the body. Also, CaP ceramics are classed as *bioactive*[2] as opposed to *bioinert*[3].

2.1.1 Clinical Usage of Calcium Phosphates

The bulk of the bone tissues can be said to be made up of a proteinaceous component (collagen) and an inorganic (CaP) component which is thought to be a poorly crystalline,

[2]"a biomaterial that is designed to elicit or modulate biological activity." (Williams et al., 1992)
[3]biomaterials which elicit little or no host response.

Table 1: Calcium Phosphate Biomaterials. (Adapted from LeGeros (2002))

Calcium phosphate ceramics (synthetic)
Calcium hydroxyapatite, $Ca_{10}(PO_4)_6OH_2$ Calcitite™, Durapatite™, Alveograf™, Osteograf™
β-tricalcium phosphate, $Ca_3(PO_4)_2$ Synthograf™, Augmen™
Biphasic calcium phosphates (mixture of HAp and β-tricalcium phosphate) Triosit™, MBCP™, Osteosynt™
Calcium deficient apatite (unsintered) Osteogen™
Calcium phosphate ceramics (natural origin)
Freeze-dried or baked bone from cadavers
Bovine bone derived BioOss™, Endobone™, Trubone™, BonAp™
Coral derived (coralline hydroxyapatite) Interpore™, Pro−Osteon™
Calcium phosphate cements BoneSource™, α−BSM™, Cementek™

non-stoichiometric form of the mineral hydroxyapatite (HAp, $Ca_{10}(PO_4)_6OH_2$).

There are many commercially available calcium phosphate biomaterials in use today (Table 1) and much work has been carried out on their effectiveness in dental and orthopaedic applications (Klein et al., 1993; Lucas et al., 1993; Oguchi et al., 1995; Søballe and Overgaard, 1996; Capello et al., 1998; Önsten et al., 1998; Yuan, Yang, Li, Zhang, de Bruijn and de Groot, 1998; Sun et al., 2001).

CaP ceramics can be made to be either dense or porous to allow bone ingrowth (Klein et al., 1993); the ideal situation for porous implants being the gradual resorption and replacement by host tissues.

Bone ingrowth can be coupled with resorption of the biomaterial. This is useful in cases where a material can be used to fill a space in the body before being replaced by natural tissues. If the material were to be replaced by bone tissue for example, bone growth factors could be impregnated into the material surface acting as a support for

tissue growth before being degraded (Yuan, Zou, Yang, Zhang, de Bruijn and de Groot, 1998; Kirker-Head, 2000; Yuan et al., 2001).

Of the two main types of CaP used as implants (β-tricalcium phosphate (β-TCP) and HAp), β-TCP is thought to be the most resorbable, however this resorption has proved to be unpredictable when compared to HAp (Manjubala et al., 2002). This has led to the use of mixed phase (biphasic) ceramic implants which contain both HAp and β-TCP (Benahmed et al., 1996; Richard et al., 1998; Toquet et al., 1999).

CaP ceramics have many uses, such as for bone graft substitutes (LeGeros and LeGeros, 1993; Lawson and Czernuszka, 1998; Tancred et al., 1998; Moore et al., 2001), which can be used in varied situations such as maxillo-facial reconstruction, repair of tissues after neoplasia and replacement of teeth. However, the mechanical properties of materials such as HAp, being brittle in nature, are not well-suited to their use in load-bearing applications, especially when a reduction in mechanical integrity is likely with any increase in degree of porosity.

2.2 Calcium Phosphate Chemistry

This section deals with the chemistry and properties of the various CaP phases. Particular attention will be given to the production of CaP phases by precipitation from solution in a synthetic rather than biological environment.

2.2.1 Amorphous Calcium Phosphate (ACP)

ACP has been described as 'non-crystalline' calcium phosphate (Eanes et al., 1965) and is thought to be the first type of CaP formed during the precipitation process. It is said to have a Ca/P molar ratio of 1.45 ± 0.05 (Nancollas and Mohan (1970) cited by Kanzaki et al. (2001)). As suggested by its name, no long range-order can be found in the structure of ACP. Although this is the case, a structure has been proposed by Posner and Betts (1975)which consists of units called Posner's clusters ($Ca_9(PO_4)_6$); these are roughly spherical and close-pack to form larger spherical entities which also contain water molecules.

Kanzaki et al. (2001) have studied the possible alternatives to the structures of Posner's clusters, looking at a family of neutral $[Ca_3(PO_4)_2]_n$ clusters using *ab initio* methods. They found that for monomer and dimer isomers ($n = 1, 2$) an O-Ca-O bonding pattern occurred in the most stable structures. Trimer isomers had two different bonding patterns, one with the calcium atoms at the surface of a cluster forming Ca-O bonds with three PO_4 groups, the other with a central calcium atom forming Ca-O bonds with the six PO_4 groups. This latter structure is the most energetically favourable (Figure 2.2). The authors conclude that the ACP isn't necessarily made up of one particular type of cluster. Compact trimers are energetically favoured to monomers and dimers. Aggregation of clusters leads to a large energy stabilisation, which conforms to Posner's proposal that these units are close-

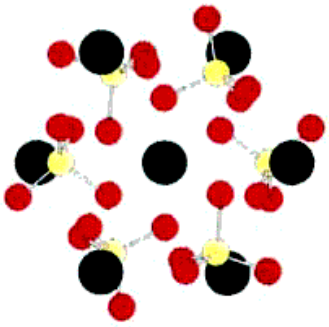

Figure 2.2: The top view of the S_6 isomer with a central calcium atom surrounded by six PO_4 groups. Three calcium atoms coincide with the C_3 symmetry axis. (Yellow = Phosphorus, Red = Oxygen, Black = Calcium) (Kanzaki et al., 2001)

packed in ACP. The formula for ACP should therefore be $[Ca_3(PO_4)_2]_n[H_2O]_m$ when taking into account the interaction of the clusters with water.

Abbona and Baronnet (1996) cite Christoffersen et al. (1989) as showing the existence of two forms of amorphous calcium phosphate, both sharing the same composition, but having different morphologies and solubilities. ACP1 is spherical, whereas ACP2 is disc-shaped.

Because ACP is thought to be a precursor in the formation of other CaP phases, studies have been carried out on the transformation process and sequence of phase changes (Eanes et al., 1965; Boskey and Posner, 1976; Feenstra and de Bruyn, 1979; Wong and Czernuzka, 1993; Abbona and Baronnet, 1996; Iijima et al., 1997; Yubao et al., 1997; Liou and Chen, 2002). Eanes et al. (1965) studied the transformation of CaP for two weeks after precipitation from solutions of high pH and high concentration. They concluded that the temperature-dependent transformation from the metastable initial phase into a 'more ordered apatitic configuration' was autocatalytic; i.e occurred by homogeneous nucleation. After this initial conversion, the crystalline surfaces can act as heterogeneous nucleators for further conversion, leading to the sigmoid-shaped relationship of transformation with

respect to time which was observed.

Boskey and Posner (1976) found that an apatitic precursor, not ACP was the first phase formed from solutions of low concentration (total Ca and total PO_4 less than 2 mmol/l). This conflicted with the presumptions that ACP was an obligatory precursor to HAp formation, no matter what the starting conditions.

2.2.2 Dicalcium Phosphate Dihydrate (DCPD)

DCPD, also known as brushite has the chemical formula $CaHPO_4.2H_2O$ and belongs to the class of Ca-PO_4 sheet-containing compounds. The chemical structure was determined by Beevers (1958) and further refined by neutron diffraction studies (Curry and Jones, 1971). DCPD has a structure belonging to the monoclinic Ia (C_8^4) space group (Curry and Jones, 1971). A structural projection diagram can be seen in Figure 2.3. From this it can be seen that the Ca and P atoms lie behind one another, with the thick continuous lines joining them to the shared oxygens. Each of these calcium atoms also makes contact with two oxygen atoms in adjacent chains, this can be seen more clearly in Figure 2.4, which shows the bonds in one of the sheets. These sheets are joined together by water molecules, the oxygens of which are numbered as 3 in Figure 2.3.

Like ACP, DCPD is thought to be a precursor of hydroxyapatite. Kumar, Desarathy and Riley (1999) studied this transformation after depositing DCPD onto titanium substrates by an electrodeposition process. One advantage of using DCPD should be the ability of any implant coated with this technique to supply increased amounts of Ca^{2+} and PO_4^{-3} ions early in the life of the implant. After this, the coating could transform into a less soluble CaP phase [HAp]. By monitoring the calcium ion concentration in various media types, in which the samples were sitting, they were able to observe the dissolution

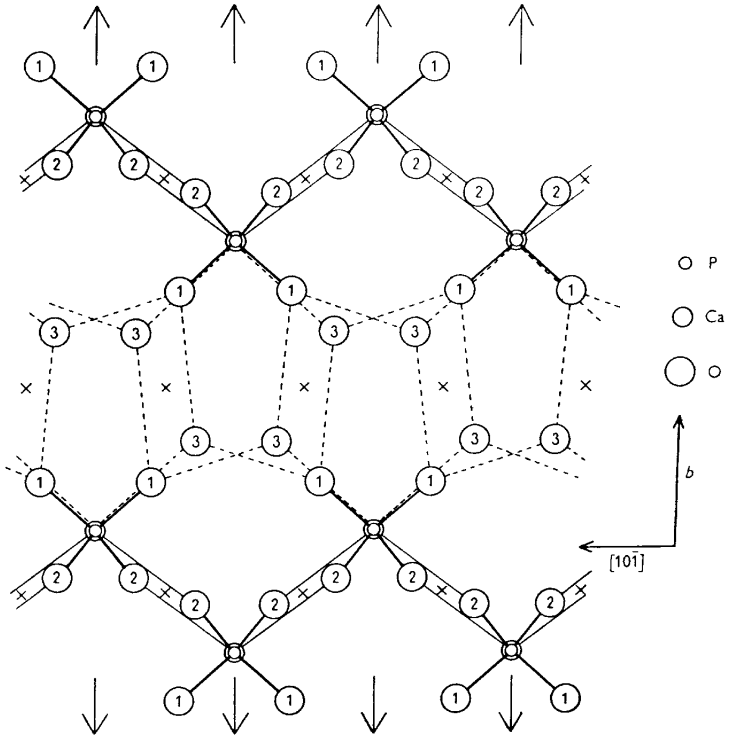

Figure 2.3: Projection of the structure of dicalcium phosphate dihydrate onto a plane perpendicular to [101] (Beevers, 1958)

and reprecipitation behaviour of the coatings. The mass change of the samples during this time was also monitored.

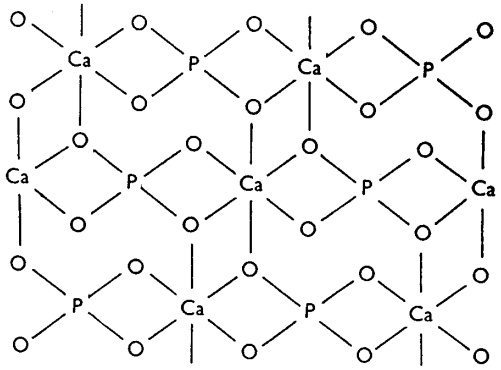

Figure 2.4: Diagram of the bonding between the atoms in one of the corrugated sheets of composition $CaPO_4$ (Beevers, 1958)

They found that the Ca^{2+} ion concentration changed with time in all the different solutions tested. For example, [Ca^{2+}] increased in deionised water and also modified Hank's solution (without Ca^{2+} and Mg^{2+}), whereas it fell in deionised water plus excess calcium. In the modified Hank's solution, after the initial increase in [Ca^{2+}], mass changes also occurred (Figure 2.5).

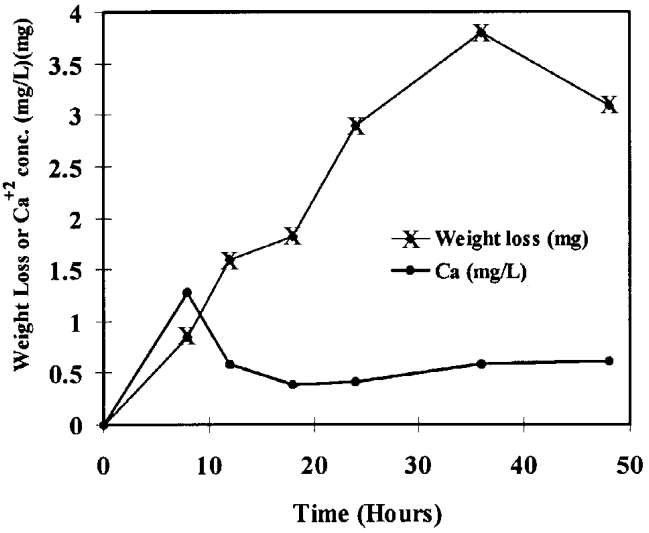

Figure 2.5: Dissolution and reprecipitation of DCPD: Data showing [Ca^{2+}] and change in mass in a modified Hank's solution without Ca^{2+} and Mg^{2+}) (Kumar, Desarathy and Riley, 1999)

There is an increase in [Ca^{2+}] after 8 hours, which drops off after 12 hours, but a mass increase only after 36 hours. The fact that the number of Ca^{2+} ions in solution is falling at the same time as the mass is still decreasing indicates the precipitation of these ions into a phase, which is richer in calcium, at the same time as phosphate groups are being lost into the solution.

Kumar and colleagues subsequently described how the KCl-supported electrolyte used in their electrodeposition process led to the formation of a type of DCPD which contains potassium-substituted brushite (Kumar, Xie, Chittur and Riley, 1999). This potassium

substitution led to a higher rate of transformation to HAp. This was possibly due to the potassium ions producing strain in the DCPD lattice.

2.2.3 Tricalcium Phosphate (TCP)

There are two main forms of tricalcium phosphate found, α-TCP and β-TCP. Both have the formula $Ca_3(PO_4)_2$ and belong to the glaserite structural type, but differ in structure and characteristics.

2.2.3.1 α-TCP

α-TCP has a monoclinic structure and belongs to the space group $P2_1/a$ (Mathew et al., 1977). In this structure, the calcium and phosphate ions are arranged in columns along [001]. One type of column contains only cations, the other type contains cations and anions (see diagram in Figure 2.6).

There has been much interest in using α-TCP as a bone-cement material (Yubao et al., 1997; Durucan and Brown, 2002). This is partly due to the metastable nature of α-TCP at low temperatures, causing it to be be malleable during implantation before it transforms into HAp (Yubao et al., 1997; Durucan and Brown, 2002). In fact α-tricalcium phosphate is thermodynamically stable between 1120 and 1470 ℃ (Mathew et al., 1977).

Durucan and Brown (2002), studied the kinetics of α-TCP hydrolysis to HAp using isothermal calorimetry. In this experiment, they found that the transition of α-TCP particles to HAp in water initially followed surface area-dependent kinetics before following an Avrami model which takes into account nucleation sites, and the morphology of the end product.

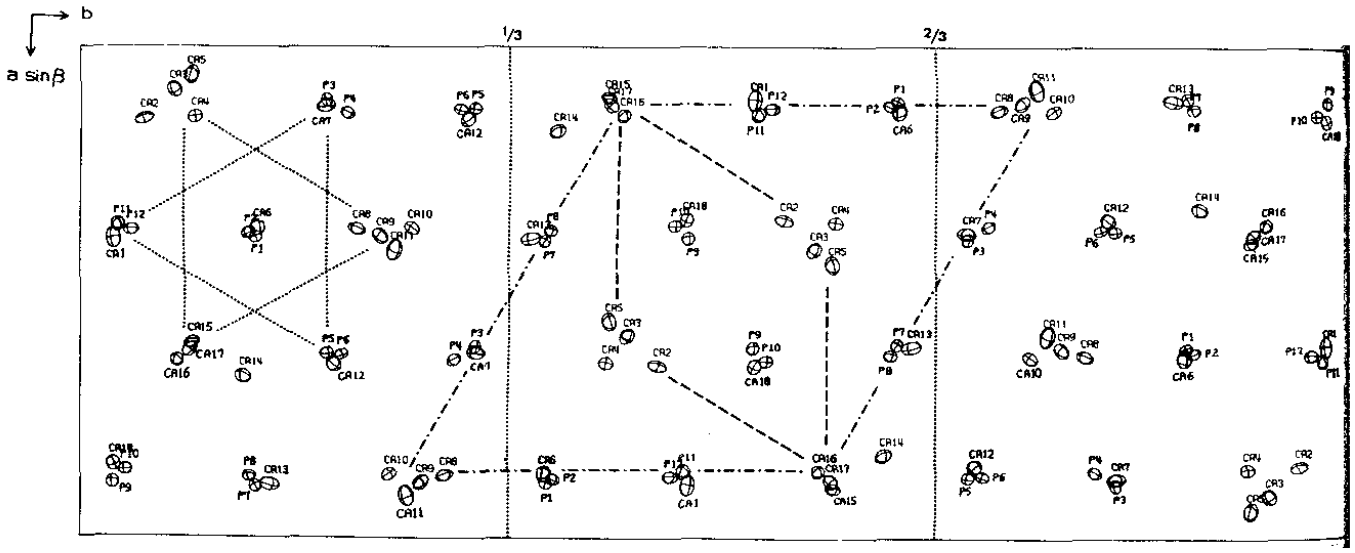

Figure 2.6: A projection of the α-TCP structure on the (001) plane to show the columnar arrangement. Oxygen atoms of PO_4^{3-} groups have been omitted for clarity. The dashed lines in the centre outline a unit cell corresponding to that of glaserite ($K_3Na(SO_4)_2$). The dotted lines on the left correspond to the a unit cell of HAp (Mathew et al., 1977)

2.2.3.2 β-TCP

β-TCP has a rhombohedral structure and belongs to the space group R3c (Rangavittal et al., 2000). A structural diagram of a unit cell can be seen in figure 2.7.β-TCP can also be seen to contain columns of Ca atoms and PO_4 tetrahedra orientated parallel to the the c axis. The structure of these columns can be seen in figure 2.8.

As mentioned previously (Section 2.1.1), β-TCP is used as a resorbable bone substitute in various clinical applications, either on its own or in a biphasic mixture with hydroxyapatite. It is generally made by sintering calcium deficient apatite (Liou and Chen, 2002), as described by equation 2.1.

$$Ca_9(OH)(HPO_4)(PO_4)_5 \longrightarrow 3Ca_3(PO_4)_2 + H_2O \tag{2.1}$$

Tang et al. (2001) analysed the dissolution kinetics of β-TCP at 37 ℃ using a constant

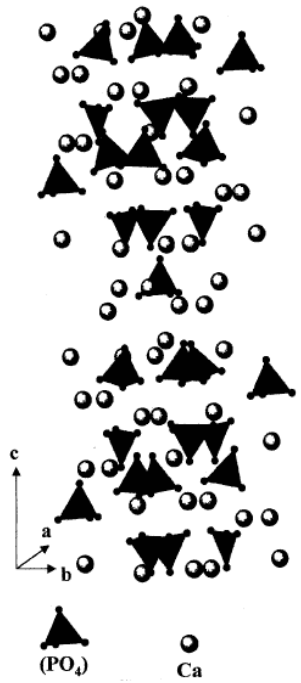

Figure 2.7: Unit cell structural diagram of β-TCP (Rangavittal et al., 2000)

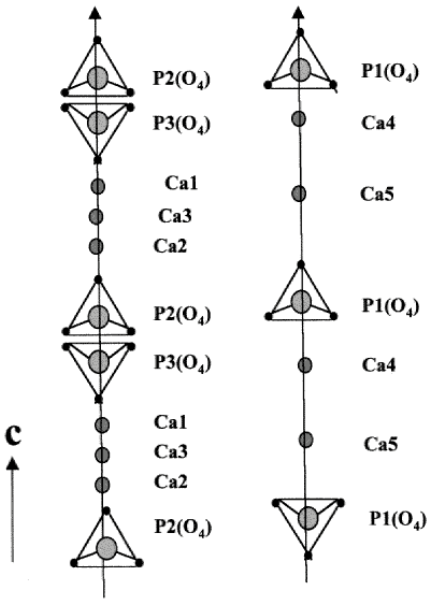

Figure 2.8: Structural model to show the two different types of column along the c-axis in β-TCP (Rangavittal et al., 2000)

composition method. The effect of Mg^{2+} and Zn^{2+} ions was also studied. At a Mg^{2+} concentration of 1×10^{-4} mol/l, the dissolution rate was less than one fifth of that found without the addition of magnesium. This was thought to be due to adsorption of the Mg^{2+} ions to the crystal surfaces. $[Zn^{2+}]$ had an even more drastic effect; the authors calculated that dissolution could be completely inhibited at 2×10^{-6} mol/l.

2.2.4 Octacalcium Phosphate (OCP)

Octacalcium phosphate or OCP, has the chemical formula $Ca_8(HPO_4)_2(PO_4)_4.5H_2O$ (Mathew and Takagi, 2001). OCP is triclinic with a structure belonging to space group $P\bar{1}$. It belongs to the apatite structural type of calcium phosphate (Brown et al., 1962). The structure can be divided into a region termed the 'apatite layer' and a region described as the 'water layer' or hydrated layer (Brown et al., 1962). A diagram illustrating a unit cell of OCP centred on the apatitic layer can be seen in figure 2.9.

Because of the layered structure and the close correspondence of the apatite layer to the structure of HAp, epitaxial over-growths of one compound over the other are very likely, forming lamellar mixed crystals of HAp and the hydrated OCP layer (Brown et al., 1962). Brown et al. (1962) suggested that these mixed crystal structures were the reason for researchers finding apatitic precipitates with Ca/P ratios of less than 5/3 (that for HAp).

Meyer and Eanes (1978) conducted an analysis of the transition between the phase first formed after the initial ACP-crystalline transformation and hydroxyapatite at 25 ℃. They suggested that the initial ACP-crystalline phase was actually OCP which transforms to HAp through a two stage reaction mechanism described in equations 2.2 and 2.3.

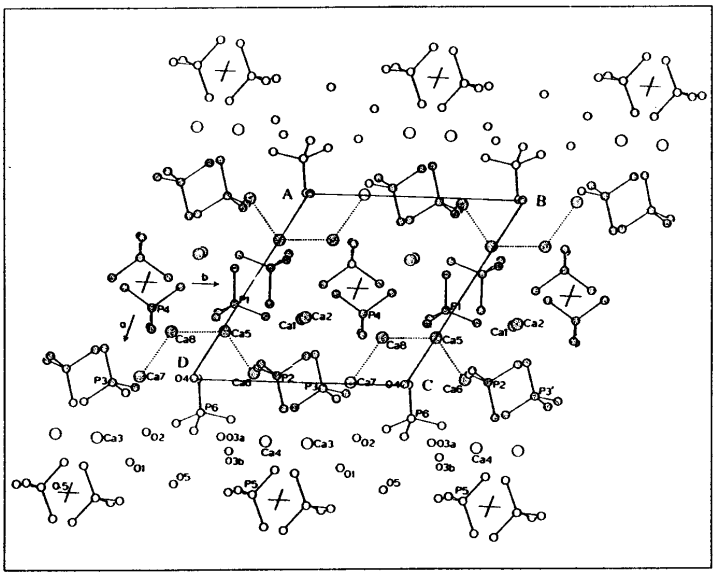

Figure 2.9: A view of the unit cell of OCP showing the apatite layer as the central region. A unit cell corresponding to HAp is shown. Hydrated layers can be seen at the top and bottom (Mathew and Takagi, 2001)

$$5Ca_4H(PO_4)_3 + Ca^{2+} + 4OH^- \longrightarrow 7Ca_3(PO_4)_2 + HPO_4^{2-} + 4H_2O \tag{2.2}$$

$$8Ca_3(PO_4)_2 + Ca^{2+} + 4OH^- + H_2O \longrightarrow 5Ca_5(PO_4)_3OH + HPO_4^{2-} \tag{2.3}$$

More recently, Iijima et al. (1997) studied the transition between OCP and HAp at *p*H 7.4 and 37℃. They suggested that when water molecules were released from the hydrated layer, the apatitic domains were left, which then grew to form HAp. A previous study by Iijima et al. looked at the effect of carbonate (CO_3^{2-}) ions on the formation of OCP from metastable calcium phosphate solutions at *p*H 7.4 and 37℃ (Iijima et al., 1995). They found that the CO_3^{2-} ion changes the OCP/apatite ratio of the reaction product, with the ratio increasing and then decreasing when $[CO_3^{2-}]$ is raised ($0 \rightarrow 20$ mmol/l). Eidelman

and Eanes (2001) report on how the hydrolysis of OCP to HAp may be accelerated by F^- and inhibited by Mg^{2+} and Zn^{2+} ions.

2.2.5 Hydroxyapatite (HAp)

Hydroxyapatite ($Ca_{10}(PO_4)_6(OH)_2$) belongs to the hexagonal system with space group $P6_3/m$ (Kay et al., 1964). This space group has a six-fold c-axis which is perpendicular to three equivalent a-axes at angles of 120° to each other. A diagram of a unit cell can be seen in figure 2.10. Alternatively, the HAp unit cell structure can be thought of consisting

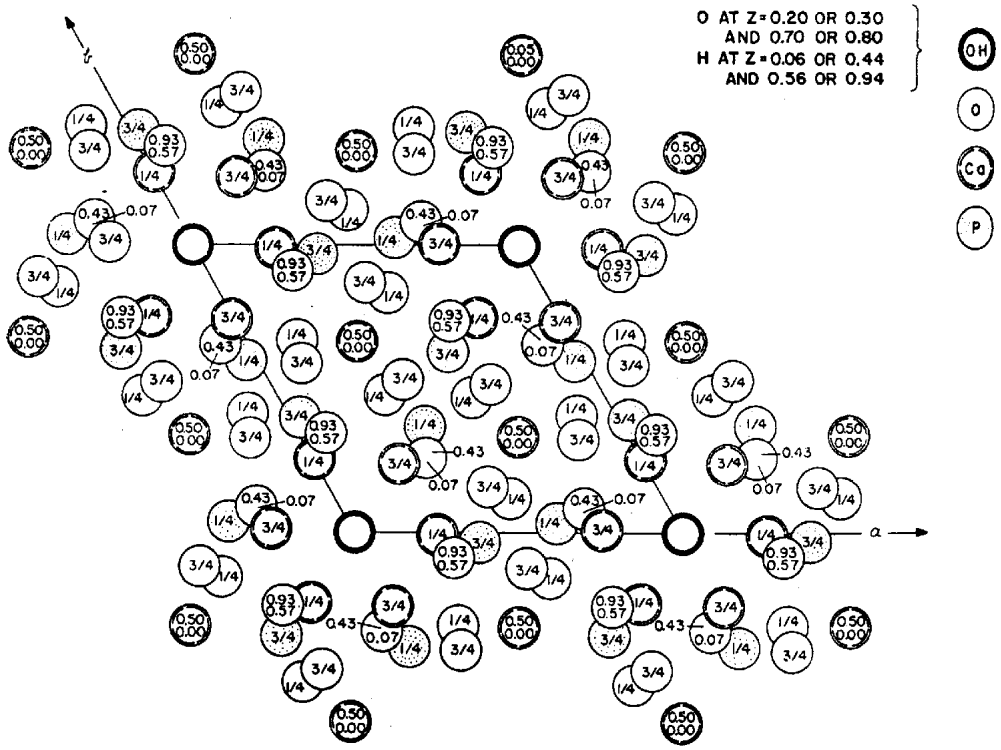

Figure 2.10: The atomic arrangement of hydroxyapatite projected on the $x - y$ plane. (Kay et al., 1964)

of two distinct types of Posner's cluster (see description of ACP section 2.1) of different chirality (right and left-handed) (Treboux et al., 2000). They have a non-centrosymmetric

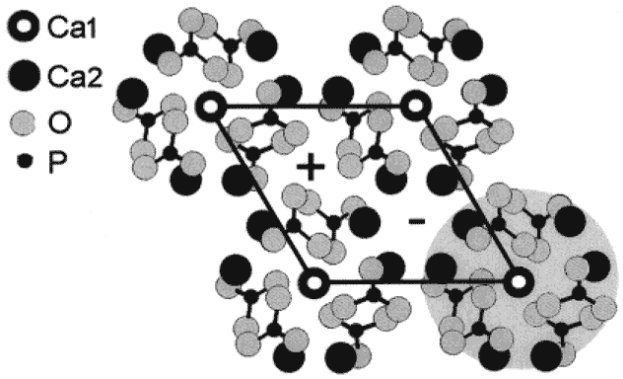

Figure 2.11: Schematic representation of the hydroxyapatite crystal projected on the *ab* plane. Four Posner's clusters ($Ca_9(PO_4)_6$) of identical chirality are represented. Positive and negative columns are formed parallel to the *c*-axis by the rest of the atoms (two OH groups and one Ca atom per unit cell). Black lines delimit the unit cell. One Posner's cluster (bottom right) is highlighted. The aggregation of three Posner's clusters of identical chirality around the positive column leads to the formation of a supplemental Posner's cluster of opposite chirality. (Treboux et al., 2000)

C_3 symmetry (3-fold rotation axis parallel to the *c*-axis). A schematic representation of this can be seen in figure 2.11.

It is very common for ion substitutions to occur in the structure of HAp. The ions incorporated can replace Ca, PO_4, or OH groups. Cations such as Pb^{2+}, Sr^{2+} and Ba^{2+} will tend to replace Ca^{2+}, . Anions such as F^- or Cl^- will substitute for OH^- and anionic groups such as CO_3^{2-} and HPO_4^{2-} will substitute for PO_4^{3-} (LeGeros, 1981). In fact, carbonate can substitute for either the hydroxyl (Type A substitution) or the phosphate groups (Type B) substitution. Suetsugu et al. (1998) determined the configuration of the carbonate ion in A-type substituted apatite. They concluded that the apatite crystal formed was hexagonal with space group $P\overline{6}$, with the CO_3 able to take up three configurations around the sixfold axis of rotatory inversion. LeGeros and LeGeros (1993) describe how the substitution of a smaller, planar carbonate group for a larger, tetrahedral PO_4 group, could cause a contraction in the *a*-axis and expansion in the *c*-axis dimensions when compared to carbonate free apatites. They also compiled data on the effects of

other ionic substitutions on crystal lattice parameters and the crystallinity of apatites. These can be seen in Table 2.

Table 2: Qualitative effects of some substituents for Ca^{2+}, PO_4^{3-} or OH^- in $Ca_{10}(PO_4)_6(OH)_2$ on the lattice parameters and crystallinity of apatites.(Adapted from LeGeros and LeGeros (1993))

Substituent	**Ionic Radius(Å)**	**Lattice Parameters (+/−0.003 Å)**		**Crystallinity**
		a-axis	**c-axis**	
for Calcium, Ca^{2+}	0.99	9.438	6.882	
Strontium, Sr^{2+}	1.12	(+)	(+)	(nc)
Barium, Ba^{2+}	1.34	(+)	(+)	(-)
Lead, Pb^{2+}	1.20	(+)	(+)	(-)
Potassium, K^+	1.33	(nc)	(nc)	(nc)
Sodium, Na^+	0.97	(nc)	(nc)	(nc)
Lithium, Li^+	0.68	(nc)	(nc)	(nc)
Magnesium, Mg^{2+}	0.66	(-)	(-)	(-)
Cadmium, Cd^{2+}	0.97	(-)	(-)	(-)
Manganese, Mn^{2+}	0.80	(-)	(-)	(-)
Zinc, Zn^{2+}	0.74	(+)	(+)	(-)
Aluminium, Al^{3+}	0.51	(+)	(+)	(-)
for OH^-				
Fluoride, F^-	1.36	(-)	(nc)	(-)
Chloride, Cl^-	1.81	(+)	(-)	(nc)
for PO_4^{3-}				
Carbonate, CO_3^{2-}		(-)	(+)	(-)
HPO_4^{2-}		(+)	(nc)	(nc)

(+) increase, (-) decrease, (nc) no change
If prepared at temperatures below 60 °C, CO_3, P_2O_7, Mg, Al, when present at a critical concentration in solution cause the formation of amorphous calcium phosphate.

Eanes and Hailer (1998) studied the effects of F^- on apatite crystal morphology, specifically those grown from physiologic-like solutions at 37 °C, whilst using constant composition methods. The formation of the apatite crystals was the result of a seeded precipitation reaction, in which apatite crystals were added to the reaction solutions. An increase in $[F^-]$ had the effect of accelerating the precipitation of new apatite. It was found that most of the F^- ions were incorporated into the newly formed solid. Physiologic carbonate concentrations in the reaction solutions were found to inhibit the apatite precipitation at

low concentrations and then slightly accelerate it at higher concentrations. The authors later concluded that the CO_3^{2-} ions promoted the growth of new crystals rather than further growth of the crystals used to seed the reaction. The addition of F^- to the carbonate containing solutions, however, had the same effect of increasing the rate of precipitation as it did in solutions which did not contain CO_3^{2-}. This reversal of the inhibitory effect of CO_3^{2-} led to a change in the morphology of the crystals resulting from the precipitation; they grew more in width rather than length.

The increased rate of formation of new apatite with the addition of F^- was proposed to be due either to the direct formation of fluoridated apatite or to increasing the rate of the hydrolysis of OCP to apatite. Mg^{2+} addition to the solution was found to strongly inhibit the formation of new solids and also there was a low uptake of the ion into the solid which did form.

A subsequent paper (Eanes and Hailer, 2000) took the constant composition experiment further, looking at the effect of various chemicals such as phosvitin, polyaspartate, polyglutamate, bovine serum albumin (BSA) and citrate on the morphology of the apatite crystals. All of the chemicals tested were found to inhibit the rate of precipitation. Citrate and BSA particularly, were found to favour the growth of smaller crystals, suggesting that growth of the seed crystals was suppressed in favour of new crystals. The other chemicals, however, were found to favour the growth of the seed material. The effect that these anionic chemicals had on the resulting crystal morphology was to increase the width of the crystals over the length, as was found previously for carbonate.

Corrand (1998) carried out an in-depth study on the effects of eight different biochemicals on the morphology and precipitation behaviour of HAp. The calcium-binding affinity (K_{ML}^{M}) of these molecules was then measured using a potentiometric method involving automated titrations and ion concentration monitoring. This allowed the ionic end groups of

the molecules to be ranked according to K_{ML}^{M}. The ranking order can be seen in equation 2.4.

$$-C-P-O_3^{2-} > -O-P-O_3^{2-} > -COO^- > -COO^-(+-NH_3^+) > -OH \qquad (2.4)$$

The molecules which had the lowest K_{ML}^{M} values (e.g. l-alanine) were found to have no significant effect on the precipitation rate of HAp (37.4 ℃, pH7.4). Those molecules which had a higher binding affinity (e.g. the phosphorylated molecules) were found to have have an antagonistic effect on the precipitation rate depending on concentration i.e their effect was competitive. At low concentrations, they would speed up the rate, but at higher concentrations, they would slow precipitation down. The molecules with the highest K_{ML}^{M} values were also found to inhibit type B carbonate substitution in the resulting apatite crystals.

2.3 Comparison of crystallographic properties

The structural properties of the calcium phosphate phases described in the previous sections are summarised in the following table:

Table 3: Structural characteristics of the calcium phosphates.

Phase	**Abbreviation**	**Chemical formula**	**Structure**	**a (Å)**	**b (Å)**	**c (Å)**
Amorphous calcium phosphate[1]	ACP	$[Ca_3(PO_4)_2]_n[H_2O]_m$	—	—	—	—
Dicalcium phosphate dihydrate[2]	DCPD	$CaHPO_4.2H_2O$	Monoclinic Ia (C_8^4)	5.812	15.180	6.239
α-Tricalcium Phosphate[3]	α-TCP	$Ca_3(PO_4)_2$	Monoclinic $P2_1/a$	12.887	27.280	15.219
β-Tricalcium Phosphate[4]	β-TCP	$Ca_3(PO_4)_2$	Rhombohedral R3c	10.43	10.43	37.39
Octacalcium Phosphate[5]	OCP	$Ca_8H_2(PO_4)_6.5H_2O$	Triclinic $P\bar{1}$	19.87	9.63	6.87
Hydroxyapatite[6]	HAp	$Ca_{10}(PO_4)_6OH_2$	Hexagonal $P6_3/m$	9.432	9.432	6.881

[1]Kanzaki et al. (2001) [2]Beevers (1958) [3]Mathew et al. (1977)
[4]Rangavittal et al. (2000) [5]Brown et al. (1962) [6]Kay et al. (1964)

2.4 Kinetics of precipitation and crystal growth

A description of the precipitation and subsequent crystal growth of calcium phosphates from aqueous solution will now be given, with particular reference to hydroxyapatite and to near-physiologic conditions (pH 7.4, 37 ℃).

2.4.1 Precipitation

2.4.1.1 Solubility

The direction of many reactions involving the calcium phosphates is determined by their solubility. For an aqueous solution containing a calcium component and a phosphate component, the solution can be described in terms of the actual components such as $Ca(OH)_2$ or H_3PO_4 and H_2O. Alternatively, the solution may be described in terms of the total calcium concentration [Ca^{2+}], the total phosphate concentration [PO_4^{3-}] and the solution pH.

Chow (2001) describes the definition of the solubility product constant for HAp. This definition makes use of the components present in the dissolution reaction of HAp:

$$Ca_5(PO_4)_3OH \text{ (solid)} \rightleftharpoons 5Ca(OH)_2 + 3H_3PO_4 - 9H_2O \tag{2.5}$$

In a saturated solution, in which the solid and solution are in equilibrium, the chemical potential for HAp at a standard state (μ°HAp) is given by:

$$\mu^\circ\text{HAp} = 5\mu Ca(OH)_2 + 3\mu H_3PO_4 - 9\mu H_2O \tag{2.6}$$

μ° of the designated component is constant at a given temperature and pressure. The chemical potentials of the components in aqueous solution, which vary with the composition of the solution (right hand side of equation 2.6) can be described by:

$$\mu\mathrm{Ca(OH)_2} = \mu^\circ\mathrm{Ca(OH)_2} + RT\ln(a_{Ca^{2+}})(a_{OH^-})^2 \tag{2.7}$$

$$\mu\mathrm{H_3PO_4} = \mu^\circ\mathrm{H_3PO_4} + RT\ln(a_{H^+})^3(a_{PO_4^{3-}}) \tag{2.8}$$

$$\mu\mathrm{H_2O} = \mu^\circ\mathrm{H_2O} + RT\ln(a_{H^+})(a_{OH^-}) \tag{2.9}$$

The quantities in parentheses are the activities (a_x, where x is the relevant ion). If equations 2.7, 2.8 and 2.9 are substituted into equation 2.6, the following is given:

$$\mu^\circ\mathrm{HAp} - (5\mu^\circ\mathrm{Ca(OH)_2} + 3\mu^\circ\mathrm{H_3PO_4} - 9\mu^\circ\mathrm{H_2O}) = RT\ln(a_{Ca^{2+}})^5(a_{PO_4^{3-}})^3(a_{OH^-}) \tag{2.10}$$

The left hand side of equation 2.10 is known as the standard free energy of dissolution for HAp ($\Delta\mathrm{G}^\circ_{\mathrm{HAp}}$):

$$\Delta\mathrm{G}^\circ_{\mathrm{HAp}} = \mu^\circ\mathrm{HAp} - (5\mu^\circ\mathrm{Ca(OH)_2} + 3\mu^\circ\mathrm{H_3PO_4} - 9\mu^\circ\mathrm{H_2O}) \tag{2.11}$$

The variable section on the right hand side of equation 2.10, $(a_{Ca^{2+}})^5(a_{PO_4^{3-}})^3(a_{OH^-})$, is known as the ionic activity product of HAp ($\mathrm{IAP_{HAp}}$). From equation 2.10 it can be seen that for any solution which is saturated with respect to HAp, $\mathrm{IAP_{HAp}}$ is related only to $\Delta\mathrm{G}^\circ_{\mathrm{HAp}}$ and is therefore a constant, termed the solubility product constant for HAp ($\mathrm{K_{sp(HAp)}}$):

$$\mathrm{K_{sp(HAp)}} = \mathrm{IAP_{HAp}} = (a_{Ca^{2+}})^5(a_{PO_4^{3-}})^3(a_{OH^-}) \tag{2.12}$$

The following table gives some experimentally determined values of $\mathrm{K_{sp}}$:

Table 4: Experimental values of K_{sp} at 37°C

K_{sp}	Value	Reference
$K_{sp(DCPD)}$	1.87×10^{-7}	Marshall (1970)
$K_{sp(TCP)}$	2.83×10^{-30}	Gregory et al. (1974)
$K_{sp(OCP)}$	5.01×10^{-50}	Moreno et al. (1960)
$K_{sp(HAp)}$	2.35×10^{-59}	McDowel et al. (1977)

2.4.1.2 Supersaturation

In order for precipitation of a phase to occur, it must be thermodynamically favourable for it to do so. This means that the solution must be supersaturated with respect to the phase which is to precipitate. Supersaturation (β), is defined as:

$$\beta = \left(\frac{\mathrm{IP}}{\mathrm{K_{sp}}}\right)^{\frac{1}{\upsilon}} \tag{2.13}$$

IP = the ionic product of the relevant ions

K_{sp} = the solubility product constant for the particular phase

υ = the number of ions in the resulting formula unit

(e.g for HAp, $\upsilon = (Ca^{2+})_{\mathbf{5}} + (PO_4^{3-})_{\mathbf{3}} + (OH^-)_{\mathbf{1}} = 9$)

The ionic product (IP), in equation 2.13 can be related to the IAP, (described earlier and in equation 2.12), by using calculated activity coefficients of ions derived from Debye-Hückel theory; this assumes that the ions behave like point charges in a continuous medium with a dielectric constant which is equal to that of the solvent. Butler (1964) described the Debye-Hückel limiting law, which applies to any completely dissociated electrolyte in sufficiently dilute solution and is given by:

$$-\log \chi = Az^2\sqrt{I} \tag{2.14}$$

χ = the activity coefficient of the ion

z = the charge on the ion

I = the ionic strength of the solution and is defined as half the sum of the concentration of each ion in the solution multiplied by the square of its charge:

$$I = \frac{1}{2}\sum_i [i] z_i^2 \tag{2.15}$$

A is a constant which is dependent upon the absolute temperature (T) and the dielectric constant of the solvent (ϵ):

$$A = 1.825 \times 10^6 (\epsilon T)^{\frac{-3}{2}} \tag{2.16}$$

The limiting law (equation 2.14) is obeyed only at ionic strengths below 1×10^{-2} molar, because of this, an extended version of the Debye-Hückel law was formulated, and was subsequently modified by Davies (1962) to give:

$$-\log \chi = Az^2 \left(\frac{\sqrt{I}}{1+\sqrt{I}} - 0.2I \right) \tag{2.17}$$

According to Butler (1964), the Davies modification gives a reasonable approximation of the values of χ, with an error of less than 3% at an ionic strength of 0.1 mol/l.

These values of χ can then be used to calculate ionic product of the solution for a particular phase by multiplying the activity coefficient by the ionic activities for the ions: For HAp, $\mathrm{IAP_{HAp}} = (a_{Ca^{2+}})^5 (a_{PO_4^{3-}})^3 (a_{OH^-})$ (as stated in 2.12) and,

$$\mathrm{IP_{HAp}} = [\mathrm{Ca^{2+}}]^5 [\mathrm{PO_4^{3-}}]^3 [\mathrm{OH^-}] \chi_1 \chi_2^5 \chi_3^3 \tag{2.18}$$

Where χ_1, χ_2 and χ_3 are are the ionic activity coefficients for z = 1, 2 and 3 respectively.

The same derivation is used to work out the ionic products for other phases:

$$\mathrm{IP_{ACP}} = [\mathrm{Ca^{2+}}]^3[\mathrm{PO_4^{3-}}]^2[\mathrm{H^+}][\mathrm{OH^-}]\chi_1^2\chi_2^3\chi_3^2 \tag{2.19}$$

$$\mathrm{IP_{TCP}} = [\mathrm{Ca^{2+}}]^3[\mathrm{PO_4^{3-}}]^2\chi_2^3\chi_3^2 \tag{2.20}$$

$$\mathrm{IP_{DCPD}} = [\mathrm{Ca^{2+}}][\mathrm{HPO_4^{2-}}]\chi_2^2 \tag{2.21}$$

$$\mathrm{IP_{OCP}} = [\mathrm{Ca^{2+}}]^4[\mathrm{H^+}][\mathrm{PO_4^{3-}}]^3\chi_1\chi_2^4\chi_3^3 \tag{2.22}$$

The solubility product ($\mathrm{K_{sp}}$) for ions of the relevant phases when in equilibrium with the solid phase can be described as follows:

$$\text{For DCPD} \quad \mathrm{CaHPO_4 \cdot 2H_2O(s) \Leftrightarrow Ca^{2+}(aq) + HPO_4^{2-}(aq)}$$

$$\mathrm{K_{sp(DCPD)}} = ([\mathrm{Ca^{2+}}]\chi_2)_{eq}([\mathrm{HPO_4^{2-}}]\chi_2)_{eq}$$

$$\text{For OCP} \quad \mathrm{Ca_4H(PO_4)_3 \cdot 2.5H_2O(s) \Leftrightarrow 4Ca^{2+}(aq) + H^+(aq) + 3PO_4^{3-}(aq)}$$

$$\mathrm{K_{sp(OCP)}} = ([\mathrm{Ca^{2+}}]\chi_2)_{eq}^4([\mathrm{H^+}]\chi_1)_{eq}([\mathrm{PO_4^{3-}}]\chi_3)_{eq}^3$$

$$\text{For HAp} \quad \mathrm{Ca_5H(PO_4)_3OH(s) \Leftrightarrow 5Ca^{2+}(aq) + 3PO_4^{3-}(aq) + OH^-(aq)}$$

$$\mathrm{K_{sp(HAp)}} = ([\mathrm{Ca^{2+}}]\chi_2)_{eq}^5([\mathrm{PO_4^{3-}}]\chi_3)_{eq}^3([\mathrm{OH^-}]\chi_1)_{eq} \tag{2.23}$$

If the value of β determined from equation 2.13 is greater than 1, then the solution is said to be supersaturated with respect to the phase in question. In this case it is thermodynamically viable for the phase to precipitate from solution.

For more detail on practical calculation of supersaturation please see Appendix A.

2.4.2 Crystal Growth of Hydroxyapatite (HAp)

Koutsopoulos (2001) has studied the crystal growth of HAp at 37℃ and *p*H 7.4 in a

metastable calcium phosphate solution. The crystal growth was initiated by adding calcium chloride solution to a phosphate solution, which already contained HAp seed crystals. The crystals were added first in order to allow the surfaces of the crystals to equilibrate with the surrounding liquid before precipitation started. Constant-composition[4] conditions were used for the kinetic studies.

The crystallisation of HAp was found to occur exclusively at active growth sites on the seed crystals, rather than through spontaneous precipitation or secondary nucleation. This could be determined because variations in seed crystal concentration did not affect the crystal-growth rate. Additionally, through variable stirring-rate experiments, the rate determining step in the growth of the crystals was found to be surface diffusion of the growth units, rather than diffusion of the growth units through a stagnant layer at the crystal surface from the bulk solution or by transport of the crystal particles into the solution.

Under these conditions, (supersaturated solution under constant composition conditions at *p*H 7.4 and 37℃), spiral growth on the crystal surface explained the data best (Koutsopoulos, 2001).

Christoffersen, Dohrup and Christoffersen (1998) describe a growth model which is based on a polynuclear mechanism in which there are very few hydroxyl ions in the surface of HAp crystals. Hydroxyl ions are produced from trapped water molecules in the surface, which dissociate as Ca^{2+} and PO_4^{3-} ions enter the crystal surface. They then used this model when looking at the growth of HAp in solutions with varying calcium to phosphate ratios (Christoffersen, Dohrup and Chrisoffersen, 1998). The model was found to describe the growth rate reasonably well. The authors concluded that the the growth

[4]Experimental procedure in which constant molarity of all of the reactants is maintained in a supersaturated solution (after Koutsoukos et al. (1980))

was strongly influenced by hydroxyl ion formation below the growing surface.

2.5 Biological Calcium Phosphate

The calcium phosphate phases discussed so far have been synthetic in origin. Although they have attracted interest due to the similarity of their composition with that of the calcified tissues in the body, many differences exist between manufactured CaP and those in nature. It is important to understand these differences in order to be able to produce materials which will be compatible with those found *in vivo*.

2.5.1 Biological Apatite

The biological apatites differ from pure HAp in terms of their stoichiometry, composition and crystallinity. According to LeGeros and LeGeros (1993), biological apatites are usually calcium-deficient and are always carbonate substituted. Many now believe that enamel, dentine and bone mineral can be said to consist of one phase, carbonatehydroxyapatite. This has the approximate formula: $(\mathrm{Ca, Mg, Na})_{10}(\mathrm{PO_4, HPO_4, CO_3})_6(\mathrm{OH, Cl, F})_2$ (LeGeros, 2002).

There has been long running controversy over whether there is an amorphous calcium phosphate phase present in bone mineral. Glimcher et al. (1981), argued that previous x-ray diffraction studies, which reported to find an amorphous component of bone were flawed. By looking at the radial density functions of the x-ray data, they concluded that order could in fact be seen in bone tissue, even in the embryonic stage. This questioned the old supposition that young bone contained a very high quantity of ACP, which transformed into more crystalline phases with age. The evidence for the presence of other phases such as OCP in biological systems has also been termed 'ambiguous' (Eidelman and Eanes,

2001), possibly due to the complexity of the tissues found and the preparation methods required in order to analyse them.

In terms of morphology, the bone mineral consists of platelets of variable length which have widths of 30 to 45 nm and a thickness of approximately 5 nm. The platlets are orientated with their *c*-axes parallel to one another and lie along the collagen fibrils (LeGeros, 2002).

2.5.2 Composition of Bone

The following table compares the composition, stoichiometry and mechanical properties of enamel, bone and HAp:

Table 5: Comparative Composition, Crystallographic and Mechanical Properties of Human Enamel, Bone and Hydroxyapatite Ceramic. (Adapted from LeGeros and LeGeros (1993))

	Enamel	**Bone**	**HAp**
Constituents (wt %)			
Calcium, Ca^{2+}	36.0	24.5	39.6
Phosphorus, P	17.7	11.5	18.5
(Ca/P) molar	1.62	1.65	1.67
Sodium, Na^{+}	0.5	0.7	trace
Potassium, K^{+}	0.08	0.03	trace
Magnesium, Mg^{2+}	0.44	0.55	trace
Carbonate, CO_3^{2+}	3.2	5.8	—
Fluoride, F^{-}	0.01	0.02	—
Chloride, Cl^{-}	0.30	0.10	—
Ash (total inorganic)	97.0	65.0	100
Total organic	1.0	25.0	—
Absorbed H_2O	1.5	9.7*	—
Trace elements: Sr^{2+}, Pb^{2+}, $Ba^{2+}, Fe^{3+}, Zn^{2+}, Cu^{2+}$, etc.			
Crystallographic properties			
Lattice parameters ($+/-$ 0.003Å)			
a-axis	9.441	9.419	9.422
c-axis	6.882	6.880	6.880
Crystallinity index	$70 - 75$	$33 - 37$	100
Crystallite size, Å	1300×300	$250 \times 25 - 50$	
Products after sintering (950°C)	HAp + TCP	HAp + CaO	HAp
Mechanical Properties			
Elastic modulus (GPa)	82.4†	20*‡	112§
Tensile strength (MPa)	70	150*	100

*Values for cortical bone
†Peyton (1968)
‡Bayrakta et al. (2004)
§de With et al. (1981)

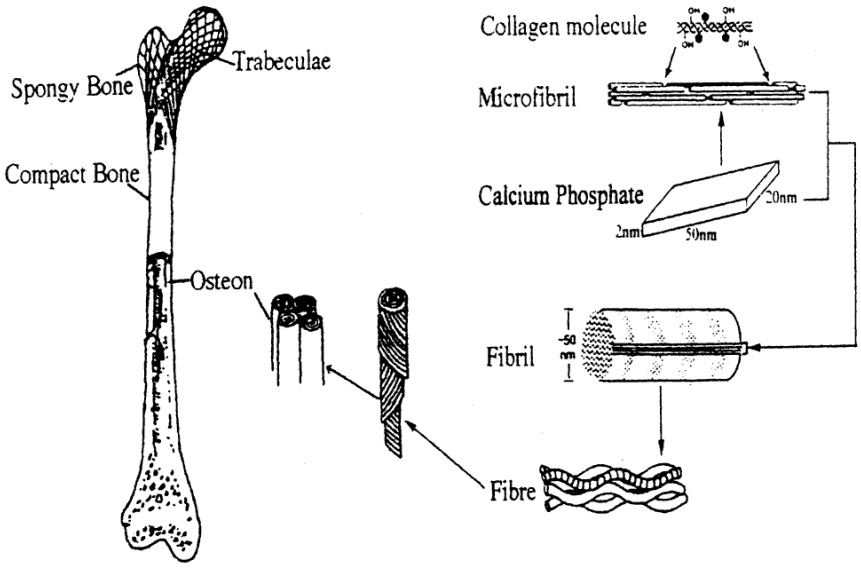

Figure 2.12: Schematic representation of the hierarchy in bone (Lawson and Czernuszka, 1998)

2.5.3 Structure of Bone

Collagen and apatite are arranged in a highly organised hierarchical structure as shown in Figure 2.5.3. Weiner and Wagner (1998) described seven levels of organisation:

(i). The major components; apatite crystals, type I collagen and water.

(ii). The combination of the plate-like apatite crystals and the collagen microfibrils forming mineralised fibrils.

(iii). Bundles of fibrils which form fibres (or fibril arrays).

(iv). A level of structure which is dependent on the way that the fibrils are organised, for example they can be parallel (as in fish bones), woven (as in mammalian embryos) or radial (as in dentin).

(v). Cylindrical motifs called osteons or Haversian systems formed as a result of bone remodelling by cells.

(vi). A macrostructure of either solid bone (also known as cortical or compact bone) or spongy (trabecular) bone.

(vi). The final level of organisation - whole bones.

2.6 Biological Mineralisation

This section will give a brief overview of the current opinions held about the process by which calcium phosphates are deposited in living tissue.

Betts et al. (1981) split their description of the different tissue mineralisation theories into three categories:

(i). Mechanisms which raise the local Ca^{2+} and PO_4^{3-} ion product to levels sufficient for spontaneous precipitation. For example, a marker for active tissue mineralisation is the enzyme alkaline phosphatase, this is said to hydrolyse phosphate esters, leading to an excess of free organic phosphate, which in turn will raise the Ca^{2+} and PO_4^{3-} ion product.

(ii). Substances or mechanisms that create nucleating sites and/or remove any barriers to these sites.

(iii). Mechanisms/substances which prevent the formation of mineral and must be rendered inactive or removed to permit calcification.

There has been much debate over whether the mineralisation process starts with organic molecules such as collagen (as reviewed by Mann (1988)) or by associations with extra-cellular matrix vesicles (Hoshi and Ozawa, 2000; Murphy and Messersmith, 2000).

The collagen theory stems from the fact that there are well-defined crystallographic relationships between the calcium phosphate crystals deposited in bone and the macromolecular substrate on which they are deposited (Mann, 1988). The configuration of collagen fibrils found in calcified tissues is a quarter-staggered arrangement this means that holes and grooves are found to be arranged across the fibrils. It is thought that nucleation of mineral phases can take place in these structures, leading to the crystallographic configuration discovered. However, according to authors such as Hoshi and Ozawa (2000), the presence of 40 to 200 nm, membrane-bound structures, observed by electron microscopy in bone formation studies, leads to the conclusion that these structures are somehow involved in the calcification process. These vesicles have been found to contain HAp crystals, suggesting that they serve as sites of initial nucleation. Boskey (1998) came to the conclusion that perhaps matrix vesicle-based mineralisation occurs alongside collagen-based mineralisation at sites where the collagen-based process is not favoured but, in other tissues, vesicles are not required.

2.7 Coating Methodology

Combining the strength of orthopaedic alloys such as TiAl(6%)V(4%) with the bioactivity of CaP materials, in the form of a coating, has been achieved by many methods. Examples of such methods include pulsed laser deposition (Clèries et al., 2000), surface coating by casting (Sohmura et al., 2001), ion-beam sputter deposition (Lucas et al., 1993), plasma spraying (Lacefield, 1993; Sun et al., 2001), biomimetic precipitation (Yan et al., 1997; Habibovic et al., 2002) and electrodeposition (Shirkhanzadeh et al., 1994; Peaker and Czernuszka, 1996; Haddow et al., 1999; Manso et al., 2000).

There are certain quality specifications for the coatings which must be met, no matter

which production technique is used. These include the phase composition, Ca/P ratio, crystallinity, microstructure, porosity, surface roughness and thickness (Sun et al., 2001; Geesink, 2002). The American Food and Drug Administration has produced guidelines to which hydroxyapatite coatings must conform (Table 6).

Table 6: Hydroxyapatite Coating Requirements.(Adapted from Geesink (2002))

Property	**Specification**
Thickness	not specified
Crystallinity	62% minimum
Phase purity	95% minimum
Ca/P ratio	1.67-1.76
Density	2.98 g/cm^3
Heavy metals	<50 ppm
Tensile strength	>50.8 MPa
Shear strength	>22 MPa
Abrasion test	not specified

Data Source: Food and Drug Administration: Calcium Phosphate (Ca-P) Coating Draft Guidance for preparation of Food and Drug Administration Submissions for Orthopaedic and Dental Endosseous Implants. Baltimore, Food and Drug Administration, 1992.

2.7.1 Current methods

There are comparative advantages and disadvantages of the various techniques used to coat the metallic substrates. Plasma spraying is the most commonly used technique. This is owing to the speed at which thick, visually uniform coatings can be produced on a large scale. However, there are many concerns over the fact that the feedstock HAp powder is accelerated to a high velocity and heated in a plasma which can reach temperatures as high as 30,000 K, before being rapidly cooled when it hits the metallic substrate (Sun et al., 2001). Because of this, the structure and composition of the coating is significantly different from the feedstock material. This means that the coating is of a lower purity (Geesink, 1989) and crystallinity than the starting HAp. New phases which are commonly found in the coating include an amorphous component as well as

tricalcium phosphate ($Ca_3(PO_4)_2$) tetracalcium phosphate ($Ca_4P_2O_9$, TTCP) and calcium oxide (CaO) (Sun et al., 2001). Residual stresses (both compressive and tensile) have been found to exist in these coatings and are said to lead to a variety of methods of failure as well as affecting the thermodynamics of coating dissolution (Sergo et al., 1997). The high temperatures involved in plasma spraying lead to the inability to add any temperature-sensitive biological molecules such as antibiotics or growth factors. Finally, the fact that the process is line-of-sight means that it is also difficult to adequately coat complex shapes and porous surfaces.

Because (plasma sprayed) HAp coatings have been in clinical use since the mid 1980's (Geesink, 1989), analyses exist of their performance when implanted into humans. For example, Önsten et al. (1998) looked at the results of a randomised series of 116 knee replacements using hydroxyapatite-augmented porous coatings, porous coatings, and cemented fixation of tibial components of the same design. The hydroxyapatite-augmented porous coatings were found to be more stable than the porous implants between 12 and 24 months post-operatively. However, no stability difference was found between HAp-augmented and cemented components.

A study by Røkkum et al. (1999) followed 100 consecutive hip arthroplasties for 7 to 9 years. Implant cups and stems coated with HAp were used in all cases. There was extensive bony incorporation in all of the components, as determined by radiography. There were no cases of stems loosening, but five acetabular cups had to be revised. Various other reports in the literature are equally positive (Kroon and Freeman, 1992; Søballe and Overgaard, 1996; Capello et al., 1998; Hamadouche and Sedel, 2000; Geesink, 2002).

Gross et al. (2002) looked at the link between variations in the microstructure of plasma sprayed HAp coatings and the pattern of coating loss on an implant removed from a subject during revision surgery. They concluded that variations in coating crystallinity may

have led to faster coating degradation on some (more amorphous) areas of the implant, releasing particles that were more crystalline in nature, such as unmelted feedstock material and other particulate matter. These particles could have then caused inflammation and implant loosening as a result of the immune response which they trigger.

2.7.2 Biomimetic methods

Biomimetic coating methods are those which mimic the bone formation process *in vivo* i.e. at low temperatures and in simulated body fluid (SBF). These methods are hoped to overcome many of the problems associated with the high temperatures and unpredictable results of plasma spraying methods.

The biomimetic method can often take up to 14 days to complete, with the SBF needing to be changed several times during coating (Li and Ducheyne, 1998). To shorten coating times, the substrate surface can be treated to enhance deposition rate, the SBF concentration increased, or a combination of both practices used (Wang et al., 2004).

Habibovic et al. (2002) suggested that there are four main advantages of biomimetic approaches:

1. The low temperature at which the process takes place allows applications on heat sensitive substrates, including polymers.

2. Apatite crystals similar to those found in bone tissue are formed. These have good resorption characteristics and are highly bioactive.

3. The coating is evenly deposited on or into complex or porous implant geometry.

4. Temperature sensitive factors, such as those which stimulate bone growth can be incorporated.

In order to increase the ionic concentration of their SBF, Habibovic et al. (2002) added CO_2 to their solutions, thereby reducing the *p*H and increasing the solubility of CaP. As the CO_2 released slowly from solution, both the *p*H and saturation of the solutions increased, leading to precipitation of the coating material. Samples were first coated with a thin layer of CaP growth nuclei by being left for 24 hours in a SBF solution at 37 ℃. This first solution contained relatively high levels of HCO_3^- and Mg^{2+} ions which slowed any precipitation. More rapid coating was then achieved by transferring the samples to a similar coating solution but this time with lower levels of the inhibitory ion species. Incubation in the second solution occurred for 48 h at 50℃. The resultant coating was described as closely resembling bone mineral and being around 30 µm in thickness.

If the initial coating with CaP nuclei was skipped and the clean Ti(6%)Al(4%)V was put straight into the second stage of the process, a more loose and non-uniform coating was obtained than when both steps were used. Habibovic et al. (2002) go on to conclude that heterogeneous and homogeneous CaP nucleation compete in the second coating stage, but since nuclei are more energetically stable on the seeded metal surface than in solution, the initial amorphous CaP primer layer (produced in the first solution) is essential.

This study has since been followed up with a much closer look at the calcium phosphate nuclei on the metal surface using techniques such as atomic force microscopy (AFM) and environmental scanning electron microscopy (ESEM) (Barrère et al., 2004). They found that CaP deposits started to form on the metal surface after just ten minutes in an SBF solution made up to five times the usual concentration (SBF×5). This formation of deposits on the surface happened long before precipitation of CaP occurred in the solution, therefore heterogeneous nucleation was taking place. Initial deposits formed were on the scale of a few nanometres across but after ≈ 2 h, these had grown to the region of 50-100 nm across. A continuous coating was found after ≈ 4 h. They also observed a glassy

matrix at the interface between the CaP globules and the titanium alloy surface. It was speculated that this could be composed of Posner's clusters ($Ca_9(PO_4)_6$, Section 2.2.1), stabilised by magnesium ions and water.

Lin et al. (2002) encountered problems when trying to deposit an apatite layer from SBF onto their heat and alkali-treated 316L stainless steel samples at 37 ℃. Iron oxides and iron chromium oxides formed at the surface of their samples, weakening the attachment of any coating produced. Increasing the reaction temperature to 80 ℃ seemed to help prevent this. The paper makes several assumptions however, for example about a 50 to 100 µm coating being necessary for bone bonding.

To determine the effectiveness of biomimetic coatings *in vivo*, a study by Yan et al. (1997) compared the bone bonding strength of uncoated titanium and apatite-layer coated titanium. The coating was produced using a SBF method. After manufacture, the samples were implanted into the tibiae of rabbits. At all time periods when the animals were sacrificed (6,10 and 25 weeks after implantation) the tensile failure load, when the implants became detached from the bone, was significantly higher for the coated as opposed to uncoated samples. Histological examination revealed that there was active bone formation directly around the apatite coated implants, whereas there was an intervening fibrous tissue layer present in the non-coated implants.

2.7.3 Electrodeposition Techniques

The current uses of electrodeposition are diverse and numerous. Boccaccini and Zhitomirsky (2002) describe many of these applications such as in the production of solid oxide fuel cells, for producing fibre reinforced ceramic matrix composites, depositing superconducting films and in producing a variety of different coating types from those used

in electronic applications to those designed for wear and corrosion resistance. Organic automotive coatings are frequently applied with the assistance of electrodeposition as are laminate coatings which can be manufactured by alternating the coating solution compositions (van der Biest and Vandeperre, 1999). However, despite the wide-ranging uses of electrodeposition, the actual mechanisms of deposition are not yet fully understood.

Electrodeposition techniques are said to share the advantages of biomimetic methods (section 2.7.2) but with many added benefits that include:

- A reduction in coating time and dependence on substrate chemistry (Haddow et al., 1999)
- added ease of process control (Rößler et al., 2002)
- better packing and uniformity of the deposit (Zhitomirsky and Gal-Or, 1997)
- regulation of coating morphology and microstructure through control of current density and loading time (Ban and Maruno, 1998b).

The mechanisms of electrodeposition of CaP materials can be divided into those which are electrophoretic and those which are electrolytic. It appears that the main characteristic distinguishing the two processes is that electrolytic deposition uses a solution of metal salts, and is used to produce thin films, rather than the suspensions of particles used in the electrophoretic process, which are used to produce thicker powder-compact coatings. Each process will now be described separately.

2.7.3.1 Electrophoretic deposition (EPD)

In their reviews of the process, van der Biest and Vandeperre (1999); Zhitomirsky (2002) and Boccaccini and Zhitomirsky (2002) describe how electrophoretic deposition is a two-

step process in which charged ceramic particles that are suspended in a liquid medium firstly migrate in an electric field and secondly collect to form a deposit on the electrode.

Charged particles in suspension are said to be surrounded by what is termed the "double layer." This is a cloud of ions with an opposite charge which are present around the particle in a concentration higher than that found in the bulk solution. A schematic of the double layer can be seen in figure 2.13.

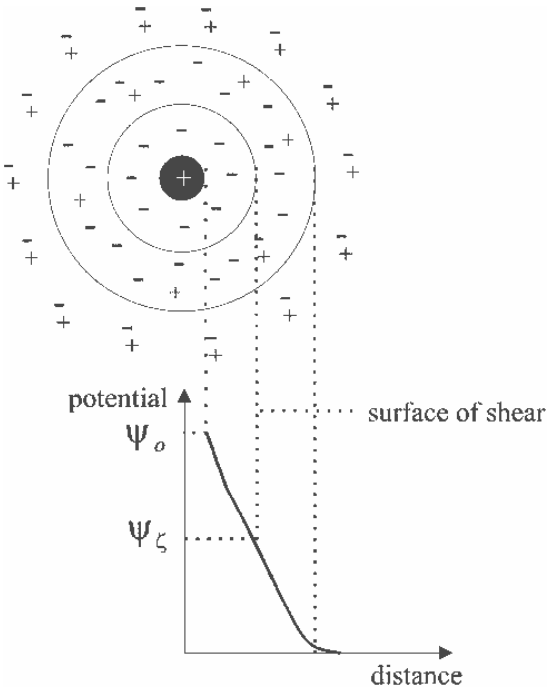

Figure 2.13: Schematic of the double layer surrounding a charged particle and the evolution of the electric potential from the surface potential, Ψ_0, to zero far from the particle. The potential at the surface of shear, the limit between the liquid moving with the particle and the liquid which does not move with the particle, is termed the zeta-potential, Ψ_ζ, and is the main parameter determining the electrokinetic behaviour of the particle (van der Biest and Vandeperre, 1999)

The ions and the particle should move in opposite directions when an electric field is applied, but these ions are also attracted by the particle. Because of this some of the ions will move along with the particle and the speed of the particle is not determined by the charge on the surface of said particle itself but by the net charge enclosed within the

liquid sphere (van der Biest and Vandeperre, 1999).

Many of the models of how EPD takes place depend upon the Derjaguin-Landau-Verwey-Overbeek (DLVO) colloidal stability theorems (Derjaguin and Landau, 1941; Verwey and Overbeek, 1948). These state that interactions between particles consist of the repulsion between their double layers and their van der Waals' attraction. The research of recent years has shown that other forces can also act which can result in particle coagulation and affect film stability (Zhitomirsky, 2002). DVLO theory is also important in current understanding of electrolytic deposition (Section 2.7.3.2).

For the deposition part of the electrophoretic process; Boccaccini and Zhitomirsky (2002); Zhitomirsky (2002) and van der Biest and Vandeperre (1999) describe many conflicting views of how it occurs. The original idea was that of Hamaker and Verwey (1940) who described deposit formation to be comparable to sedimentation due to gravity. This way, the particles can overcome their repulsion to each other, when close to the electrode, due to the pressure that is being exerted by the incoming particles.

Reactions taking place at the electrodes and the resultant change in the chemistry of the surrounding solution are agreed to have a direct effect on the deposition process. For example the reduction of water at the cathode will lead to an increase in *p*H due to the formation of OH^- ions (equation 2.24) as will the reduction of any dissolved oxygen (equation 2.25).

$$2H_2O + 2e^- \rightarrow H_2 + 2OH^- \tag{2.24}$$

$$O_2 + 2H_2O + 4e^- \rightarrow 4OH^- \tag{2.25}$$

This *p*H increase will affect the solubility of many ions in solution and will also affect the zeta potential (Ψ_ζ, Figure 2.14) of the particles. Studies specifically looking at the

*p*H change around electrodes during electrodeposition will be described later on (Section 2.7.3.3).

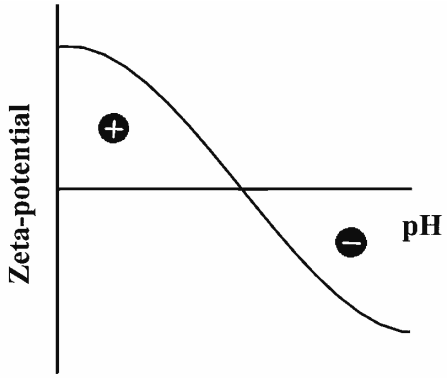

Figure 2.14: Zeta potential of ceramic particles versus *p*H of suspension (Zhitomirsky, 2002)

A decrease in the magnitude of the interparticle repulsive forces can lead to flocculation of the fine particles which then collapse into a deposit. Koelmans (1955) suggested that the increase in electrolyte or hydroxyl ion concentration around the electrode would be sufficient to flocculate the particles, whereas Grillon et al. (1992) suggested that particles lose their charge upon coming in contact with the electrode or the deposit. Sarkar and Nicholson (1996) took the view that the thinning of the double layer ahead of a particle in motion and recombination with the counter ions which move along with the particle, could account for overcoming the repulsion barrier between the particles that form a deposit.

Whatever the specific mechanisms of deposit formation, the fact that the coating formed is only a powder compact means that some sort of post-deposition densification step is required. This may take the form of curing, sintering, or firing to reducing coating porosity and agglomerate the powder (van der Biest and Vandeperre, 1999; Boccaccini and Zhitomirsky, 2002). This is obviously a particular problem if heat sensitive substrates or coating additives are going to be used.

In their study on the EPD of HAp, Zhitomirsky and Gal-Or (1997) overcame poten-

tial problems of water being adsorbed onto the particles by carrying out the process in isopropyl alcohol. This is also said to have reduced the gas evolution which occurs when using water as a suspension medium. The weight of the deposit formed was found to increase with the voltage and deposition time. Presedimentation of the powders allowed larger particles to be removed from the solution resulting in the deposits being made up of finer particles alone. Using lower voltages (i.e. 20 V rather than 200 V) also led to a finer structure.

Gottlander et al. (1997) deposited calcium deficient HAp electrophoretically on to commercially pure titanium implants. The EPD process was carried out in isopropyl alcohol with a potential of 60 V. After sintering at 900℃ the implants were inserted into the femurs and tibiae of rabbits.

After four weeks, the bone to implant contact percentage was found to be 5.4% for the control (uncoated) tibial implants, whereas it was 17.4% for the CaP coated implants. However, after six months, there was no significant difference in this value between the two types of implant (37.6% for the control, 37.8% for the coated). The control implants were found to have significantly more bone growing in the threads of the implant after six months when compared to those that had been CaP coated.

Peaker and Czernuszka (1996) used an alternative electrophoretic method where, according to the authors, the particles of HAp were formed in a continuously precipitating CaP. These particles initially form as ACP which coalesces in the solution to form gel-like sheets. The HAp crystals are said to nucleate within these sheets and continue to grow after the sheets have been deposited onto the cathode. The HAp crystals were deposited with their *c*-axis perpendicular to the substrate. Optimum coating conditions were said to be an electrode spacing of 2.25 cm at 52℃ with a starting calcium concentration of 1.75 mmol/l and a starting *p*H of 7.4.

2.7.3.2 Electrolytic deposition (ELD)

In the electrolytic process metal ions or complexes are hydrolysed by base molecules generated in electrode reactions (Equations 2.24 and 2.25, Section 2.7.3.1) to form colloidal particles which then coagulate to form deposits on the electrode substrate. The electrolytic process is usually cathodic. As in the case of electrophoretic deposition (Section 2.7.3.1), increased electrolyte concentrations around the electrode are thought to initiate a flocculation process (Zhitomirsky, 2002). Therefore many of the same theorems and models of particle interaction and deposition are valid for both ELD and EPD (e.g. DLVO theory).

Electrolytic deposition is generally seen as useful in the production of thin, nanostructured ceramic films as opposed to the thick powder agglomerate films produced by the electrophoretic process (Zhitomirsky, 2002).

Ban and Maruno (1993) used an ELD technique in simulated body fluid (SBF) buffered to a starting *p*H of 7.2 at 22℃. The potential used was 2 V. Amorphous calcium phosphates were formed with the amount of product being proportional to the square root of the deposition time. It was concluded that the diffusion of ions around the cathode was the rate determining step. In a later paper, the authors went on to study what effect the buffering of the electrolytic solution had on the deposition (Ban and Maruno, 1994). Much more CaP was deposited on the cathode in the presence of buffer than without *p*H stabilisation. This could be attributed to the fact that the *p*H rose sharply in the whole solution without buffering, leading to the precipitation of CaP, even far away from the electrode. The buffer served to maintain the status quo in the solution apart from in the area immediately surrounding the cathode, where deposition could take place.

Shirkhanzadeh et al. (1994) produced HAp coatings by electrolysis at 65℃. The sam-

ples were then treated in steam for four hours before being calcined at 425℃ for six hours. Sodium fluoride was added to the coating solution during the manufacture of one set of samples. The F^- ions were found to successfully substitute for the OH^- groups in the hydroxyapatite crystal structure. The other samples were said to consist of pure HAp.

Many other experiments have been carried out on ELD of calcium phosphate coatings often with very similar methods using a modified SBF (Ban et al., 1997; Ban and Maruno, 1998a;b; Haddow et al., 1999), these were often carried out at temperatures much higher than those found in physiological systems. Rößler et al. (2002) claimed to be the first to carry out electrodeposition of CaP at both near physiological *p*H and temperature. They carried out their coating process at 36℃ at *p*H 6.4. The process of CaP formation was followed by atomic force microscopy. From the data gathered, they formed a model of how they thought that this first layer formed (Figure 2.15). The model involves the formation of channels which act as pathways for the hydrogen and hydroxyl acid in the growing layer. The calcium phosphate 'prelayer' and the ACP spheres which were found

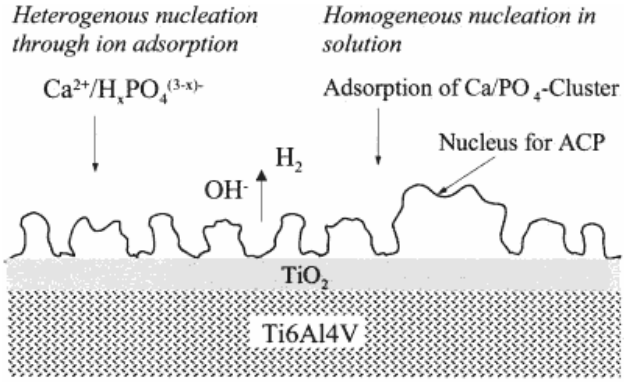

Figure 2.15: Scheme of nucleation and growth of a calcium phosphate prelayer on a cathodically polarised titanium surface. (Rößler et al., 2002)

upon it were suggested to be made up of $Ca_3(PO_4)_2$ clusters which were able to transform directly into HAp needles.

Instead of using a CaP prelayer, Park et al. (2004) treated their pure titanium substrates with NaOH before coating by electrodeposition from a modified SPF. This coating was found to contain mainly HAp and DCPD (section 2.2.2), which nearly all transformed to HAp after five days in a SBF at 36.5℃. By contrast, the control coatings, deposited on substrate which was not pretreated, consisted mainly of ACP and DCPD which was also described as less dense and less uniform in appearance. Most of this coating was also converted to HAp after 5 days maturation in SBF.

2.7.3.3 *p*H distribution around the electrodes

The first study to measure the *p*H at the substrate solution interface during CaP electrodeposition used a *p*H-microsensor technique (Zhang et al., 1998). The sensor was made from iridium oxide that had been electrochemically deposited onto platinum wire. During the CaP deposition (starting *p*H 4.5 at 60℃) the *p*H rose sharply during the first five minutes of coating (up to *p*H 8.4 for the highest current density tested of 5 $mA/cm)^2$ before beginning to decrease again very gradually. The *p*H increase was related to the current density that they used, as was the type of CaP that was deposited. For low densities ($\approx$ 1 $mA/cm)^2$ mainly DCPD and OCP were deposited as opposed to HAp being deposited at the highest current density.

Ban and Maruno (1999) used a *p*H imaging microscope during their process, which started at *p*H 7.2 and 80℃. Buffered and unbuffered solutions were compared. In the experiments without buffer, the *p*H at the electrode surface rose immediately, followed by the *p*H of the bulk of the solution in the electrolytic cell, which reached *p*H 11.9 after the current had been switched on for approximately 90 s. The *p*H also increased at the electrode surface in the presence of buffer, although this increase was not as dramatic. Far away from the electrode ($>$ 5 mm away), the *p*H was maintained at roughly the same

level as measured initially, however there was a layer of the solution ≈ 4 mm away from the electrode where the *p*H dropped to 2.8 during coating. This was attributed to the vigorous formation of H_2 gas on the electrode which was then adsorbed into the solution.

2.7.4 Coating adhesion

The American Society for Testing and Materials (*Definition of Terms Relating to Adhesion*, 1970) defines adhesion as the

> "condition in which two surfaces are held together by either valence forces or by mechanical anchoring or by both together."

Dini (1993) cites Chapman (1974) when describing how the mechanisms of adhesion can be split into the following types:

- **Interfacial adhesion.** Adhesive forces centred around a well defined interface with minimal atomic mixing.
- **Interdiffusion adhesion.** In this case the interface is more diffuse and extends for many atomic layers.
- **Intermediate layer adhesion.** The coating and substrate are separated by one or more layers of a different material (e.g. an oxide layer).
- **Mechanical interlocking.** This occurs whenever the substrate surface is not atomically flat.

Dini (1993) goes on to describe how various methods can be used to increase adhesion between substrate and coating. One such example is that of etching the substrate in acid

which provides a much increased surface area and many sites for mechanical interlocking of the coating.

When considering thin films, Baglin (1991) describes how the energy of adhesion (E_{ad}) at a planar interface between materials A and B is defined as as the energy gained per unit area by bringing these materials into contact to produce an interface free energy (γ_{int}) such that:

$$E_{ad} = E_A + E_B - \gamma_{int} \tag{2.26}$$

Where E_A and E_B are the surface free energies of materials A and B respectively. Large values of γ_{int} could prevent adhesion, while a small value could permit a large energy of adhesion.

In the research on CaP coatings which has been described in this chapter, there is very little discussion of the specific coating adhesion mechanisms observed. Even studies, in which many of the conclusions depend upon scratch-test adhesion results, fail to mention the possible manner in which the coatings are thought to adhere. Work by Lin et al. (2002), which was described at the end of Section 2.7.2, explained how poor adhesion was found between biomimetically deposited apatite and heat and alkali treated stainless steel substrates. The researchers suggested the need for an "inter-compound" of Na_4CrO_4 (produced during alkali treatment) in order to form a stable interface between the stainless steel and the HAp because of differences in their atomic bonding structure.

2.7.5 Incorporation of biochemical factors into coatings

As mentioned previously (Sections 1.0.2 and 2.7.2), there is now interest in combining CaP coatings with biologically active factors. A summary of a number of the studies carried out to date will be given here.

The antibiotic vancomycin was incorporated into eletrophoretically deposited HAp coatings by soaking the coated Ti(6%)Al(4%)V samples in a SBF containing either 1 or 10 mg/ml of the drug (Radin et al., 1997). Some of the samples underwent a second stage where they were coated with the lipid egg phosphatidylcholine (Section 2.8.1.1). All of these samples were compared with vancomycin loaded polymethyl-methacrylate (PMMA) cement in drug release and bacterial growth inhibition assays. The samples loaded with the lower concentration of the antibiotic were found not to inhibit bacterial growth at any time; the samples loaded in the 10 mg/ml solution exhibited an inhibitory effect after 1 h but not after 24 and 168 h. There was a 'burst' of drug release from these samples in the first hour. The lipid-coated samples, however, showed a much more gradual drug release, even up to 72 h after immersion in solution with a corresponding inhibition of bacterial growth. The authors could find no evidence of vancomycin release from the PMMA cement.

Campbell et al. (2000) exposed modified titanium alloy substrates to a supersaturated CaP solution. The heterogeneously induced mineralisation process that occurred was termed surface induced mineralisation (SIM). After this initial coating of CaP was applied, the samples were coated for subsequent cycles by refreshing the coating solution. Some of the samples underwent treatments with solutions that contained the antimicrobial agent chlorhexidine which was said to precipitate as chlorhexidine phosphate upon reaction with KH_2PO_4 and Na_2HPO_4. After coating had finished, some of these samples were also coated with a lipid 'overlayer' consisting of phosphatidylcholine. Bacterial growth inhibition and chlorhexidine release assays were then carried out. In the samples without the lipid overlayer, 80% of the antimicrobial agent appeared to release within the first two to three hours of sitting in aqueous solution. Release from the lipid coated samples took in the region of 24 h. The lipid-coated samples also displayed the largest zone of

bacterial growth inhibition around the samples. However, the growth inhibition tests were not carried out at different time intervals as in the previous study described (Radin et al., 1997).

Several studies have used a two step biomimetic procedure in order to incorporate various factors into CaP coatings. This procedure involved precalcification followed by immersion in a supersaturated CaP solution (containing the factor), this process was termed co-precipitation. Three studies used the technique in order to incorporate the protein bovine serum albumin (BSA) into coatings (Wen et al., 1999; Liu et al., 2001; 2003), they are summarised here:

- Wen et al. (1999)looked at simply incorporating one concentration (2 mg/ml) of BSA into the coatings. When looked at using scanning electron microscopy (SEM), the coatings containing the protein were seen to be denser than those which were protein free. No BSA was found to release from these coatings into phosphate buffered saline (PBS) solution at *p*H 7.4 over a 14 day period. However, BSA release into PBS at *p*H 4.0 was rapid over the first two days in solution and then leveled off, possibly due to *p*H changes instigated by coating dissolution.

- Liu et al. (2001) compared the co-precipitation of the BSA at various concentrations between 10 ng/ml and 100 µg/ml with the deposition of the same range of protein concentrations onto the surface of plates which had been precoated with CaP. At the highest BSA concentration used, 16.7 µg/mg of protein had been incorporated into those coatings formed by co-precipitation and 7.3 µg/mg of protein had been deposited onto the surface of the other set of samples (precoated with CaP). In release kinetics experiments, all of the protein that had associated with the precoated samples dissociated into the surrounding solution within six hours. In the samples

where BSA was co-precipitated with CaP, only 0.85% of the protein that had been taken up into the coating was released into solution after the experiment had been running for six days. This fact led the authors to conclude that the protein had somehow become incorporated into the crystal lattice of the coating.

- The mechanical strength and rate of dissolution of coatings containing BSA was looked at by Liu et al. (2003). The BSA was co-precipitated with CaP using the same method as in the experiments described previously (Wen et al., 1999; Liu et al., 2001). Dissolution tests in an acidic saline solution revealed that Ca^{2+} ions were released more slowly from coatings that contained the protein and that this rate of dissolution didn't vary with the protein concentration. The mechanical tests revealed that the critical load, where the scratch test used failed to generate a clean cut, increased with the concentration of BSA incorporated. Scratch tests involving HAp and BSA had previously been performed by Wong (1993).

A very similar biomimetic method was used in order to incorporate the antibiotic tobramycin into a carbonated HAp coating (Stigter et al., 2002). This co-precipitation of the antibiotic with the coating was compared with soaking plasma-spray-coated samples in solutions containing the same compound. The concentration of antibiotic which was incorporated into the coatings was much lower for those that had been soaked ($\approx$ 0.3 µg/mg) as opposed to those formed by co-precipitation ($\approx$ 3 µg/mg). The release of tobramycin from co-precipitated samples was measured in solutions buffered at *p*H 5.0 and *p*H 7.3. Approximately 90% of the drug was released from the coating in a time of 180 min at *p*H 5.0 and 60 min at *p*H 7.3. This is much more rapid than the release rate reported previously for BSA (Liu et al., 2001). The antibiotic was shown to inhibit the growth of *Staphylococcus aureus* in a petri dish based bacterial growth inhibition test.

More recently, the biomimetic technique has been used to incorporate recombinant human bone morphogenetic protein 2[5] (rhBMP-2) into CaP coatings (Liu et al., 2004). Testing of the coatings in a culture of rat bone marrow cells revealed that the activity of the cells (as determined by measurement of the enzyme alkaline phosphatase) increased in a manner related to the concentration of rhBMP-2 incorporated. The biological potency of the protein in this situation was said to be higher than that of a drug freely suspended in solution.

Electrochemically-assisted methods are now being tried in order to incorporate molecules into the coatings. In a study by Cheng et al. (2004) ELD was used firstly used for the purpose of forming a prelayer of CaP, which was then converted to HAp by heating for 24 h at 185℃ in an aqueous solution. Calcium phosphate and BSA co-precipitation was then carried out on these HAp samples in the presence of an electric field at 37℃. In release experiments (*p*H 7.4, 37℃), only approximately 15% of the BSA incorporated into this coating was released in a 70 h time period. For pre-prepared coatings which had simply been soaked in BSA solution, 100% of the protein was released within two hours under the same conditions.

Electrolytic deposition was used by Fan et al. (2005) to produce a CaP coating that contained collagen fibrils on a silicon substrate. This was done by adding 0.1 to 0.5 mg/ml of soluble type I collagen to an electrochemical cell at 30℃, 4.5 mmol/l Ca^{2+} ions and 9 mmol/l PO_4^{3-} ions. The potential on the cathode was between 1 and 3 V. The form of CaP that was deposited with the collagen was determined to be OCP (Section 2.2.4). During coating, an 'opaque zone' was observed adjacent to the cathode. This was attributed to the self assembly of collagen fibrils in solution as a result of the *p*H increase

[5]One of the proteins said to be responsible for initiating events involved in bone formation *in vivo*. These events include migration and differentiation of precursor cells into functional osteoblasts

near the electrode. No dissolution experiments were carried out in order to assess any collagen release but scratch tests revealed that the collagen/OCP composite coating was stronger than a coating with OCP alone.

2.8 Liposomes

In this section the structure of lipids and liposomes and methods of lipid vesicle manufacture will be described. Diffusion processes will also be considered before looking at methods currently used to study liposomes.

2.8.1 Structural aspects

Liposomes are structures formed out of amphipathic[6] molecules (amphiphiles) such as phospholipids or synthetic molecules (e.g. various surfactants). The initial stage in the formation of a liposome is the self assembly of these molecules into a bilayer sheet in aqueous environments. Liposomes can then form through the development of this bilayer structure into a spherical entity, containing an entrapped aqueous compartment. The amphipathic molecules looked at in this case will be the phospholipids.

2.8.1.1 Phospholipids

Phospholipids make up one of the three major groups of membrane lipids, the others being the glycolipids and cholesterol. They are derived either from glycerol or another type of alcohol called sphingosine. Like most other lipids, phospholipids are composed of:

- A polar head group.
- One or more hydrophobic tail regions.
- A backbone structure that connects the two.

Glycerophospholipids (phosphoglycerides), those which are derived from glycerol, are composed of two fatty acid chains esterified to C-1 and C-2 of glycerol-3-phosphate. The

[6]Molecules that contain both a hydrophilic and hydrophobic moiety

acyl chains of the fatty acids are typically 8 to 24 carbons in length. They can be saturated, unsaturated, or even coupled, forming a macrocycle (Collier and Messersmith, 2001a). This structure (the glycerophosphate termed phosphatidate) is then linked to a head group compound, such as choline, serine or ethanolamine via an ester linkage. This leads to the formation of phosphatidylcholine, phosphatidylserine or phosphatidylethanolamine respectively. A diagram of the structure of phosphatidylcholine can be seen in Figure 2.16.

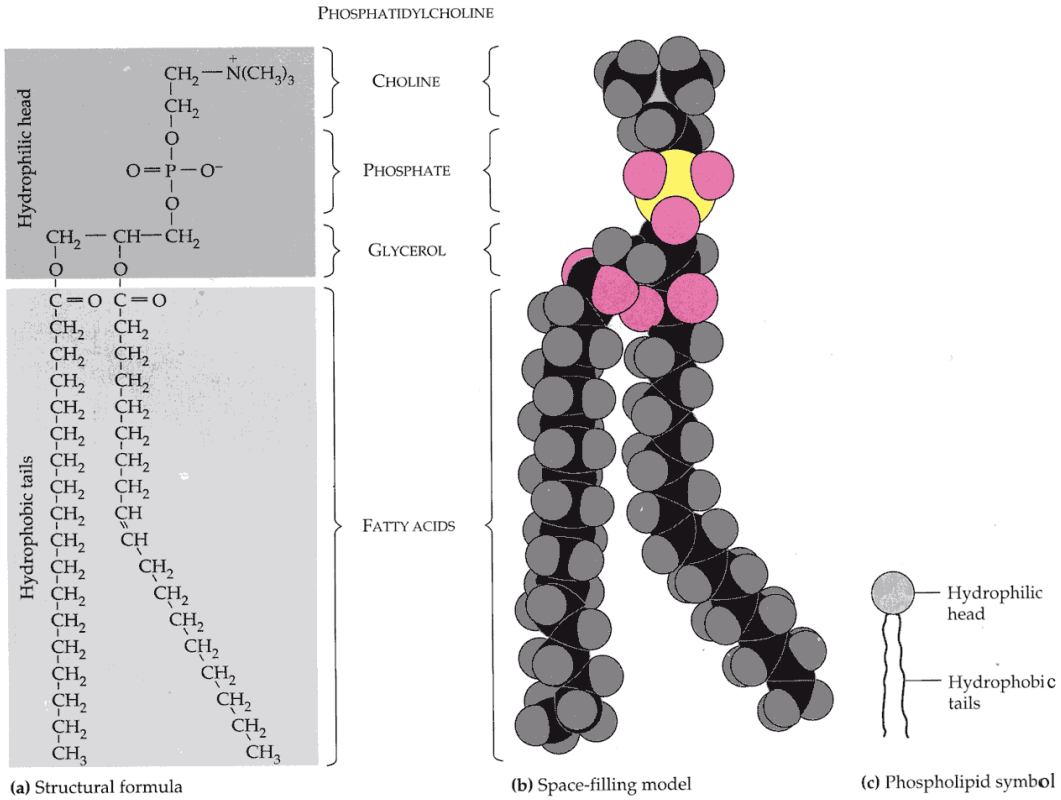

Figure 2.16: The structure of phosphatidylcholine (Campbell, 1996)

2.8.1.2 Bimolecular sheets

One fascinating property of these phospholipid molecules is the way in which they can self-organise into specific-macroscopic aggregates in the form of bilayer membranes (Figure 2.17). These bimolecular sheets form rapidly and spontaneously in an aqueous solvent. Stryer (1995) states that the major driving force in this process is the hydrophobic interactions of the molecules. The bilayers are then held together by reinforcing, non-covalent interactions. The clustering of the lipid molecules in a conformation that minimises the number of exposed hydrocarbon tails is also favourable in terms of the van der Waals forces between these hydrocarbon groups.

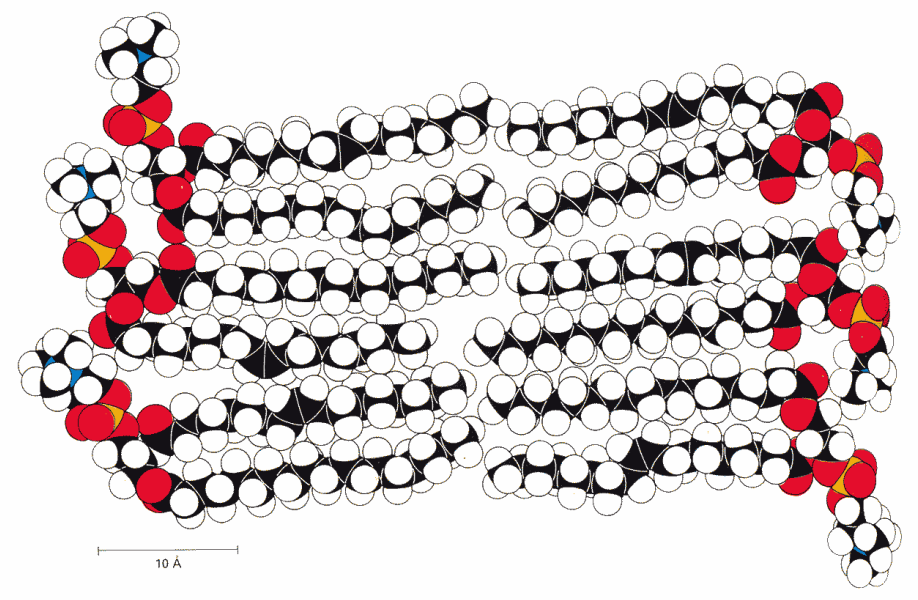

Figure 2.17: A space filling model of a phosopholipid bilayer membrane (Stryer, 1995)

Stryer (1995) goes on to explain three of the consequences of the energetic factors which govern bilayer formation. These are that:

(i). Lipid bilayers have a tendency to be extensive.

(ii). Lipid bilayers tend to close on themselves so that there are no exposed hydrocarbon chains at the edges. This results in the formation of a compartment.

(iii). Due to the fact that a hole in the bilayer is energetically unfavourable, lipid bilayers are self-sealing.

Another aspect of the fact that the interactions between hydrophobic moieties are weak, in comparison to covalent bonds, is that the bilayer membrane is generally very fluid (above the phase transition temperature, T_c). The majority of the lipid molecules and some membrane-bound proteins are able to move laterally in the plane of the membrane. Phospholipids are able to to move along the plane of the membrane at speeds of up to 2 µm/s at 37℃ (Stryer, 1995). The rotation of lipids from one face of the bilayer to the other is, however, very rare.

The fluidity of the membrane is dependent on composition as well as temperature. For example, T_c will be higher when many of the hydrocarbon chains are saturated. Close-packing is relatively simple in this case due to the straight nature of these chains. This means that the membrane will also be more rigid at a given temperature above T_c. Unsaturated chains, which contain a *cis* double bond will not be straight, interfering with the packing arrangement required for solidification (lowering T_c) and making the membrane more fluid.

Cholesterol is a key regulator of membrane fluidity in eukaryotes[7]. It prevents crystallisation of the fatty acid chains by fitting between them (lowering T_c). The fact that cholesterol can block the large motions of fatty acyl chains, means that the membranes are less fluid as a result.

[7]Higher organisms with membrane bound organelles, e.g. protoctista, fungi, plants and animals as opposed to prokaryotes such as bacteria

Experiments and theoretical models by Corvera et al. (1992) looked at the effect of cholesterol addition to membranes made up of dipentadecanoylphosphatidylcholine and dipalmitoylphosphatidylcholine. These showed that from pure membranes up to those which had a 10% percentage content of cholesterol, there was an increase in membrane permeability to sodium ions. Above 20% cholesterol content, however, the membrane permeability decreased with increasing content.

2.8.1.3 Lipid Vesicles

When energy is imparted upon a suspension of lipids in an an aqueous solution, spherical structures can be formed when the lipid molecules regroup after being dispersed by said energy. Examples of ways of delivering this energy to lipid suspensions include sonication and homogenisation. These spherical objects are called lipid vesicles or liposomes. A certain amount of the aqueous solution and any solutes dissolved within it are entrapped within the central compartment of the liposome. Any lipid-soluble solutes can be trapped within the bilayer itself.

Liposomes can range in size from tens of nanometres to tens of microns in diameter (Collier and Messersmith, 2001b). As Lasic (1998) explains, after they are formed, liposomes are generally not colloidally stable and will slowly clump together and fuse into larger and more lamellar structures. The two main forms of liposome described in the literature are multilamellar vesicles (MLVs) and unilamellar vesicles (ULVs). MLVs are made up of several lipid bilayers in an 'onion skin' fashion. ULVs consist of a single bilayer surrounding a fluid core (Figure 2.18).

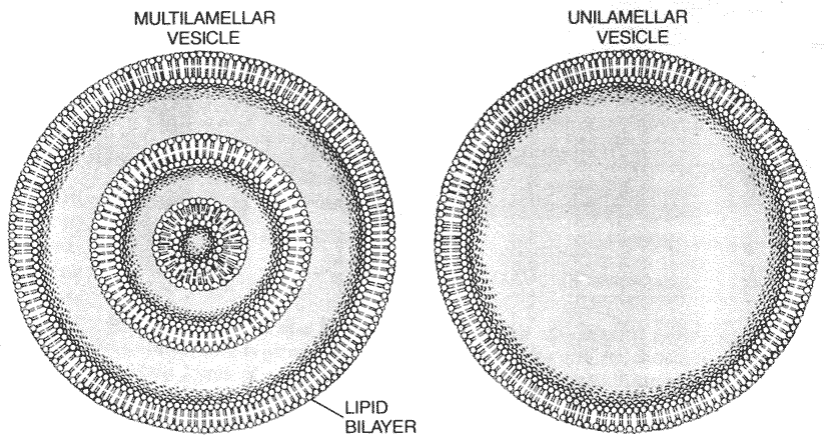

Figure 2.18: Diagram showing multilamellar (left) and unilamellar (right) liposomes (Ostro, 1987)

2.8.2 Manufacture of liposomes

According to New (1996), all methods of manufacturing liposomes can be said to consist of four basic stages:

1. Drying down of lipids from organic solvents.
2. Dispersion of lipids in aqueous media.
3. Purification of liposomes.
4. Analysis of resulting product.

The lipids are generally dispersed in chloroform, methanol, or a mixture of both substances. Addition of other liposome constituents such as cholesterol happens at this stage. The solvent can be evaporated off, either in a rotary evaporator at low pressure, or in a stream of inert gas. Potential oxidative effects on the lipids must be minimised at all times. Incorporation of anti-oxidants such as α-tocopherol can prolong the life of lipids and the resultant liposomes as well as increasing bilayer rigidity in a similar manner to cholesterol (Halks-Miller et al., 1985; Kulkarni et al., 1995).

Kulkarni et al. (1995) describe how efficient hydration of the bilayer is achieved best by forming a thin film with a large surface area. Ways of increasing surface area include drying the lipids down onto round-bottomed or pear-shaped flasks and/or by the addition of contact masses such as glass beads.

The most simple methodology for liposome manufacture is to add aqueous solution to a round-bottomed flask in which a layer of lipids has been dried onto the sides. Gentle, manual agitation will then cleave layers of lipid off the glass surface. The vesicles formed through this method are generally multilamellar in morphology.

According to New (1996), many other methods of liposome manufacture exist and the one chosen has to fit the morphology of the end product required and the facilities available.

Mayhew et al. (1984) described the use of a microemulsifier for preparing large volumes of liposomes in a continuous manner. Generally, hand-shaken liposomes are in the > 1 µm size range. This can be reduced to less than 0.1 µm after ten minutes in a microemulsifier. The fact that high concentrations of lipid (300 µmol/ml) can be processed, means that a high entrapment efficiency can be achieved.

Gruner et al. (1985) carried out a study in which they produced a particular kind of liposomes, which they termed stable plurilamellar vesicles (SPLVs). According to the authors, the standard methods of MLV production result in the separation of water from its dissolved solutes, leading to vesicles with solute-depleted aqueous compartments. In turn, this leads to an osmotic gradient on the MLVs, reducing their stability.

The manufacture of SPLVs involved dissolving lipids that had been dried onto the sides of a flask, in ethyl ether. A small quantity of aqueous-phase solution containing the solutes to be entrapped was then added to the lipid/ether mixture. Sonication of the solution under a flow of inert gas led to the evaporation of the ether, leaving a cake of

liposomes which could then be suspended in buffered solution.

By entrapping a calcium sensitive dye within their liposomes and adding the vesicles to a suspension containing Ca^{2+} ions, it was discovered that MLVs leaked within a few days, whereas the SPLVs had not started to release their contents after 15 months.

Perrett et al. (1991) described the preparation of a 'proliposome' mixture made by drying down lipid before dissolving it in ethanol and buffered aqueous solution. This mixture was then heated to 60℃ for several minutes before being allowed to cool to room temperature. This mixture could then be converted into a liposome mixture through the addition of extra buffered solution when needed. This transformation from proliposome to liposome was explained in terms of the three-phase system between phosphatidylcholine, ethanol and water, where changes in the ratios of each would result in the formation of solubilised lipid, precipitated stacks of lipid bilayers or a suspension of liposomes. The liposomes formed were described as multilamellar in morphology with an average size of ≈ 0.5 µm in diameter.

2.8.3 Aspects of diffusion

The ability of liposome vesicles to entrap solutes has caused much interest in their potential use as drug delivery devices. The use of these carriers allows control over any compromise between the potential toxicity of many drugs and the natural processes of dilution and degradation of any foreign substance which enters living tissue (Ostro, 1987; Barenholz, 2001; Ti Tien and Ottova, 2001). In the context of orthopaedic implants, these vesicles could be used to deliver bone growth factors or drugs to prevent implant associated infection. An understanding of the diffusion processes in vesicles is important in cases such as these.

In general, lipid bilayer membranes have very low permeability to ions and most polar molecules. Water is the exception to this rule as it readily traverses these membranes. Stryer (1995) describes how a small molecule may transverse the bilayer by first shedding its solvation shell of water before becoming dissolved in the hydrocarbon core of the membrane. After it has diffused through the core to the other side, it becomes resolvated by water. Because of this, an ion such as Na^{2+} will traverse the membrane very slowly, as removal of its coordination shell of water is energetically unfavourable. This description is not supported by authors such as Wilson and Pohorille (1996). They explained how the simplest theoretical treatment of this problem is based on a model in which water and the bilayer can be represented as continuous dielectric media, with dielectric constants ϵ_w and ϵ_b respectively. If the ion in question is then modelled as a point charge, located in the centre of a cavity of radius a, then the free energy of transferring the ion from bulk water to the centre of the bilayer (width d) is expressed as :

$$\Delta H(TS) = \frac{q^2}{2a}\left[\frac{1}{\epsilon_b} - \frac{1}{\epsilon_w}\right] - \frac{q^2}{\epsilon_b d}\ln\left(\frac{2\epsilon_w}{\epsilon_w + \epsilon_b}\right) \tag{2.27}$$

If values are substituted into equation 2.27 for Na^{2+}, (effective ionic radius 1.68 Å) a membrane permeability of 10^{-30} m/s results. This is about 15 orders of magnitude lower than the value measured experimentally. The authors stated that these discrepancies suggest that a model in which a naked ion is transferred across a sharp interface does not give an adequate description of the process. Other models suggested include the theory that the ions move through the membrane with their first hydration shell still intact, or that they move through transient pores or structural defects. By using a molecular modelling approach, the authors then discovered that defects in the membrane would increase the permeability by approximately 14 orders of magnitude. Because this is a

better reflection of the value measured experimentally, it was concluded that this was possibly the mechanism that was occurring.

Males et al. (1998) detailed how many other factors need to be considered, such as membrane asymmetry (including inner and outer surface area and volume), varying permeant molecule lipophobicity and permeation of weak acids and bases. They described a set of equations for passive diffusion through the membranes of large unilamellar vesicles (LUVs) in response to either a concentration or pH gradient. Their analysis uses a four component model (figure 2.19) in which there are inner (i) and outer (o) aqueous compartments as well as internal (mi) and external membranous regions (mo). A scheme for the passive diffusion of a weak acid and weak base can be seen in figure 2.20; where A represents the acid and B its conjugate base. K_a is the dissociation constant of the acid in aqueous solution. Equations can then be written describing the flow of a_x and b_x, where

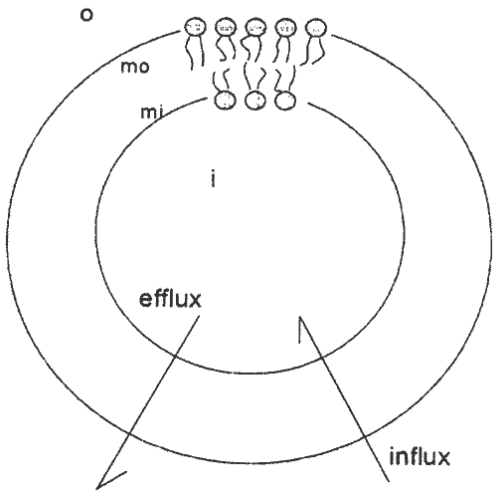

Figure 2.19: Representation of a large unilamellar vesicle (LUV) showing the four regions occupied by the the molecules. These are: The outer aqueous solution (o), the external membraneous region (mo), the internal membranous region (mi) and the inner aqueous solution (i). The arrow labelled efflux depicts an experiment in which the bulk of the permeant is trapped inside the vesicle at time $t = 0$. The arrow labelled influx depicts an experiment with the bulk of the permeant outside the vesicles at $t = 0$ (Males et al., 1998)

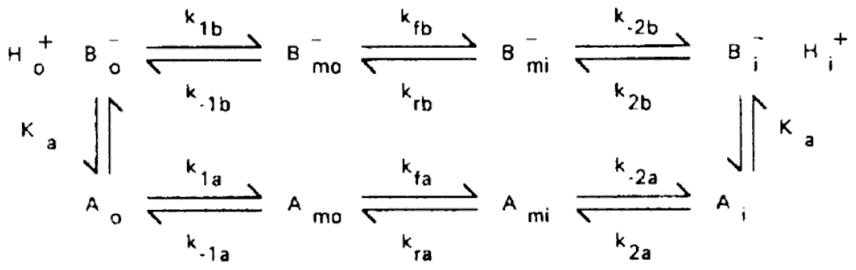

Figure 2.20: Scheme for passive diffusion for weak acids and bases (Males et al., 1998)

a and b represent the numbers of molecules of A and B respectively and x is the specified region. Due to the difficulty in detecting the difference between acid and conjugate base under experimental conditions, equations can be written in the form of $N_x = a_x + b_x$ which can be used to describe the number of molecules of both A and B in region x.

If acid and base are both lipophobic, a_{mo}, b_{mo}, a_{mi} and b_{mi} are all approximately constant with time. The flow of molecules inside and outside the vesicles becomes:

$$\frac{dN_{\mathrm{o}}}{dt} = -\frac{dN_{\mathrm{i}}}{dt} = -\gamma_{ss}\left(N_{\mathrm{o}} - N_{\mathrm{o}}^{eq}\right) \tag{2.28}$$

N_{o}^{eq} is the number of molecules in the outside aqueous compartment at equilibrium. γ_{ss} is the apparent rate constant given by:

$$\gamma_{ss} = \frac{P_1 A_{\mathrm{o}}}{V_{\mathrm{o}}} + \frac{P_2 A_{\mathrm{i}}}{V_{\mathrm{i}}} \tag{2.29}$$

A_{o} and A_{i} are the outer and inner surface areas of the vesicle respectively. V_{o} and V_{i} are the outer an inner volumes. P_1 and P_2 are the permeability coefficients, which are related to the diffusion coefficient within the membrane, D_{mem}, and the width of the membrane, δr, such that $P = KD_{mem}/\delta r$ (K is a constant). P_1 is the permeability coefficient from the inner to the outer membranous region (mi $\rightarrow$ mo) and P_2 is the permeability coefficient

from the outer to the inner membranous region (mo → mi). Accepted values of the permeability coefficient for water through egg phosphatidylcholine liposomes are in the range of $P = 2 \times 10^{-4}$ cm/s (Kaiser and Hoffman, 1996).

2.8.3.1 Methods of study

A number of different techniques can be used to look at properties such as entrapment efficiencies, diffusion profiles and stability of liposomes.

For example, differential scanning calorimetry is said to be useful for quality control of liposome preparations (Biltonen and Lichtenberg, 1993). This technique can measure the gel to lipid-phase transition temperature (T_{m}) which is dependent on factors such as the lipid acyl chain length and saturation. Any impurities in the lipid membrane will affect the packing of the molecules and thus lower T_{m}.

Gruner et al. (1985) used a wide variety of characterisation techniques in order to compare SPLVs with MLVs. These techniques included gas chromatography (to determine any residual solvent contamination from manufacture), X-ray diffraction (to look at the radial stacking of liposome membranes), Electron microscopy (to determine vesicle size), electron spin resonance (to determine the rate of ascorbate penetration into the membranes), nuclear magnetic resonance (to compare solute depletion), enzyme digestion (to gain information about the solute distribution within the vesicles), and entrapment of radio-labelled substances (to determine entrapment efficiency). The use of such a wide range of techniques in one study is the exception rather than the rule, however.

Rather than using expensive radio-labelled substances, which often pose an inherent safety risk, many studies use dyes as marker molecules to determine entrapment efficiency and study diffusion processes (Allen and Cleland, 1980; Allen, 1984; Hernández-Caselles et al., 1990; Perrett et al., 1991; Hara et al., 1999; Shi et al., 2001). Examples of such

molecules include 5,6-carboxyfluorescein and a related compound named calcein, the use of which will now be described.

Calcein The original use of calcein was as an indicator for calcium quantification owing to the fact that, when used at *p*H 12, calcein is brown and its calcium complex is yellow-green (Diel and Ellingboe, 1956). It was later discovered that the fluorescent properties of this compound were related to the quantities of alkaline earth metals present in solution and these properties could be used to quantify the presence of calcium at milligram levels (Wallach et al., 1959). Later still, it was discovered that the self-quenching of the fluorescent properties of calcein at high concentration could be used to advantage in studies on liposomes (Allen and Cleland, 1980). When encapsulated at high concentration in vesicles, any fluorescence is quenched, but as the calcein leaks from the liposomes it becomes diluted and therefore dequenched, a resultant increase in fluorescence can then be seen. The structure of calcein at acid and neutral *p*H can be seen in figure 2.21.

According to Allen and Cleland (1980), the various advantages of using calcein include:

- A very large amplification in fluorescence upon release of the calcein from the liposomes allows use of a small liposome sample size.
- The fluorescence signal can be monitored continuously with time, allowing very rapid leakage processes to be measured.
- Fluorescence of calcein is virtually independent of *p*H over the range of *p*H 6.0-8.5.

As a result of these factors, calcein has become a model substance for studying entrapment and leakage of chemicals in liposome studies (Hara et al., 1999; Memoli et al., 1999; Ishii and Nagasaka, 2001).

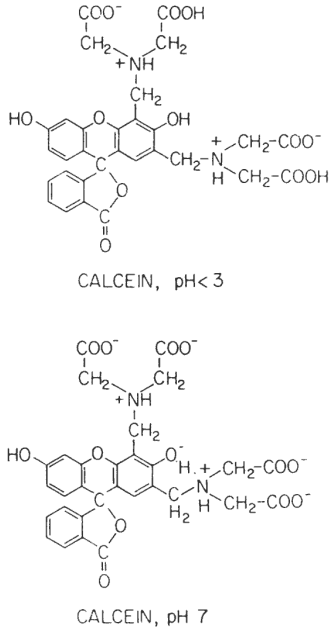

Figure 2.21: Structure of calcein at acidic and neutral *p*H conditions (Allen, 1984)

2.9 Calcium Phosphate-Liposome Composites

Aspects of both calcium phosphate chemistry and liposome structure have now been looked at separately. This section aims to review the literature on composite structures made up of CaP phases and lipid vesicles.

Much knowledge of the ability of phospholipids to interact with CaP phases has been gained from the fact that Ca-phospholipid-PO_4 complexes can be found in living organisms, especially in regions of bone development (Cotmore et al., 1971; Boskey and Posner, 1977).

Cotmore et al. (1971) studied the effect which phosphate and magnesium ions had on a system containing calcium and phospholipids. Liposomes were used, these consisted of the acidic phospholipid phosphatidylserine (PS). Magnesium ions were found to weakly inhibit the interaction between Ca^{2+} and PS. The addition of PO_4^{3-} ions was found to

increase the rate of Ca^{2+} ion migration from solution to a solid phase on the vesicles. It was calculated that at physiological *p*H, one calcium ion complexes with two PS molecules.

Boskey and Posner (1977) looked at the effects which the addition of liposomes (made up from various acid phospholipids) and also Ca-phospholipid-PO_4 complexes had on metastable calcium phosphate solutions. The Ca-phospholipid-PO_4 complexes had been extracted from animal tissues. When added to metastable solutions, these complexes initiated the removal of Ca^{2+} and PO_4^{3-} ions from solution. The calcium to phosphate ratio of this ion removal was 1.7:1, this indicated that a CaP phase with a similar Ca/P ratio to that of hydroxyapatite was being formed. When phosphatidylserine or phosphatidylinositol liposomes were added, Ca^{2+} ions were initially removed from solution. After a time lag, the PO_4^{3-} ion concentration began to fall also. The Ca/P ratio of ions removed from solution was the same as exhibited upon addition of the complexes.

Eanes et al. (1984) studied CaP formation in a suspension of MLVs. These vesicles contained an aqueous phosphate solution. Through the addition of an ion channel, which allowed the permeation of calcium ions, CaP phase formation was studied upon addition of Ca^{2+} ions to the solution surrounding the liposomes. Ca^{2+} ions were taken up rapidly into the liposomes and a solid phase formed inside and eventually on the surface of the liposomes. The growth of a large amount of CaP in the vesicles was found to interfere with the integrity of the membrane. A subsequent study using electron microscopy examined the products formed during this experiment (Heywood and Eanes, 1987). This revealed that apatite clusters were formed in the lumen of the vesicle, close to inner lipid membranes. The formation of CaP is not limited to the internal compartments of these structures; after an extended period of precipitation, the bulk of the deposits are to be found on the outside of the vesicles. The initial formation of CaP on the inside of the liposomes is thought to lead to the nucleation of apatite on the outside of the membranes,

possibly by nucleating crystals passing through the bilayer (Eanes and Hailer, 1985).

In the context of studying the processes which may lead to the formation of calcified arterial plaques in heart disease, Hirsch et al. (1992) looked at the interactions between HAp crystals and liposomes. Addition of HAp seed crystals to phosphatidylcholine liposome suspensions led to an increased rate of aggregation of the vesicles when compared to suspensions without addition of these crystals. It was concluded that the interaction between HAp and the liposomes was stronger than inter-liposomal interactions. The shape of the aggregates was also modified by HAp, with the liposomes becoming irregularly-shaped with angular contours rather than the series of smooth spheres seen in the absence of the seed crystals.

Pongsaanutin (2002) studied many factors concerned with CaP-liposome complexes. The specific effect of CaP on the membranes of phosphatidylcholine liposomes was looked at. The adsorption of Ca^{2+} ions onto the membrane was thought to cause repulsive interactions between the lipid molecules, causing various shape changes in the vesicles. In many cases, along with HAp penetration of the bilayer, these factors led to the breakdown of the liposome structure. Addition of cholesterol to the vesicles was found to stabilise the membranes to some degree, reducing the disruption caused by CaP. Negatively charged phospholipids such as PS were shown to promote the formation of ACP as opposed to HAp, when compared to neutral lipids.

Pongsaanutin (2002) also looked at the possibility of using CaP-liposome composites in a system for the low temperature electrodeposition of HAp onto metal substrates. The addition of the composite was found to reduce the crystallinity of the coating. The initial formation of dot-like structures on the membrane was thought to perhaps be due to the attachment of complexes. The coating later built up into a more uniform layer. Tubular micelles were seen in coatings with the cholesterol-stabilised complexes added.

Schmidt and Ostafin (2002) used liposomes as a template on which to grow calcium phosphate 'nanoshells.' This was done by firstly adding just enough Ca^{2+} ions to form a monolayer on the outside of the liposomes. Then enough phosphate was added to form a monolayer over this, allowing CaP precipitation to occur on the surface of the liposomes. This procedure of alternately adding Ca^{2+} and then PO_4^{3-} ions was repeated many times, building up a thick shell of CaP. Electron microscopy studies revealed a CaP shell of between 2 nm to more than 10 nm in thickness was formed.

This technique of growing the nanoshells has since been refined (Schmidt et al., 2004). This was done through the addition of the liposomes to a supersaturated CaP solution. The authors hypothesised that this growth occurred through initial electrostatic interactions between the negatively charged lipids, that were used, and the ions in solution. This was said to lead to localisation of the ions, forming an electric double layer in which the high level of saturation of chemical species allowed crystallisation to occur. After a certain period of growth of CaP on the periphery of the liposomes, the reaction could be halted through addition of the molecule carboxyethylphosphoric acid (CEPA). This was said to act as a capping molecule, preventing any further growth of the CaP layer.

2.10 Summary

- Calcium phosphates are one of the many types of ceramic biomaterials used in clinical medicine today. Many CaP materials are available for use in a variety of situations.
- CaP coatings allow the combination of the load-bearing strength of a metallic substrate with the potential bioactive benefits of a ceramic surface, which is similar in composition to bone mineral.
- Clinical studies on CaP-coated implants have been positive in many cases, however there is still room for improvement.
- The calcium phosphate phases in existence are diverse in structure as well as having the ability to transform into other phases.
- The precipitation of the CaP phases from solution is driven by a thermodynamic force called supersaturation.
- A number of CaP crystal growth mechanisms have been proposed.
- Many methods of manufacturing CaP coatings exist. The most commonly used method, plasma spraying has a number of drawbacks which can possibly be overcome by some of the newer techniques.
- The electrodeposition of CaP phases can be divided into electrolytic (electrochemical) and electrophoretic mechanisms.
- Various low-temperature coating methodologies have been used to incorporate molecules of biological interest, such as antibiotics, into CaP coatings.

- Liposomes are structures capable of forming in aqueous solutions due to the amphipathic nature of their constituent lipid molecules.
- There are many techniques available for manufacturing and then refining the population characteristics of liposomes.
- The combination of liposomes with CaP phases has been studied. The interaction of the phases and any resultant effect on the membrane of the liposome is of interest.

Chapter 3

Experimental Procedures

In this chapter the methods which were used to study a low temperature electrodeposition process will be outlined. As well as a description of how the process itself was performed, the manufacture and study of liposome vesicles and CaP-coated liposomes will be delineated, accompanied by the manufacture of coatings which contain these CaP-liposome composites.

Unless stated otherwise, all chemicals were supplied by Sigma-Aldrich Ltd., Poole. Distilled water was used in all experiments unless stated otherwise.

3.1 General Methods

3.1.1 Measurement and calculation of CaP phase supersaturation

During the coating process, knowledge of the calcium phosphate solution chemistry (described in Section 2.2) combined with use of sensitive monitoring equipment (pH, Ca^{2+}

and temperature electrodes (Radiometer Ltd., Copenhagen)) allowed real-time assessment of the supersaturation of a number of the CaP phases. Figure 3.1 shows a diagram of this monitoring equipment.

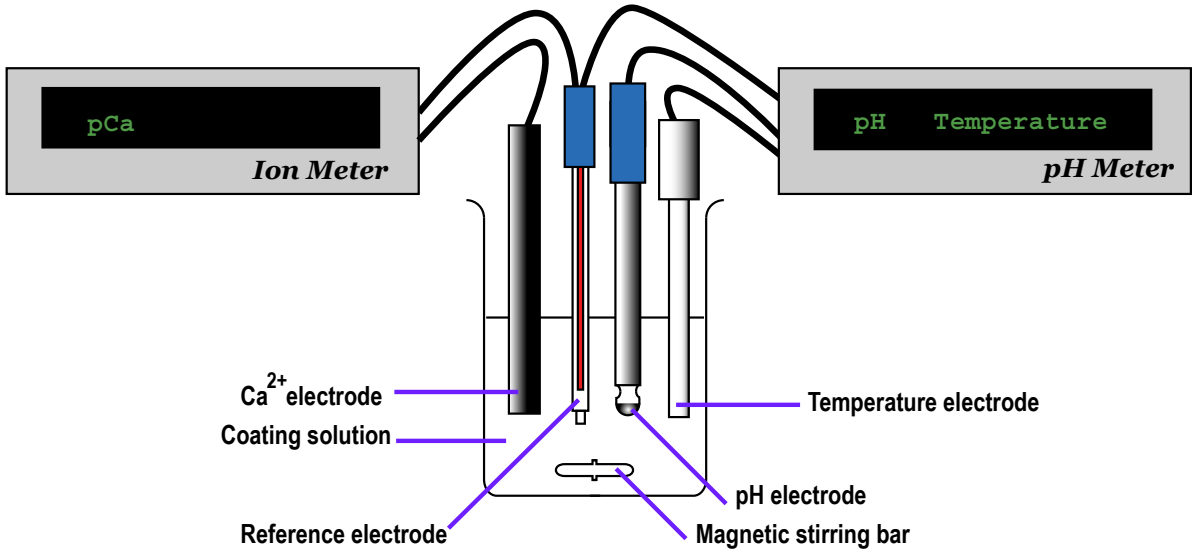

Figure 3.1: Diagram of solution monitoring apparatus (not to scale)

*p*H, *p*Ca and temperature readouts from the meters (Radiometer Ltd., Copenhagen) were entered into a spreadsheet written to calculate supersaturation values with respect to the most relevant CaP phases (HAp, OCP, DCPD). For more information on the practical details of supersaturation calculation see Appendix A.

3.1.2 Manufacture of stock coating solutions

Separate Ca^{2+} and PO_4^{3-} aqueous stock solutions were made. These were diluted to the required solution molarity when needed. Both of the stock solutions and the diluting solution were made up to contain 0.1 mol/l KCL and 10 mmol/l HEPES ((N-) [2-hydroxyethyl] piperazine-N'-[2-ethane-sulphonic acid]) as a buffer. In addition to this, the Ca^{2+} stock

solution contained 50 mmol/l Ca^{2+} ions by way of addition of 7.35 g/l of calcium chloride dihydrate ($CaCl_2 \cdot 2H_2O$). The PO_4^{3-} stock solution contained 30 mmol/l PO_4^{3-} ions by way of addition of 4.08 g/l of potassium dihydrogen orthophosphate (KH_2PO_4). All solutions were titrated with 0.75 mol/l KOH to *p*H 7.4 at 37℃.

3.2 Electrodeposition coating procedure

A sample holder was made which separated a platinum anode from the cathodic sample by a distance of 2.25 cm. This had been previously determined to be the optimum separation distance (Peaker, 1995). For general experiments, the sample consisted of a piece of 1.25 mm thick 304 sheet stainless steel which had the same dimensions as the anode.

Coating solutions containing the required molar concentrations of Ca^{2+} and PO_4^{3-} ions were made up by mixing the stock solutions manufactured in section 3.1.2 with the required amounts of diluting solution (0.1 mol/l KCL, 10 mmol/l HEPES, *p*H 7.4 at 37℃).

Before each coating cycle, the diluted Ca^{2+} and PO_4^{3-} solutions were warmed to 37℃ in a water bath before being mixed together. A nitrogen gas bubbler was then placed in the solution in order to displace any dissolved CO_2. The electrodes for monitoring solution supersaturation (section 3.1.1) were also placed in the coating vessel. If liposomes were to be included in the coating, they were added to the solution at this point and left for five minutes before carrying out the next stage of the procedure.

After the sample holder was placed on the coating vessel, the Pt anode and the sample were connected to a Philips PM2831 programmable power supply (Philips, Netherlands). Coating commenced when the power supply was turned on with a constant voltage of 2.5 V. A diagram of the coating apparatus can be seen in figure 3.2.

Coating was stopped when the calculated supersaturation of HAp was seen to drop

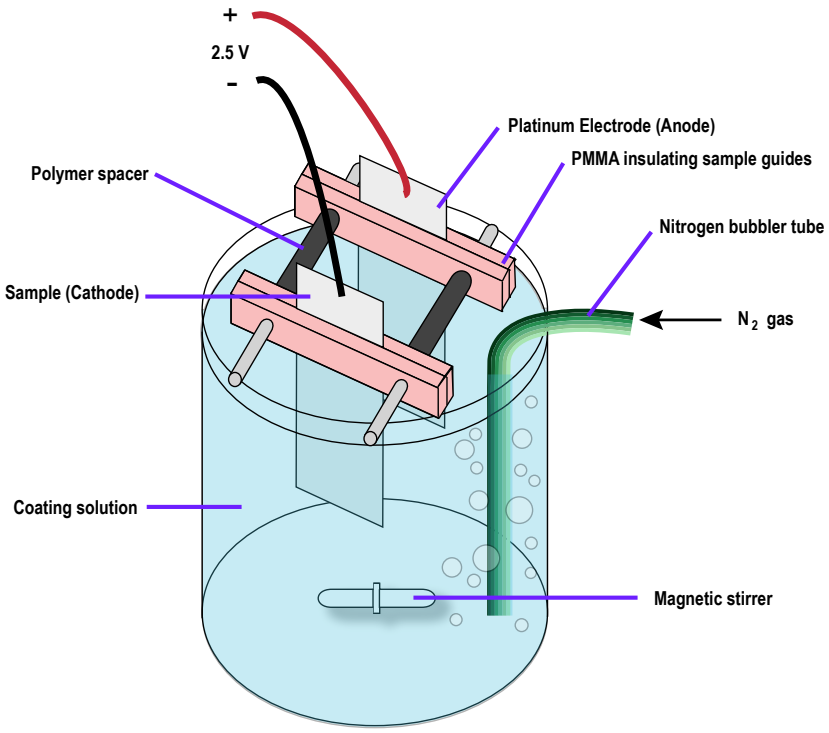

Figure 3.2: Diagram of the equipment set-up during coating

sharply. This was usually after around 20 minutes.

If further coating was to take place, fresh coating solution was added before repeating the procedure above.

After coating was completed, the samples were rinsed with distilled water before being dried.

3.3 Summary of samples prepared

During the course of this study a number of coated samples were prepared on different substrates. The following table (Table 7) aims to clarify which substrates were used in each instance. In all cases, the substrate was sonicated (using a bath sonicator, Kerry Ultrasonics Ltd) in acetone for 10 min and then rinsed with distilled water before coating.

Table 7: Summary explanation of coated samples used in this study and where the method and results are described.

	Substrate material	**Surface treatment**	**Coated area (cm^2)**	**No. of samples**	**Described in section**
Thick ($\approx$ 20 micron) coating	Orthopaedic TiAl(6%)V(4%)	Shot-blasted	6.25	1	3.6 and 4.1.2
XRD reference coating	ASTM 304 Stainless steel	Shot-blasted	3.14	1	3.4.1 and 4.1.1.3
Maturation coatings - air dried	ASTM 304 Stainless steel	None	6.25	20	3.7, 4.1.1.3 and 4.1.3
Maturation coatings - critical point dried	ASTM 304 Stainless steel	None	6.25	20	3.7, 4.1.1.3 and 4.1.3
Composite coatings	Orthopaedic TiAl(6%)V(4%)	Polished	0.79	20	3.10 and 4.3

3.4 Characterisation techniques

3.4.1 X-ray diffraction

Samples of coating attached to substrate were placed in a $\theta - 2\theta$ X-ray diffractometer (Phillips PW1729 generator and Phillips PW1820 detector). Scans were performed between 2θ of 2° and 70° with a step size of 0.01° 2θ with a measurement time of 1.25 seconds per step. The wavelength of the Cu $K\alpha$ radiation was 0.154 nm at 35 kV. The position of peaks were compared with those for CaP phases listed in the JCPDS files (International Centre for Diffraction Data). An estimate of crystallite size could be made using the Scherrer formula (equation 3.1).

$$t = \frac{k\lambda}{B\cos\theta_B} \tag{3.1}$$

Where t = thickness of the crystal (nm)

λ = X-ray wavelength

θ_B = Bragg angle

B = line broadening (given by the Warren formula (equation 3.2))

k = constant which depends on the shape of the particle

$$B^2 = B_M^2 - B_S^2 \tag{3.2}$$

Where B_M is measured peak width from the sample of interest at half peak height (in radians)

B_S is the corresponding peak width from a standard material

As well as comparing the XRD scans to a standard reference material from the literature, a sample was made by ten repeated electrodeposition cycles onto a stainless steel substrate. An XRD scan was performed on this sample. The coating on the sample was thicker than the coatings produced in other experiments and therefore a good signal was produced from the coating itself without artifacts from the substrate. This was then be used in conjunction with the reference from the literature in analysis of the XRD results.

3.4.2 Transmission electron microscopy (TEM)

Coatings were grown directly onto holey carbon TEM grids (Agar Scientific, Essex), which had been attached to the cathodic substrate during the coating process. Silver conducting paint (Electrolube, Derbyshire) was used to facilitate a good electrical contact during this procedure. A picture of this attachment can be seen in figure 3.3.

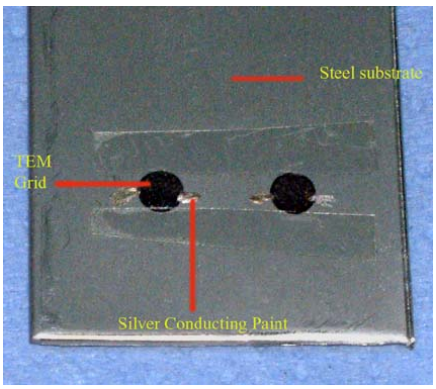

Figure 3.3: Photograph of carbon-coated copper TEM grids attached to stainless steel substrate.

The grids were then carbon coated in an Edwards coating apparatus. Transmission electron microscopy was carried out in a Jeol 200CX microscope at an accelerating voltage of 120 kV. Images were recorded to film (Kodak Electron Image Film, Kodak, New York, USA) along with a record of the magnification achieved.

3.4.3 Electron diffraction

Samples were prepared as in the transmission electron microscopy section (section 3.4.2). Diffraction patterns were obtained on the Jeol 200CX TEM operating at 120 kV. Patterns were recorded to film (Kodak Electron Image Film, Kodak, New York, USA)) along with a record of the camera length. This information could then be used to calculate crystal lattice dimensions.

3.4.4 Scanning electron microscopy

Samples of CaP coating on 304 stainless steel substrate were cut down to a size smaller than 1.5 cm^2 using a guillotine (to allow them to fit in the microscope chamber). These samples were then carbon coated using an Edwards evaporator. The samples were then viewed in a Low Voltage Field Emission Gun Scanning Electron Microscope (Jeol 840F LV-FEG-SEM) at accelerating voltages or between 1.5 and 3 kV. Micrographs were recorded to film (Ilford 120) along with the magnification achieved.

3.4.5 Measurement of mechanical strength (Lap Shear)

The extent of the mechanical bonding between the coating and the substrate was tested by way of a lap-shear method. The coated 304 stainless steel samples were attached to uncoated, but otherwise identical steel blanks in a lap joint using epoxy resin (Araldite, Bostick Findlay, Staffordshire). The resin was allowed to cure in a vice for 12 hours at 25℃. The areas of overlap between the samples and the blanks were then measured and recorded.

These samples were then pulled apart in a Hounsfield tensile testing rig (at a rate of 10 mm/min). The maximum load before fracture was recorded. The test was repeated in

order to minimise errors. A diagram showing the procedure can be seen in figure 3.4.

The lap-shear strength can then be calculated by using equation 3.3.

$$\tau_{int} = \frac{F_{max}}{A_c} \tag{3.3}$$

Where τ_{int} is the interfacial shear strength

F_{max} is the force at breaking point (N)

and A_c is the area of contact between the two members of the lap joint (m ^{2}).

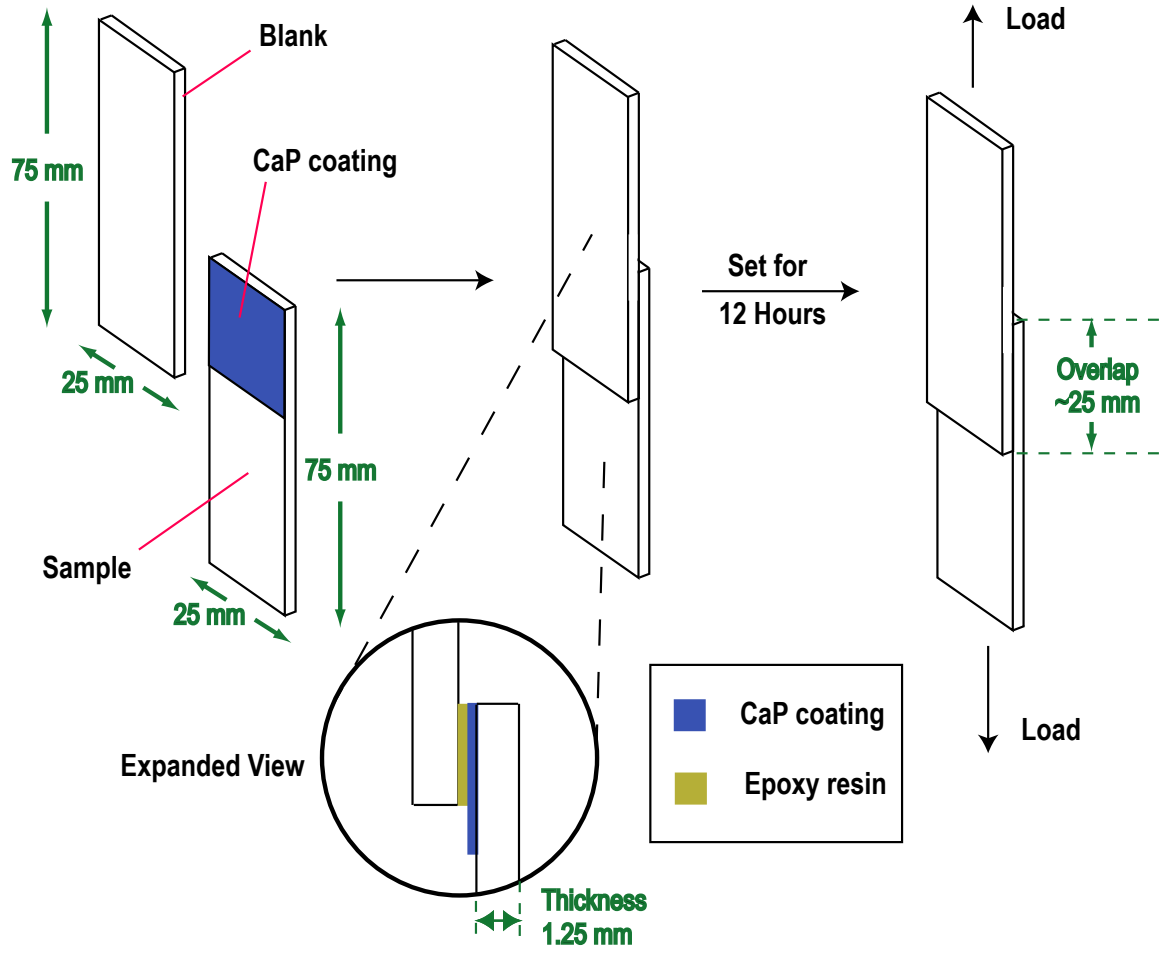

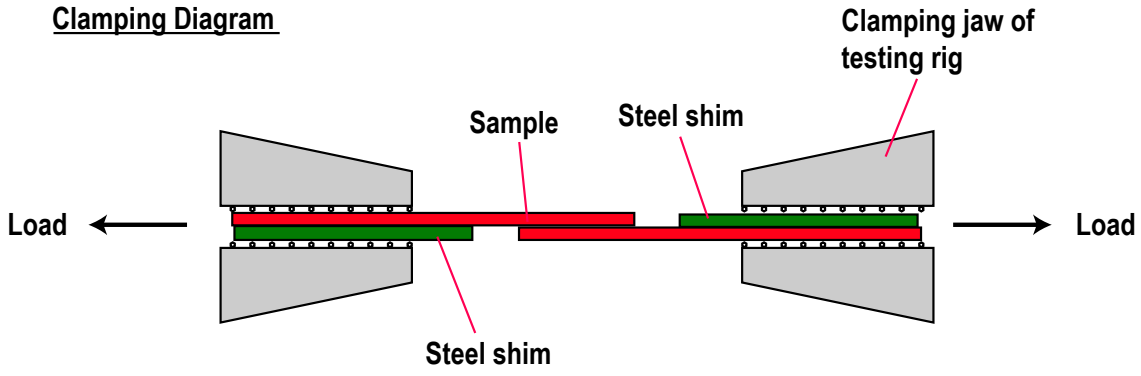

Figure 3.4: Figure showing the lap-shear testing procedure used

3.5 The use of different drying methods

The two different methods used to dry the samples are outlined here.

3.5.1 Air drying

Air drying was the standard method used after completing the coating stage. This involved placing the samples in a desiccator containing anhydrous $CaCl_2$ for 24 hours.

3.5.2 Critical point drying (CPD)

Samples were dehydrated by passing them through a series of ethanol/water mixtures of 30%, 50%, 70%, 90% and 100% ethanol, starting with the lowest ethanol percentage. Samples were left for five minutes in each solution.

Samples were then then transferred to a Polaron critical point dryer along with 20 ml of fresh ethanol. The chamber was sealed and CO_2 was then added until liquid CO_2 could be seen to have reached a level which adequately covered the samples when observed through the viewing window in the side of the vessel. Every 30 minutes, the ethanol was vented from the bottom of the chamber and the liquid CO_2 was topped-up to its original level in the chamber. This was continued for at least three hours or until ethanol was no longer found during venting. Water which had been heated to 40℃ was then pumped through the jacket of the CPD chamber. This had the effect of causing the liquid CO_2 to pass through its critical point and transform into a gas. This gas was slowly vented over a period of 5 minutes to prevent condensation forming in the chamber. The dry sample could then be removed from the CPD apparatus. A picture of the drying apparatus can be seen in figure 3.5.

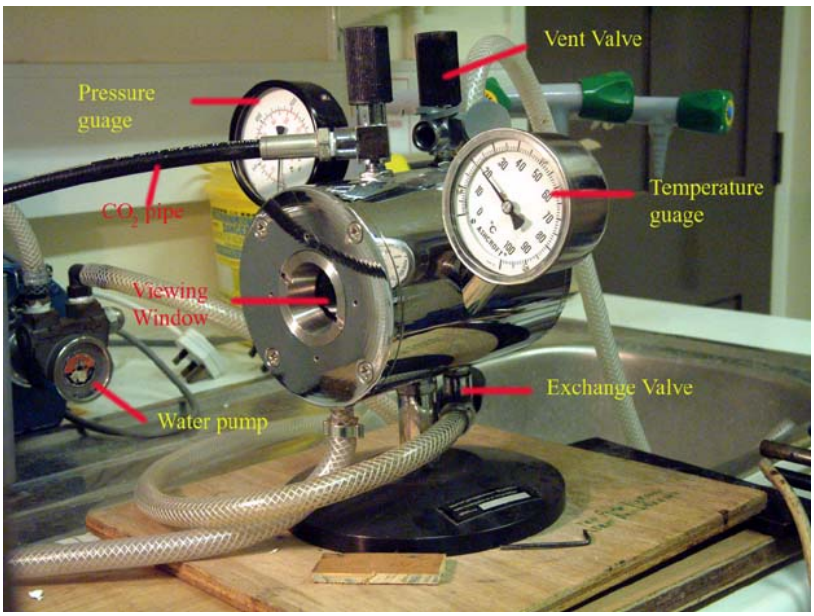

Figure 3.5: Photograph of the Polaron CPD apparatus

3.6 Manufacture of thick ($>$ 10 µm) coatings

The same electrodeposition method described in section 3.2 was used to try and make thicker coatings. Coating thickness could be measured by either a micrometer gauge, optical microscopy or impedance (if on a ferrous substrate). The orthopaedic grade, shot-blasted TiAl(6%)V(4%) substrate used for this sample was provided by AEA Technology Plc. Harwell, Oxfordshire, who later used this sample in their own mechanical tests.

3.6.1 Scale-up of coating process

To increase the thickness of coating produced during each coating cycle (the period during which coating could take place before having to replenish the coating solutions), the reservoir of available Ca^{2+} and PO_4^{3-} ions was enlarged by:

1. Increasing the volume of coating solutions used from 125 ml of each solution to 250

ml of each and coating in larger vessels.

2. Increasing the concentration of the coating solution from a concentration of 3 mmol/l Ca^{2+} and 1.8 mmol/l PO_4^{3-} ions to 6.25 mmol/l Ca^{2+} and 3.75 mmol/l PO_4^{3-} ions.

As well as these measures to increase the size of the ion reservoir, many coating cycles were used on the same sample ($>$ 20 cycles) in order to try and build up a more substantial CaP layer.

3.7 Effect of coating maturation time

To assess the effects of leaving the samples standing in coating solution after the first coating cycle had taken place, two sets of samples were made using 304 stainless steel subsrates.

Set 1. Coated for one coating cycle. Samples were left to stand in coating solution for 0, 1, 3, 5 and 13 hours. Four samples were made for each time period and no further coating cycles were performed.

Set 2. Coated for 5 coating cycles. The time for which samples were left standing in solution after the first cycle was varied (0, 1, 3, 5 and 13 hours). Four samples were made for each time period.

Three of the four samples made for each time period were studied using lap-shear mechanical testing (Section 3.4.5) the other sample was characterised using X-ray diffraction (Section 3.4.1) and LV-SEM (Section 3.4.4).

A set of TEM grids were also coated for one cycle and allowed to stand in solution for the same time periods, before TEM (Section 3.4.2) and electron diffraction (Section 3.4.3) were used to analyse the samples.

Table 8: Explanation of maturation time experiment samples.

	Total No. of coating cycles	**Maturation time after cycle 1 (hours)**	**No. of coating cycles after maturation time**	**No. of samples made for each time period**
Set 1. One-coat samples	1	0, 1, 3, 5, 13	0	4
Set 2. Five-coat samples	5	0, 1, 3, 5, 13	4	4

Initial sets of samples were air-dried (Section 3.5.1). A subsequent set of four samples for each time period were made and dried using critical point drying (Section 3.5.2) for comparison.

3.8 Liposomes

3.8.1 Manufacture of multilamellar vesicles (MLVs)

This method is based upon that described by New (1996).

Approximately 0.1 grams of Lα-phosphatidylcholine was dissolved in a 2:1 mixture of chloroform and methanol. If cholesterol was required it was also added at this stage.

The liposome solution was then dried onto the sides of a 100 ml round-bottomed flask by swirling under a stream of nitrogen or argon gas. This was then left for a further two hours to allow more of the solvent to evaporate.

10 ml of aqueous solution containing the solvents to be entrapped were then added to the flask. This solution was then swirled around vigorously before being placed into a bath sonicator (Kerry Ultrasonics Ltd). Sonication continued until the solution became clear which took approximately 15 minutes. This liposome suspension was then left to stand for at least one hour before use.

3.8.2 Manufacture of stable plurilamellar vesicles (SPLVs)

Stable plurilamellar vesicles were made based on the method first described by Gruner et al. (1985).

0.1 g of Lα-phosphatidylcholine dissolved in chloroform was measured out or 0.1 g of solid EPC was weighed out and dissolved in chloroform. Cholesterol and/or α-tocopherol were also added at this point.

The solution was then dried onto the sides of a 100 ml round bottomed flask by swirling under a stream of nitrogen or argon gas. This was then allowed to dry under vacuum in a bell jar overnight.

5 ml of diethyl-ether was then added to the flask and swirled to dissolve all of the lipid. 300 µl of the aqueous solution to be entrapped was then added to the lipid in ether solution. This was then sonicated in an ultrasonic bath sonicator (Kerry Ultrasonics Ltd) whilst under a stream of nitrogen or argon gas to evaporate the ether. This was continued for four minutes or until the scent of ether could no longer be detected.

The pellet of liposomes was then suspended in 9.7 ml of standard 0.1 mol/l KCL and 10 mmol/l HEPES buffer solution (Section 3.1.2). The suspension of liposomes was then washed by centrifuging the suspension at 1,800 $\times g$ for five minutes in a microcentrifuge (Denver Instrument, Göttingen), removing and discarding the supernatant and then resuspending the pellets in fresh buffer. Washing was repeated three times. The final solution was then made up to 10 ml with fresh buffer solution.

3.8.3 Optical microscopy of liposome suspensions

Liposome suspension was diluted three-fold with standard 0.1 mol/l KCL and 10 mmol/l HEPES buffer solution (Section 3.1.2) before a drop of this solution was placed onto a

glass slide and a coverslip carefully placed on the solution droplet. The sample was viewed with a Leitz Laborlux S optical microscope (Leitz Wetzlar, Germany) to which a CCD camera had been fitted (Watec, Japan). Images were captured using imaging software (TCPro, Coreco Software,USA).

3.8.4 Coating liposomes with calcium phosphate phases

Liposome suspensions were first mixed together with PO_4^{3-} solution which had been made up to the desired concentration as described in section 3.1.2 and heated to 37℃. After 5 minutes of incubation with stirring, Ca^{2+} solution of the relevant concentration and also at 37℃, was added. The suspensions and solutions were then left to incubate in a water bath for five more minutes.

3.9 Diffusion studies

3.9.1 Utilising calcein for liposome studies

The fluorescent marker molecule calcein (described in section 2.8.3.1) was incorporated into liposomes as follows:

Firstly a calcein and buffer solution was made up to contain 70 mmol/l calcein, 10 mmol/l HEPES buffer and 65 mmol/l KCl (added in order to keep the osmolarity close to that of the standard HEPES buffer i.e 210 mosmol/l). This was done by adding 0.012 g of HEPES and 0.024g of KCL to 2 ml of water before adding 0.218 g of calcein and raising the *p*H with 0.7 mol/l KOH solution until all of the calcein dissolved. The *p*H was then adjusted to 7.4 at 37℃ with concentrated HCl (32% solution) before the solution was made up to a final volume of 5 ml with water.

3.9.1.1 Measurement of calibration curve

A starting solution containing 100 mmol/l calcein was made using the same technique as described in section 3.9.1. This was then serially diluted with HEPES buffer solution (section 3.1.2) to produce solutions of various concentrations down to 30 nmol/l. The fluorescence of each solution was measured separately in a Hitachi 3010 fluorescence spectrophotometer (Hitachi, Japan) with an excitation wavelength of 490 nm. Emission spectra between 500 nm and 550 nm were recorded for each concentration. The relative intensity of the emission peaks could then be plotted against calcein concentration.

3.9.1.2 Interaction of calcein with CaP

A calcein calibration curve was made in exactly the same way as in section 3.9.1.1, but this time each standard was made up to contain 2 mmol/l Ca^{2+} ions and 1.2 mmol/l PO_4^{3-} ions as well as the relevant calcein concentration.

3.9.1.3 Measurement of entrapment efficiency

In order to determine the percentage efficiency of calcein entrapment (% EE), a method based on that of Ishii and Nagasaka (2001) was used. First 1.5 ml of liposome suspension was placed into a cuvette. A measurement of calcein concentration was then performed in a Hitachi 3010 fluorescence spectrophotometer with an excitation wavelength of 490 nm. The emission maximum between 500 and 550 nm could then be used in conjunction with the calibration curve constructed in section 3.9.1.1 in order to find the calcein concentration. A second reading was then taken after disrupting the liposomes with 2 ml of ethanol for every ml of suspension and measuring the fluorescence intensity again. The

% EE could be calculated using equation 3.4.

$$\%EE = \frac{(C_F - C')}{C_F} \times 100 \tag{3.4}$$

Where C_F is the calcein concentration after disrupting the liposomes and C' is the calcein concentration before disruption.

3.9.1.4 Measurement of calcein release from coated/uncoated liposomes

2 ml of liposome suspension were put into each of four different vessels and heated to 37℃ in a water bath. Standard 0.1 mol/l KCL and 10 mmol/l HEPES buffer solution (Section 3.1.2) as well as solutions made up to contain initial concentrations of 8 mmol/l Ca^{2+} ions and 4.8 mmol/l PO_4^{3-} ions in 0.1 mol/l KCL and 10 mmol/l HEPES buffer solution (Section 3.1.2) were heated at the same time. Liposome samples in two of the vessels were coated with CaP by using the method described in section 3.8.4 with 1 ml of each ion solution. 2 ml of the standard HEPES buffer solution was added to the other two vessels which were incubated for the same time as the coated samples.

Initial fluorescence readings were taken of all the samples by transferring 1.5 ml of each sample to a cuvette and recording the maximum emission peak height between 500 and 550 nm with an excitation wavelength of 490 nm in a Hitachi 3010 fluorescence spectrophotometer. Samples were then kept in their cuvettes and placed in a distilled water bath at 37℃. Subsequent fluorescence readings were taken at regular intervals.

Final readings of fluorescence were taken after disrupting the liposomes with 2 ml of ethanol for every ml of liposome suspension.

Concentrations of calcein were then found using the calibration curve constructed

in section 3.9.1.2. The percentage release of calcein with time was calculated by using equation 3.5 which is a modification of that used by Hara et al. (1999).

$$\text{Percentage release} = \frac{(C' - C_0)}{(C_t - C_0)} \times 100 \tag{3.5}$$

Where C' is the calcein concentration calculated at that time point, C_0 is the initial calcein concentration and C_t is the final calcein concentration.

3.9.2 Entrapping the antibiotic gentamicin

Experiments were carried out in order to assess the viability of entrapping the antibiotic gentamicin. These procedures were similar to those described for calcein (section 3.9.1).

3.9.2.1 Discovery of fluorescence peak

In order to be able to quantify the concentration of gentamicin in solution, an assessment of any possible fluorescent activity was carried out.

A solution was made by weighing out 0.0215 g of gentamicin (651 µg of gentamycin base per mg) and dissolving in 5 ml of distilled water. 1.5 ml of this solution was then transferred to a cuvette and placed in a Hitachi 3010 fluorescence spectrophotometer. Scans were carried out of both the emission and the excitation spectra of the solution.

The optimum excitation wavelength was found to be 330 nm which gave emission peaks at between 400 and 420 nm. This information was then used in subsequent experiments.

3.9.2.2 Measurement of calibration curves

A stock solution of 50 mg/ml of gentamicin was made up in distilled water and serial dilutions were made down to a concentration of 500 ng/ml gentamicin. These solutions were placed in fresh cuvettes and analysed in a Hitachi 3010 fluorescence spectrophotometer. The heights and positions of the emission peaks found between 400 nm and 420 nm were recorded with an excitation wavelength of 330 nm.

Buffered solutions of gentamicin were also made up and tested in the spectrophotometer. These contained 0.1 mol/l KCL and 10 mmol/l HEPES buffer. The solution was titrated with KOH to a *p*H of 7.4 at 37℃.

It was also discovered that in order to counteract the effect of low fluorescence emission intensity at low concentrations of antibiotic in solution, most consistent results could be gained by using the spectrophotometer in 'High PM Gain' mode. This increased the voltage across the photomultiplier and allowed lower emission intensities to be measured.

The gentamicin solution fluorescent emission peak heights could then be plotted against concentration in order to form a calibration curve.

3.9.2.3 Incorporation of gentamicin into liposomes

A buffered solution of 10 mmol/l HEPES, 0.1 mol/l KCL and 50 mg/l of gentamicin was made up and titrated to *p*H of 7.4 at 37℃ with 0.1 mol/l KOH.

This solution was used during the manufacture of SPLV liposomes as described in section 3.8.2.

3.9.2.4 Measurement of entrapment efficiency

In order to determine the percentage efficiency of gentamicin entrapment (% EE), a method based on that of Ishii and Nagasaka (2001) was again used as in section 3.9.1.3. First 1.5 ml of liposome suspension was spun down in a microcentrifuge at $1,800 \times g$ for five minutes. The supernatant was then placed into a cuvette. A measurement of gentamicin concentration was then performed in the fluorescence spectrophotometer with an excitation wavelength of 330 nm. The emission maximum between 400 and 420 nm could then be used in conjunction with the calibration curve constructed in section 3.9.2.2. A second reading was then taken after disrupting the liposomes with 2 ml of ethanol for every ml of suspension and measuring the fluorescence intensity again. The % EE could be calculated using equation 3.6.

$$\%EE = \frac{(C_F - C')}{C_F} \times 100 \tag{3.6}$$

Where C_F is the gentamicin concentration after disrupting the liposomes and C' is the gentamicin concentration before disruption.

3.9.2.5 Measurement of gentamicin release from liposomes

Unlike calcein, gentamicin fluorescence does not quench at high concentration. Therefore the method described for monitoring calcein release from liposomes (section 3.9.1.4) was modified in order to include a centrifugation stage before each reading was taken (apart from the final, disrupted reading). Samples were centrifuged for five minutes at $1,800 \times g$ before a reading of the fluorescence emission (400-420 nm) of the supernatant was taken with an excitation wavelength of 330 nm. The concentration of gentamicin could then

be calculated from the calibration curve constructed in section 3.9.2.2. The pellet of liposomes was resuspended in the supernatant before leaving the samples to incubate again until the next reading was taken. The experiment was only carried out with uncoated liposomes.

3.10 Manufacture of liposome-CaP composite coatings

3.10.1 General procedure

Liposomes were made as described in section 3.8. These were then incorporated to the electrodeposition procedure described in section 3.2. Liposomes were coated with CaP phases immediately prior to the coating cycle. This was done by adding the required quantity of liposome suspension to the buffered PO_4^{3-} ion solution and incubating with stirring for 5 minutes. Then the buffered Ca^{2+} ion solution was added and the suspension was incubated for five more minutes. Coating then proceeded as normal, with a constant voltage of 2.5 V. The solution supersaturation was monitored (Section 3.1.1) in order to determine when to replace it and the procedure was repeated for each coating cycle. The initial coating cycle was carried out without liposomes and the sample then allowed to mature in solution for one hour prior to coating again. This was done on the basis of results from the experiments on maturation time, described earlier in this chapter (Section 3.7). Subsequent alternate coating cycles had liposomes added.

3.10.2 Calcein containing liposome-CaP composite coatings

3.10.2.1 Maximising entrapment

In this specific case, SPLVs were manufactured with entrapment efficiency maximised as a result of the calcein studies (Section 3.9.1). All glassware used was washed in Decon detergent (Decon, East Sussex) before overnight soaking in a base bath made up of saturated NaOH in isopropyl alcohol. After rinsing in pure water (BDH AnalaR, UK), the glassware was then washed in concentrated nitric acid followed by further rinses in pure water. Solutions made from AnalaR water were then degassed in an attempt to reduce any oxidation from dissolved O_2.

For each batch of liposomes, 0.079 g of high purity (99 %) Lα-phosphatidylcholine was used along with 30 mol% cholesterol (0.018 g) and 4 mol% α-tocopherol (0.003 g).

3.10.2.2 Use of the disaccharide trehalose

The non-reducing sugar trehalose has been shown to protect biological membranes and liposomal membranes during dehydration including during the use of freeze-drying (Madden et al., 1985; Crowe et al., 1986; Crowe and Crowe, 1988; Crowe et al., 1988; 1998; Hincha et al., 2002). In making calcein containing liposome-CaP composite coatings, trehalose was included in the calcein solution entrapped in the liposomes. This solution was made up to contain 70 mmol/l calcein, 100 mmol/l trehalose, 10 mmol/l HEPES buffer and 15 mmol/l KCl (added in order to keep the osmolarity close to that of the standard HEPES buffer). This was done by adding 0.189 g of trehalose, 0.012 g of HEPES and 0.006g of KCL to 2 ml of water before adding 0.218 g of calcein and raising the *p*H with 0.7 mol/l KOH solution until all of the calcein dissolved. The *p*H was then adjusted to 7.4 at 37℃ with concentrated HCl (32% solution) before the solution was made up to a

final volume of 5 ml with water.

A special version of the standard HEPES buffer solution (originally described in Section 3.1.2) was made with the intention of being used in freeze-drying. After manufacture, the composite coatings would be placed in this solution during the drying procedure so that trehalose would be present both inside and outside the liposomal membranes as proved effective in previous studies (Madden et al., 1985; Crowe et al., 1986; 1988). This solution was made up to contain 100 mmol/l trehalose, 10 mmol/l HEPES and 50 mmol/l KCl. This solution was titrated with 0.75 mol/l KOH to *p*H 7.4 at 37℃.

Initial experiments were also carried out where liposomes containing calcein and trehalose solution were manufactured according to the method described in Section 3.8.2 with the exception of the final step, where fresh buffer solution containing trehalose was used to make up the suspension to a final volume of 10 ml, rather than the standard buffer used in previous experiments. The entrapment efficiency of this suspension was then measured according to the method described in Section 3.9.1.3. The remaining 8.5 ml of this liposome suspension was then poured into a 50 ml round-bottomed flask which was then spun for 1 h in a rotary shell freezer (Edwards, UK) that used a bath of 2-propanol cooled to -35℃. The flask was then attached to a vacuum drying apparatus (MicroModulo, Edwards, UK) for 24 hours.

The dried liposome suspension was rehydrated by adding 8.5 ml of buffer solution and mixing for five minutes. The entrapment efficiency of the suspension was measured again according to the method described in Section 3.9.1.3 and was compared with the efficiency recorded before freeze-drying.

3.10.2.3 Mounting of samples

The substrates to be coated were orthopaedic TiAl(6%)V(4%) alloy discs with a diameter of 1 cm and thickness of 2.5 mm (Figure 3.6 (a)) . After unsuccessful attempts at coating the samples by attaching them with carbon-coated adhesive pads to a stainless steel plate, a sample holder was made from ASTM 304 stainless steel (Figure 3.6 (b)). A combination of carbon pads for adhesion and silver conducting paint (Electrolube, Derbyshire) for a good electrical contact, were used to mount the samples in the holder (Figure 3.6 (c)). The sample holder and platinum anode were placed in the same configuration as described in Section 3.2, a picture of this can be seen in Figure 3.6 (d).

3.10.2.4 Coating procedure

Coating was carried out in the same way as described in Section 3.10.1 using 260 ml of coating solution with a starting concentration of 3.25 mmol/l Ca^{2+} ions and 1.95 mmol/l PO_4^{3-} ions. For the first coating attempts, 10 ml of calcein-containing SPLV liposome suspension (manufacture described in Section 3.8.2) were added during each coating cycle that used liposomes, this was modified to 1.5 ml of liposome suspension for subsequent attempts. Samples were coated for a total of ten coating cycles, five of which included liposomes.

3.10.2.5 Freeze-drying of coatings

After coating, samples were removed from the sample holder and placed in 100 ml round-bottomed flasks containing 25 ml of buffered solution containing trehalose (Section 3.10.2.2). These flasks were then attached to a rotary shell freezer (Edwards, UK) which spun them in a bath of 2-propanol cooled to a temperature of -35℃. After an hour,

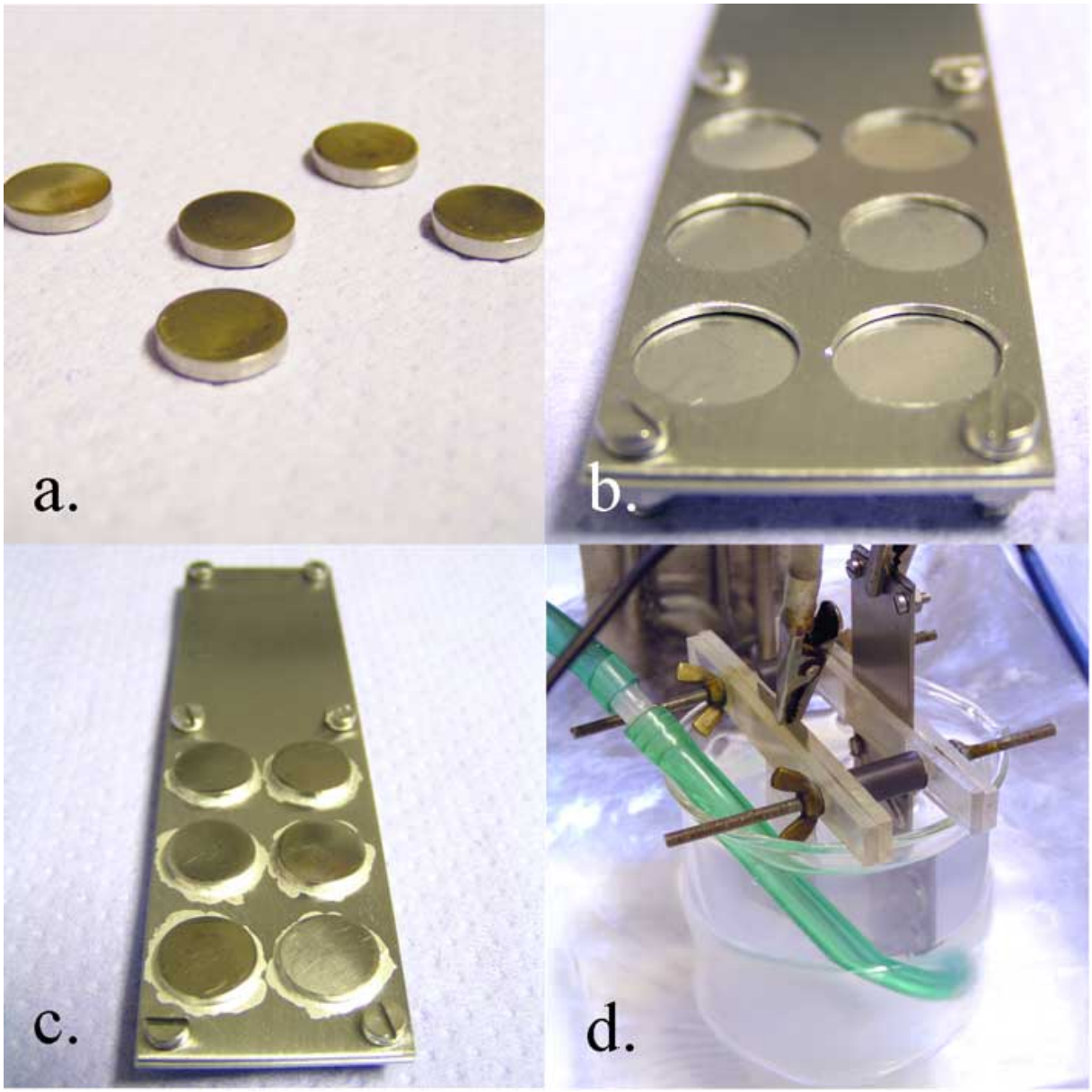

Figure 3.6: Laboratory photographs of procedure during manufacture of calcein containing liposome-CaP composite coatings. (a) Orthopaedic TiAl(6%)V(4%) alloy discs (diameter 1 cm, thickness 2.5 mm). (b) Sample holder for the discs. (c) Sample holder and discs mounted with adhesive carbon pads and silver conducting paint. (d) Set-up during coating (as described in Section 3.2)

the flasks were transferred to a vacuum drying apparatus (MicroModulo, Edwards, UK). The dried samples were removed after 24 hours.

3.10.2.6 Storage in calcifying solution

As an alternative to freeze-drying, samples were placed in sterile tubes (Bibby Sterilin Ltd, Staffordshire) containing 50 ml of buffered coating solution (as described in Section 3.1.2) made up to contain 1.5 mmol/l Ca^{2+} ions and 2.5 mmol/l PO_4^{3-} ions.

Chapter 4

Results

In this chapter, the results recorded will be presented in three main sections. Firstly results relating to experiments on coatings alone, followed by results of liposome experiments and then finally those relating to composite coatings.

4.1 Coatings

4.1.1 Preliminary Experiments

4.1.1.1 Coating Time

Figure 4.1 shows an example of calculated supersaturation for various CaP phases against time during coating by electrodeposition onto stainless steel (Section 3.2). The solution was monitored as described in Section 3.1.1. It can be seen that the supersaturation of HAp is much higher than that of OCP or DCPD during the coating process. The change in supersaturation with time starts to level off for HAp after approximately 20 minutes of coating. This knowledge allowed optimisation of the time for which coating took place

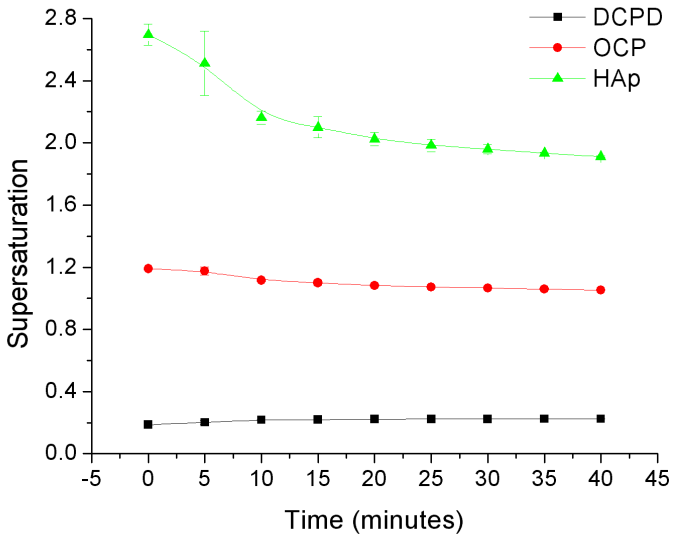

Figure 4.1: Example graph of calculated supersaturation (β) against time for various phases during electrodeposition of CaP. Starting solution concentration 6.25 mmol/l Ca^{2+} ions. Ca^{2+}:PO_4^{3-} ratio of 5:3. Error bars represent standard error of the mean (n=2)

in many of the subsequent experiments.

4.1.1.2 Coating solution concentration

Figures 4.2, 4.3 and 4.4 show the calculated supersaturation against time for different starting solution concentrations of Ca^{2+} and PO_4^{3-} ions. Each graph is for a specific phase of CaP.

It can be seen that the rate at which the supersaturation of OCP and HAp changes with time varies significantly with the initial concentration of the coating solution. For both phases, the drop in calculated supersaturation over the 40 minute coating period increases with the initial concentration of the coating solution. For OCP (Figure 4.2), this drop is around 0.04 units for an initial coating solution concentration of 2.5 mmol/l Ca^{2+} and 1.5 mmol/l PO_4^{3-} ions as opposed to a drop of approximately 0.14 units for an

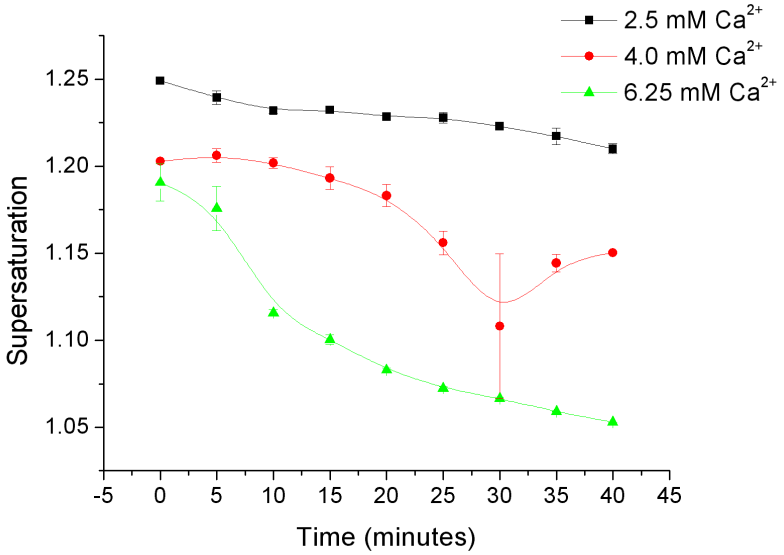

Figure 4.2: Graph of calculated supersaturation (β) against time for OCP at different coating solution starting concentrations. Ca^{2+}:PO_4^{3-} ratio of 5:3. Error bars represent standard error of the mean (n=2)

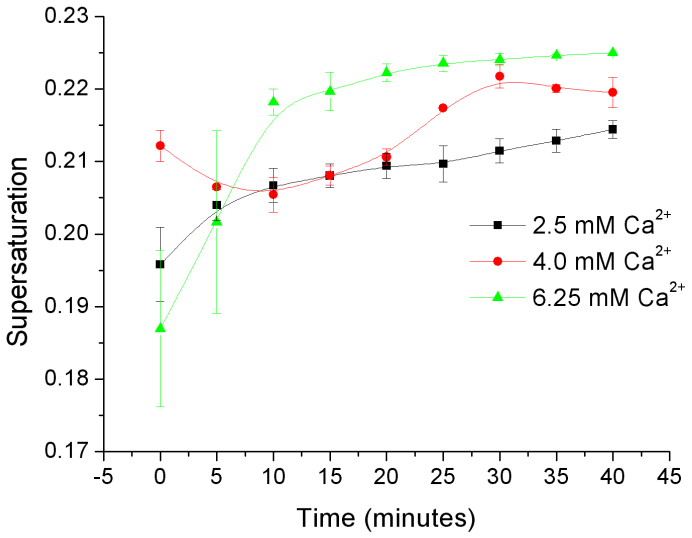

Figure 4.3: Graph of calculated supersaturation (β) against time for DCPD at different coating solution starting concentrations. Ca^{2+}:PO_4^{3-} ratio of 5:3. Error bars represent standard error of the mean (n=2)

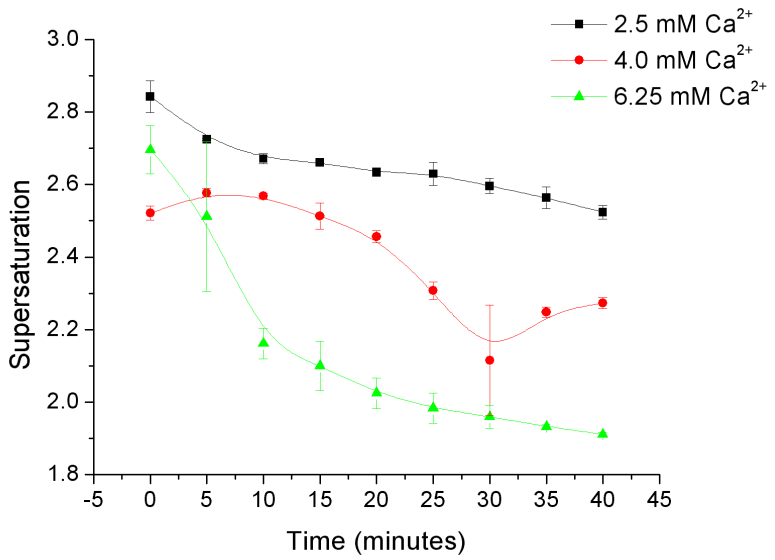

Figure 4.4: Graph of calculated supersaturation (β) against time for HAp at different coating solution starting concentrations. Ca^{2+}:PO_4^{3-} ratio of 5:3. Error bars represent standard error of the mean (n=2)

initial coating solution concentration of 6.25 mmol/l Ca^{2+} and 3.75 mmol/l PO_4^{3-} ions. For HAp (Figure 4.4), the drop is around 0.3 units for the lowest initial coating solution concentration (2.5 mmol/l Ca^{2+} and 1.5 mmol/l PO_4^{3-} ions), as opposed to a drop of approximately 0.8 units for an initial coating solution concentration of 6.25 mmol/l Ca^{2+} and 3.75 mmol/l PO_4^{3-} ions.

For DCPD the situation is more opaque (Figure 4.3). A significant increase in saturation of approximately 0.04 units can be seen over the 40 minute coating period when coating at the highest initial coating solution concentration (6.25 mmol/l Ca^{2+} and 3.75 mmol/l PO_4^{3-} ions). A much more gradual increase of approximately 0.02 units is seen for the lowest initial concentration but for the intermediate concentration (4 mmol/l Ca^{2+} and 2.4 mmol/l PO_4^{3-} ions) there is an initial saturation drop in the first ten minutes of coating followed by a rise, with a net increase over the entire time period of approximately 0.01 units.

4.1.1.3 Identification of phases

Figure 4.5 shows an XRD scan of a standard HAp reference material against which all scans produced in this study can be compared.

In order to determine the phase of calcium phosphate produced by the electrodeposition technique described in Section 3.2, a thick coating was produced by ten repeated coating cycles. Fresh solution with an initial concentration of 2.5 mmol/l Ca^{2+} and 1.5 mmol/l PO_4^{3-} ions was used for each cycle. The XRD scan for this sample can be seen in Figure 4.6. The positions of the peaks for HAp have been marked as the scan fits this profile as listed in the JCPDS files (International Centre for Diffraction Data). This thick sample was made in order to increase the signal to noise ratio from the coating and to reduce the signal from the stainless steel substrate, which dominated scans of thinner coatings.

After ascertaining the d-spacings of the planes, Equation 4.1 which relates this spacing to the Miller indices and crystal dimensions for hexagonal crystals, was applied to the scan in Figure 4.6. This gave crystal lattice dimensions of $a = 9.93$ Å and $c = 7.11$ Å.

$$\frac{1}{d^2} = \frac{4}{3}\frac{(h^2 + hk + k^2)}{a^2} + \frac{l^2}{c^2} \tag{4.1}$$

Where d is the distance between planes in the set (hkl).

On the same sample, the Scherrer formula (Equation 3.1) gave an approximate crystallite thickness of 43 nm for the 002 peak and 141 nm for the 211 peak. Further calculations according to the method of Frank (1965) gave crystallite dimensions of 43 nm along the c axis, 34 nm along the b axis and 136 nm along the a axis.

When comparing the scan of the HAp reference material (Figure 4.5) and the scan of the electrodeposited coating in Figure 4.6 major differences can be seen. Firstly, the

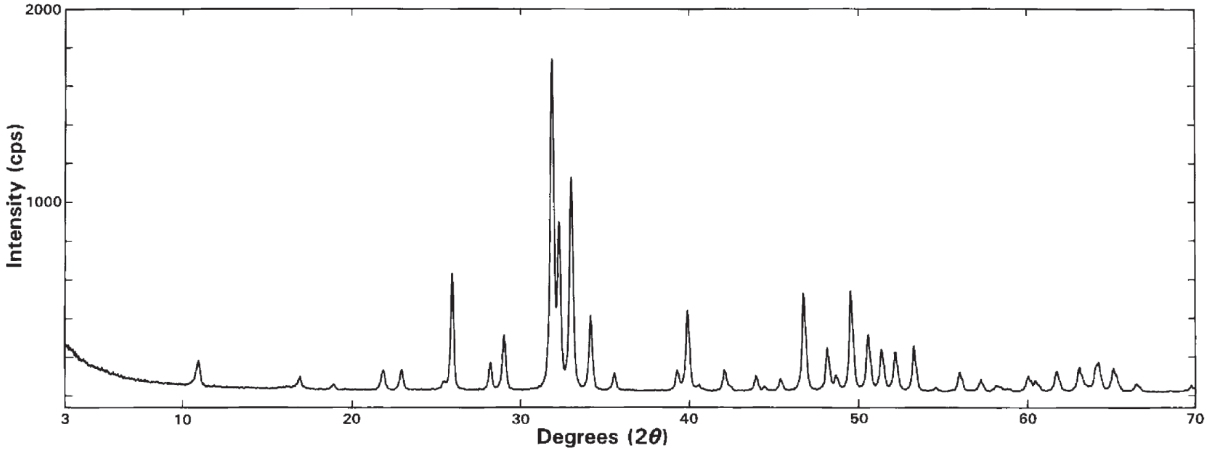

Figure 4.5: Control: XRD scan of highly pure, crystalline, homogeneous HAp standard reference material (Markovic et al., 2004).

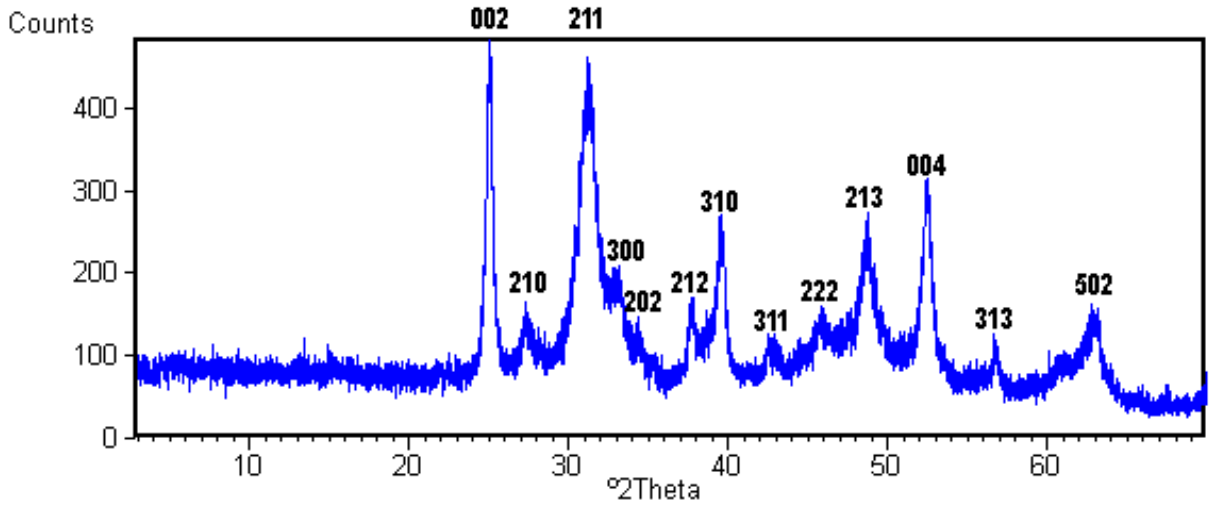

Figure 4.6: XRD scan of a coating produced by ten repeated electrodeposition cycles. Peaks representing planes of hydroxyapatite crystals have been marked.

resolution of peaks in the electrodeposited sample is much lower. Many of the peaks appear to have combined into wider peaks. Secondly, the ratios of the peak intensities are very different to those seen in the standard material. For example, the 002 peak gives the strongest signal in the coated sample as opposed to the 211 peak in the standard material. This difference in ratios implies that the crystallites in the coating had some sort of preferred orientation.

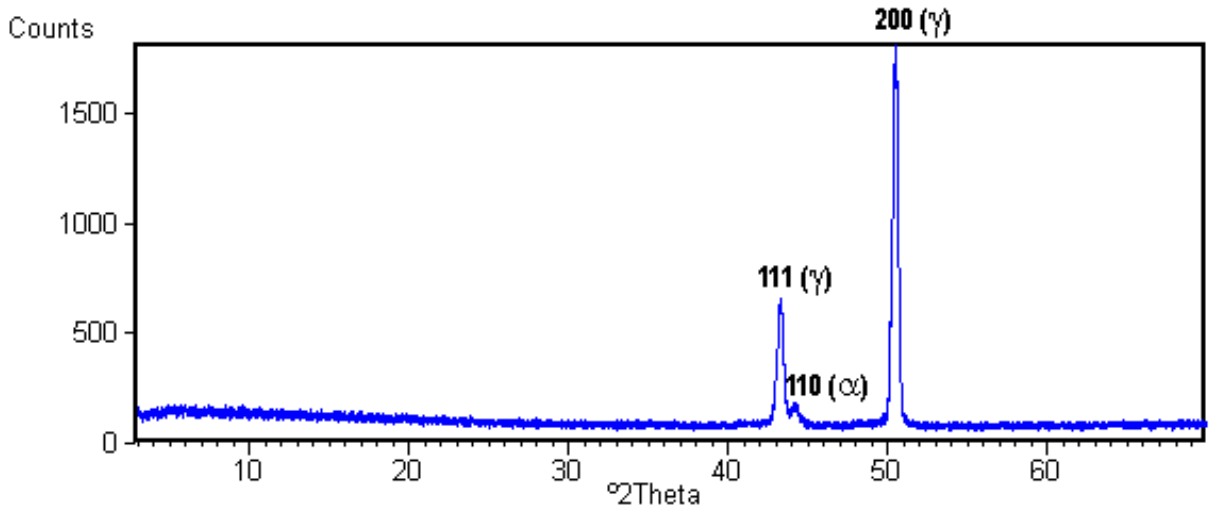

Figure 4.7: XRD scan of uncoated 304 stainless steel sample. The peaks representing planes of austenite (γ) and martensite (α) have been marked.

X-ray diffraction scans were also done of samples which had been coated for one cycle and then given different amounts of time to mature in solution before being removed. The maturation time periods used were 0 h, 1 h, 3h, 5h and 13 h. A control scan was done of an uncoated 304 stainless steel sample which can be seen in Figure 4.7.

Figures 4.8 and 4.9 show the samples coated once then given zero hours maturation time and one hour maturation time respectively. No peaks can be observed other than those of the steel substrate on the scan of the sample without maturation. After one hour of maturation, the HAp 002 and 211 peaks can be observed (Figure 4.9). Figure 4.10

shows an XRD scan of the sample given three hours to mature in solution after the 20 min coating cycle. As well as the 002 and 211 peaks, the 004 peak can now be seen. The next two figures (Figure 4.11 and Figure 4.12) show the XRD scans for the samples given five and thirteen hours respectively to mature. Although the scans are still dominated by the steel substrate peaks, the HAp peaks appear to be more distinct with increasing maturation time.

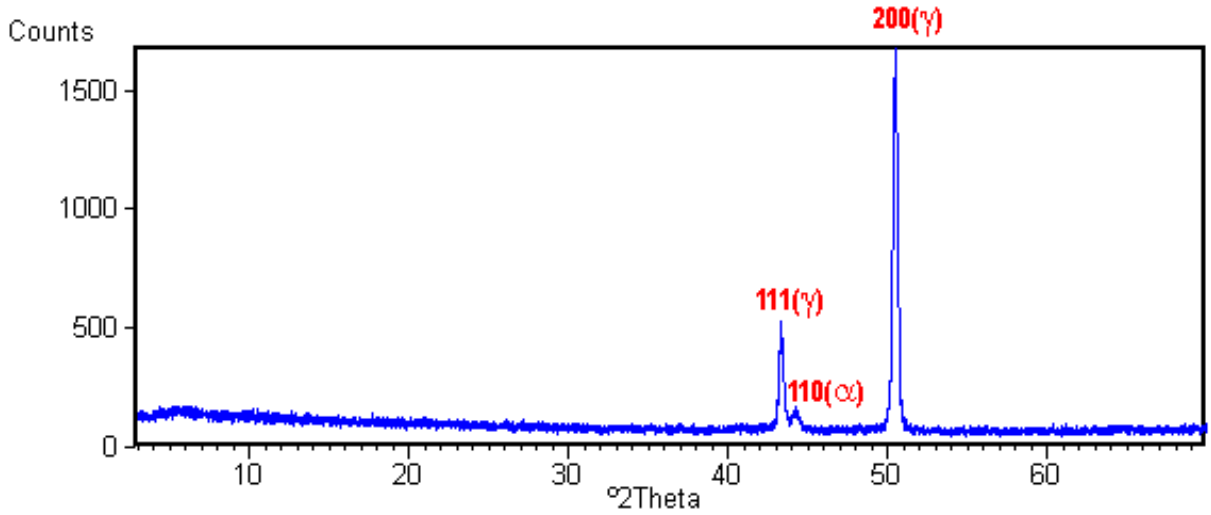

Figure 4.8: XRD scan of a coating produced by one coating cycle and no maturation time. The peaks in red are those representing planes of austenite (γ) and martensite (α) phases of the substrate. Coating thickness 0.5 µm ± 0.1 µm (Standard error of the mean (n=3)).

Figures 4.8 and 4.9 show the samples coated once then given zero hours maturation time and one hour maturation time respectively. No peaks can be observed other than those of the steel substrate on the scan of the sample without maturation. After one hour of maturation, the HAp 002 and 211 peaks can be observed (Figure 4.9). Figure 4.10 shows an XRD scan of the sample given three hours to mature in solution after the 20 min coating cycle. As well as the 002 and 211 peaks, the 004 peak can now be seen. The next two figures (Figure 4.11 and Figure 4.12) show the XRD scans for the samples given five and thirteen hours respectively to mature. Although the scans are still dominated

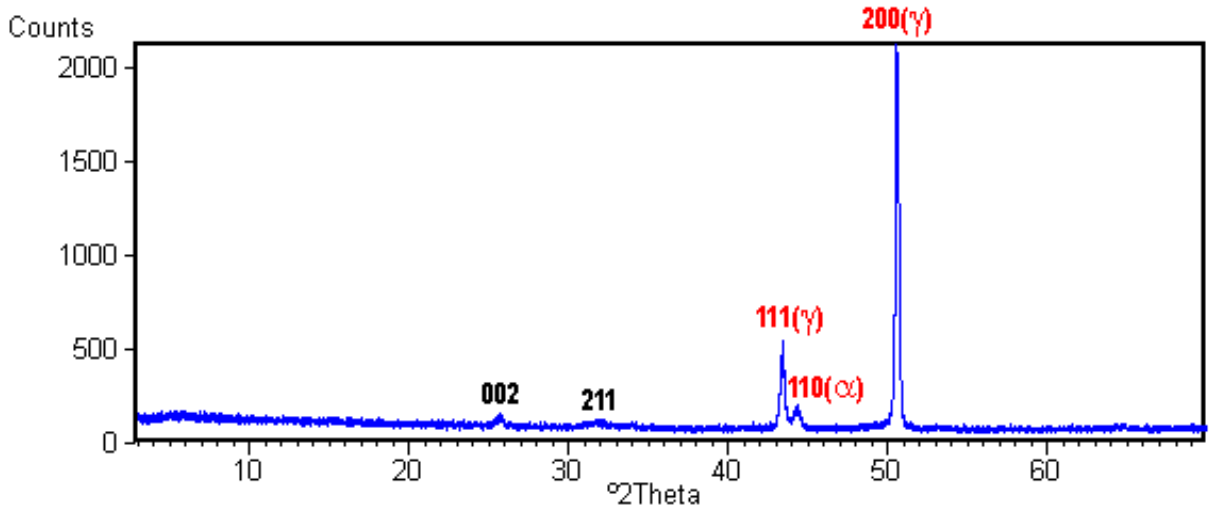

Figure 4.9: XRD scan of a coating produced by one coating cycle and one hour maturation time. The peaks in red are those representing planes of austenite (γ) and martensite (α) phases of the substrate. Peaks representing HAp are marked in black. Coating thickness 3.3 µm ± 0.7 µm (Standard error of the mean (n=3)).

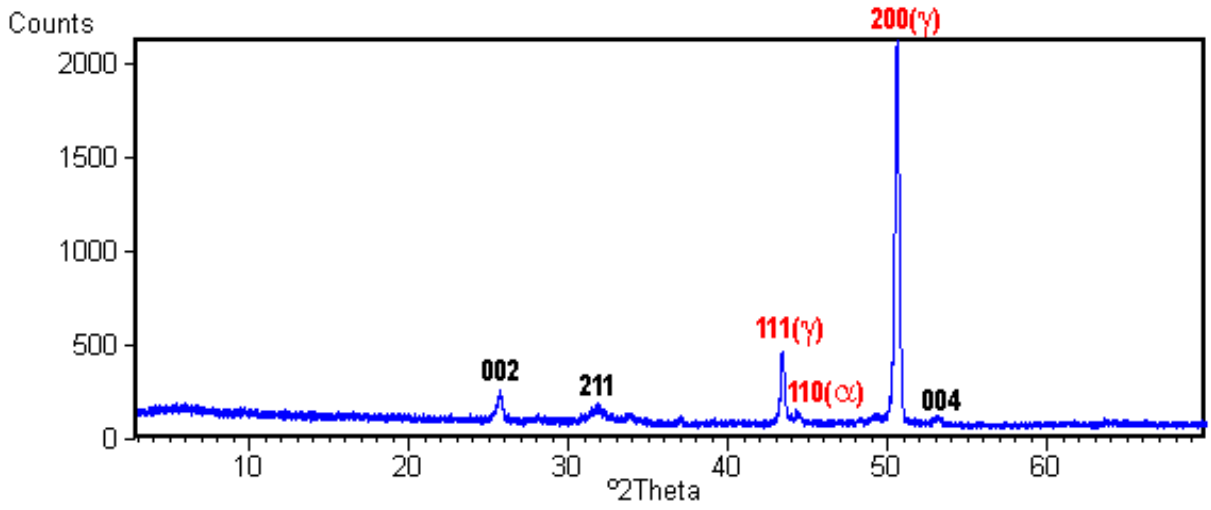

Figure 4.10: XRD scan of a coating produced by one coating cycle and three hours maturation time. The peaks in red are those representing planes of austenite (γ) and martensite (α) phases of the substrate. Peaks representing HAp are marked in black. Coating thickness 3.5 µm ± 0.6 µm (Standard error of the mean (n=3)).

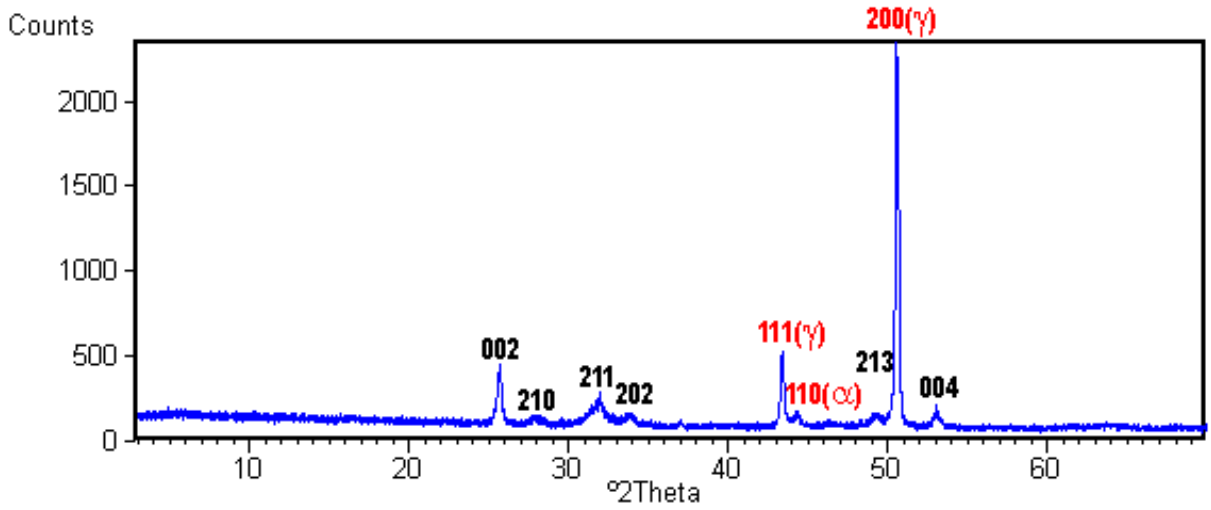

Figure 4.11: XRD scan of a coating produced by one coating cycle and five hours maturation time. The peaks in red are those representing planes of austenite (γ) and martensite (α) phases of the substrate. Peaks representing HAp are marked in black. Coating thickness 5.0 µm ± 0.6 µm (Standard error of the mean (n=3)).

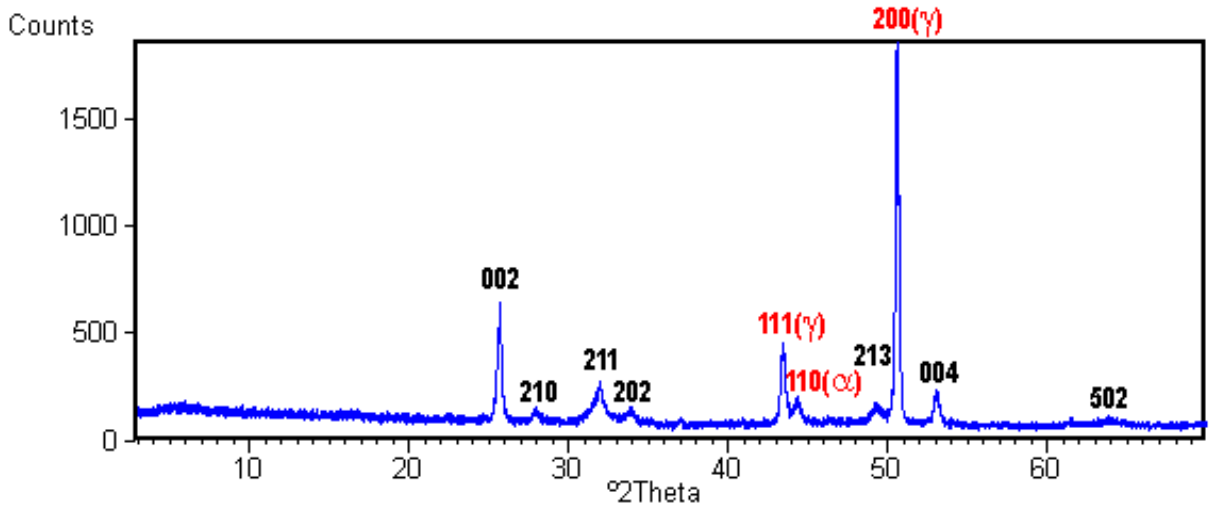

Figure 4.12: XRD scan of a coating produced by one coating cycle and thirteen hours maturation time. The peaks in red are those representing planes of austenite (γ) and martensite (α) phases of the substrate. Peaks representing HAp are marked in black. Coating thickness 4.5 µm ± 0.3 µm (Standard error of the mean (n=3)).

by the steel substrate peaks, the HAp peaks appear to be more distinct with increasing maturation time.

When comparing the scans in Figures 4.8 to 4.12 to that of the standard (Figure 4.5), the ratios of intensities of the peaks differ. This can been seen most clearly in the sample given 13 hours maturation in solution after electrodeposition ceased (Figure 4.12) where the 002 peak dwarfs that produced by the 211 reflection.

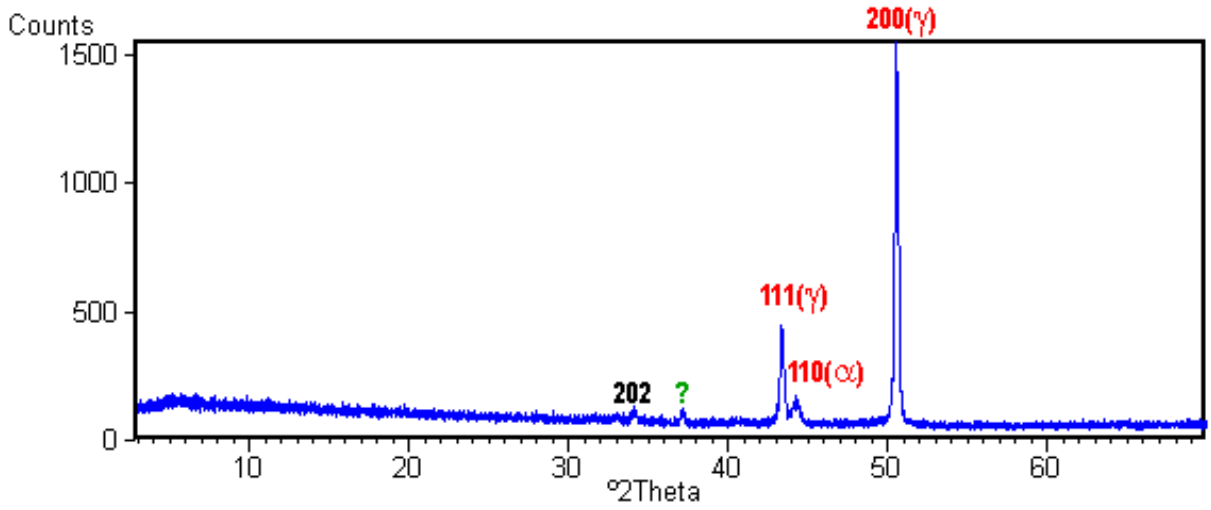

Figure 4.13: XRD scan of a coating produced by five coating cycles. The peaks in red are those representing planes of austenite (γ) and martensite (α) phases of the substrate. Peaks representing HAp are marked in black. The question mark is marking an unknown peak. Coating thickness 2.3 µm ± 0.2 µm (Standard error of the mean (n=3)).

XRD scans of samples coated once, allowed to mature in solution for various amounts of time and then coated for four subsequent coating cycles are displayed in Figures 4.13, 4.14 and 4.15. Unlike in the previous samples (Figures 4.8 to 4.12), the first peaks to be definable are the 202 peak and a peak which cannot be indexed (denoted by the question mark in Figure 4.13). This peak could be have been created by a reflection from any one of a number of phases including DCPD and β-TCP. In the absence of other peaks it is difficult to determine which phase is responsible.

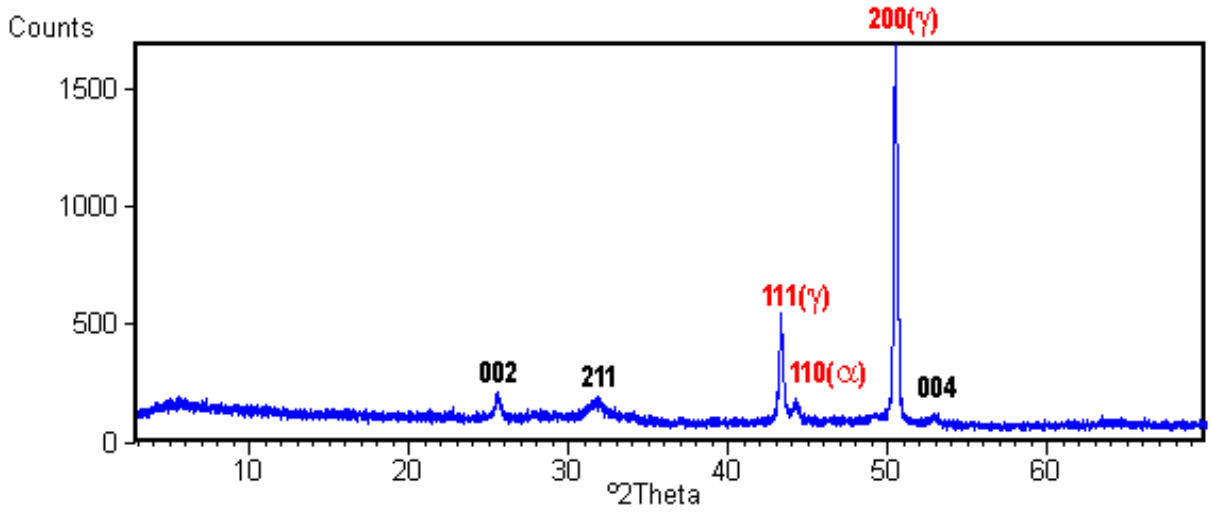

Figure 4.14: XRD scan of a coating produced by one coating cycle and one hour maturation time followed by four more coating cycles. The peaks in red are those representing planes of austenite (γ) and martensite (α) phases of the substrate. Peaks representing HAp are marked in black. Coating thickness 5.6 µm ± 0.3 µm (Standard error of the mean (n=3)).

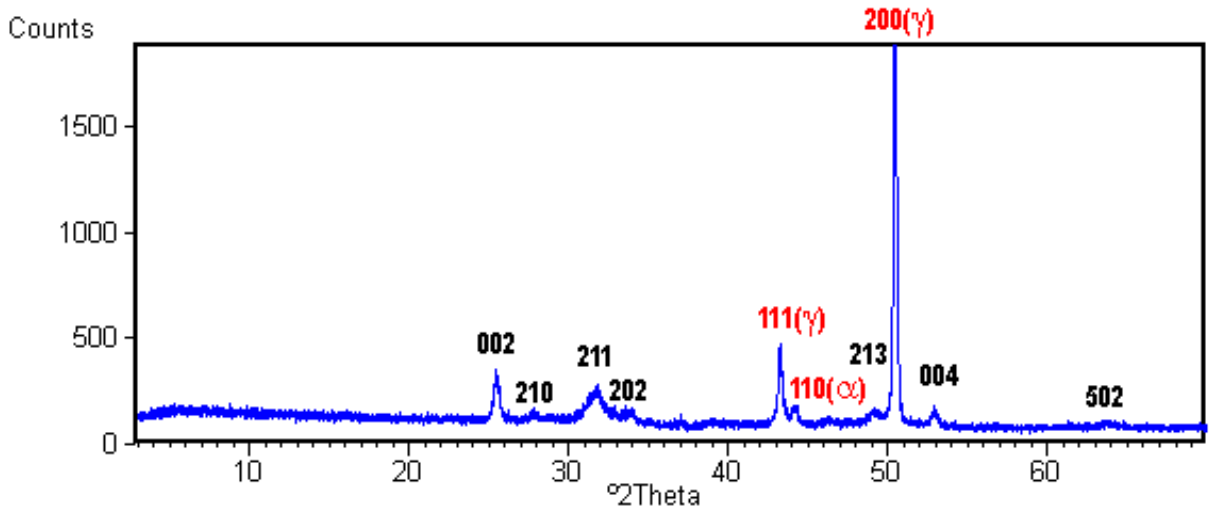

Figure 4.15: XRD scan of a coating produced by one coating cycle and three hours maturation time followed by four more coating cycles. The peaks in red are those representing planes of austenite (γ) and martensite (α) phases of the substrate. Peaks representing HAp are marked in black. Coating thickness 10.0 µm ± 0.0 µm (Standard error of the mean (n=3)).

Figures 4.14 and 4.15 show the peaks for HAp appearing as the maturation time and the resulting coating thickness increase. Again the ratio of peak heights is different to the standard (Figure 4.5) although the difference in intensities of the 002 peak to the 211 is not as great as that seen for the one-coat samples (eg. Figure 4.12).

4.1.2 Increasing coating thickness

A CaP coating of approximately 20 µm was successfully produced after 24 successive 20 minute coating cycles onto a shot-blasted TiAl(6%)V(4%) orthopaedic alloy sample. A picture of this sample can be seen in Figure 4.16. A relatively high coating solution concentration of 6.25 mmol/l Ca^{2+} and 3.75 mmol/l PO_4^{3-} ions was used. At this concentration, a thick precipitate was immediately formed upon mixing of the calcium and phosphate solutions.

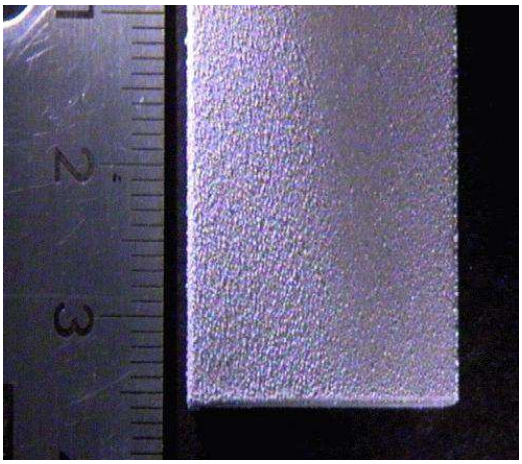

Figure 4.16: Photograph of a thick (≈ 20 µm) CaP coating deposited onto shot-blasted TiAl(6%)V(4%) substrate

The coating was relatively powdery in surface texture and the top surface of the coating could be removed easily using a fingertip, revealing an more dense lower layer of coating.

4.1.3 Effects of drying method and maturation time on coating morphology and shear strength

As described in section 3.7, two different sets of samples, one set coated for five cycles the other for one cycle, were made and allowed to stand in the coating solution after the first

coat for various time periods. Scanning Electron microscopy (Section 3.4.4) and lap-shear testing (Section 3.4.5) results from these samples which were dried either in air (Section 3.5.1) or using critical point drying (Section 3.5.2) are presented here.

4.1.3.1 LV-SEM

Figure 4.17 is a low-voltage scanning electron micrograph of the control sample which was coated without the presence of Ca^{2+} or PO_4^{3-} ions.

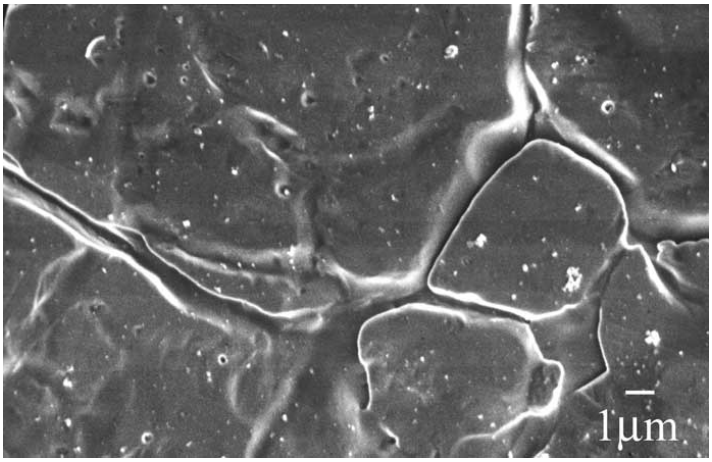

Figure 4.17: Control: Low voltage scanning electron micrograph of stainless steel substrate coated for 20 minutes in buffered solution containing no Ca^{2+} or PO_4^{3-} ions.

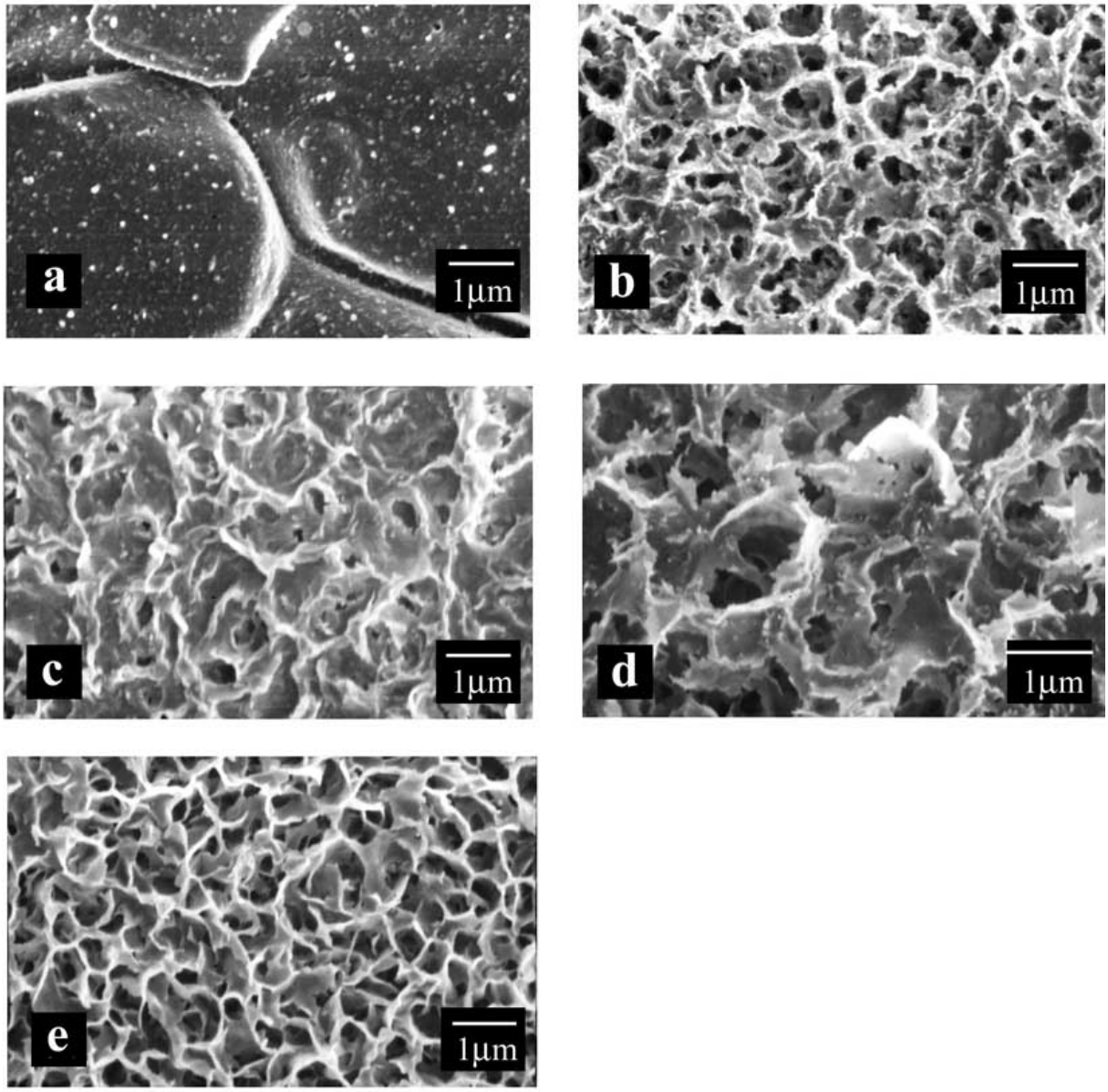

Figure 4.18: Low-voltage scanning electron micrographs of one-coat samples left to mature in coating solution for different amounts of time before being air dried. (a) 0 hours maturation time (thickness 0.5 ± 0.0 µm). (b) 1 hour maturation time (thickness 3.3 ± 0.7 µm). (c) 3 hours maturation time (thickness 3.5 ± 0.6 µm). (d) 5 hours maturation time (thickness 5.0 ± 0.6 µm). (e) 13 hours maturation time (thickness 4.5 ± 0.3 µm).

Air drying

One-coat samples Figure 4.18 shows five micrographs of the set of samples which were coated for one 20 minute coating cycle before being allowed to mature in solution for various amounts of time prior to air drying. The coating solution contained 2.5 mmol/l Ca^{2+} and 1.5 mmol/l PO_4^{3-} ions.

Figure 4.18 (a) shows the surface of a sample which has had no time left standing in solution after coating. A very thin layer of CaP can be seen with regular specks of thicker material. To the naked eye the coating could be seen as a multi-coloured layer on the substrate due to thin film interference with light waves.

A drastic difference can be seen in Figure 4.18 (b), a much thicker, porous CaP coating has formed on the substrate in the one hour extra that this sample has spent in solution after the applied electric field was removed.

Figure 4.18 (c) shows that more precipitation has occurred in the two hours extra standing time that this sample has endured (3 hours total). The pores seen in the previous picture appear to have started to close up.

Figure 4.18 (d) is a micrograph of a sample that was left in solution for a total of five hours. The morphology of this appears very similar to that of the sample in Figure 4.18 (c).

Figure 4.18 (e) shows a sample which was left to mature in coating solution for 13 hours after the coating cycle had finished. In this time, the rather closed, ridged structure seen in pictures (c) and (d) has grown thicker, with delicate layers of CaP forming a porous structure.

Five-coat samples Figure 4.19 shows four micrographs of the set of samples which were coated for one 20 minute coating cycle before being allowed to mature in solution for various lengths of time. The samples then underwent four more coating cycles before being air dried. The coating solution contained 2.5 mmol/l Ca^{2+} and 1.5 mmol/l PO_4^{3-} ions.

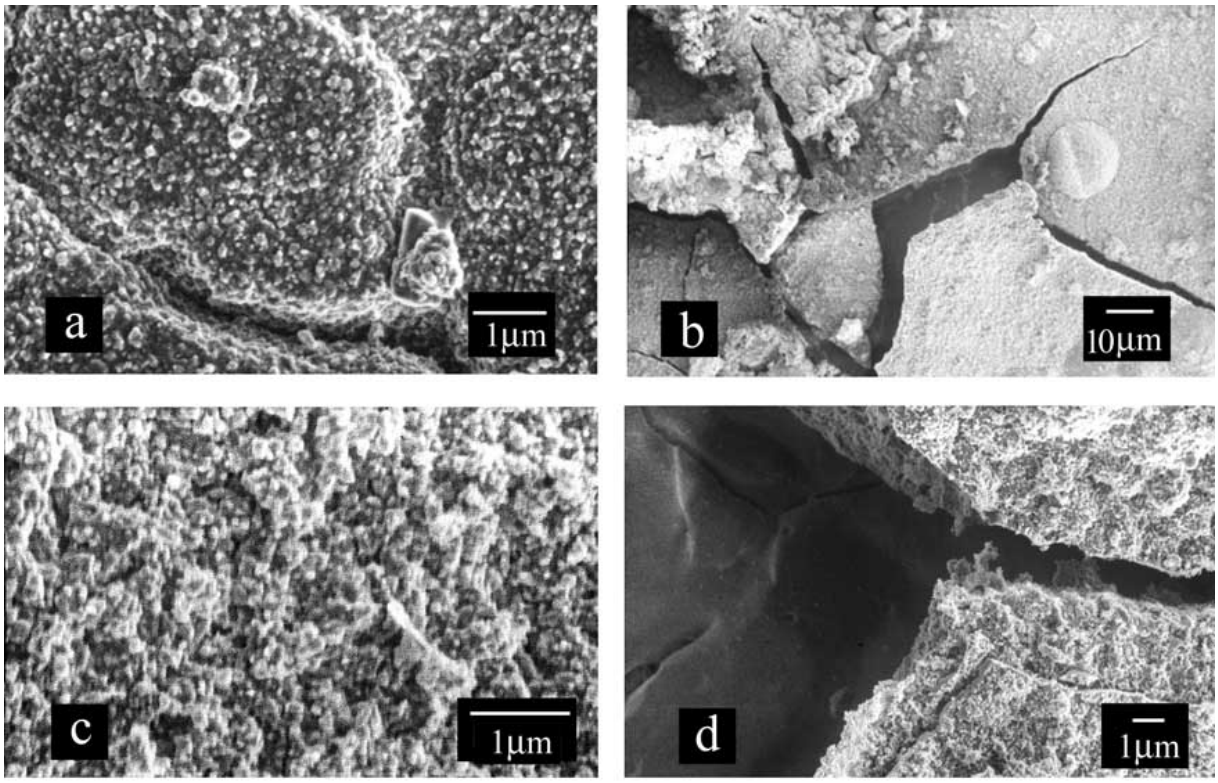

Figure 4.19: Low-voltage Scanning electron micrographs of samples coated once, then left to stand in solution for various lengths of time and then coated four more times before air drying (a) No maturation time between 1st and 2nd coats (thickness 2.3 ± 0.2 µm). (b) 1 hour maturation time. Low magnification (thickness 5.7 ± 0.3 µm). (c) 1 hour maturation time. Higher magnification. (d) 3 hours maturation time after first coat (thickness 10 ± 0.0 µm).

Figure 4.19 (a) shows the surface of a sample which was coated for five successive cycles with no standing time. The coating can be seen to be granular in appearance and relatively thick when compared to a sample which has been coated for just one cycle (Figure 4.18 (a)).

Figure 4.19 (b) is a relatively low magnification view of a sample which has been allowed to stand in solution for one hour between the first and second cycles of the five coatings that it has undergone. The thick coating can be seen to be forming large cracks in its surface. A magnified view of the same sample can be seen in Micrograph 4.19 (c), from which it is possible to tell that the coating has a dense, rough structure unlike the more delicate and porous examples seen in Figure 4.18.

Figure 4.19 (d) shows a sample left in solution for three hours between the first and second coating cycles. The extreme nature of the cracks present can be seen along with the relatively dense and granular coating.

The samples which were left to mature for the the two other time periods (5 hours and 13 hours), were also made, but after drying, the coatings present on both of these were flaky and formed spalls that did not allow any analysis to be performed.

Critical Point Drying

One coat samples Figure 4.20 shows five micrographs of the set of samples which were coated for one 20 minute coating cycle before being allowed to mature in solution for various amounts of time prior to critical point drying. The coating solution contained 2.5 mmol/l Ca^{2+} and 1.5 mmol/l PO_4^{3-} ions.

Figure 4.20 (a) (0 hours maturation time) shows that this sample had virtually no visible coating present after drying had been completed. Just the surface of the steel substrate can be seen, as is obvious when comparing this sample with the control (Figure 4.17).

There is a noticeable difference between Figure 4.20 (a) and Figure 4.20 (b), with the presence of a 'spiky' CaP coating on the sample, which has been left to stand for an hour

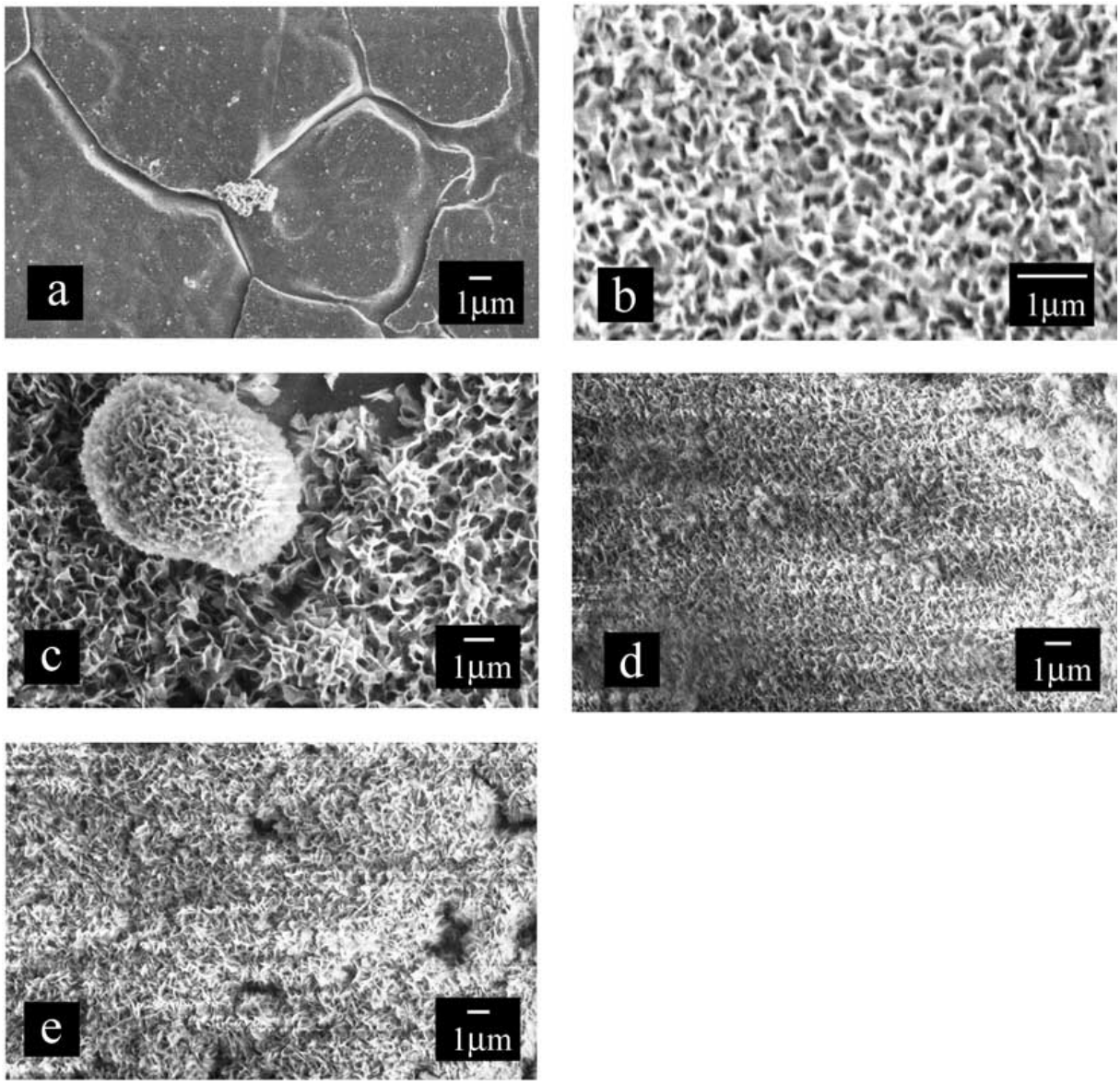

Figure 4.20: Low-voltage scanning electron micrographs of one-coat samples left to mature in coating solution for different amounts of time before critical point drying. (a) 0 hours maturation time (thickness 0.1 ± 0.1 µm). (b) 1 hour maturation time (thickness 3.7 ± 0.6 µm). (c) 3 hours maturation time (thickness 6.3 ± 0.3 µm). (d) 5 hours maturation time (thickness 6.0 ± 0.6 µm). (e) 13 hours maturation time (thickness 5.2 ± 0.9 µm).

in solution before undergoing the drying procedure.

Figure 4.20 (c) focuses on a 'bobble' of material found on the surface of this, a sample which had been allowed to mature for three hours. In fact much of the surface of this sample was covered with these structures which ranged in size from around 2 µm to around 8 µm. The underlying coating consisted of jagged platelets of CaP with a much more porous structure than seen in the coating which was dried in air (Figure 4.18 (c))

The spherical structures discovered on the three sample were not found on the sample left to mature for five hours (Figure 4.20 (d)). The coating on this particular sample was more dense and uniform than that seen in Figure 4.20 (c).

Thirteen hours of maturation time led to the development of a relatively uniform coating but with occasional lumps and hollows caused by thickness variations, as can be seen in Figure 4.20 (e).

Five-coat samples Figure 4.21 shows three micrographs of the set of samples which were coated for one 20 minute coating cycle before being allowed to mature in solution for various lengths of time. The samples then underwent four more coating cycles before being dried in the CPD apparatus.

The coating present after five consecutive coating cycles with no maturation time was very thin, with a scattering of fine particles on the substrate surface (Figure 4.21 (a)). This contrasts greatly with the sample coated in exactly the same way, but dried in air rather than through the critical point method (Figure 4.19 (a)).

Figure 4.21 (b) and (c) show that a relatively intact coating was found after three hours (4.21 (b)) and also even after five hours (4.21 (c)) maturation between the first two coating cycles. This was unlike that seen in the air dried samples left for the same periods of time.

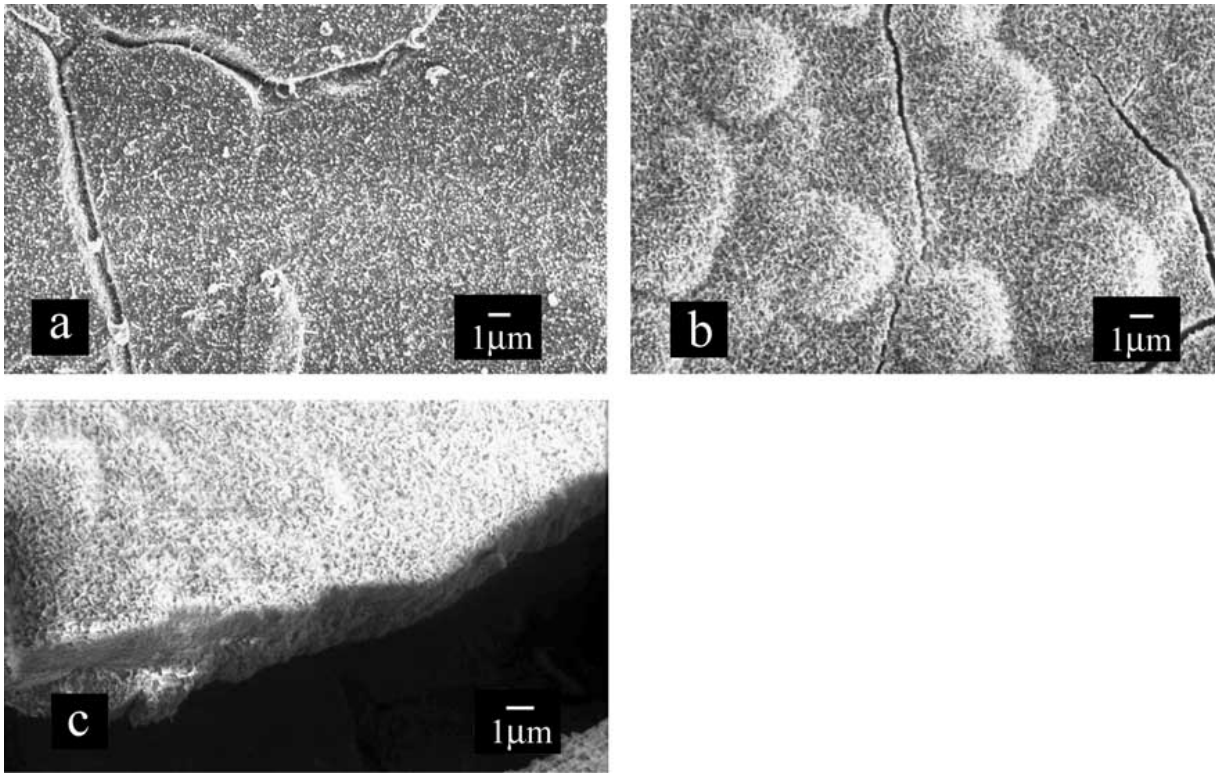

Figure 4.21: Low-voltage Scanning electron micrographs of samples coated once, then left to stand in solution for various lengths of time and then coated four more times before critical point drying (a) No maturation time between 1st and 2nd coats (thickness 0.5 ± 0.0 µm). (b) 3 hours maturation time (thickness 8.0 ± 1.0 µm). (c) 5 hours maturation time (thickness 6.3 ± 0.3 µm).

A series of circular convex eruptions in the coating can be seen in Figure 4.21 (b). An idea of the thickness of the CaP deposited when the sample was allowed to stand for five hours can be gauged in Figure (c), which focuses in on the edge of a part of the coating which is starting to peel off the stainless steel. This thickness was measured by optical microscopy as approximately 6.3 µm.

As was the case for the air dried five-coat samples, the sample left to stand for 13 hours after the first coat was too poorly adhered to the substrate to carry out any analysis.

4.1.3.2 Coating thickness and maturation time

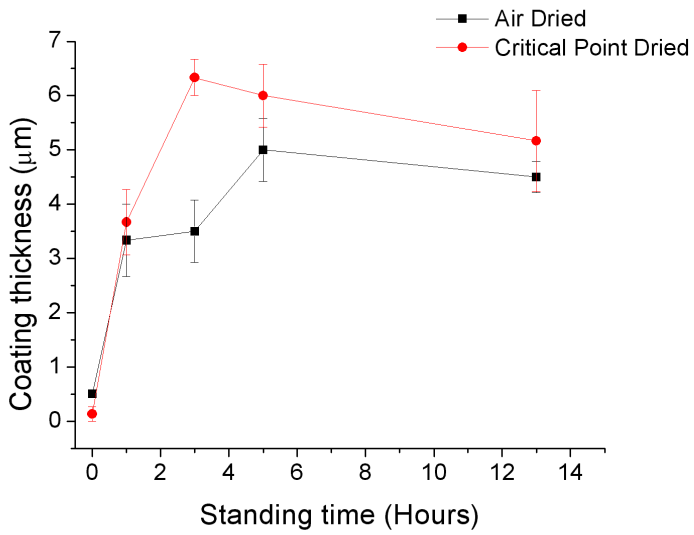

Figure 4.22: Coating thickness against maturation time for one-coat samples. Error bars represent standard error of the mean (n=3).

Figure 4.22 shows the variation in coating thickness with maturation time for the one coat samples which had been dried in air and by critical point drying. It can be seen that the thickness of the air dried coating increases rapidly in the first hour of maturation and then rises more slowly to a maximum of around 5 µm after five hours before levelling off.

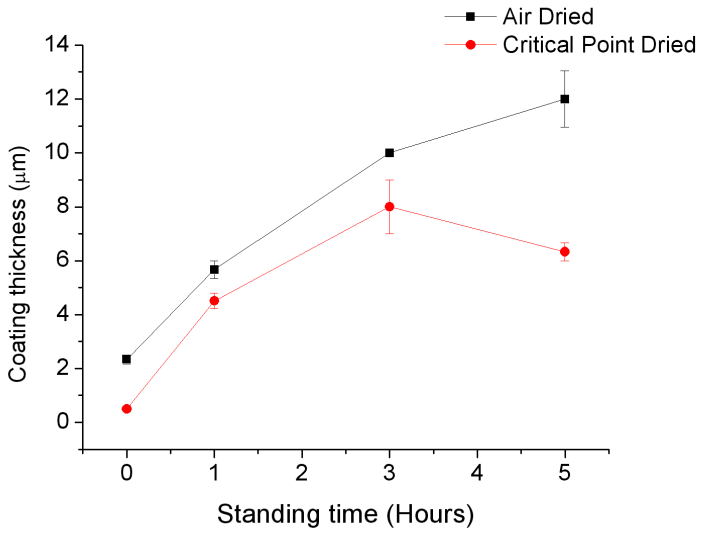

Figure 4.23: Coating thickness against maturation time for five-coat samples. Error bars represent standard error of the mean (n=3).

The thickness of the coating dried using the critical point method rises rapidly until three hours of maturation ($\approx$ 6 µm in thickness) where it also levels off. The critical point dried coating is less thick than the air dried coating in samples given no maturation time but thicker than the air dried coating after three hours of maturation.

Figure 4.23 shows the thickness variation with maturation time for the five-coat samples. The thickness of the air dried samples rises from around 2 µm with no maturation time to 12 µm after five hours maturation. The air dried samples are thicker at each time period than those which have been critical point dried. In fact, the thickness of the critical point dried samples falls slightly between three and five hours of maturation.

4.1.3.3 Lap-shear strength

Control The control sample was made from two uncoated samples tested in the same way as for all of the other lap shear samples (Section 3.4.5). The resulting shear strength

was calculated as 9.1 MPa ± 80 kPa (Standard Error).

One coat samples Figure 4.24 shows a graph of the lap shear strength against maturation time for the samples coated once.

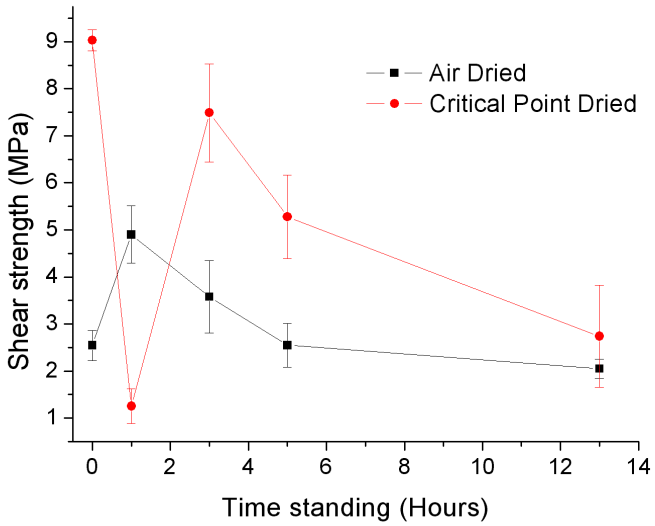

Figure 4.24: Lap-shear strength against maturation time for one coat samples. Error bars represent standard error of the mean (n=3).

For the air-dried samples, the initial trend in shear strength can be seen to be a doubling from around 2.5 MPa to around 5 MPa with an hour of maturation time. This is followed by a decline in shear strength as the standing time increases.

For the critical point dried samples, the trend in strength is an initial sharp drop from a maximum of around 9 MPa at zero hours standing time to a shear strength of around 1 MPa after one hour maturing in solution. The strength then jumps up to approximately 7.5 MPa for the three hour samples before starting to decline with increasing time.

It is also clear from the graph that the shear strength of the critical point dried samples is higher than that recorded for the air dried samples at maturation times of zero, three

and five hours.

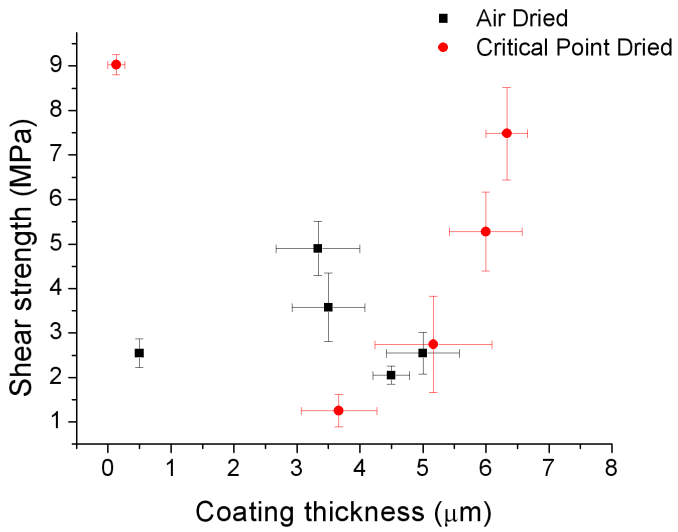

Figure 4.25: Lap-shear strength against coating thickness for one-coat samples. Error bars represent standard error of the mean (n=3).

Figure 4.25 shows a plot of coating lap-shear strength against coating thickness for the one-coat samples. There is no obvious relationship between the two variables for the air dried samples. The shear strength of those coatings which were dried using the critical point method appears to show an increase in shear strength with increasing coating thickness above ≈ 3.5 µm. The shear strength for the CPD samples is however highest at the lowest coating thickness.

Five coat samples Figure 4.26 shows lap shear strength against maturation time for the samples coated for one coat, left to mature in solution and then coated for four more cycles before being dried.

From the data collected for the air dried samples, it is only possible to say that there is a slight increase in shear strength after three hours maturation time when compared

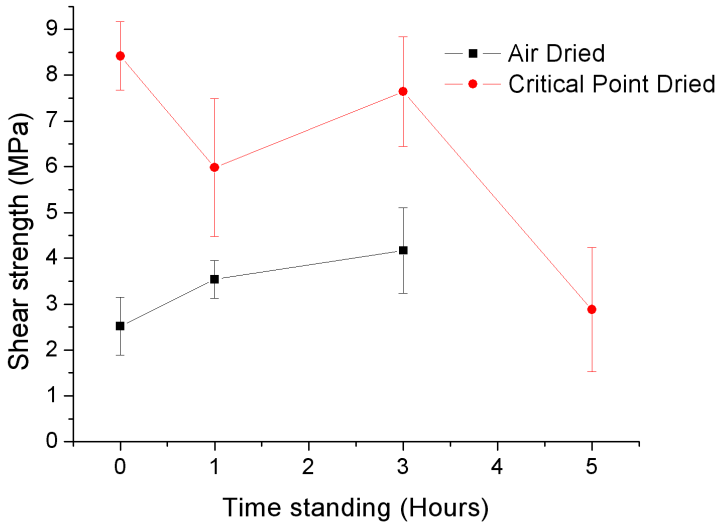

Figure 4.26: Lap-shear strength against maturation time after the initial coating cycle for five-coat samples. Error bars represent standard error of the mean (n=3).

with the samples left standing for zero hours.

There is a slight reduction in shear strength for the critical point dried samples after one hour maturation time as compared with those given no maturation time. There is a large reduction in shear strength in the five hour samples when compared with all the other samples.

The shear strength of the critical point dried samples is higher than that for air dried samples at zero, one and three hours.

Figure 4.27 shows a plot of coating lap-shear strength against coating thickness for the five-coat samples. There is a slight increase in shear strength of the air dried samples as the coating thickness increases from around 2.5 µm to 10 µm. The relationship between the variables for the CPD samples is not clear, with the highest coating shear strength occurring at both the lowest and highest coating thicknesses.

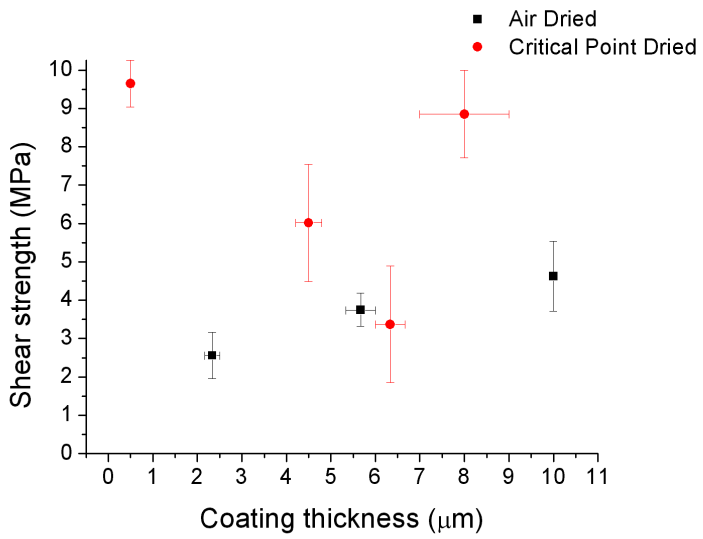

Figure 4.27: Lap-shear strength against coating thickness for five-coat samples. Error bars represent standard error of the mean (n=3).

4.1.4 SEM investigation of lap-shear fracture surfaces

Micrographs of some of the post shear test surfaces of the coated samples and the blanks which had been cemented to them are presented here.

Figure 4.28 shows post-fracture surfaces of the blanks which were stuck to the one coat samples before testing. These blanks were the uncoated pieces of stainless steel that were coated in epoxy resin and then attached to the coated samples. Therefore, these micrographs show the underside of any coating material that was pulled off the coated samples since the fracture path was found to be between the coating and the original substrate to which it was attached. A diagram explaining this can be seen in Figure 4.29.

Figure 4.28 (a) shows a relatively low magnification view in which a pattern of steel grain boundaries can be seen. This pattern is protruding from the layer of epoxy and coating that has been pulled off from the coated sample. Flecks of the coating that have been pulled off can be seen sparsely covering the epoxy surface. Figure 4.28 (b) shows a

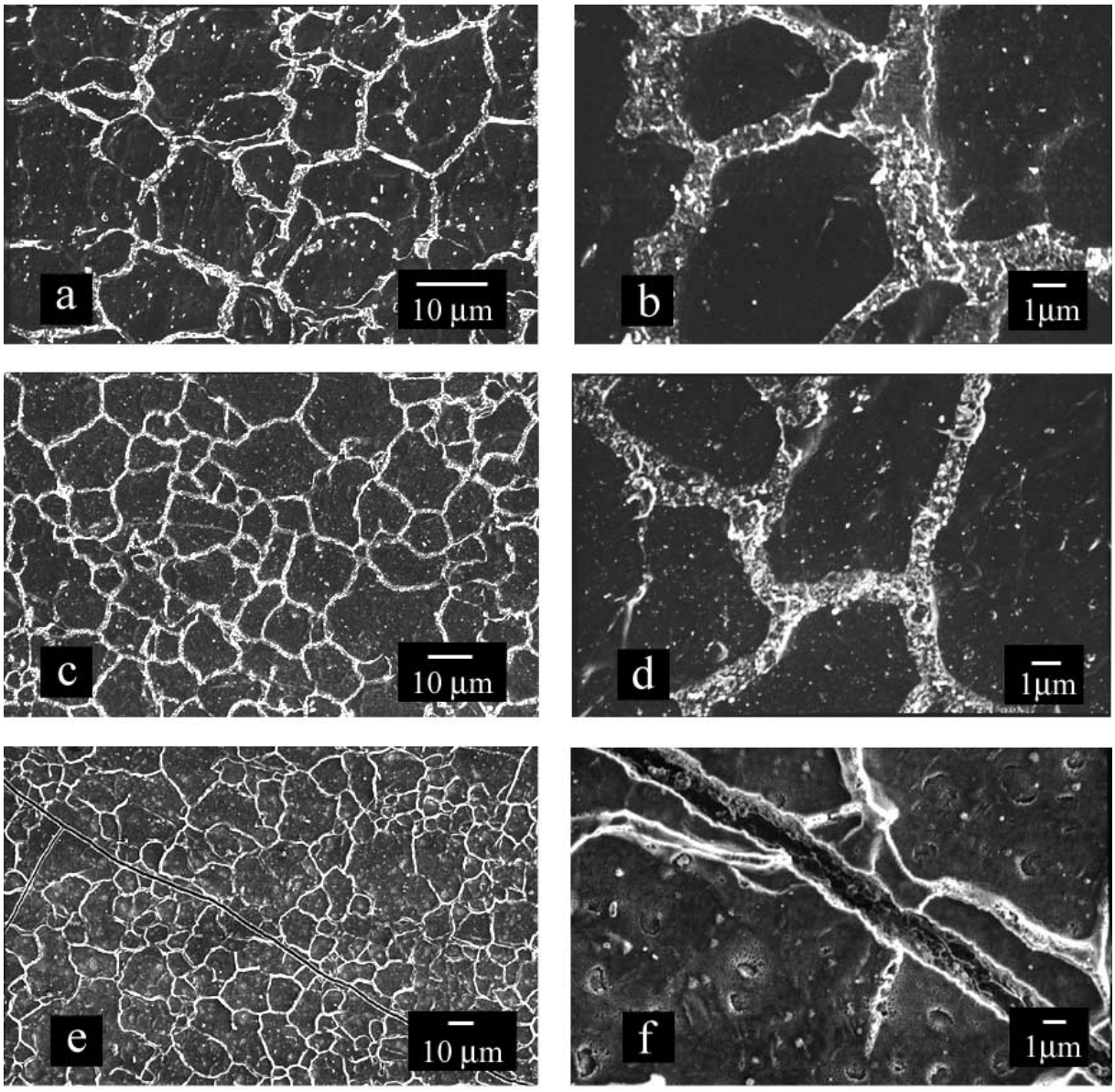

Figure 4.28: Micrographs of the fracture surfaces of blanks used during lap-shear testing of one coat samples. (a) Pull off from sample left to mature for one hour. (b) Higher magnification view of sample in Micrograph 1. (c) Pull off from sample left to mature for three hours. (d) Higher magnification view of sample in Micrograph 3. (e) Pull off from sample left to mature for thirteen hours. (f) Higher magnification view of sample in Micrograph 5.

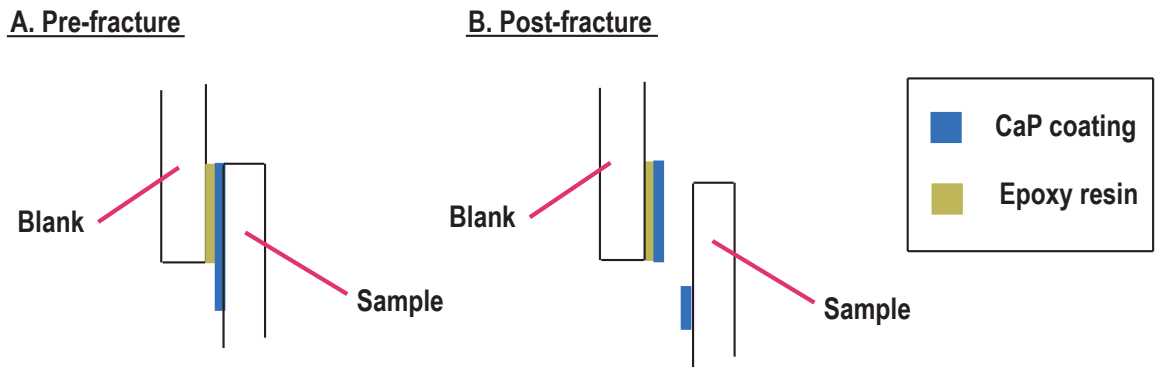

Figure 4.29: Diagram explaining views of post-fracture surfaces. (A) Pre-fracture. (B). Post-fracture where the the fracture path was found to be between the coating and the substrate, leaving both CaP and epoxy resin attached to the blank.

higher magnification view of this surface.

The low and high magnification micrographs of the pulled off coatings from a sample left to mature in solution for three hours after coating (Figure 4.28 (c) and (d)) are similar to Figures 4.28 (a) and (b) in many respects. However, the flecks of coating are less well defined and more closely spaced than for the samples given zero hours maturation time. It is difficult to say whether there is a continuous layer of coating covering the epoxy pull-off. Because of the brightness of the protruding grain boundary imprints (magnified in Figure 4.28 (d)), it is also difficult to determine whether these are covered in a layer of the CaP coating.

The LV-SEM pictures of the pull off from a sample allowed to stand in solution for 13 hours after coating can be seen in Figure 4.28 (e) and (f). The bulk of the coating in the low magnification view can be seen to be covered in many light patches in the gaps between the grain boundary imprints. In the higher magnification view (Figure 4.28 (f)), these patches can be seen to consist of pits in the coating pull off. In comparison to the samples left to mature for shorter time periods, the grain boundary imprints appear to

be smoother and more raised in morphology.

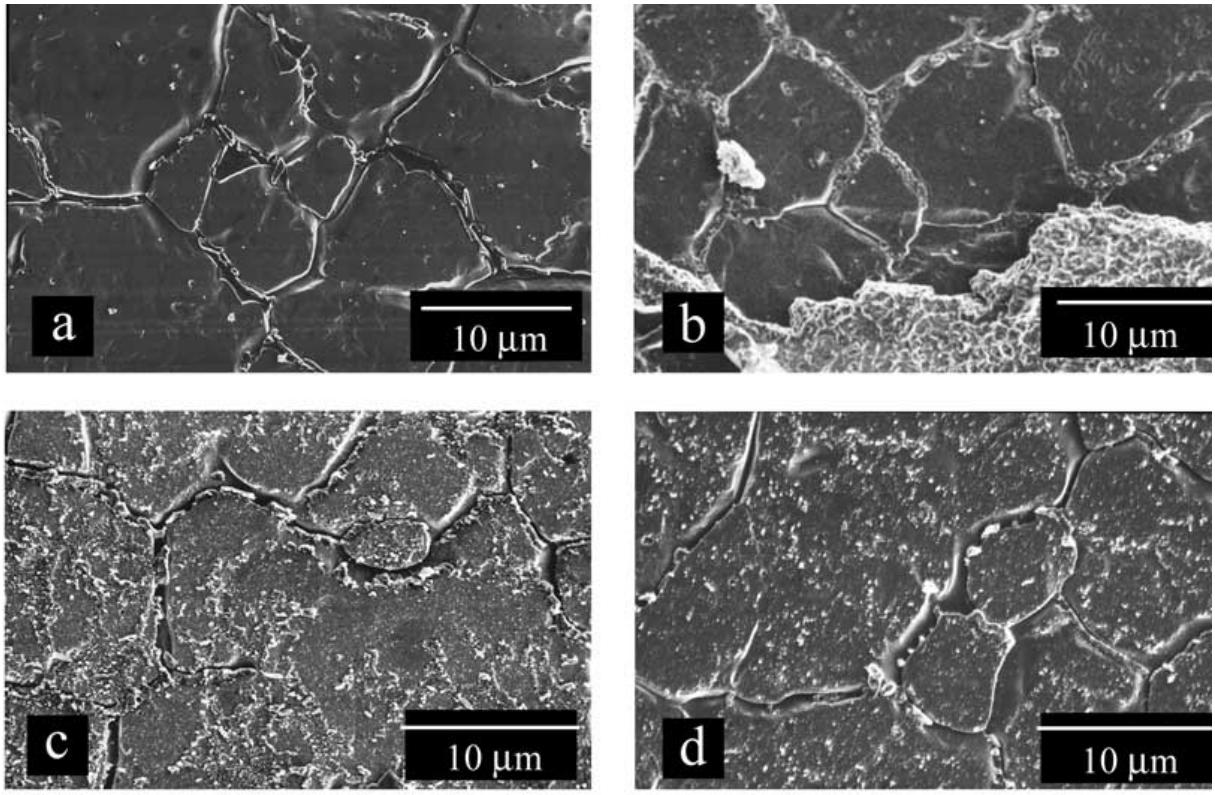

Figure 4.30: Micrographs of the post-fracture surfaces of one coat samples used for lap-shear testing. (a) Sample coated once, without any maturation time in solution prior to the coating being sheared off. (b) One-coat sample left to mature for one hour prior to the coating being sheared off. (c) One-coat sample left to mature for five hours prior to the coating being sheared off. (d) One-coat sample left to mature for thirteen hours prior to the coating being sheared off.

Figure 4.30 shows LV-SEM micrographs of the post-fracture surfaces of the one-coat samples that had been coated before having uncoated blanks attached to them. A diagram explaining this can be seen in Figure 4.29.

Figure 4.30 (a) shows that virtually all of the coating present, on the sample which did not have any time standing in solution, was removed by the epoxy-coated blank during the lap shear test. All that can be seen to remain is a few scattered particles. For the sample which received a one hour maturation in coating solution (Figure 4.30 (b)), the

area where the coating has been pulled off is similar to that seen in Figure 4.30 (b), but with a larger amount of particulate matter in the grain boundaries. In this particular micrograph a section of coating that has not been pulled off can be seen in the bottom of the image.

The situation is very different when it comes to the sample given five hours maturation time (Figure 4.30 (c)). Many fragments of the original coating remain. The remains of the coating appear thicker in certain areas. The coating remaining on the 13 hour sample (Figure 4.30 (d)) is not as thick as that seen in Figure 4.30 (c), but appears to be more particulate in nature.

4.1.5 Effect of maturation time on coating crystallinity

Unfortunately XRD scans on the various samples manufactured for the maturation time studies gave a very poor signal to noise ratio due to the relatively thin coatings. Transmission electron microscopy and electron diffraction of samples grown on to grids (method described in Sections 3.4.2 and 3.4.3), gave more reliable results.

Examples of TEM bright field micrographs and corresponding selected area diffraction patterns (SADP) can be seen in Figure 4.31. Figure 4.31 (a) shows the coating after one 20 minute coating cycle, with no maturation time in solution. The substance present can be seen to be relatively amorphous, with clumps made up of spheres. Figure 4.31 (b) shows the SADP corresponding to Figure 4.30 (a). This confirms the amorphous nature of the material seen in the bright field image. Figure 4.31 (c) shows the coating after one 20 minute coating cycle and then one hour maturation time in solution. Here, the substance can also be seen to be amorphous in nature, with spheres of material made up of smaller spheres. The SADP of Figure 4.31 (c) can be seen in Figure 4.31 (d) confirming

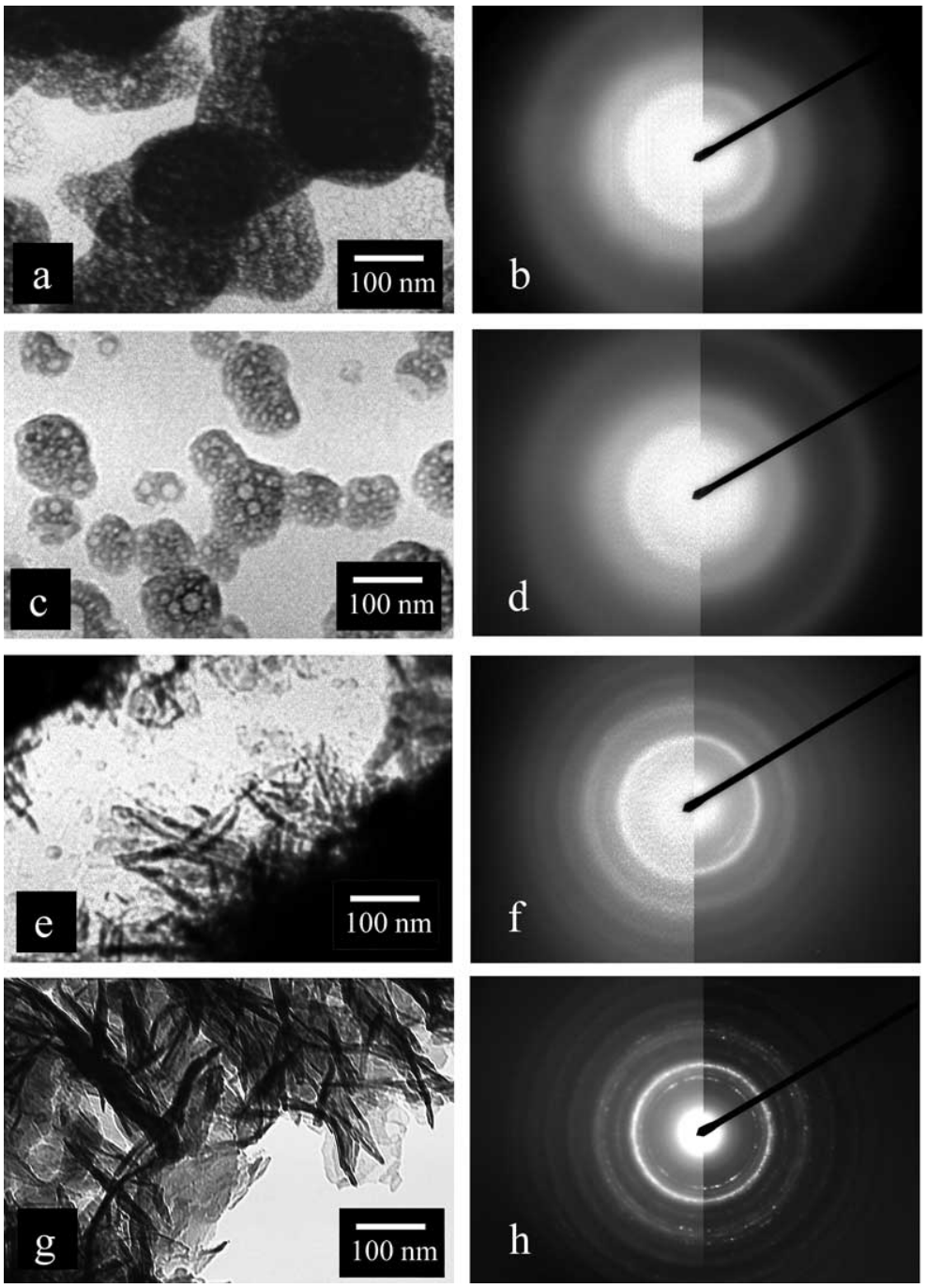

Figure 4.31: TEM bright field micrographs and corresponding selected area diffraction patterns of coatings produced by one coating cycle on holey carbon grids. Samples were allowed to mature in solution for various amounts of time. (a) Bright field image of sample without any maturation time. (b) Selected area diffraction pattern relating to image (a). (c) Bright field image of sample with 1 hour maturation time. (d) Selected area diffraction pattern relating to image (c). (e) Bright field image of sample given 3 hours maturation time. (f) Selected area diffraction pattern relating to image (e). (g) Bright field image of sample given 5 hours to mature in solution. (h) Selected area diffraction pattern relating to image (g).

the relatively amorphous nature of the material.

For the sample given three hours to mature in solution (Figure 4.31 (e), SADP Figure 4.31 (f)), material which is more crystalline in nature can be seen to have formed. Needle-like crystals can be seen at the edge of an area of coating in the bright field micrograph and a defined set of diffraction rings can be made out in the SADP. These crystals can be seen to have been grown further after a further two hours in solution (total time 5 hours), as seen in Figure 4.31 (g). The corresponding SADP (Figure 4.31 (h)) shows a polycrystalline pattern with ring spacing characteristic of hydroxyapatite. After indexing these rings to the planes of HAp (with the brightest ring being the (211) set of planes) and calculating the corresponding d-spacings, Equation 4.1 was used to calculate the crystal lattice dimensions. This gave results of $a = 9.53$ Å and $c = 6.87$ Å.

4.2 Liposomes

4.2.1 Preliminary experiments

A long period of preliminary experimentation occurred. This was mainly concerned with finding a method of liposome manufacture that was capable of reliably entrapping solutes given the equipment and raw materials available.

4.2.1.1 Maximising entrapment efficiency

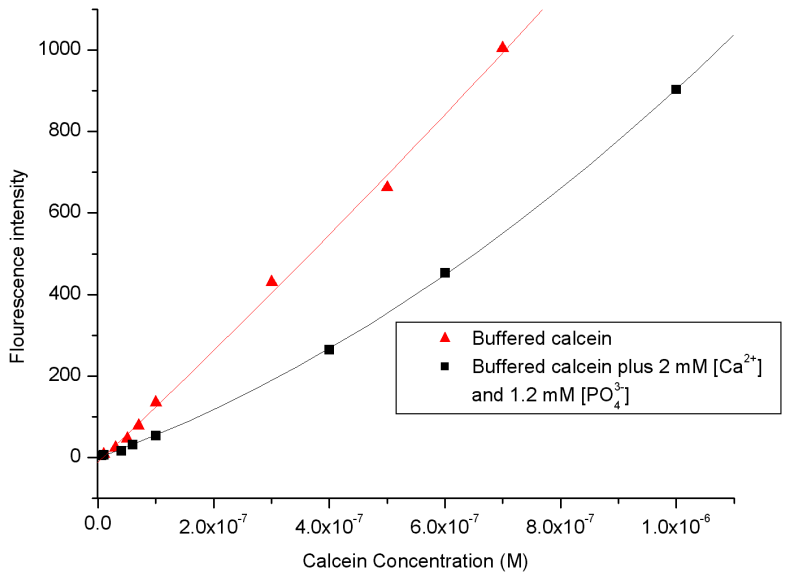

Figure 4.32: Calibration curve for the fluorescence of calcein and calcein with the addition of 2 mmol/l Ca^{2+} and 1.2 mmol/l PO_4^{3-} ions. Both sets of solutions were buffered at *p*H 7.4 with 10 mmol/l HEPES.

Calcein calibration As described in Section 3.9.1, methods were employed that used the fluorescent marker molecule, calcein. Figure 4.32 shows the calibration curves for calcein and calcein with Ca^{2+} and PO_4^{3-} ions added. The recorded fluorescence intensity increased sharply with a relatively small change in calcein concentration for both sets

of samples, with a concentration increase of approximately 3×10^{-7} mol/l doubling the relative fluorescence of the solution (in the case of the solution without CaP added). The rate of increase in fluorescence with concentration was slightly less for calcein solutions that also contained Ca^{2+} and PO_4^{3-} ions.

This information could then be used for quantification of calcein concentration, allowing entrapment efficiency to be calculated through the method described in Section 3.9.1.3. For experiments involving calcein in the presence of CaP (such as in the case of CaP-coated liposomes, Section 3.8.4), the calibration curve obtained with the addition of Ca^{2+} and PO_4^{3-} ions was used.

Method of manufacture The initial method used in order to manufacture liposomes was that described in section 3.8.1. This was later abandoned due to the need to use a large volume of solution (10 ml) containing the solutes to be entrapped. This meant the process was intrinsically inefficient at entrapping the solutes. The process to manufacture SPLV's (Section 3.8.2) was then used instead. In this method only 0.3 ml of solution, containing the solute to be entrapped, was required in order to produce the same volume of liposome suspension as in the initial methodolgy.

Optical micrographs of SPLVs containing 70 mmol/l buffered calcein solution can be seen in Figure 4.33.

From these micrographs it can be seen that the population of SPLVs varies widely in size from the nanometre range to several microns in diameter.

Entrapment efficiency Initial experiments on determining entrapment efficiency of calcein gave very low percentage entrapment results (≈ 0.6 %). This was later increased to approximately 8 % through measures such as replacing the solid phosphatidylcholine used

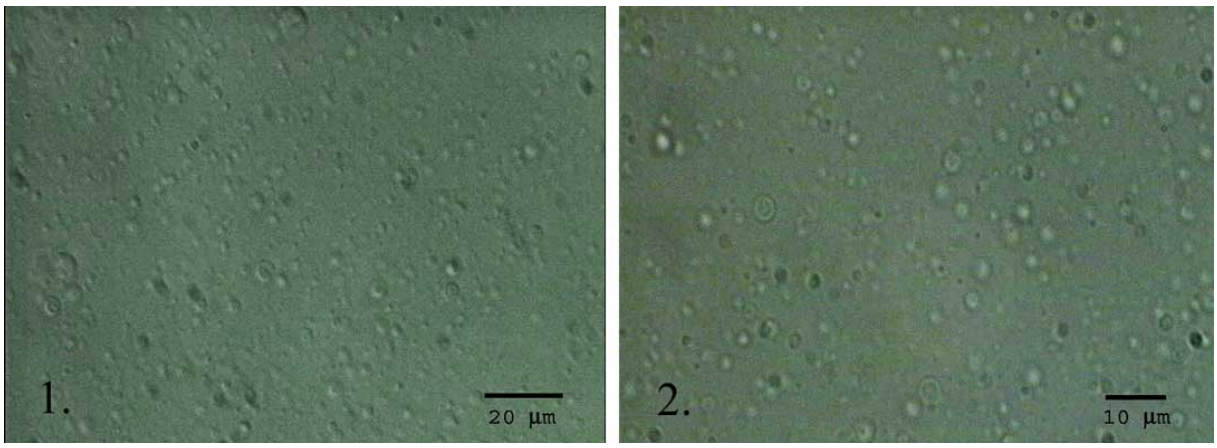

Figure 4.33: Optical micrographs of SPLVs containing entrapped calcein solution. (1) Low magnification micrograph (× 500). (2) Higher magnification micrograph (× 750).

initially (60 % pure) with lipid that had been pre-dissolved in chloroform and packaged in a protective atmosphere (99 % pure). Example fluorescence spectra from an entrapment experiment can be seen in Figure 4.34.

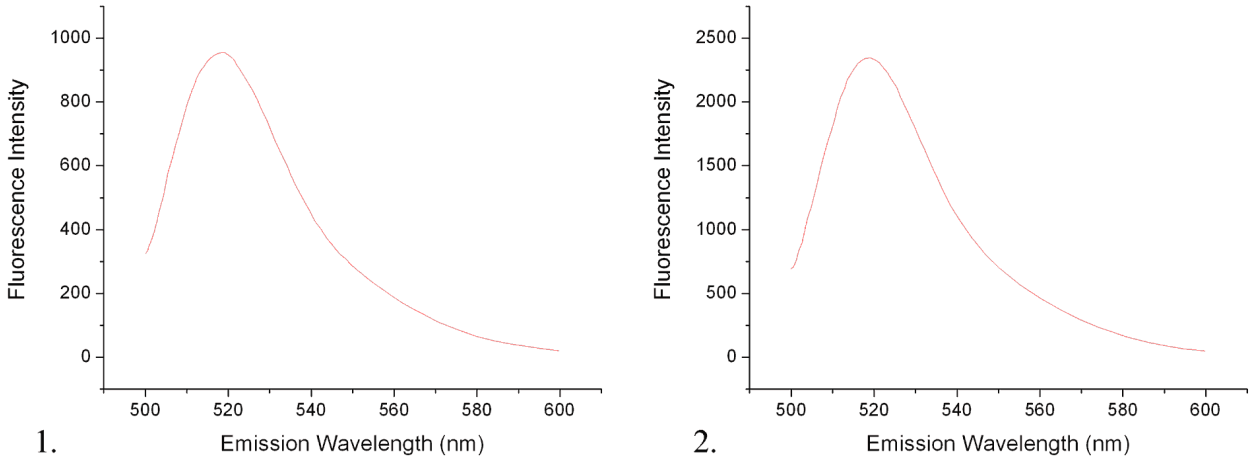

Figure 4.34: Example calcein fluorescence spectra used to calculate entrapment efficiency. Excitation wavelength 490 nm. (1) Spectrum from liposome population with entrapped calcein (2) Spectrum from the same liposome population after the liposomes have been disrupted with ethanol, releasing the calcein.

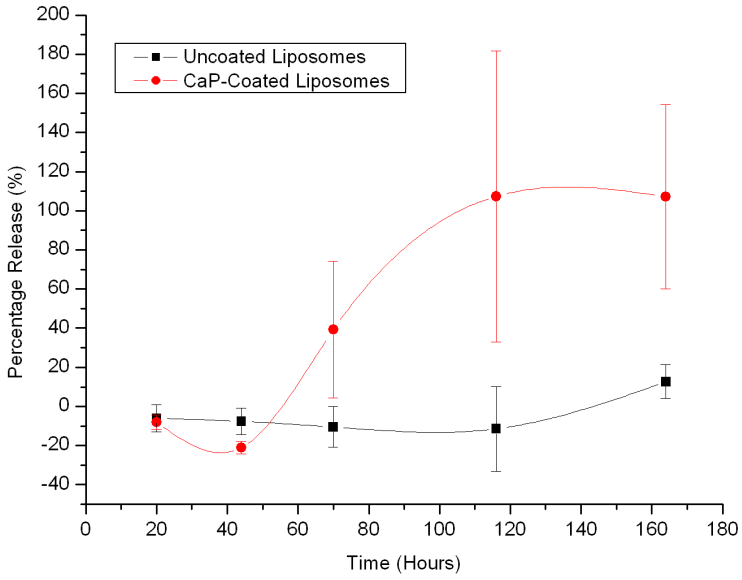

Figure 4.35: Graph showing the percentage release of calcein over time for CaP-coated and non-coated liposomes incubated at 37℃. Solutions were buffered to *p*H 7.4. Error bars represent the standard error of the mean (n=2).

4.2.2 Diffusion studies

4.2.2.1 Calcein release from coated and uncoated liposomes

Figure 4.35 shows the percentage release of calcein over time from two populations of liposomes, one CaP coated, the other uncoated. The experimental method used was described in Section 3.9.1.4.

The graph shows that the percentage release of calcein from the two liposome populations was similar at the first measurement period (20 h), but differed widely at all subsequent time periods. At 44 h the percentage release value for the CaP coated liposomes was lower than for the uncoated samples. From 70 h onwards, more calcein had been released from those liposomes coated with CaP phases. No change in molecule re-

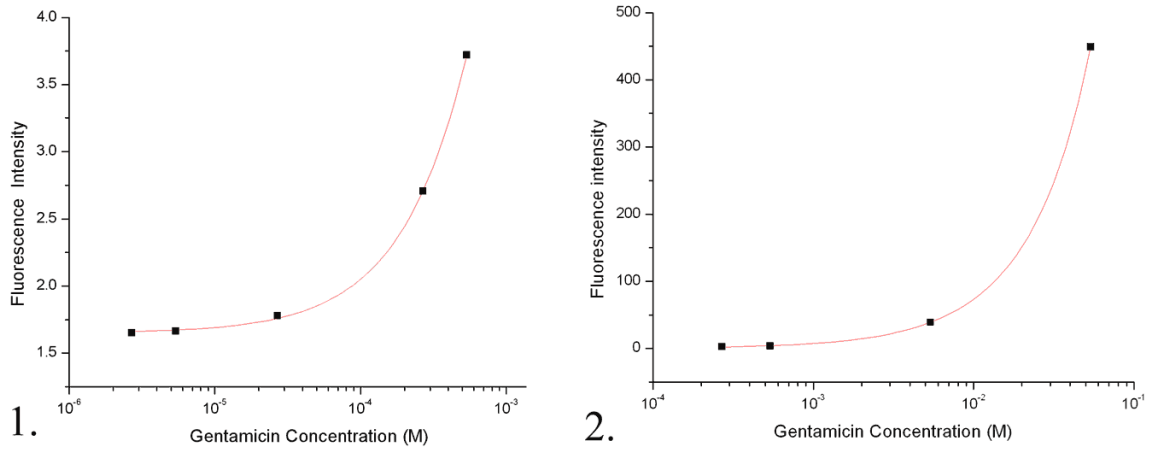

Figure 4.36: Calibration curves for buffered gentamicin solutions at (1) relatively low and (2) relatively high concentrations.

lease could be seen for the first 116 h in uncoated liposomes, with the release at 164 hours being slightly higher than that observed at 20 h. Release of calcein from coated liposomes had increased greatly after just 70 h.

4.2.2.2 Studies on gentamicin

Calibration Figure 4.36 shows two different calibration curves constructed using buffered gentamicin solutions (as described in Section 3.9.2.2). Equations of the curves were used to calculate gentamicin concentrations for fluorescence values recorded in the low (reading of < 5 units) or high (reading of > 5 units) regions of the measurements.

Example scans of solutions containing gentamicin is shown in Figure 4.37.

Release from uncoated liposomes Figure 4.38 shows results from a preliminary experiment on release of gentamicin for uncoated SPLVs. In this graph, it can be seen that the percentage release of the antibiotic from the liposomes is greater at 19 h and beyond than for the reading taken after approximately 1.5 hours. The readings taken at 25 hours

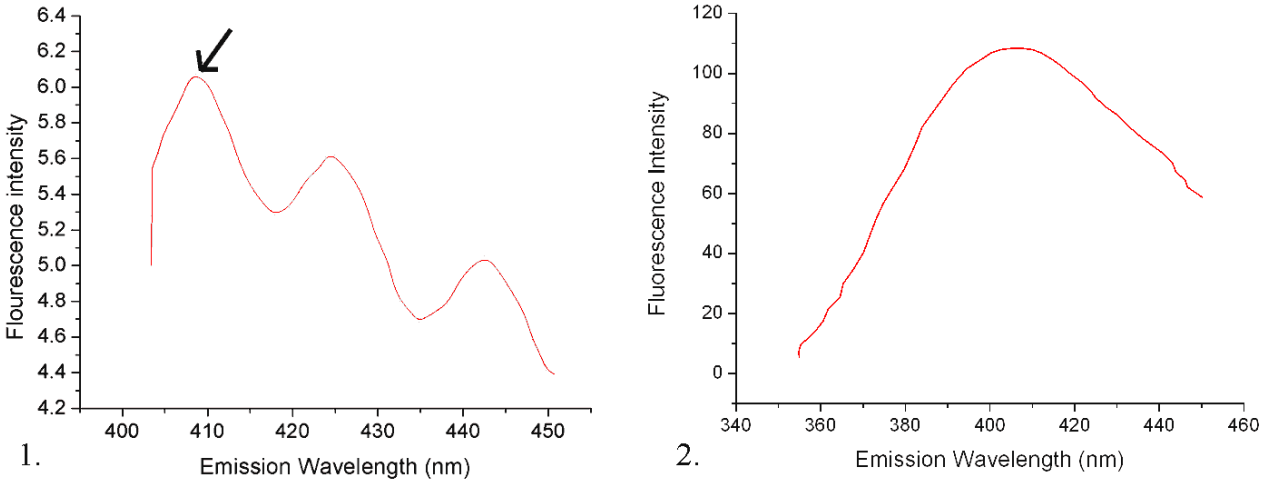

Figure 4.37: Example scans of gentamicin fluorescence. Excitation wavelength 330 nm. (1) Scan of low concentration of gentamicin (1 mmol/l). The arrow points to the peak used for gentamicin quantification. (2) Scan of higher concentration of gentamicin (15 mmol/l)

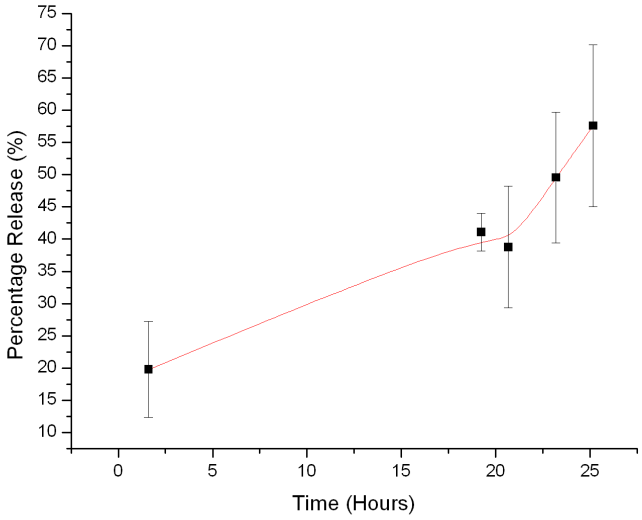

Figure 4.38: Percentage release of gentamicin from uncoated liposomes at 37 ℃. Error bars represent the standard error of the mean (n=2)

show that the percentage release of gentamicin at this time is greater than that at 19 h. There is no difference between the values of any other readings.

4.3 Composite coatings

4.3.1 Effect of liposomes upon coating solutions

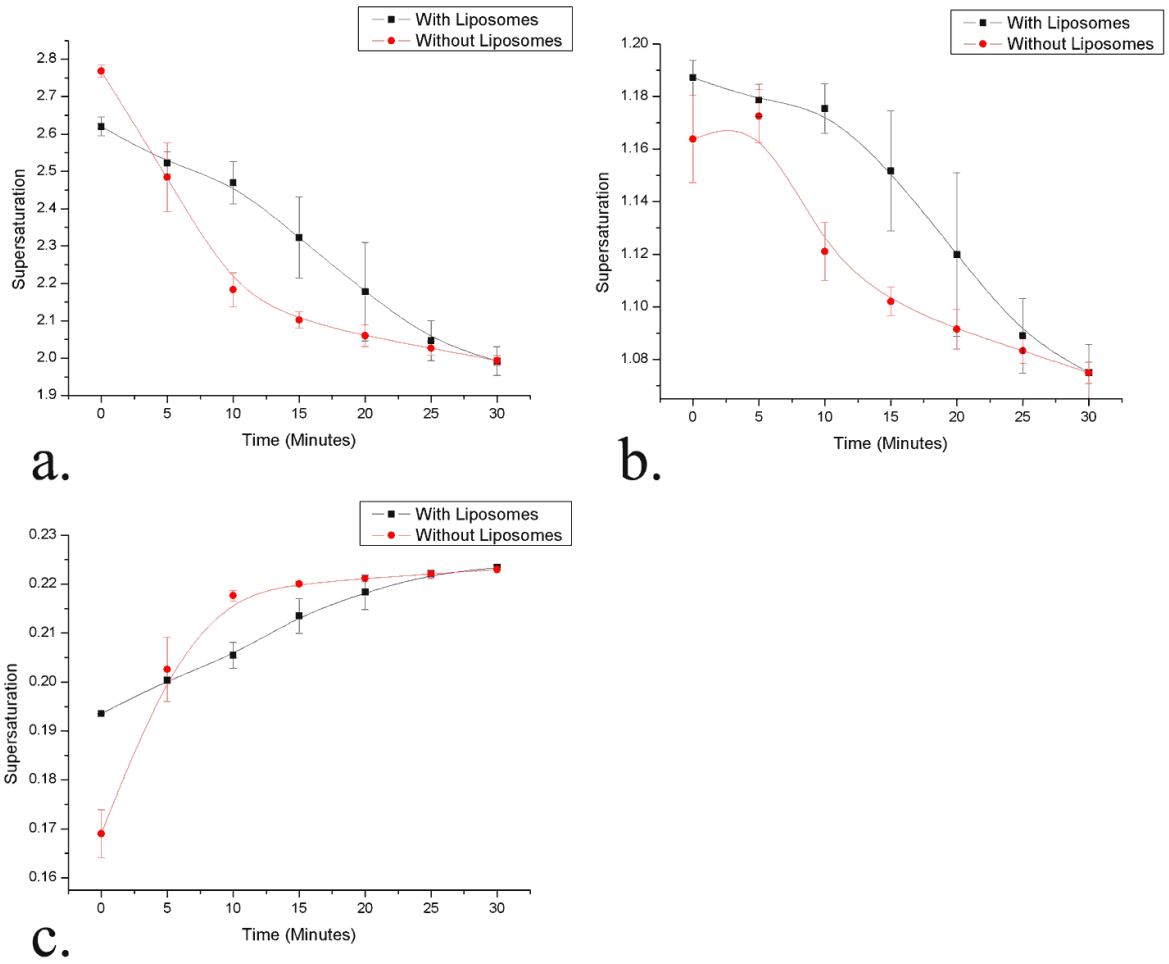

Figure 4.39: Graphs showing supersaturation of CaP phases against time during electrodeposition of CaP with and without the addition of liposomes. Starting Ca^{2+} concentration 6.25 mmol/l. (a) HAp supersaturation against time. (b) OCP supersaturation against time. (c) DCPD supersaturation against time. Error bars represent standard error of the mean (n=2)

Figure 4.39 shows graphs of the supersaturation of HAp, OCP and DCPD against time during the electrodeposition of CaP with and without liposomes. The graph for HAp (Figure 4.39 (a)) shows that the fall in supersaturation in the presence of liposomes

takes the form of a steady decline as opposed to a rapid drop followed by a leveling off, which is the case for electrodeposition without the vesicles. This modulation of rate of supersaturation drop is much less clear in the case of OCP (Figure 4.39 (b)), although the drop in supersaturation for the solution without liposomes can be said to be greater between five and fifteen minutes of electrodeposition commencing than that observed for the solution containing vesicles. Figure 4.39 (c) shows that there is a relatively rapid rise in the supersaturation of DCPD during the first ten minutes of coating without liposomes which subsequently levels off. The supersaturation rise in the coating solution with liposomes present is much more consistent for the entire time period of observation.

4.3.2 Calcein containing liposome-CaP composite coatings

A number of months were spent manufacturing composite coatings with calcein-containing liposome vesicles for an orthopaedics company with the view to data on the release of the calcein being made available for this study (see Section 3.10 for method). Unfortunately the company lost the samples and therefore only a description and resolution of problems encountered during their manufacture can be described here.

4.3.2.1 Maximising entrapment

As already described in Section 4.2.1.1, efforts to improve on the entrapment efficiency of SPLVs led to an increase in entrapment from ≈ 0.6 % to approximately 8 %.

4.3.2.2 Use of the disaccharide trehalose

The sugar trehalose was added to solutions present both inside and outside the liposomes in order to protect the membranes during freeze-drying. The entrapment efficiency was

measured of liposomes containing calcein and trehalose solution both before and after freeze-drying and rehydration (Section 3.10.2.2). The entrapment efficiency was ≈ 7.5% before drying and was ≈ 0.5% after drying and rehydration. This indicated that 93% of all the calcein originally entrapped in the liposomes had leaked out during the drying and rehydration process.

4.3.2.3 Freeze-drying of coatings

Despite poor retention of vesicle contents during freeze-drying (Section 4.3.2.2), attempts were made to use the freeze-drying technique for composite coatings on orthopaedic TiAl(6%)V(4%) alloy discs (method described in Section 3.10.2.5).

Before drying, the wet composite coatings appeared to completely cover the entire coated surface of the discs, with no cracking visible to the naked eye. The coatings appeared to be in the order of several microns in thickness and had a yellow tinge to their colour. After drying, the coatings were flaking off the substrate and forming spalls, there was also a layer of encrusted, dried sugar covering the samples. After several repetitions of this drying procedure with the same result, it was decided to leave the coatings in a wet condition for storage by storing them in calcifying solution as described in the experimental procedures section (Section 3.10.2.6).

Chapter 5

Discussion

In this section, the results presented in the previous chapter will be looked at in more detail and discussed with reference to current scientific knowledge as described in the literature review (Chapter 2).

5.1 Coating time and solution concentration

Monitoring of calcium ion concentration, temperature and *p*H during the coating of stainless steel substrates by electrodeposition (method described in Section 3.2), allowed the saturation of the various CaP phases to be quantified as the procedure commenced. Graphs of the calculated supersaturation used to determine coating time and the effect of coating solution concentration can be seen in Sections 4.1.1.1 and 4.1.1.2.

Because of the make up of the coating solution, including the high ionic strength, achieved through addition of 0.1 mol/l of potassium chloride, the calculated saturations of the predominant phases present in solution showed that HAp was the most highly saturated phase present (most supersaturated). This meant that it was thermodynamically

most favourable for HAp to precipitate out of solution during the coating procedure. OCP had the next highest supersaturation. DCPD, however was not defined as supersaturated since the level of supersaturation did not rise above 1 (described in Equation 2.13 in Section 2.4.1.2).

5.1.1 Coating time

The observed drop in HAp and OCP supersaturation, which occurred up to approximately 20 minutes of coating time for the higher coating concentrations (Section 4.1.1.1), was likely to be due to depletion of the available Ca^{2+} and PO_4^{3-} ions in solution. By the time that this drop occurred, any buildup of coating (or CaP particles) around the electrode would also have been likely to interfere with the process of electrogeneration of base, as described in Equations 2.24 and 2.25. This inability to induce a *p*H increase around the electrode, would in turn slow down the precipitation of CaP phases from solution, leading to a reduction in the rate at which the supersaturation dropped. Because of these factors, it was at this time that coating was stopped and the solution replaced before commencing any subsequent coating cycles.

The saturation of DCPD could be seen to increase slightly during the experiment. The level of saturation was always below a value of 1, at which point a solution can be said to be supersaturated with respect to that phase.

5.1.2 Initial coating solution supersaturation

The effect that altering the initial concentration of calcium and phosphate ions in the coating solution had upon the supersaturation of OCP and HAp prior to coating (shown in Figures 4.2 and 4.4, Section 4.1.1.2), would have been expected to be a direct consequence

of the relationship between the concentration of these ions and the relative supersaturation of the products that they were likely to produce i.e. The initial supersaturations of HAp and OCP would be expected to be highest at the start of the coating experiment that used the highest concentration of Ca^{2+} and PO_4^{3-} ions in solution. However, this was not necessarily the case. For HAp, the initial supersaturation in the experiments run with a solution concentration of 6.25 mmol/l Ca^{2+} ions was lower than for where the solutions contained 2.5 mmol/l Ca^{2+} ions. Both of these sets of experiments started with a higher HAp supersaturation than for the intermediate solution concentration. When observing OCP, the initial conditions prior to coating were such that the experiments carried out with the lowest starting calcium and phosphate concentrations also had the highest supersaturation. Experimental errors that may have occurred during the making of the stock solutions, their dilution to make the coating solutions and the calibration of the monitoring equipment were minimised. So this phenomenon may be explained by precipitation prior to coating. It is the case that, for the highest coating solution concentration in particular, the coating solution turned from transparent and colourless, to opaque and white instantaneously upon mixing the calcium and phosphate-containing constituents of the solution. Thus, the concentration of any free Ca^{2+} and PO_4^{3-} ions in solution would fall dramatically prior to coating as these ions formed solid CaP phases in suspension. This would cause a lowering in the solution supersaturation before the conditions had been measured at the start of the electrodeposition procedure. The initial formation of precipitate in solution would also allow homogeneous nucleation of the CaP phases to occur rapidly upon the particulate matter, which could act as seeding nuclei, allowing the supersaturation of these phases to drop even further, when compared to the drop seen for other solution concentrations.

Upon mixing the constituent calcium and phosphate containing parts of the solution

of intermediate concentration (starting concentration 4 mmol/l Ca^{2+} ions), a very faint 'milkiness' could be seen. During the course of the coating procedure, this faint indication of precipitation became more obvious with time; the solution becoming translucent in character at the end of the 40 minute period. This may help to explain why, in the cases of OCP and HAp (Figures 4.2 and 4.4), the intermediate coating concentration had a lower supersaturation during the experiment than that observed for the lowest calcium and phosphate ion concentration (2.5 mmol/l Ca^{2+} and 1.5 mmol/l PO_4^{3-}).

For DCPD, the saturation of the intermediate concentration coating solution was higher than for the other concentrations at the outset of the experiment. This is the reverse of the situation seen for HAp. It may help to describe DCPD as undersaturated (being the opposite of supersaturated) and then the intermediate concentration could be described as having the lowest undersaturation of the three concentrations at the initial time period. Undersaturation (σ) can be defined in a similar way to supersaturation:

$$\sigma = 1 - \left(\frac{\mathrm{IP}}{\mathrm{K_{sp}}}\right)^{\frac{1}{\upsilon}} \tag{5.1}$$

Where IP and K_{sp} are defined as in Equation 2.13 in Section 2.4.1.2.

5.1.3 Change in supersaturation

As described in the results section (Section 4.1.1.2), the drop in the saturation of HAp and OCP over the entire coating period increased with the initial concentration of the coating solution. Since supersaturation gives a measure of the viability of precipitation occurring, any drop in supersaturation is more likely when the supersaturation is high. Therefore it would be expected to be self-limiting in that the rate of fall in supersaturation should level off asymptotically as it approaches 1 (the transition point between a

solution being undersaturated and supersaturated). The precipitation that occurred both immediately upon mixing of the calcium and phosphate solutions and over a period of time during the electrodeposition process gave rise to nuclei in solution capable of seeding the further growth of CaP, allowing this high rate of fall in saturation to continue, even if the supersaturation driving this precipitation had fallen itself. This effect can be seen in the cases of OCP and HAp, which continued to have a falling saturation level even though in these same graphs it can be seen that the actual saturation of the 2.5 mmol/l Ca^{2+} solution was much higher for most of the experimental time period and should therefore have facilitated a higher rate of precipitation.

Another factor to be taken into consideration is that these measurements were taken in the bulk of the solution, the situation near the surface of the electrodes is likely to have been very different, with the electrogeneration of base raising the local *p*H and thus increasing the level of HAp and OCP supersaturation. This would allow continued precipitation out of solution even when the driving force of this precipitation was low in the bulk solution.

For DCPD, the saturation increased most rapidly for the experiments carried out with the 6.25 mmol/l Ca^{2+} solution. This trend is again the reverse of that seen for OCP and HAp. There was a very slight overall saturation rise over the 40 minute coating period for the intermediate concentration and a more significant rise in the case of the lowest solution concentration. It is difficult to draw any simple conclusions based on the same grounds as for OCP and HAp, since the solutions were undersaturated with respect to DCPD for the entire coating period. Since no DCPD precipitate is likely to have formed, it is not possible to say that any direct nucleation effect can be seen. The changing saturation values of the DCPD over the coating time period are likely to be a direct result of the changing solution conditions induced by the precipitation of OCP and HAp as well as the

electrogeneration of base, rather than any direct formation of DCPD itself.

5.2 Identification of phases by XRD

In Section 4.1.1.3, the results determined from the use of X-ray diffraction on coated samples are described. In order to overcome the problem of the signal from the stainless steel substrate dominating the scan, a thick coating was made so that the phase of CaP deposited could be determined. As shown (Figure 4.6), the diffraction pattern recorded fits the profile of HAp in terms of the positions of the peaks. However, the ratios of the peak intensities are different to that seen in a scan of standard reference HAp (Figure 4.5). In particular, the (002) and (004) peaks are large in proportion to the other peaks when compared with the standard. According to Danilchenko et al. (2004), the peak area is proportional to the total area of reflecting planes and therefore the area of the (002) and (004) peaks are proportional to the number of crystallites with their [001] planes perpendicular to the substrate surface. Because of this, it can be concluded that there is a preferred orientation of crystallites with their *c*-axis perpendicular to the substrate in the electrodeposited sample. The fact that the peaks in the scan of this sample are not clearly distinguishable from one another means that the coating can be described as a poorly crystalline HAp.

From the monitoring of solutions described in the previous section, it was shown that OCP was likely to have been precipitating out of solution during the coating process, however no XRD peaks for OCP could be found in the coating which resulted. This could simply be due to the fact that any signal from OCP was masked by the HAp, which was likely to be present in a higher proportion. The fact that electrode measurements were taken in the bulk of the solution and therefore did not necessarily indicate what was

occurring at the electrode surface also needs to be considered. However, the set of planes with highest intensity of reflection for OCP are the (010) set which would show as a peak at $2\theta = 4.7°$ which is in a region where no HAp peaks occur. The lack of this peak leads to the assumption that OCP is not present in this sample (coated for 10 successive cycles) and therefore any OCP which had been present in the coating must have transformed during the time that the sample was undergoing the coating procedure. Alternatively HAp may have formed directly without an OCP precursor phase.

Samples manufactured for the maturation time experiments (described in Section 3.7) were also subjected to XRD analysis. For the sample coated once with no maturation time, the only signal to be seen in the XRD scan (Figure 4.8) is that of the stainless steel substrate. This was to be expected as the coating is only around 0.5 µm in thickness. As maturation time of the one-coat samples increases (Figures 4.9 to 4.11), the coating thickness and the strength of the signal from the coating also increase. The first peaks discernable peaks are those of the HAp (002) and (211) which can be seen on the scan of the sample given an hour to mature (Figure 4.9). The presence of the the (002) peak before many others implies a preferred orientation of the HAp crystallites with their *c*-axis perpendicular to the substrate. A further two hours of maturation (Figure 4.10) leads to the appearance of the (004) HAp peak, which is relatively small on the scan of the randomly-orientated standard (Figure 4.5) again supporting the fact that HAp has a preferred orientation in this coating.

The differences in the scans of the one-coat samples given five and thirteen hours to mature (Figures 4.11 and 4.12) are interesting to note as the coatings are of approximately the same thickness (4.5 to 5 µm). When comparing the (002) peak relative to the (211) peak in these samples, the peak seems to grow with extra maturation, suggesting that maturation time affects the preferred orientation of the crystallites in the coating.

The scans from the five-coat samples also show more HAp peaks as maturation time after the first coat and coating thickness increase (Figures 4.13 to 4.15). The scan of the sample that simply underwent five coating cycles with no maturation (Figure 4.13) shows a very small HAp (202) peak as well as another very small peak. As already stated in the results section, this other peak could be one of a number of phases including DCPD or β-TCP but absence of an alternative peak from the same phase does not allow an exact identification to be made. The fact that the first definable HAp peak is not the (002), as was seen in the one-coat samples is interesting to note.

The five-coat sample given an hour of maturation after the initial coating cycle (scan shown in Figure 4.14), is of comparable thickness to the one-coat samples given five and thirteen hours maturation, the scans of which are shown in Figures 4.11 and 4.12. When comparing these profiles, it is clear that even thought the five-coat sample is of approximately equal thickness, fewer HAp peaks are present. Along with the amorphous 'bump' at $\approx 2\theta = 5.5°$, this suggests a less crystalline coating. When assessing the peaks which are there, the size of the (002) peak compared to the (211) is much smaller in the five-coat sample, suggesting less preferred orientation effects. More of the HAp peaks can be seen in the scan of the five-coat sample given three hours maturation after the initial coat (Figure 4.15). Considering the relatively thick coating in this case ($\approx$10µm) the signal to noise ratio and number of distinct peaks is rather low when compared to the one-coat samples. This may suggest a relatively non-crystalline coating structure. Again, there is also less of a preferred orientation effect parallel to the HAp c-axis when compared to the one-coat samples.

The crystal dimensions were determined from the (002) and (310) sets of planes of the scan shown in Figure 4.6. The values calculated (a = 9.93 Å and c = 7.11 Å) are large compared with those determined by Kay et al. (1964) (a = 9.423 Å and c = 6.881

Å). There are a number of possible reasons for this discrepancy including calibration of the XRD machine, calculation errors and peak shifting caused by the underlying signals of other phases or the substrate material. The difference in crystal dimensions are not necessarily outside the boundaries of error when looked at in percentage terms, the calculated a dimension in this case being approximately 5% larger than the standard value and the c dimension being $\approx$ 3% larger.

The Scherrer calculation on the XRD pattern was performed twice, once on the 002 peak and once on the 211 peak. The average dimensions of the a, b and c axes of the crystallites (a = 136 nm b = 34 nm and c = 43 nm) indicate that the HAp is 'tablet shaped'.

The one-off specimen used for the calculation of crystallite dimensions was manufactured specifically for that purpose as the small signal to noise ratio and dominance of substrate in the other samples would have led to high degrees of error. This particular sample can be said to be representative of the other coatings to some extent as the same basic coating procedure and solution concentrations were used in the manufacture of all of the samples. Obviously by nature of varying maturation times after the initial CaP coat as well as the addition of four subsequent coatings in some cases, there will be some differences between the thick coating used here as a reference (Figure 4.6) and the other coatings (Figures 4.8 to 4.15). This reference coating, however, does give a good idea of the different peak ratios and any slight differences in peak positions in the CaP coatings produced by this technique and measured using settings on this particular diffractometer, as opposed to the standard from the literature (Figure 4.5). It is obvious from comparing the scan in Figure 4.6 with the standard, that this coating represents a poorly crystalline HAp rather than a highly crystalline specimen. Since this sample did not undergo a maturation period, it cannot be concluded that all of the thinner coatings shown in Figures

4.8 to 4.15 are also poorly crystalline. In this respect, the one-off specimen is unrepresentative. Changes in coating crystallinity with maturation time are discussed in Section 5.6.

5.3 Increasing coating thickness

A coating of around 20 µm in thickness was achieved though 24 repeated coating cycles at a relatively high coating solution concentration, (6.25 mmol/l Ca^{2+}, 3.75 mmol/l PO_4^{3-} ions) and then drying in air. As mentioned previously the volume of calcium phosphate coating solution was also enlarged from that already used in order to provide a larger reservoir of calcium and phosphate ions.

This experiment was carried out in order to see if producing 20 µm or over coatings was viable in a laboratory setting. It was thought that thicker coatings would have a number of advantages:

- Longer coating resorption times when implanted.
- An increased volume of coating into which liposomes and their contents could be incorporated thereby increasing the potential delivery of bioactive moieties from the coating.
- The provision of a more substantial and visible coating comparable to the thick, white, plasma sprayed coatings currently used by orthopaedic surgeons.

Additionally, due to the insulating nature of the coatings produced, it was thought that there would be some sort of limit to the thickness produced by an electrodeposition technique.

The resulting coating in this study, although thick, had a powdery surface texture, easily removable by use of a finger or by tapping the sample on a hard surface. Underneath this powder-like surface a more coherent and robust coating could be found.

Since the mixing of the calcium and phosphate constituents of the coating solutions resulted in a thick precipitate being formed immediately when using such a high coating concentration, it is assumed that an electrophoretic mechanism was involved in the electrodeposition process in these cases. A possible mechanism of the growth of the coating under similar circumstances was given by Peaker and Czernuszka (1996) (as described at the end of Section 2.7.3.1). In that particular set of experiments, the highest starting Ca^{2+} concentration was 1.75 mmol/l; much lower than in the case currently being considered. The coating in that instance was described as resulting from an electrophoretic mechanism and so it can be safely assumed that coating using 6.25 mmol/l Ca^{2+} was occurring by the same mechanism. The powdery texture of the coating was a result of the agglomeration of CaP particles in suspension which were transported electrophoretically to the electrode. Although this was an effective method to manufacture thick coatings, it sacrificed mechanical integrity. As a result, most of the subsequent experiments were done using a much lower coating solution concentration (2.5 mmol/l Ca^{2+}) and experimentation was carried out on ways of increasing the strength of coatings by varying the maturation time of the coatings in solution and also altering the drying method.

5.4 Effects of drying method and maturation time on coating morphology and shear strength

This section of the discussion refers to the results set out in Section 4.1.3. First the morphology changes and then changes in the coating shear strength with varying standing time and drying methods will be considered.

5.4.1 Effects upon coating morphology

The use of low-voltage scanning electron microscopy allowed visualisation of the very surface layer of the samples while minimising any beam damage.

Imaging of the control sample (Figure 4.17) shows that there are occasional small flecks of debris on samples coated in solution without any added calcium or phosphate ions. These flecks indicate contamination deposited during storage and/or dust and debris from the guillotine used to cut the stainless steel down to a size suitable for the microscope chamber. This is the image which can be compared to all of the other micrographs to show what effect on the substrate can be put down to coating technique and sample handling rather than interactions of CaP phases with the samples.

5.4.1.1 Air dried

The differences between the control sample and the very thin coating covered in flecks of thicker material, (Figure 4.18 (a)), can be attributed to one 20 minute coating cycle at 37℃ with 2.5 mmol/l Ca^{2+} coating solution followed by air drying. The differences between this first sample and all of those subsequently seen in the figure (Figure 4.18, Micrographs (b) to (e)) are attributable to changes in the time that these samples were

left standing in solution after coating.

Comparisons can be made between the situation seen in this case, with a thin amorphous layer of CaP formed (Figure 4.18 (a)) which then appears to act as a seeding face for subsequent coating growth (Figure 4.18 b to e) and the two stage coating procedures used by many researchers. Several studies have been described which used a two stage coating process involving an initial coating of CaP growth nuclei and a subsequent rapid stage of coating onto this first layer. Some of these studies were described in the context of biomimetic techniques (Section 2.7.2, Habibovic et al. (2002) and Barrère et al. (2004), Section 2.7.5, Wen et al. (1999), Liu et al. (2001), Stigter et al. (2002) and Liu et al. (2003)), whereas one of these two-stage procedures involved electrodeposition followed by heat treatment (Section 2.7.5, Cheng et al. (2004)).

Barrère et al. (2001) used a two step procedure to produce OCP coatings on titanium. They described their initial coating, produced after 24 h of soaking in a simulated body fluid containing crystal growth inhibitors at 37℃ as

> "a dense and uniform CaP film ... composed of spherical CaP globules of about 0.1 µm in diameter."

This description, along with the SEM micrograph that they displayed of this sample, depict a thicker version of the coating seen in Figure 4.18 (a). They then used this layer as the seeding surface for the subsequent deposition of CaP from a second solution, without the presence of crystal growth inhibitors. The morphology of the final coating produced in the study by Barrère et al. (2001) was comprised of many delineated (OCP) crystals rather than the continuous network of CaP with pores produced during experiments reported here (Figure 4.18 (b) to (e)). This is likely to be due to the different composition of their coating solutions when compared with the ones used in this particular study. The

formation of the thicker OCP coating on top of the initial seeding layer was described as a process that involves the dissolution of some of the initial CaP film and then reprecipitation of the crystalline phase from the coating solution. As previous results have shown (Sections 4.1.1.1 and 4.1.1.2), HAp was the most supersaturated phase in this study, and therefore if a similar growth mechanism occurred to that described by Barrère et al., it is likely that HAp would be the phase to precipitate out of any solution surrounding the surface of the sample, thereby forming a deposit on top of the CaP layer produced during the initial coating cycle. The evidence of increasing coating crystallinity from the TEM and electron diffraction in this study (Section 4.1.5) supports the possibility of this growth mechanism.

The same group of researchers involved in the Barrère et al. (2001) study, carried out further studies on the two stage procedure (Habibovic et al. (2002) and Barrère et al. (2004), for a summary see Section 2.7.2). In these studies, it was hypothesised that the use of two stages in producing a coherent coating was important due to competing heterogeneous and homogenous nucleation of CaP in solution. The initial amorphous CaP layer provides a surface where nucleation of ions onto the surface is energetically favoured over precipitating into the solution. Once at their critical size, the seeds can then grow into crystals. After a certain amount of time standing the coating solution, the CaP supersaturation will have dropped to such an extent that the solution and the coating are in equilibrium. At this stage, a denser and more uniform coating may be formed by dissolution and reprecipitation of the coating (Habibovic et al., 2002). These explanations fit in with what is seen in the changing morphologies of the coatings with varying standing time (Figure 4.18). The difference between the coating on the sample given no maturation time (Figure 4.18 (a)) and that on the sample given one hour maturation (Figure 4.18 (b)) is due to the rapid growth of the CaP seeds, which were deposited during the

electrodeposition cycle, as the sample stands in the supersaturated coating solution. The change in morphology of the coating in the subsequent micrographs can be put down both to precipitation of the coating and to dissolution and reprecipitation of the existing coating.

Effects of successive coating cycles on an initial CaP layer which had been subjected to different standing times in solution have been displayed in Figure 4.19, Section 4.1.3. All of these samples were also air dried. Figure 4.19 (a) shows the coating formed by five successive coating cycles with no pause for maturation. The difference between the sample in this micrograph and that seen in Figure 4.18 (a), is caused by the four extra coating cycles. The thicker, granular coating produced by the extra coating cycles could be the result of the growth of the CaP seeds deposited by the initial coating cycle. Since the coating solution was changed for each cycle, there was no chance for equilibration between the coating and the solution, which may have occurred if the sample had simply been standing in solution. Therefore, there would have been a constant driving force for the growth of the initial seeds, as OCP and HAp supersaturation remained relatively high and base was constantly being generated by electrode reactions. This constant 'pressure' of high supersaturation and readily available base, may have been the cause of the formation of a dense granular coating rather than a more porous one.

The difference between the sample seen in Figure 4.19 (b) and Figure 4.19 (c) and the sample seen in Figure 4.18 (b) is caused by four coating cycles on top of the initial one that was allowed to mature for one hour. Again, the extended period of coating appears to have made coating denser and thicker. The pores in the underlying coating may have filled as the CaP layer continued to grow. These pores could have served as traps for the base generated from the electrode, increasing the local supersaturation. Alternatively, the dense layer may have grown on top of the porous layer.

The extended period of coating after maturation of the initial coat appears to have had the same effect when looking at the sample shown in Figure 4.19 (d). Again, the underlying coating in this case was relatively porous in nature (Figure 4.18 (c)). In fact, apart from coating thickness, the main difference between the coatings on samples seen in Figure 4.19 appears to be the degree to which the coating has become fragmented and starts to peel off the substrate. Since it was postulated that this may have been related to the method of drying the samples, similar coating experiments were then done with an alternative drying technique.

5.4.1.2 Critical point drying

The samples seen in Section 4.1.3, Figure 4.20 are comparable to those in Figure 4.18, the only difference in their manufacture being the method of drying used.

In the first micrograph, virtually no coating can be seen covering the substrate. This suggests that the critical point drying process has removed the initial layer of coating, which was deposited during the electrodeposition cycle. As was described in the experimental procedure for CPD (Section 3.5.2), the samples were first soaked in a series of ethanol solutions for a total period of 25 minutes before being placed in the CPD apparatus. While in this apparatus, the samples were subject to repeated flushing and periods of soaking in liquid CO_2 for at least three hours. Although, CPD can be thought of as a 'gentle' drying method due to the water in the sample being replaced gradually by ethanol, itself then replaced by liquid carbon dioxide, the extended time period for which the coating was resting in these solutions may have been the reason why at the end of the process, the thin ($\approx$ 0.5 µm) coating was no longer present. For example, the first dehydration solution contained 70% water with no calcium or phosphate ions present and the coating could have easily dissolved into it.

The situation in subsequent micrographs is different, with the thicker coatings, produced by the extended soaking time in solution, surviving the drying process. Figure 3.5.2 (b) shows the LV-SEM image of the sample allowed one hour maturation before undergoing CPD. When compared with the equivalent air-dried sample, the coating can be seen to be similar in general morphology with a network of interlinked CaP, however the scale of this network is much finer in the CPD sample, with more pores per unit area. The reasons for this are that the finer, more fragile spikes of CaP are better preserved in the case of the CPD, giving the sample the appearance of being porous. This is possible due to the lack of any mechanical effects resulting from surface tension changes during drying (unlike in the the case of air drying). It is this preservation effect which may have led to the one coat samples, given maturation times of more than one hour, being thicker than the equivalent air dried samples (as seen in Figure 4.22, Section 4.1.3.2).

The same situation is found when comparing Figures 4.18 (c) and (d) and 4.20 (c) and (d). The critical point dried samples seem to retain more of their fine 'skeletal' structure when compared with those that were air dried. Unfortunately, it is difficult to compare the samples given 13 hours maturation due to the differing scales and image qualities of the micrographs (Figures 4.18 (e) and 4.20 (e)), but the CPD sample appears to have more fine spalls of CaP covering the surface than seen on the other coating.

The sample coated for five cycles without any maturation time and which then underwent critical point drying (Figure 4.21(a)), has a thinner and less granular coating than the equivalent air-dried sample (Figure 4.19 (a)). This is a similar phenomenon to that seen for the one coat samples given no maturation time and which had then undergone CPD and is likely to have happened for the same reasons. This can be determined since the coating seen in the one coat sample with no maturation time (Figure 4.20 (a)) can be said to be thinner as a consequence of the CPD process and the underlying coating for

this five-coat sample with no maturation time would have been more similar to that seen in the air dried set (Figure 4.18 (a)).

Figure 4.21 (b) shows the result of four coating cycles on top of an initial coating given three hours to mature in solution and is the critical point dried equivalent of Figure 4.19 (d). It is possible to see that the CPD sample is less dense and granular to that which was air dried, with a very compacted latticework structure. Also the CPD sample had survived the drying process much better, with less peeling. The circular shapes seen in the coating may have been caused by build up of gasses generated at the electrode surface, under the coating.

Figure 4.21 (c) shows the sample given five hours maturation between the initial coat and the final four coatings. The existence of this sample is testament to the fact that the CPD process was more gentle than air drying since the equivalent air dried sample was too fragile to be analysed. However, large cracks were present in this particular sample and the sample given 13 hours maturation was far too fragile to undergo any study. The morphology of the coating in this sample can be seen to be very dense in nature. This serves to back-up the theory that the extra coating cycles serve not only to increase coating thickness, but also coating density as the porous regions, seen in the one coat samples, are filled by CaP as it continues to grow under the driving force of high supersaturation due to electrogenerated base. The granular structure of the air dried samples compared to the CPD samples suggests that this granularity is a result of the drying process, perhaps due to the slow release of water from the dense coatings during drying. This slow release would give time for dissolution and reprecipitation events to take place in the absorbed water.

When comparing the thicknesses of the five-coat samples (Figure 4.23, Section 4.1.3.2) the air dried samples are thicker than the equivalent samples which have been critical point

dried. This may have been due to the dissolution of the coatings during the CPD process as discussed at the beginning of this section. It is unclear though why the same difference is not seen in the one-coat samples with more than one hour maturation time (Figure 4.22), but it can be speculated that the preservation of the fine, porous structure of the one-coat samples more than compensates for any thinning of the coating that occurs during the CPD process.

5.4.2 Coating Shear strength

The results for lap shear testing carried out on the sets of samples given different maturation times, numbers of coats and subjected to different drying methods were described in Section 4.1.3.3.

5.4.2.1 One-coat samples

The plot displaying the shear strength of air-dried and critical point-dried samples that were given different amounts of time maturing in solution (Figure 4.24), shows an interesting pattern of variations, dependent on the drying method as well as the standing time.

When considering the air dried samples, the initial relatively low shear strength, calculated for the sample given no maturation time in solution, could be said to be due to the thin, powder-like nature of the coating (seen Figure 4.18 (a), Section 4.1.3). The sudden doubling of the shear strength after an hour of maturation time signifies the formation of a more coherent coating structure, able to resist the shear forces imposed upon it in a more holistic manner. The reasons behind the subsequent decline in shear strength are unclear, although are most likely to be due to the increasing ease with which a crack can

form within the coating as the thickness increases. The dissolution and reprecipitation of the coating whilst standing in solution could also gradually degrade any fixation of the coating to the substrate. Amorphous CaP may be important in forming this bond between the coating and the stainless steel. The increase in crystallinity during this period as seen in the TEM pictures (Figure 4.31) is also likely to make the coating more brittle in nature. The changes in CaP structure which occur during transition from an amorphous phase to a more crystalline one are likely to cause shrinkage in the coating structure. This shrinkage is likely to lead to crack formation. Any leaching of ions from the stainless steel into the coating during the extended periods of soaking could also affect matters.

At first sight, the pattern of shear strength variation with coating time for the CPD one-coat samples appears to bear little relation to that seen for the air dried samples. On closer inspection, it can be seen that the low initial strength of the air dried samples is mirrored in the one-hour CPD sample and that the sudden increase in the shear strength of the air dried sample at one hour maturation is mirrored by the CPD samples at three hours maturation. Therefore the pattern seen for the air dried samples is shifted along for those that underwent CPD. One possible reason for this the fact that CPD coating that was not subjected to any maturation time was seen to have barely any coating present on the substrate surface (as seen in Figure 4.20 (a) and discussed in Section 5.4.1). The shear strength calculated for this sample was around 9 MPa which is similar to that measured for the control sample that consisted of epoxy resin attached to a bare stainless steel surface (9.1 MPa $\pm$ 80 kPa).

The top layer of all of the coatings being removed by the CPD process may account for why the pattern of shear strengths against time is shifted along from that of the air dried samples. In this case it would be expected that the CPD coating given one hour in solution would appear to be the similar in surface morphology to the air dried sample

given no maturation in solution. This is not the case, with the CPD sample (Figure 4.20 (b)) being very different to the air dried one (Figure 4.18 (a)). The CPD process may have weakened the bond between the coating and the substrate in this case, but the evidence for this is limited since the CPD coatings at three and five hours maturation had much greater shear strength than the air dried coatings.

The theory is that increased crystallinity of coatings that have undergone longer maturation periods leads to more brittle coatings, as backed up by the evidence of increasing crystallinity seen by electron diffraction (Section 4.1.5). This fits in to an explanation of the effects of CPD upon the coatings. The critical point drying process may prevent this increase in crystallinity by removing absorbed water more rapidly from the coatings than in the air drying process. In turn, this would prevent further crystallisation within the coatings since the presence of water is important for the transition of the CaP phases to more crystalline ones. At the same time that the CPD process delayed an increase in crystallinity, the increase in thickness of the coatings with maturation time may have led to the formation of coatings that were able to dissipate the effects of a shear force through their structure better. The fact that CPD coatings had a better preserved microstructure than those samples which were air dried could have allowed for shear forces to be distributed better through the coating structure, preventing stress concentrations.

When comparing the shear strength with coating thickness for the one-coat samples (Figure 4.25) there is not much that can be concluded from the points relating to those samples which had been air dried . The coating shear strength is relatively low when the coating is thin ($\approx$ 0.5 µm) or when it is thicker ($\approx$ 5 µm). Shear strength seem to be highest at an intermediate thickness ($\approx$ 3.5 µm). The reasons for the changes in the shear strength of these coatings have already been discussed in the context of maturation time. The lack of any definite relationship between shear strength and coating thickness here

implies that the effects seen with relation to altering the standing time in solution are not related simply to the changes in coating thickness which also occur during maturation.

For the CPD samples, there is a high shear strength for the thinnest coating tested, as discussed previously, this is because there was very little coating present on this sample and as a result the shear strength recorded was the same as for the control sample ($\approx$ 9 MPa). After this initial point, there are a series of points which suggest an increase in shear strength as the coating thickness increases from around 3.5 µm to around 6.5 µm. This could be taken as an indication that the shear stresses are distributed more effectively in the thicker coatings produced by CPD. It has already been noted that the coating microstructure of these samples was well preserved when compared with the air dried samples and speculated that this structure would help to distribute stresses during mechanical testing.

5.4.2.2 Five-coat samples

As stated previously, there were only three air dried and four critical point dried five-coat samples which could be analysed. This was due to the cracking and degradation that occurred in the samples given long maturation periods in solution.

The slight increase in the shear strength of the air dried samples between zero and three hours maturation goes against the trend of decreasing strength due to cracking and peeling. There is a possibility that this increased strength is simply due to epoxy getting into the cracks that had formed in the coating, thereby increasing the strength of bonding between the sample and the blank.

The shear strength of the CPD coatings remains relatively high, with no reduction in coating strength, even with three hours standing in solution. This helps to confirm the hypothesis that the CPD process is much more gentle, preserving the coating microstruc-

ture and any bond between coating and substrate better than the air drying method. The decline in shear strength at 5 hours maturation is a sign of the cracking and peeling seen in the micrographs of these coatings (Figure 4.21). The fact that this drying method cannot prevent such cracking may be due to a number of reasons.

- The dehydration experienced, as the samples are put through solutions of increasing ethanol concentration, may still be too fast to maintain the integrity of the coating.
- The thicker coatings produced through longer periods of maturation may be prone to differing rates of dehydration from different areas, leading to stresses within the coatings.
- The change in phase of CaP may change the coating volume, also leading to stresses in the structure.

When comparing the shear strength with coating thickness for the five coat samples (Figure 4.27), there appears to be relatively constant shear strength with coating thickness for the air dried samples. For those coatings which underwent the CPD process, there is a decrease in shear strength with increasing thickness until the last data point ($\approx$ 8 µm) where the strength rises. The difficulty in describing a trend in this case shows that coating thickness was not the most important factor in determining coating shear strength for the five-coat CPD samples.

5.5 Investigation into Lap shear fracture surfaces using SEM

LV-SEM micrographs of the of the fracture surfaces from some of the air dried one-coat samples were displayed in Section 4.1.4.

The micrographs of the surfaces of the blanks post-fracture (Figure 4.28) have one main aspect in common. This is the imprint of grain boundaries, which existed on the stainless steel making up the substrate of the coated samples, that can be seen in all of the images. This is unsurprising in one respect, as any coating that was present on the samples would be expected to conform to the shape of the substrate. However, on closer inspection of the micrographs for both the sample given one hour maturation and for that which was given three hours maturation (Figure 4.28 (a) to (d)), rather than the these imprints appearing to be a part of the coatings ripped off the substrate, the main material appears to be epoxy resin. In fact, the only remnants of CaP seems to be the 'white' flecks that can be seen on the smooth material between the grain impressions. Any bulk of coating that had been pulled off would not have been expected to be as dense in nature or as smooth as that which is seen as dark areas in these micrographs.

The main reason for this is likely to be that the epoxy had penetrated the entire structure of the coatings, even down to the level of the substrate. The pressure exerted on the lap joint, as it was clamped in a vice during the setting of the resin, would have served to aid this penetration. If this is true, then perhaps rather than the lap shear tests being used to determine the shear strength of a CaP coating, they would actually have been recording the strength of a CaP-epoxy composite. From the lap-shear results already described and discussed, it is clear the the shear strengths of these samples was not nearly that of the epoxy control alone. Also, it would have been expected that the

thinnest coatings (those with least maturation) would always be the strongest if the shear strength was related to the epoxy penetration. These conflicting arguments could be resolved if it were the case that the penetration of the epoxy and the incorporation of the CaP structure into this resin, somehow led to the weakening of any potential bonding between the epoxy and the substrate.

The pull-off from the sample given 13 hours standing time after coating (Figure 4.28 (e) and (f)), appears to represent the underside of a CaP coating more than that which was seen for the first two samples. Firstly the raised grain boundary imprints are smoother than those seen in the other micrographs and secondly, the area between these ridges can be seen to be pitted. This suggests that this surface is made up of a softer material. The epoxy resin used during the lap-shear test is less likely to have been able to penetrate through the coating in this case as it was thicker.

The reasons for the appearance of the surfaces of the samples that had been coated prior to shear testing (Figure 4.30) are perhaps more straight forward to determine. When looking at all four of the micrographs in this figure, it is possible to see that more coating debris remains in the samples given a longer maturation time. This implies that the the actual structure of the coating failed during lap shear testing as well as any failure in the bonding between coating and substrate. This may have lead to the gradual decline in shear strength of the coatings that was seen, as the coating as well as the bond to the substrate degraded. The pits that were seen in the final micrograph of the previous figure discussed (Figure 4.28), can be seen to have probably been formed by the removal of lumps of material from the underside of the coating which then remained on the substrate. This could be a sign that the coatings became more brittle in nature as the maturation time increased.

5.5.1 Mechanism of Adhesion

When discussing the adhesion of coatings produced by electrodeposition, the exact mechanisms involved will depend on the combination of a number of factors including the coating conditions, the chemistry and surface microstructure of the substrate and the chemistry and structure of the material being deposited. Post-deposition treatments such as calcining or drying method are also likely to be important. A summary of the mechanisms of coating adhesion was given in Section 2.7.4.

In the series of experiments described in this thesis it is still not clear what the exact mechanism of adhesion is. There will certainly be a component of mechanical interlocking as the steel surfaces of the lap-shear sample substrates had physical features such as the grain boundaries seen in SEM micrographs (Section 4.1.3). When looking at the underside of coatings that have been pulled off samples during lap-shear testing (Figure 4.28 (a) to (f)) the imprint can be seen of the topography of the substrate to which the coating had been attached before fracture. This is evidence to support the presence of mechanical interlocking.

There is no evidence for or against other adhesion mechanisms being important for these samples, or whether these mechanisms might alter as a result of maturation time in solution. When considering the X-ray diffraction scans of the samples (Section 4.1.1.3) there is no visible change in the signal from the steel substrate as the samples undergo maturation, however, any formation of a very thin layer of compounds such as Na_4CrO_4 would be extremely difficult to detect when using this particular method.

The lack of obvious chemical changes in the substrate does not rule out the presence of the van der Waals interactions which could act between the CaP and the steel. Although these are generally weak in nature when compared to other intermolecular forces,

the action of these forces over a large area combined with mechanical interlocking could account for the adhesion observed.

5.6 Effect of maturation time on coating crystallinity

Electron diffraction. The description and figure in the relevant section of the results (Section 4.1.5) depict how the TEM imaging and electron diffraction patterns of the coatings grown onto grids show the increasing crystallinity of these coatings with maturation time.

The initial amorphous layer seen in Figure 4.31 (a) is what was speculated to exist as the initial layer formed by the electrodeposition procedure. This also links together with the model suggested by Barrère et al. (2001), which was discussed in Section 5.4.1.1. The subsequent changes in coating morphology and crystallinity during the time standing in coating solution are therefore likely to be due to a similar dissolution and reprecipitation mechanism.

As has been mentioned, particulary with reference to the lap-shear strength of the coatings, the increased crystallinity seen in the coatings exposed to the coating solution for a long time period, could be a reason for an increase in coating brittleness. The pictures seen in Figure 4.31 partly confirm this theory.

The thickness of the coatings given longer maturations in solution meant that diffraction patterns and images could only be recorded at the edge of the samples. It is unclear whether this led to different results to what may have been found for the bulk of the coating material.

After five hours maturation in solution the calculated lattice dimensions of $a = 9.53$ Å and $c = 6.87$ Å correlate very closely to the standard dimensions calculated by Kay

et al. (1964) (a = 9.423 Å and c = 6.881 Å). The difference between these calculated dimensions and the standard are 1% for the a dimension and 0.1% for the c dimension. This indicates the formation of HAp.

XRD. X-ray diffraction results (Section 4.1.1.3) have already been discussed in Section 5.2 in the context of identifying the phase of CaP which precipitated and in calculating the crystallite size and orientation within the coatings. Using these scans to support the electron diffraction results in showing an increase in crystallinity with increase in maturation time is not straightforward. This is mainly because of the small signal to noise ratio and the low signal from the coatings when compared to that from the substrate. Methods exist of determining crystallinity from the ratio of peak areas to the ratio of amorphous areas, however, in the case of such low signal size from the relatively thin coatings, it is difficult to accurately determine peak area or to determine where the area of amorphous signal to be measured is located in the scans.

Since a diffraction pattern from a very crystalline substance with large crystallites will have sharp, defined peaks, perhaps a subjective comparison can be made of the 'sharpness' of the peaks in the samples given different maturation times. However, in many scans, the only peaks which appear to be made up of a single reflection rather than the overlapping of two or more reflections are the (002) and (004) peaks. For example, in the scan of a thick coating shown in Figure 4.6, the (211) peak can be seen to be overlapping with the (300) and the (202) peaks. The broad appearance of the (211) peak in scans of the thinner coatings is likely to be for the same reason. The fact that these peaks are overlapping in such a way, unlike in the standard reference scan shown in Figure 4.5, shows that the coating is not as crystalline as the reference material but this difference in crystallinity cannot be quantified due to problems already described with the scans of the thin coatings.

As described previously (Section 5.2), it can be safely concluded that the scan shown in Figure 4.6 is that of poorly crystalline, rather than highly crystalline, HAp. The lack of many distinguishable, separated peaks in the scans in Figures 4.8 to 4.15 may suggest that these coatings are also poorly crystalline when compared to the standard reference, but the relative differences between the crystallinity of the coatings with changing maturation time cannot be determined using these XRD results alone.

5.7 Schema for the mechanism of deposition

Using the information presented in the literature review (Section 2.7.3) along with the results and discussion presented in this study, a clearer description of the electrodeposition process used can now be given. Much of this is speculative, however, as many of the actual mechanisms involved in both electrophoretic and electrolytic deposition are yet to be determined.

In order to gain insight into the processes taking place in these particular experiments, a distinction needs to be made between:

(i). The first coating cycle.

(ii). Maturation of the coating when standing in solution after electrodeposition has ceased.

(iii). Subsequent coating cycles on top of the initial coat.

(iv). Coating carried out with relatively high solution concentrations, as in the manufacture of the sample described in Section 4.1.2.

First coating. A high differential *p*H between solution surrounding the cathodic substrate and solution a short distance away (the bulk of the solution) is created mainly by the reduction of water and dissolved oxygen (Equations 2.24 and 2.25, Section 2.7.3.1). This *p*H differential is maintained with the aid of the HEPES buffer in the coating solutions, as seen in the work of Ban and Maruno (1999) (described in Sections 2.7.3.2 and 2.7.3.3). Positively charged electrolytes (such as K^+ ions) will be present close to the electrode in higher concentrations than in the bulk solution. This combination of high *p*H and high electrolyte concentration will raise the supersaturation of HAp and any precursor phases in this volume of solution. In turn, this will increase the likelihood of aggregation of molecular clusters to form critical nucleating clusters in solution or alternatively, nucleating seeds will form through heterogeneous mechanisms on the cathodic substrate surface. Once critical clusters are present on the metal surface, spontaneous growth can occur through transport of ions from the bulk solution. At the same time as this CaP seed growth is starting, electrolytic mechanisms will continue to lead to particle flocculation in solution and subsequent deposit formation on the surface. After 20 minutes of coating, there is a thin layer of coating growing on the metal surface and occasional flecks of flocculated particular debris, as seen in the SEM micrograph (Figure 4.18 (a), Section 4.1.3).

Maturation of the initial coating. During maturation, the processes described in the work of Barrère et al. and previously discussed in Section 5.4.1.1 become relevant. The initial pre-layer of CaP deposited during the electrodeposition cycle becomes an important substrate for growth of a thicker, more crystalline layer through dissolution and crystal regrowth processes. This occurs as the supersaturation of CaP phases in the solution drops, resulting in a shift in the equilibrium between the solution and the pre-

layer. The resulting HAp coating becomes more crystalline with increasing maturation time (discussed in Section 5.6) and shows a preferred orientation with the crystal *c*-axis growing perpendicular to the plane of the sample surface (as seen in the increased relative 002 and 004 peak areas in Figures 4.9 to 4.12 in Section 4.1.1.3). SEM micrographs of these samples can be seen in Figure 4.18 (b) to (e), Section 4.1.3.

Subsequent coating cycles. The schema is here divided into those coating cycles carried out on top of an initial coating which has not had time to mature and those cycles onto coatings which have undergone various periods of maturation (maturation procedure explained in Section 3.7).

After no maturation time. Following the initial coating cycle, immediate replenishment of the coating solutions and reinstatement of the potential difference between the electrodes allows for conditions of high supersaturation around the cathode to be maintained. As a result, the process of particle flocculation and deposition will continue along with growth of nuclei already on the substrate surface. Since the coating and solution are not given time to equilibrate, the fine, porous structure that is observed in coatings given the maturation time period (see above) does not have the opportunity to form. The resulting coating is dense and granular as seen in the SEM micrograph (Figure 4.19 (a), Section 4.1.3). The XRD scan of this sample (Figure 4.13, Section 4.1.1.3) only shows the signal from the substrate along with the HAp 202 peak and a reflection from an unknown substance.

After maturation of the initial coating. In this case the substrate onto which CaP is being coated is the fine, 'cellular' structure seen in the SEM micrographs of the one-coat samples which have been given maturation time (Figure 4.18 (b) to (e), Section

4.1.3). Rather than a continuation of the dissolution and reprecipitation mechanism which is assumed to be taking place during maturation, the replenished coating solution and renewed electric potential mean that solution supersaturation in the vicinity of the sample will be high. Electrolytic mechanisms will also be taking place, leading to particle growth through flocculation. It is possible that the cells in the coating will be sites where the *p*H increases the most as hydroxyl ions generated at the metal surface become trapped leading to precipitation of CaP and a plugging of the spaces in the coating. The resulting coatings are dense and granular (Figure 4.19 (b) to (d), Figure 4.21 (b) and (c)) and appear to show less defined HAp XRD spectra (Figures 4.14 and 4.15, Section 4.1.1.3) than seen in scans performed on one-coat samples (Figures 4.9 to 4.12).

Coatings deposited with high solution concentrations. As described previously, a coating of approximately 20 µm in thickness was manufactured using the method described in Section 3.6. The coating concentrations used were 6.25 mmol/l Ca^{2+} and 3.75 mmol/l PO_4^{3-} ions. Upon mixing of these solutions, a thick white precipitate formed immediately. When coating in these conditions, the mechanism is electrophoretic deposition (described in Section 2.7.3.1). Because of this, the resulting coating was powdery with poor adhesion to the substrate as it was formed through the electrophoretic motion of the CaP particles that simply combined into a powder compact on the substrate surface.

5.8 Liposomes

This discussion now turns to the area of the experiments to do with liposomes and the molecules to be entrapped within them.

5.8.1 Calcein calibration

It is sometimes stated that calcein does not interact with calcium ions at neutral *p*H (Allen, 1984). The fact that the original use of calcein was as a fluorescent marker for calcium titrations and quantity determination, albeit at alkaline *p*H, (Diel and Ellingboe, 1956; Wallach et al., 1959) led to some suspicion that this might not be the case. In the results (Section 4.2.1), it can be seen that the interaction of Ca^{2+} and PO_4^{3-} ions with calcein at *p*H 7.4 led to a reduction in the rate at which the relative fluorescence of the molecule increased with concentration (Figure 4.32). According to Allen (1984), the transition metals quench calcein fluorescence at neutral *p*H whereas the alkaline earth metals increase calcein fluorescence at alkaline *p*H. So it is not clear whether any possible interaction with calcium ions at neutral *p*H would be expected to cause either a rise or fall in calcein fluorescence. Perhaps the *p*H rather than the type of ion interacting with the calcein molecule is the deciding factor.

5.8.2 Method of manufacture

As described in Section 2.8.2, the method of Gruner et al. (1985) to produce SPLVs was determined to be especially effective at producing stable liposomes due to the evenly distributed nature of the solutes between the compartments in these multilamellar vesicles. Because of this stability, as well as the need to only use a small volume of the potentially expensive solutes which were to be entrapped, it was decided that this method was advantageous when compared to the MLV manufacture of New (1996).

The lack of any post manufacture procedure to homogenise the population size of the liposomes led to the wide range of vesicle diameters seen in Figure 4.33. In hindsight, a more standardised population of liposomes may have been preferable but the expense and

complications of post-processing prevented this from happening.

5.8.3 Entrapment efficiency

The problems of low entrapment efficiency (EE) were very difficult and time consuming to overcome. The achievement of a high percentage EE was found to be dependent on a large number of factors working well together during the manufacturing process of the liposomes.

The first EE results of below 1% were achieved using the standard cheap form of egg phosphatidylcholine (EPC), which came in a solid form and was designated as only 60% pure. The fact that 40% of the phospholipid membrane was made up of impurities was very likely to affect its structure and therefore permeability.

Oxidation of the lipids was also a problem. The required amount of lipid had to be cut off a larger lump and then dissolved into chloroform solution. This involved long periods of exposure to oxygen in the air. Grit and Crommelin (1993) described how the oxidative degradation of liposomal phospholipids could be reduced by the use of high quality raw materials, preparation under an oxygen free atmosphere and the addition of antioxidant molecules. As stated before (Section 2.8.2), the molecule α-tocopherol can be added to the phospholipid preparation and has been shown to reduce lipid oxidation as well as reducing bilayer permeability (Halks-Miller et al., 1985; Kulkarni et al., 1995). The first steps in increasing the EE in this study included using much purer phospholipid preparations which were predissolved in chloroform and packaged under argon. Also, α-tocopherol was then added to molecular percentage of 4%. Along with these measures, 30 molecular % of cholesterol was added in order to reduce membrane permeability (as in experiments by Corvera et al. (1992)).

Apart from altering the materials from which the liposomes were made, the environment in which they were manufactured and stored was also changed in order to improve the EE. A rigourous glass washing regime was instigated which involved prewashing in special detergent (Decon, East Sussex) before overnight soaking in a base bath made up of saturated NaOH in isopropyl alcohol. After rinsing in pure water (BDH AnalaR, UK), the glassware was then washed in concentrated nitric acid followed by further rinses in pure water. Solutions made from AnalaR water were then degassed in an attempt to reduce any oxidation from dissolved O_2.

The destructive forces of the effects of osmosis also had to be countered. This meant careful balancing of the total solute concentration inside and outside of the liposomes. This prevented water from flowing out of the vesicles causing collapse or into the vesicles, causing rupture. Other factors which served to aid in the improvement in EE were a reduction in both the centrifugation time and speed in the washing procedure in the manufacture of the SPLVs (described in Section 3.8.2), when compared to that used in the original method (Gruner et al., 1985).

According to Lasic (1998), because of the complicated interplay of so many different factors including the structure of the lipids and factors related to the chemical to be entrapped, in industrial settings, generally 20-35% EE is all that can be obtained.

The result of all the efforts in this study was that the EE eventually rose to around 8%.

5.8.4 Calcein release from coated and uncoated liposomes

Figure 4.35 shows the difference between the percentage release of calcein over time for CaP coated and uncoated liposomes. There are two possible reasons for the increased

release of entrapped marker from the coated liposomes at the later time periods.

1. The presence of calcium and phosphate, either as ions in solution or in the form of CaP on the liposomal membranes, increased the permeability of these membranes to calcein.

2. The same presence of calcium and phosphate, either as ions in solution or in the form of CaP on the liposomal membranes, was responsible for disrupting the structure of the liposomes and causing them to release their contents.

From the results of previous work done on CaP coated liposomes that were coated using the same technique by Pongsaanutin (2002), along with the information about the increasing crystallinity of the CaP phases as they transform into HAp in coating solutions of similar concentration and supersaturation, (Sections 4.1.5 and 5.6) the second of these suggested mechanisms is by far the most likely. As was described by Pongsaanutin (2002) and summarised previously in Section 2.9, the combination of repulsions between adsorbed Ca^{2+} ions on the surface of the phospholipid molecules and the growth of crystalline HAp particles into the membrane, eventually leads to disruption of the membranes of the liposome. The continued growth and crystallisation of CaP during extended periods of being exposed to calcium phosphate coating solutions has already been shown in this study. It is quite likely that although the substrate in this case is the surface of a liposomal membrane rather than a sheet of stainless steel, a similar maturation process is occurring.

This obviously has implications in the context of the stability of any CaP-coated liposome if it were to be incorporated into a coating. The environment in that particular scenario would be very different to that found when standing in coating solution. The immediate surroundings of any liposomes in this context would be the structure of the calcium phosphate coating which would also mature into more crystalline forms of CaP

in the presence of water, especially in the case of further coating cycles occurring in order to build up a thick coating layer. Disruption of the structure of the liposome would be very likely in these cases, releasing any entrapped contents prematurely.

Theoretically it is possible to determine whether the release of entrapped contents from a population of liposomes is a result of diffusion or disruption by using the profile of release. This is possible due to the self quenching properties of calcein at high concentrations. However, it requires a good degree of accuracy in order to monitor the change in a particular coefficient, calculated in turn from a curve of residual calcein fluorescence within the liposomes. The accuracy required for such a complex sequence of measurements is outside the scope of the equipment and methods available in this case. As can be seen in the graph of calcein release (Figure 4.35), the errors in both method and measurement led to values which were sometimes negative and sometimes greater than 100% being recorded for the percentage release. This highlights the potential degrees of inaccuracy in measuring anything more subtle than simple release over time.

The fact that no significant release of calcein was seen during the first 116 hours of the experiment for the uncoated liposomes implies that the SPLVs were relatively stable with no adverse effects, such as high osmotic gradients or contamination of the solutions with enzymes, affecting them.

5.8.5 Studies on gentamicin

The procedures found in the literature for determination of gentamicin concentration vary widely in methodology from various immunoassay techniques to chromatographic methods (Frutos et al., 2000). These are often complex, use hazardous chemicals (Lewis and Janna, 2004), are expensive or simply impractical when monitoring release from liposomes as they

require a high temperature step (Frutos et al., 2000). In their paper on their gentamicin quantification method, which involves using ninhydrin as a derivatising agent, Frutos et al. (2000) state that an indirect spectrophotometric method is necessary because gentamicin poorly absorbs ultraviolet and visible light.

In this study however, the simple technique of determining gentamicin concentration through fluorescence spectrophotometry was shown to be effective for the concentrations used (Section 4.2.2.2). The technique was shown to be reliable by producing consistent calibration curves, which can be seen in Figure 4.36. The examples of a gentamicin scans (Figure 4.37) show the three peaks detected at low concentrations (Scan (1)) which possibly relate to the three isomers of gentamicin that were stated as existing in the specifications of the product. At higher concentrations these separate peaks could no longer be observed (Scan (2)).

A graph of the results of a simple release experiment carried out in uncoated SPLVs can be seen in Figure 4.38 with significant release being seen after just 19 hours. The make up and manufacture of the liposome vesicles themselves was the same as for those used in the calcein studies. Again, steps were taken to balance to the osmolarity of the contents of the liposomes with the surrounding buffer to prevent osmotic damage.

In this study, after 25 hours, between 40 to 70 percent of the original entrapped gentamicin had escaped from the liposomes (Figure 4.38). It would appear that this is much more rapid than the ideal. It is often thought that the antibiotic release profile which is likely to be most effective in preventing infection in a clinical context is a long, sustained release over several days or even weeks. In that case, a balance would need to be met between a release rate which is high enough to prevent growth of pathogenic bacteria and release over a long enough period for the immune defences to take over in the area traumatised by surgery. However, a review undertaken on behalf of the NHS

by Glenny and Song (1999) concludes otherwise. Their review of research relating to the effectiveness of antibiotic prophylaxis in total hip replacement surgery, concluded that use of antibiotics for more than one day post-operatively shows no extra benefits in reducing infection. In fact, they suggest that long courses of antibiotics would be undesirable for a number of reasons including cost, toxicity and increased chance of antibiotic resistance developing in the bacteria after sustained exposure.

In light of the above facts, perhaps a short, high-dose release of antibiotic would not be a disadvantage. However, a longer release profile is likely to be preferable for bone growth factors. These have been shown to induce more favourable traits in osteoblast cell populations with longer exposure periods (Puleo, 1997) and should be released over the whole period of bone growth around the implant (weeks rather than days).

5.9 Composite coatings

5.9.1 Effect of the liposomes upon coating solutions

The graphs of phase supersaturation during the electrodeposition of CaP with and without liposomes present (Figure 4.39, Section 4.3.1), are revealing in that they show a definite modulation in the change in supersaturation of the phases monitored.

Previous work by Pongsaanutin (2002) has found that introducing liposomes into coating solutions delayed the formation of any crystalline HAp and that the end product of the electrodeposition procedure consisted of poorly crystalline HAp containing some organic material. It is unclear whether the slowed decline in HAp supersaturation in this case (Graph 1, Figure 4.39) shows agreement with the findings of Pongsaanutin as the overall reduction in HAp supersaturation over the coating period is similar with and without

liposomes present, it is the profile of this change which is modulated.

It should be noted that in this set of experiments, the starting coating solution was relatively high (Ca^{2+} concentration 6.25 mmol/l) and the instant formation of amorphous CaP in the form of precipitation would have preceded the start of the solution monitoring in the experiment. The reduction in the initial rate of drop in supersaturation of HAp was possibly caused by the liposomes interfering with the normal homogenous nucleation process, which would have occurred in their absence. The presence of the liposomes, which may have acted as heterogenous seeds would have added a further competing factor in the battle between heterogenous and homogenous nucleation (as described by Habibovic et al. (2002)). This competition may have slowed the down the precipitation of HAp from solution as the liposomes were limited in number in comparison with the CaP seeds in solution.

Another factor that may have been affected by the addition of liposomes, is the rate at which base could be generated at the cathode due to alterations in the electrical properties of the solution.

5.9.2 Manufacture of composite coatings

As mentioned previously, studies on the production of composite coatings have been carried out by Pongsaanutin (2002). The vesicles used in that particular study were not used in order to entrap any marker molecule which could then be trapped within the coating. The fact that organic material was found in the composite coating manufactured by Pongsaanutin implied that the liposomes were incorporated to some extent in the coating structure. It is not clear however if the vesicles survived intact.

The experiment carried out in this study (Section 3.10) aimed to use CaP-coated

liposomes that incorporated the marker molecule calcein. This was done in order to see whether the calcein was incorporated into the coating and whether this incorporation was inside intact vesicles.

The samples manufactured using the calcein containing liposomes had a yellow colouring to the coating as opposed to the white seen in the absence of these liposomes. Since calcein at neutral *p*H has a orange/yellow colour this implies that some of the chemical was at least incorporated in some way.

Since no methods existed for drying the coatings without destroying the liposomes (use of ethanol in CPD) or exposing them to oxygen (air dying), attempts were initially made to add the sugar trehalose to the liposomes and the buffers used and freeze dry the coatings. This sugar has proved successful in many studies in order to preserve membrane structures during freeze drying (Madden et al., 1985; Crowe et al., 1986; 1988; 1998; Hincha et al., 2002). The sugar prevents the fusion of liposomes that is normally seen during drying. The fusion and resulting leakage of contents is prevented as the vesicles are embedded in a matrix of trehalose (Crowe et al., 1988). During drying, there is usually a transition between the liquid crystalline phase of the phospholipids to a gel phase. The vesicles become leaky during this phase transition. Trehalose suppresses this transition so that the lipids remain in liquid crystalline phase even when water molecules have been removed (Madden et al., 1985; Crowe et al., 1988).

In the experiment presented in this study, which tested whether the calcein entrapped before freeze-drying was still present after drying and rehydration, over 90% of the contents had escaped from the vesicles. The reasons for this are unclear. It may be that the concentration of trehalose (100 mmol/l) was too low to afford protection. Madden et al. (1985) found that a trehalose concentration of 125 mmol/l was necessary to prevent major structural changes to the liposomes during drying and rehydration, whereas Crowe et al.

(1986) stated that the mass ratio of carbohydrate:lipid is the most important parameter determining success. The maximum retention of liposomes was found to occur above approximately 1 g of trehalose to 1 g of lipid. In the experiment in this study, more than 3 g of trehalose was added for each gram of lipid, so the escape of vesicle contents was not caused by a low quantity of the sugar.

Freeze-drying of the coatings caused them to crack and flake away from the substrate (Section 4.3.2.3). The most likely explanation for this is the differing coefficients of thermal expansion of TiAl(6%)V(4%) alloy and the CaP coating. When the samples were cooled to -35℃, the alloy would have contracted to a much greater degree than the coating, leading to the cracking that was observed.

As freeze-drying had proved unsuccessful, the samples were presented within a mild calcifying solution in order to prevent any bulk dissolution of the coating.

5.9.2.1 Expectations of composite coatings

It was hoped that the liposomes present in the coating would behave as they do in solution and entrap their contents in discrete 'packets' which are gradually released with time. Unfortunately the loss of these samples by the orthopaedics company hinders much further discussion on the matter. However, as stated previously (Section 5.8.4), it can be speculated that results comparing release of calcein from coated and uncoated liposomes (Section 4.2.2.1) has implications in the context of the stability of any CaP-coated liposome if it were to be incorporated into a coating. Maturation of this coating around the liposomes would lead to more crystalline structures, able to disrupt the membranes. Because of this, alternatives to liposomes such as block copolymers should perhaps be considered for any drug delivery role as they may be more resistant to this disruption.

Chapter 6

Conclusions

This chapter represents the final, summarised outcome of this study. The initial aims of this project were to look at three separate areas:

1. *Coatings.* To look at effects such as maturation time and drying conditions on the strength, thickness and microstructure of the coatings produced, as well as trying to draw conclusions from monitoring of coating solution supersaturation.

2. *Liposomes.* To study the entrapment of chemicals into these vesicles and their subsequent release. Comparing CaP-coated and uncoated liposomes.

3. *Composite coatings.* To manufacture a composite coating which incorporates marker molecules, the release of which can be studied.

The main conclusions were as follows:

6.1 Coatings

6.1.1 Supersaturation

Of the phases monitored during electrodeposition, hydroxyapatite was found to be the most supersaturated, followed by octacalcium phosphate (OCP) and then dicalcium phosphate dihydrate (DCPD), which was undersaturated. Altering initial calcium and phosphate concentrations of the coating solution did not necessarily alter initial supersaturations of the CaP phases in a predictable way, due to precipitate forming in solution. The drop in supersaturation of the HAp and OCP over the 20 minute coating period increased when the initial concentration of the coating solution was increased. Consideration should be given to the fact that supersaturation is a value calculated from measurements taken in the bulk of the coating solution rather than at the electrode surfaces.

6.1.2 Coating mechanism

The initial coating cycle allowed the formation of a thin amorphous layer of CaP, which then acts as a seeding site for subsequent coating growth. One hour or more of maturation time in solution after one 20 minute electrodeposition cycle led to a drastic change in coating surface morphology when compared to samples prepared without this maturation period. The coating thickness of these samples also increases by approximately ten times during the first three hours of maturation. For samples coated with a single coating cycle, electron diffraction studies showed and increase in crystallinity of a the coating with maturation time, which is likely to be due to to dissolution and reprecipitation of CaP. Four extra coating cycles on top of the matured CaP layer served to increase the observed density of the coatings through continued exposure to high solution supersaturation. The

mechanism of electrodeposition at starting solution concentrations of 4 mmol/l Ca^{2+} and 2.4 mmol/l PO_4^{3-} ions and below is likely to be predominantly electrolytic in nature. A CaP coating of approximately 20 µm in thickness was produced onto an orthopaedic Ti(6%)Al(4%)V alloy substrate by repeated electrodeposition cycles under high calcium and phosphate concentration coating conditions. The deposition mechanism in this case was electrophoretic.

6.1.3 Characterisation

X-ray diffraction analysis revealed that the coating was made up of poorly crystalline HAp with a preferred orientation of crystallites with their *c*-axis perpendicular to the substrate. The HAp crystallites were found to be tablet-shaped with dimensions of $a = 136$ nm $b = 34$ nm and $c = 43$ nm. XRD of the samples coated for one cycle and then given time to mature in solution suggested that the preferred HAp coating orientation perpendicular to the *c*-axis became more pronounced with increasing maturation time.

Critical point drying (CPD) of the samples led to the removal of some of the coating material at the same time as protecting the microstructure of the coatings. The lap-shear strength of the air dried sample coated for one cycle, doubled after an hour of maturation in solution. The shear strength of the air dried samples, coated a multiple number of times with maturation, remained relatively constant until a weakening of the coatings took place and the coatings started to peel. A similar pattern was seen for the CPD set. The shear strength of the CPD samples given one coating cycle was found to be generally higher than for the air dried samples, possibly due to protected microstructure. However, electron microscopy revealed that the main material on the pull-off (uncoated blank) side of the lap joint, for the majority of samples, appeared to be epoxy resin. This resin may

have penetrated through the entire coating layer and down to the substrate before setting. There was no clear relationship between coating thickness and shear strength.

6.2 Liposome studies

Calcium and phosphate ions in solution were found to interact with the fluorescent marker molecule calcein, reducing the rate of increase in fluorescence intensity with increasing concentration. Entrapment efficiencies of around 8% were achieved after readjustment of the equipment and other materials used in the manufacture of stable plurilamellar vesicles (SPLVs). A higher percentage of calcein was released from liposomes coated in CaP phases than from uncoated vesicles when incubated for more than 70 hours at 37°C. This was probably due to the growth of crystalline HAp particles on the surface of the liposomes, which eventually disrupt their membrane structure (Pongsaanutin, 2002). A simple technique of concentration determination was used to determine that the antibiotic gentamicin was successfully incorporated into SPLVs. Gentamicin release was monitored as it released over time at 37°C, where up to 70% of the antibiotic had escaped after 25 h.

Experiments which attempted to use the sugar trehalose to preserve liposomes during free-drying and rehydration were unsuccessful, with over 90% of the vesicle contents released during the process.

6.3 Composite coatings

The addition of CaP-coated SPLVs to the coating solutions during the electrodeposition process modulated the drop in HAp and OCP supersaturation and the increase in DCPD saturation over the coating period. The initial rate at which the supersaturation of HAp

fell was lower with the liposomes present, although the total reduction in supersaturation over the entire coating period (20 min) was similar.

Coatings were manufactured with the addition of CaP-coated liposomes containing calcein and trehalose. Coatings had a yellow-orange colouration, indicative of calcein. Freeze-drying of the coatings was unsuccessful, with the dried coatings cracking and forming spalls.

6.4 General conclusions

When considering electrodeposited coatings, the results of these studies show the importance of some of the factors involved after the electric field has been turned off. This is especially true in the case of allowing the coatings time to mature in solution. Longer maturation times lead to alterations in structure and crystallinity that could be used in tailoring coatings to specified requirements. Drying method is also important, with shear strength studies showing that, when comparing to air drying, critical point drying appears to increase the shear strength of samples in some cases (such as samples given one coating cycle) and reduces the shear strength of samples in others (those given four coatings on top of this initial layer). Careful examination of the the lap-shear method is also needed, as epoxy resins appear to readily infiltrate into porous coating structures.

The increased release of entrapped molecules from coated populations of liposomes compared to uncoated populations after a certain time period, shows that in the context of incorporating potential drug delivery devices into a coating structure, a great deal of information about changes in the structure with time of that coating may be needed, as these changes are likely to directly influence the potential effectiveness of these devices.

Chapter 7

Further work

The study described here leads to many further possibilities for work in this area. This work may take the form of:

- Further investigation into the effects of maturation time on coating structure and crystallinity.
  - Assessment of changes in coating solution phase supersaturation during the maturation period.
  - Effect of altering coating solution concentration on the changes that occur during maturation.
- Thorough characterisation of the surface of the metallic substrates to link in with coating lap-shear and crystallinity results.
- Optimising coating shear strength through factors such as substrate surface roughness.
- Using constant composition techniques to maintain the make-up of the coating so-

lution during electrodeposition. This would reduce the need to change the coating solution and allow the speedier production of the coatings.

- More analysis of the effect of CaP coating solutions on the structure of liposome vesicles.
  - Characterisation of the effect that CaP coating has on the zeta potential of liposome suspensions.
- A study of the release of calcein from composite coatings.
  - Possibly involving microscopy using UV light.
- Incorporation of a substance into liposome vesicles that could be visualised easily by electron microscopy or electron probe microanalysis, when these liposomes are incorporated into composite coatings.
- An effective methodology for drying/preserving composite coatings once manufactured in order to improve their potential shelf life.
  - Work on freeze drying the coatings after manufacture in the presence of trehalose.
  - Incorporating liposomes with different substance release profiles.
- Manufacture of composite coatings containing gentamicin
  - Bacterial growth inhibition assays.
- Incorporation of bone morphogenetic proteins into composite coatings
  - Human osteoblast growth assays.

- Work on a 'tougher' alternative to liposomes such as vesicles made up from block copolymers, which may be able to withstand HAp crystal growth for a longer time period.

Bibliography

Abbona, F. and Baronnet, A.: 1996, A XRD and TEM study on the transformation of amorphous calcium phosphate in the prescence of magnesium, *Journal of Crystal Growth* **165**, 98–105.

Allen, T. M.: 1984, Calcein as a tool in liposome methodology, *in* G. Gregoriadis (ed.), *Targeted drug delivery and biological interaction*, Vol. 3 of *Liposome Technology*, CRC Press, Florida, chapter 12, pp. 177–182.

Allen, T. M. and Cleland, L. G.: 1980, Serum-induced leakage of liosome contents, *Biochimica et Biophysica Acta* **597**, 418–426.

Baglin, J. E. E.: 1991, Interface design for thin film adhesion, *in* L. H. Lee (ed.), *Fundamentals of Adhesion*, Plenum Press, New York, chapter 13, pp. 363–382.

Ban, S. and Maruno, S.: 1993, Deposition of calcium phosphate on titanium by electrochemical process in simulated body fluid, *Japanese Journal of Applied Physics* **32**, L1577–L1580.

Ban, S. and Maruno, S.: 1994, Effect of *p*H buffer on electrochemical deposition of calcium phosphate, *Japanese Journal of Applied Physics* **33**, L1545–L1548.

Ban, S. and Maruno, S.: 1998a, Hydrothermal-electrochemical deposition of hydroxyapatite, *Journal of Biomedical Materials Research* **42**, 387–395.

Ban, S. and Maruno, S.: 1998b, Morpholgy and microstructure of electrochemically deposited calcium phosphates in a modified simulated body fluid, *Biomaterials* **19**, 1245–1253.

Ban, S. and Maruno, S.: 1999, *p*H distribution around the electrode during electrochemical depositon process for producing bioactive apatite, *Japanese Journal of Applied Physics* **38**, L537–L539.

Ban, S., Maruno, S., Arimoto, N., Harada, A. and Hasegawa, J.: 1997, Effect of electrochemically deposited apatite coating on bonding of bone to HA-G-Ti composite and titanium, *Journal of Biomedical Materials Research* **36**, 9–15.

Barenholz, Y.: 2001, Liposome application: problems and prospects, *Current Opinion in Colloid and Interface Science* **6**, 66–77.

Barrère, F., Layrolle, P., van Blitterswijk, C. A. and de Groot, K.: 2001, Biomimetic coatings on titanium: a crystal growth study of octacalcium phosphate, *Journal of Materials Science: Materials in Medicine* **12**, 529–534.

Barrère, F., Snel, M. M. E., van Blitterswijk, C. A., de Groot, K. and Layrolle, P.: 2004, Nano-scale study of the nucleation and growth of calcium phosphate coating on titanium implants, *Biomaterials* **25**, 2901–2910.

Bates, R. G.: 1951, *Journal of Research of the National Bureau of Standards* **47**, 127–136.

Bayrakta, H. H., Morgan, E. F., Niebur, G. L., Morris, G. E., Wong, E. K. and Keaveny,

T. M.: 2004, Comparison of the elastic and yield properties of human femoral trabecular and cortical bone tissue, *Journal of Biomechanics* **37**, 27–35.

Beevers, C. A.: 1958, The crystal structure of dicalcium phosphate dihydrate, $CaHPO_4.2H_2O$, *Acta Crystallographica* **11**, 273–277.

Benahmed, M., Bouler, J. M., Heymann, D., Gan, O. and Daculsi, G.: 1996, Biodegredation of synthetic biphasic calcium phosphate by human monocytes *in vitro:* a morphological study, *Biomaterials* **17**, 2173–2178.

Betts, F., Blumenthal, N. C. and Posner, A. S.: 1981, Bone mineralization, *Journal of Crystal Growth* **53**, 63–73.

Biltonen, R. L. and Lichtenberg, D.: 1993, The use of differential scanning calorimetry as a tool to characterize liposome preparations, *Chemistry and Physics of Lipids* **64**, 129–142.

Boccaccini, A. R. and Zhitomirsky, I.: 2002, Application of electrophoretic and electrolytic deposition techniques in ceramics processing, *Current Opinion in Solid State and Materials Science* **6**, 251–260.

Boskey, A. L.: 1998, Biomineralization: Conflicts, challenges, and opportunities, *Journal of Cellular Biochemistry Supplements* **30/31**, 83–91.

Boskey, A. L. and Posner, A. S.: 1976, Formation of hydroxyapatite at low supersaturation, *The Journal of Physical Chemistry* **80**(1), 40–45.

Boskey, A. L. and Posner, A. S.: 1977, The role of synthetic and bone extracted Ca-Phospholipid-PO_4 complexes in hydroxapatite formation, *Calcified Tissue Research* **23**, 251–258.

Brown, W. E., Smith, J. P., Lehr, J. R. and Frazier, A. W.: 1962, Octacalcium phosphate and hydroxyapatite, *Nature* **196**(4859), 1048–1053.

Butler, J. N.: 1964, *Ionic Equilibrium: A mathematical Approach*, Adidison-Wesley, Reading, Massachucetts.

Campbell, A. A., Song, L., Shari, X., Nelson, B. J., Bottoni, C., Brooks, D. E. and DeJong, E. S.: 2000, Development, characterization, and anti-microbial efficacy of hydroxyapatite-chlorhexidine coatings produced by surface-induced mineralization, *Journal of Biomedical Materials Research (Applied Biomaterials)* **53**, 400–407.

Campbell, N. A.: 1996, *Biology*, fourth edn, The Benajamin/Cummings Publishing Company Inc., California.

Capello, W. N., D'Antonio, J. A., Manley, M. T. and Feinberg, J. R.: 1998, Hydroxyapatite in total hip arthroplasty, *Clinical Orthopaedics and Related Research* **355**, 200–211.

Chapman, B. N.: 1974, Thin film adhesion, *Journal of Vacuum Science and Technology* **11**, 106–118.

Charnley, J.: 1961, Arthroplasty of the hip: A new operation, *Lancet* **1**, 1129–1132.

Cheng, X., Filiaggi, M. and Roscoe, S. G.: 2004, Electrochemically assisted co-precipitation of protein with calcium phosphate coatings on titanium alloy, *Biomaterials* **25**, 5395–5403.

Chow, L. C.: 2001, Solubility of calcium phosphates, *in* L. C. Chow and E. D. Eanes (eds), *Octacalcium Phosphate*, Vol. 18 of *Monographs in Oral Science*, Karger, Basel, pp. 94–111.

Christoffersen, J., Christoffersen, M. R., Kibalezye, W. and Andersen, A.: 1989, A contribution to the understanding of the formation of calcium phosphates, *Journal of Crystal Growth* **94**, 767–777.

Christoffersen, J., Dohrup, J. and Chrisoffersen, M. R.: 1998, The importance of formation of hydroxyl ions by dissociation of trapped water molecules for growth of calcium hydroxyapatite crystals, *Journal of Crystal Growth* **186**(275-282).

Christoffersen, M. R., Dohrup, J. and Christoffersen, J.: 1998, Kinetics of growth and dissolution of calcium hydroxyapatite in suspensions with variable calcium to phosphate ratio, *Journal of Crystal Growth* **186**, 283–290.

Clèries, L., Fernánde-Pradas, J. M. and Morenza, J. L.: 2000, Bone growth on and resorbtion of calcium phophate coatings obtained by pulsed laser deposition, *Journal of Biomedical Materials Research* **49**, 43–52.

Collier, J. H. and Messersmith, P. B.: 2001a, Phospholipid strategies in biomineralisation and biomaterials research, *Annual Reveiw of Materials Research* **31**, 237–263.

Collier, J. H. and Messersmith, P. B.: 2001b, Phospholipid strategies in biomineralisation and biomaterials research, *Annual Reveiw of Materials Research* **31**, 237–263.

Cooper, C. and Melton, L. J.: 1992, Epidemiology of osteoporosis, *Trends in Endrocrinology and Metabolism* **3**, 224–229.

Corrand, D. M.: 1998, *The effects of some biochemicals on the precipitation behaviour of hydroxlapatite*, PhD thesis, University of Oxford.

Corvera, E., Mouritsen, O. G., Singer, M. A. and Zuckermann, M. J.: 1992, The perme-

ability and the effect of acyl-chain length for phospholipid bilayers containing cholesterol: theory and experiment, *Biochimica et Biophysica Acta* **1107**, 261–270.

Cotmore, J. M., Nichols Jr., G. and Wuthier, R. E.: 1971, Phosholipid-calcium phosphate complex: Enhanced calcium migration in the presence of phosphate, *Science* **172**, 1339–1341.

Crowe, J. H., Carpenter, J. F. and Crowe, L. M.: 1998, The role of vitrification in anhydrobiosis, *Annual Reveiw of Physiology* **60**, 73–103.

Crowe, J. H. and Crowe, L. M.: 1988, Factors affecting the stability of dry liposomes, *Biochimica et Biophysica Acta* **939**, 327–334.

Crowe, J. H., Crowe, L. M., Carpenter, J. F., Rudolph, A. S., Wistrom, C. A., Spargo, B. J. and Anchordoguy, T. J.: 1988, Interactions of sugars with membranes, *Biochimica et Biophysica Acta* **947**, 367–384.

Crowe, L. M., Womersley, C., Crowe, J. H., Reid, D., Appel, L. and Rudolph, A.: 1986, Prevention of fusion and leakage in freeze-dried liposomes by carbohydrates, *Biochimica et Biophysica Acta* **861**, 131–140.

Currey, J. D., Brear, K. and Zioupos, P.: 1996, The effects of ageing and changes in mineral content in degrading the toughness of human femora, *Journal of Biomechanics* **29**(2), 257–260.

Curry, N. A. and Jones, D. W.: 1971, Crystal structure of brushite, calcium hydrogen orthophoshate dihydrate: A neutron diffraction investigation., *Journal of the Chemical Society (A)* p. 3725.

Danilchenko, S. N., Moseke, C., Sukhodub, L. F. and Sulkio-Cleff, B.: 2004, X-ray diffraction studies of bone apatite under acid demineralization, *Crystal Research and Technology* **39**(1), 71–77.

Davies, C.: 1962, *Ion Association*, Butterworth, London.

de Groot, K., Wolke, J. G. C. and Jansen, J. A.: 1998, Calcium phosphate coatings for medical implants, *Proceedings of the Institute of Mechanical Engineers* **212H**, 137–147.

de With, G., van Dijk, H. J. A., Hattu, N. and Prijs, K.: 1981, Preparation, microstructure and mechanical properties of dense polycrystalline hydroxyapatite, *Journal of Materials Science* **16**, 1592–1598.

Dee, K. C., Reuger, D. C., Andersen, T. T. and Bizios, R.: 1996, Conditions which promote mineralization at the bone-implant interface: a model *in vitro* study, *Biomaterials* **17**, 209–215.

Definition of Terms Relating to Adhesion: 1970, *Technical report*, American Society for Testing and Materials, Philadelphia, PA.

Derjaguin, B. and Landau, L.: 1941, Theory of the stability of strongly charged lyophobic sols and the adhedion of strongly charged particles in solution of electrolytes, *Acta Physiochimica URSS* **14**, 633–662.

Diel, H. and Ellingboe, J. L.: 1956, Indicator for titration o calcium in prescence of magnesium using disodium dihydrogen ethylenediamine tetraacetate, *Analytical Chemistry* **28**(5).

Dini, J. W.: 1993, *Electrodeposition: the materials science of coatings and substrates*, Noyes Publications, New Jersey, pp. 46–89.

Dolan, P. and Torgerson, D. J.: 1998, The cost of treating osteoporotic fractures in the united kingdom female population, *Osteoporosis International* **8**(6), 611–617.

Durucan, C. and Brown, P. W.: 2002, Kinetic model for α-tricalcium phosphate hydrolysis, *Journal of the American Ceramic Society* **85**(8), 2013–2018.

Eanes, E. D., Gillessen, I. H. and Posner, A. S.: 1965, Intermediate states in the precipitation of hydroxyapatite, *Nature* **208**, 365–367.

Eanes, E. D. and Hailer, A. W.: 1985, Liposome-mediated calcium phosphate formation in metastable solutions, *Calcified Tissue International* **37**, 390–394.

Eanes, E. D. and Hailer, A. W.: 1998, The effect of fluoride on the size and morphology of apatite crystals grown from physiologic solutions, *Calcified Tissue International* **63**, 250–257.

Eanes, E. D. and Hailer, A. W.: 2000, Anionic effects on the size and shape of apatite crystals grown from physiological solutions, *Calcified Tissue International* **66**, 449–455.

Eanes, E. D., Hailer, A. W. and Costa, J. L.: 1984, Calcium phosphate formation in aqueous suspensions of multilamella liposomes, *Calcified Tissue International* **36**, 421–430.

Eidelman, N. and Eanes, E. D.: 2001, Role of OCP in biological processes, *in* L. C. Chow and E. D. Eanes (eds), *Octacalcium Phosphate*, Vol. 18 of *Monographs in Oral Science*, Karger, Basel, pp. 50–76.

Fan, Y., Duan, K. and Wang, R.: 2005, A composite coating by electrolysis-induced collagen self-assembly and calcium phosphate mineralization, *Biomaterials* **26**, 1623–1632.

Feenstra, T. P. and de Bruyn, P. L.: 1979, Formation of calcium phosphates in moderately supersaturated solutions, *The Journal of Physical Chemistry* **83**(4), 475–479.

Frank, F. C.: 1965, *Acta Crystallographica* **18**, 862.

Frèche, M. and Heughebaert, J. C.: 1989, Calcium phosphate precipitation in the 60–80°c range, *Journal of Crystal Growth* **94**(4), 947–954.

Frutos, P., Torrado, S., Perez-Lorenzo, M. E. and Frutos, G.: 2000, A valdated quantitative colormetric assay for gentamicin, *Journal of Pharmaceutical and Biomedical Analysis* **21**, 1149–1159.

Geesink, R. G. T.: 1989, Experimental and clinical experience with hydroxyapatite-coated hip implants, *Orthopaedics* **12**, 1239–1242.

Geesink, R. G. T.: 2002, Osteoconductive coatings for total joint arthroplasty, *Clinical Orthopaedics and Related Research* (395), 53–65.

Glenny, A. M. and Song, F.: 1999, Antimicrobial prophylaxis in total hip replacement: a systematic review., *Health Technology Assessment* **3**(21).

Glimcher, M. J., Bonar, L. C., Grynpas, M. D., Landis, W. J. and Roufoss, A. H.: 1981, Recent studies of bone mineral: Is the amorphous calcium phosphate theory valid?, *Journal of Crystal Growth* **53**, 100–119.

Gottlander, M., Johansson, C. B., Wennerberg, A., Albrektsson, T., Radin, S. and Ducheyne, P.: 1997, Bone tissue reactions to an electrophoretically applied calcium phosphate coating, *Biomaterials* **18**, 551–557.

Gregory, T. M., Moreno, E. C. and Brown, W. E.: 1970, Solubility of CaHPO4.2H2O in the system Ca(OH)2 - H3P04 - H2O at 5, 15, 25, and 37.5℃, *Journal of Research of the National Bureau of Standards A* **74A**(461-475).

Gregory, T. M., Moreno, E. C., Patel, J. M. and Brown, W. E.: 1974, *Journal of Research of the National Bureau of Standards A* **78A**, 667.

Grillon, F., Fayeulle, D. and Jeandin, M.: 1992, Quantitiative image-analysis of electrophoretic coatings, *Journal of Materials Science Letters* **11**, 272–275.

Grit, M. and Crommelin, D. J. A.: 1993, Chemical stability of liposomes: implications for their physical stability, *Chemistry and Physics of Lipids* **64**, 3–18.

Gross, K. A., Ray, N. and Røkkum, M.: 2002, The contribution of coating microstructure to degredation and particle release in hydroxyapatite coated prostheses, *Journal of Biomedical Materials Research (Applied Biomaterials)* **63**, 106–114.

Gruner, S. M., Lenk, R. P., Janoff, A. S. and Ostro, M. J.: 1985, Novel multilayered lipid vesicles: Comparison of physical characteristics of multilamellar liposomes and stable plurilamellar vesicles, *Biochemistry* **24**, 2833–2842.

Habibovic, P., Barrière, F., van Blitterswijk, C. A., de Groot, K. and Layrolle, P.: 2002, Biomimetic hydroyapatite coating on metal implants, *Journal of the American Ceramic Society* **85**(3), 517–522.

Haddow, D. B., Thompson, M. S., Berry, S. R. and Czernuszka, J. T.: 1999, Composiitonal and structural control in bone regenerative coatings, *Journal of Materials Science: Materials in Medicine* **10**, 219–222.

Halks-Miller, M., Guo, L. S. S. and Hamilton, R. L.: 1985, Tocopherol-phospholipid liposomes: Maximum content and stability to serum proteins, *Lipids* **20**(3), 195–200.

Hamadouche, M. and Sedel, L.: 2000, Ceramics in orthopaedics, *The Journal of Bone and Joint Surgery - British Edition* **82-B**(8), 1095–1099.

Hamaker, H. C. and Verwey, E. J. W.: 1940, *Transactions of the Faraday Society* **36**, 180–185.

Hara, M., Yuan, H., Yang, Q., Hoshino, T., Yokoyama, A. and Miyake, J.: 1999, Stabilization of liposomal membranes by thermozeaxanthins: carotenoid-glucosode esters, *Biochimica et Biophysica Acta* **1461**, 147–154.

Harned, H. S. and Owen, B. B.: 1958, *The Physical Chemistry of Electrolytic Solutions*, 3 edn, Reinhold, New York.

Hench, L. L. and Wilson, J.: 1993, *in* L. L. Hench and J. Wilson (eds), *An Introduction to Bioceramics*, Vol. 1 of *Advanced Series in Ceramics*, World Scientific Publishing Co., Singapore, chapter 1, pp. 1–24.

Hernández-Caselles, T., Villalaín, J. and Gómez-Fernández, J. C.: 1990, Stability of liposomes on long term storage, *Journal of Pharmacy and Pharmacology* **42**, 397–400.

Heywood, B. R. and Eanes, E. D.: 1987, An ultrastructural study of calcium phosphate formation in multilamellar liposome suspensions, *Calcified Tissue International* **41**, 192–201.

Hincha, D. K., Zuther, E., Hellwege, E. M. and Heyer, A. G.: 2002, Specific effects of fructo- and gluco-oligosaccharides in the preservation of liposomes, *Glycobiology* **12**(2), 103–110.

Hirsch, D., Landis, W. J., Azoury, R. and Sarig, S.: 1992, Liposome interactions with hydroxyapatite crystals: A possible mechanism in the calcification of atherosclerotic plaques, *Calcified Tissue International* **50**, 261–265.

Hoshi, K. and Ozawa, H.: 2000, Matrix vesicle calcification in bones of adult rats, *Calcified Tissue International* **66**, 430–434.

Iijima, M., Kamamizu, H., Wakamatsu, N., Goto, T., Doi, Y. and Moriwaki, Y.: 1995, Effects of CO_3^{-2} ion on the formation of octacalcium phosphate at *p*H 7.4 and 37℃, *Journal of Crystal Growth* **135**, 229–234.

Iijima, M., Kamemizu, H., Wakamatsu, N., Goto, T., Doi, Y. and Moriwaki, Y.: 1997, Transition of octacalcium phosphate to hydroxyapatite in solution at *p*H 7.4 and 37℃, *Journal of Crystal Growth* **181**, 70–78.

Ishii, F. and Nagasaka, Y.: 2001, Simple and convenient method for estimation of marker entrapped in liposomes, *Journal of dispersion science and technology* **22**(1), 97–101.

Kaiser, S. and Hoffman, H.: 1996, Transport of ions through vesicle bilayers, *Journal of Colloid and Interface Science* **184**, 1–10.

Kanzaki, N., Treboux, G., Onuma, K., Tsutsumi, S. and Ito, A.: 2001, Calcium phosphate clusters, *Biomaterials* **22**, 2921–2929.

Kay, M. I., Young, R. A. and Posner, A. S.: 1964, Crystal structure of hydroxyapatite, *Nature* **204**, 1050–1052.

Kim, H. D. and Valentini, R. F.: 1997, Human osteoblast response *in vitro* to platelet-derived growth factor-β delivered from controlled-release polymer rods, *Biomaterials* **18**, 1175–1184.

Kirker-Head, C. A.: 2000, Potential applications and delivery strategies for bone morphogenetic proteins, *Advanced Drug Delivery Reviews* **43**, 65–92.

Klein, C. P., Wolke, J. G. C. and de Groot, K.: 1993, Stability of calcium phosphate ceramics and plasma sprayed coating, *in* L. L. Hench and J. Wilson (eds), *An Introduction to Bioceramics*, Vol. 1 of *Advanced Series in Ceramics*, World Scientific Publishing Co., chapter 11, pp. 199–221.

Koelmans, H.: 1955, *Philips Research Reports* **10**, 161–193.

Koutsopoulos, S.: 2001, Kinetic study on the crystal growth of hydroxyapatite, *Langmuir* **17**, 8092–8097.

Koutsoukos, P. G., Amjad, Z., Tomson, M. B. and Nancollas, G. H.: 1980, *Journal of the American Chemical Society* **102**, 1553.

Kroon, P. O. and Freeman, M. A. R.: 1992, Hydroxyapatite coating of hip prostheses, *The Journal of Bone and Joint Surgery - British Edition* **74**, 518–522.

Kulkarni, S. B., Betageri, G. V. and Singh, M.: 1995, Factors affecting microencapsulation of drugs in liposomes, *Journal of Microencapsulation* **12**(3), 229–246.

Kumar, M., Desarathy, H. and Riley, C.: 1999, Electrodeposition of brushite coatings and their transformation to hydroxyapatite in aqueous solutions, *Journal of Biomedical Materials Research* **45**, 302–310.

Kumar, M., Xie, J., Chittur, K. and Riley, C.: 1999, Transformation of modified brushite to hydroxyapatite in aqueous solution: Effects of potassium substitution, *Biomaterials* **20**, 1389.

Lacefield, W. R.: 1993, Hydroxylapatite coatings, *in* L. L. Hench and J. Wilson (eds), *Bioceramics*, Vol. 1 of *Advanced Series in Ceramics*, World Scientific Publishing Co., Singapore, pp. 223–238.

Lasic, D. D.: 1998, Novel applicatons of liposomes, *Trends in Biotechnology* **16**, 307–320.

Lawson, A. C. and Czernuszka, J. T.: 1998, Collagen-calcium phoshate composites, *Proceedings of the Institute of Mechanical Engineers* **212**, 413–425.

LeGeros, R. Z.: 1981, Apatites in biological systems, *Progress in Crystal Growth and Characterization of Materials* **4**, 1–45.

LeGeros, R. Z.: 2002, Properties of osteoconductive biomaterials: Calcium phosphates, *Clinical Orthopaedics and Related Research* (395), 81–98.

LeGeros, R. Z. and LeGeros, J. P.: 1993, Dense hydroxyapatite, *in* L. L. Hench and J. Wilson (eds), *An Introduction to Bioceramics*, Vol. 1 of *Advanced Series in Ceramics*, World Scientific Publishing Co., Singapore, chapter 9, pp. 139–180.

Lewis, G.: 1997, Properties of acrylic bone cement: State of the art review, *Journal of Biomedical Materials Research (Applied Biomaterials)* **38**, 155–182.

Lewis, G. and Janna, S.: 2004, The *in Vitro* elution of gentamicin sulfate froma commercially available gentamicin-loaded acrylic bone cement, VersaBond^{TM} AB, *Journal of Biomedical Materials Research (Applied Biomaterials)* **71B**, 77–83.

Li, P. and Ducheyne, P.: 1998, Quasi-biological apatite film induced by titanium in a simulated body fluid, *Journal of Biomedical Materials Research* **48**, 341–348.

Lin, F.-H., Hsu, Y.-S., Lin, S.-H. and Sun, J.-S.: 2002, The effect of Ca/P concentration and temperature of simulated body fluid on the growth of hydroxyapatite coating on alkali-treated 316L stainless steel, *Biomaterials* **23**, 4029–4038.

Liou, S.-C. and Chen, S.-Y.: 2002, Transformation mechanism of different chemically precipated apatitic precursors into β-tricalcium phosphate upon calcination, *Biomaterials* **23**, 4541–4547.

Liu, Y., Hunziker, E. B., Layrolle, P., de Bruijn, J. D. and de Groot, K.: 2004, Bone morphogenetic protein 2 incorporated into biomimetic coatings retains its biological activity, *Tissue Engineering* **10**(1/2), 101–108.

Liu, Y., Hunziker, E. B., Randall, N. X., de Groot, K. and Layrolle, P.: 2003, Proteins incorporated into biomimetically prepared calcium phosphate coatings modulate their mechanical strength and dissolution rate, *Biomaterials* **24**, 65–70.

Liu, Y., Layrolle, P., de Bruijn, J., van Blitterswijk, C. and de Groot, K.: 2001, Biomimetic coprecipitation of calcium phosphate and bovine serum albumin on titanium alloy, *Journal of Biomedical Materials Research* **57**, 327–335.

Lucas, L. C., Lacefield, W. R., Ong, J. L. and Whitehead, R. Y.: 1993, Calcium phosphate coatings for medical and dental implants, *Colloids and Surfaces A: Physiochemical and Engineering Aspects* **77**, 141–147.

Lucas, P. A., Syftestad, G. T., Goldberg, V. M. and Caplain, A. I.: 1989, Ectopic induction of cartilage and bone by water-soluble proteins from bovine bone using a collagenous delivery vehicle, *Journal of Biomedical Materials Research* **23s**, 23–9.

Madden, T. D., Bally, M. B., Hope, M. J., Cullis, P. R., Schieren, H. P. and Janoff, A. S.:

1985, Protection of large unilamellar vesicles by trehalose during dehydration: retention of vesicle contents, *Biochimica et Biophysica Acta* **817**, 67–74.

Males, R. G., Phillips, P. S. and Herring, F. G.: 1998, Equations describing passive transport through vesicular membranes, *Biophysical Chemistry* **70**, 65–74.

Manjubala, I., Sivakumar, M., Sureshkumar, R. V. and Sastry, T. P.: 2002, Bioactivity and osseointegration study of calcium phosphate ceramic of different chemical composition, *Journal of Biomedical Materials Research (Applied Biomaterials)* **63**, 200–208.

Mann, S.: 1988, Molecular recognition in biomineralization, *Nature* **332**, 119–124.

Manso, M., Jiménez, C., Morant, C., Herrero, P. and Martínez-Duart, J. M.: 2000, Electrodeposition of hydroxyapatite coatings in basic conditions, *Biomaterials* **21**, 1755–1761.

Markovic, M., Fowler, B. O. and Tung, M. S.: 2004, Preparation and comprehensive characterization of a calcium hydroxyapatite reference material, *Journal of Research of the National Institute of Standards and Technology* **109**, 553–568.

Marshall, R.: 1970, PhD thesis, State University of New York at Buffalo, New York.

Mathew, M., Schroeder, L. W., Dckens, B. and Brown, W. E.: 1977, The crystal structure of $\alpha-Ca_3(PO_4)_2$, *Acta Crystallographica* **B33**, 1325–1333.

Mathew, M. and Takagi, S.: 2001, Crystal structures ofcalcium orthophosphates, *in* L. C. Chow and E. D. Eanes (eds), *Octacalcium Phosphate*, Vol. 18 of *Monographs in Oral Science*, Karger, Basel, pp. 1–16.

Mayhew, E., Lazo, R., Vail, W. J., King, J. and Green, A. M.: 1984, Characterization of liposomes prepared using a microemulsifier, *Biochimica et Biophysica Acta* **775**, 169–174.

McDowel, H., Gregory, T. M. and Brown, W. E.: 1977, *J. Res. Natl. Bur. Stand.* **81A**, 273.

Memoli, A., Palermiti, L. G., Travagli, V. and Alhaique, F.: 1999, Effects of surfactants on the spectral behaviour of calcein (II): a method of evaluation, *Journal of Pharmaceutical and Biomedical Analysis* **19**, 627–632.

Meyer, J. L. and Eanes, E. D.: 1978, A thermodynamic analysis of the secondary transistion in the spontaneous precipitation of calcium phosphate, *Calcified Tissue Research* **25**, 209–216.

Moore, W. R., Graves, S. E. and Bain, G. I.: 2001, Synthetic bone graft substitutes, *The Austrailian and New Zealand Journal of Surgery* **71**, 354–361. Reveiw.

Moreno, E. C., Brown, W. E. and Osborn, G.: 1960, *Soil Surv. Proc.* p. 99.

Mosekilde, L.: 1990, Sex differences in age-related changes in vertebral body size, density and biomechanical competence in normal individuals, *Bone* **11**(2), 67–73.

Murphy, W. L. and Messersmith, P. B.: 2000, Compartmental control of mineral formation: adaptation of a biomineralization strategy for biomedical use, *Polyhedron* **19**, 357–363.

Nancollas, G. H. and Mohan, M. S.: 1970, The growth of hydroxyapatite crystals, *Archives of Oral Biology* **15**, 731–745.

National Statistics Online.: 2001, Census 2001, www.statistics.gov.uk/census2001.

New, R. R. C.: 1996, Preparation of liposomes, *in* R. R. C. New (ed.), *Liposomes: A practical approach*, IRL Press, Oxford, UK.

Oguchi, H., Ishikawa, K., Mizoue, K., Seto, K. and Eguchi, G.: 1995, Long-term histological evaluation of hydroxyapatite ceramics in humans, *Biomaterials* **16**, 33–38.

Önsten, I., Nordqvist, A., Carlsson, Å. S., Besjakov, J. and Shott, S.: 1998, Hydroxyapatite augmentation of the porous coating improves fixation of tibial components. a randomised RSA study in 116 patients, *The Journal of Bone and Joint Surgery - British Edition* **80-B**(3), 417–425.

Ostro, M. J.: 1987, Liposomes, *Scientific American* **256**, 90–101.

Park, J.-H., Lee, D.-Y., Oh, K.-T., Lee, Y.-K. and Kim, K.-N.: 2004, Bioactive calcium phosphate coating on sodium hydroxide-pretreated titanium substrate by electrodeposition, *Journal of the American Ceramic Society* **87**(9), 1792–1794.

Peaker, A.: 1995, *The effect of electric field on the formation of hydroxyapatite coatings*, Master's thesis, University of Oxford.

Peaker, A. J. S. and Czernuszka, J. T.: 1996, The effect of electric field on the formation of hydroxyapatite coatings, *Thin Solid Films* **287**, 174–183.

Perrett, S., Golding, M. and Williams, W. P.: 1991, A simple method for the preparation of liposomes for pharmaceutical applications: Characterisation of the liposomes, *Journal of Pharmacy and Pharmacology* **43**, 154–161.

Peyton, F. A.: 1968, Materials in restorative dentistry, *Annals of the New York Academy of Sciences* **146**, 96–105.

Pongsaanutin, T.: 2002, *Fabrication and characterisation of calcium phosphate and liposome composites for potential drug delivery devices*, PhD thesis, University of Oxford.

Posner, A. S. and Betts, F.: 1975, Synthetic amorphous calcium phosphate and its relation to bone mineral structure, *Accounts of Chemical Research* **8**, 273–281.

Puleo, D. A.: 1997, Dependence of mesenchymal cell responses on duration of exposure to bone morphogenetic protein-2 *in vitro*, *Journal of Cellular Physiology* **173**, 93–101.

Puleo, D. A. and Nanci, A.: 1999, Understanding and controlling the bone-implant interface, *Biomaterials* **20**, 2311–2321.

Radin, S., Campbell, J., Ducheyne, P. and Cuckler, J. M.: 1997, Calcium phosphate ceramic coatings as carriers of vancomycin, *Biomaterials* **18**(11), 777–782.

Rangavittal, N., Landa-Cánovas, A. R., González-Calbet, J. M. and Vallet-Regí, M.: 2000, Structural stability and stability of hydroxyapatite and β-tricalcium phosphate: Two important bioceramics, *Journal of Biomedical Materials Research* **51**, 660–668.

Richard, M., Aguado, E., Cottrel, M. and Daculsi, G.: 1998, Ultrastuctural and electron diffraction of the bone-ceramic interfacial zone in coral and biphasic CaP implants, *Calcified Tissue International* **62**, 437–442.

Røkkum, M., Brandt, M., Bye, K., Hetland, K. R., Waage, S. and Reigstad, A.: 1999, Polyethylene wear, osteolysis and acetabular loosening with HA-coated hip prosthesis. a follow-up of 94 consecutive arthroplasties, *The Journal of Bone and Joint Surgery - British Edition* **81-B**, 582–9.

Rößler, S., Sewing, A., Stölzel, M., Born, R., Scharnweber, D., Dard, M. and Worch,

H.: 2002, Electrochemically assisted deposition of thin calcium phosphate coatings at near-physiological *p*H, *Journal of Biomedical Materials Research* **64A**, 655–663.

Sarkar, P. and Nicholson, P. S.: 1996, Electrophoretic deposition (EPD): Mechanisms, kinetics, and application to ceramics, *Journal of the American Ceramic Society* **79**(8), 1987–2002.

Schmidt, H. T., Gray, B. L., Wingert, P. A. and Ostafin, A. E.: 2004, Assembly of aqueous-cored calcium phosphate nanoparticles for drug delivery, *Chemistry of Materials* **16**, 4942–4947.

Schmidt, H. T. and Ostafin, A. E.: 2002, Liposome directed growth of calcium phosphate nanoshells, *Advanced Materials* **14**(7), 532–535.

Sergo, V., Sbaizero, O. and Clarke, D. R.: 1997, Mechanical and chemical consequences of the residual stresses in plasma spayed hydroxyapatite, *Biomaterials* **18**(6), 477–482.

Shi, X., Ma, W., Sun, C. and Wu, S.: 2001, The aggregation behaviour of collagen in aqueous solution and its property of stabilizing liposomes *In vitro*, *Biomaterials* **22**, 1627–1634.

Shirkhanzadeh, M., Azadegan, M., Stack, V. and Schreyer, S.: 1994, Fabrication of pure hydroxyapatite and flouridated-hydroxyapatite coatings by electocrystallisation, *Materials Letters* **18**, 211–214.

Søballe, K. and Overgaard, S.: 1996, The current status of hydroxyapatite coating of prostheses, *The Journal of Bone and Joint Surgery - British Edition* **78-B**(5), 689–691.

Sohmura, T., Tamasaki, H., Ohara, T. and Takahashi, J.: 2001, Calcium-phosphate sur-

face coating by casting to improve bioactivity of titanium, *Journal of Biomedical Materials Research (Applied Biomaterials)* **58**, 478–475.

Stigter, M., de Groot, K. and Layrolle, P.: 2002, Incorporation of tobramycin into biomimetic hydroxyapatite coating on titanium, *Biomaterials* **23**, 4143–4153.

Stryer, L.: 1995, *Biochemistry*, fourth edn, W. H. Freeman and Company, New York.

Suetsugu, Y., Shimoya, I. and Tanaka, J.: 1998, Configuration of carbonate ions in apatite structure determined by polarized infrared spectroscopy, *Journal of the American Ceramic Society* **81**(3), 746–748.

Sun, L., Berndt, C. C., Gross, K. A. and Kucuk, A.: 2001, Material fundamentals and clinical performance of plasma-sprayed hydroxyapatite coatings: A review, *Journal of Biomedical Materials Research (Applied Biomaterials)* **58**, 570–592.

Tancred, D. C., McCormack, B. A. O. and Carr, A. J.: 1998, A synthetic bone implant macroscopically identical to cancellous bone, *Biomaterials* **19**, 2303–2311.

Tang, R., Wu, W., Haas, M. and Nancollas, G. H.: 2001, Kinetics of the dissolution of β-tricalcium phosphate, *Langmuir* **17**, 3480–3485.

Ti Tien, H. and Ottova, A. L.: 2001, The lipid bilayer concept and its experimental realization: from soap bubbles, kitchen sink, to bilayer lipid membranes, *Journal of Membrane Science* **189**, 83–117. Reveiw.

Toquet, J., Rohnanizadeh, R., Guicheux, J., Couillaud, S., Passuti, N., Daculsi, G. and Heymann, D.: 1999, Osteogenic potential *in vitro* of human bone marrow cells cultured on macroporous biphasic calcium phosphate ceramic, *Journal of Biomedical Materials Research* **44**, 98–108.

Torgerson, D.: 2001, The effective management of osteoporosis, *in* D. Barlow, R. Francis and A. Miles (eds), *UK Key Advances in Clinical Practice*, Aesculapiuf Medical Press, chapter 9.

Treboux, G., Layrolle, P. and Kanzaki, N.: 2000, Symmetry of posner's cluster, *Journal of the American Chemical Society* **122**, 8323–8324.

van der Biest, O. O. and Vandeperre, L. J.: 1999, Electrophoretic depsition of materials, *Annual Reviews in Materials Science* **29**, 327–52.

Vanderzee, C. E. and Quist, A. S.: 1961, *Journal of Physical Chemistry* **65**, 118–128.

Verwey, E. J. W. and Overbeek, J. T. G.: 1948, *Theory of the stability of lyophobic colloids*, Elsevier, Amsterdam.

Wallach, D. F. H., Surgenor, D. M., Soderberg, J. and Delano, E.: 1959, Preparation and properties of 3, 6-dihydroxy-2,4-bis[N,N'-di(carboxymethyl)-aminomethyl, *Analytical Chemistry* **3**, 456–460.

Wang, E. A., Israel, D. I., Kelley, S. and Luxenberg, D. P.: 1993, Bone morphogenitic protein 2 causes commitment and differentiation in c3h10t1/2 and 3t3 cells, *Growth Factors* **9**, 57–71.

Wang, J., Layrolle, P., Stigter, M. and de Groot, K.: 2004, Biomimetic and electrolytic calcium phosphate coatings on titatium alloy: physiochemical characteristics and cell attachment, *Biomaterials* **25**, 583–592.

Weiner, S. and Wagner, H. D.: 1998, The material bone: Structure-mechanical function relations, *Annual Reviews in Materials Science* **28**, 271–298.

Wen, H. B., de Wijn, J. R., van Blitterswijk, C. A. and de Groot, K.: 1999, Incorporation of bovine serum albumin in calcium phosphate coating on titanium, *Journal of Biomedical Materials Research* **46**, 245–252.

Willert, H. G.: 1977, Reactions of the articular capsule to wear products of artificial joint prostheses, *Journal of Biomedical Materials Research* **11**(157-164).

Willert, H. G., Ludwig, J. and Semlitsch, M.: 1974, Reaction of bone to methacrylate after hip arthroplasty. a long term gross, light microscopic, and scanning electron microscopic study., *The Journal of Bone and Joint Surgery -American Edition* **56**, 1368–1382.

Williams, D. F., Black, J. and Doherty, P. J.: 1992, *in* P. J. Doherty, R. L. Williams, D. F. Willams and A. J. C. Lee (eds), *Biomaterial-Tissue Interfaces. Advances in Biomaterials*, Vol. 10, Elsevier, Amsterdam.

Wilson, M. A. and Pohorille, A.: 1996, Mechanism of unassisted ion transport across membrane bilayers, *Journal of the American Chemical Society* **118**, 6580–6587.

Wong, A. T. C.: 1993, *Precipitiaton Behaviour of Calcium Phosophate - A Model for Hard Tissue Mineralisation*, PhD thesis, University of Oxford.

Wong, A. T. C. and Czernuzka, J. T.: 1993, Transformation behaviour of calcium phosphate 1. theory and modelling, *Colloids and Surfaces A: Physicochemical and Engineering Aspects* **78**, 245–253.

Yan, W.-Q., Nakamura, T., Kawanabe, K., Nishigochi, S., Oka, M. and Kokubo, T.: 1997, Apatite layer-coated titanium for use as bone bonding implants, *Biomaterials* **18**, 1185–1190.

Yuan, H., de Bruijn, J. D., Zhang, X., van Blitterswijk, C. A. and de Groot, K.: 2001, Use of and osteoinductive biomaterial as a bone morphogenetic protein carrier, *Journal of Materials Science: Materials in Medicine* **12**, 761–766.

Yuan, H., Yang, Z., Li, Y., Zhang, X., de Bruijn, J. D. and de Groot, K.: 1998, Osteoinduction by calcium phosphate biomaterials, *Journal of Materials Science: Materials in Medicine* **9**, 723–726.

Yuan, H., Zou, P., Yang, Z., Zhang, X., de Bruijn, J. D. and de Groot, K.: 1998, Bone morphogenetic protein and ceramic-induced osteogenesis, *Journal of Materials Science: Materials in Medicine* **9**, 717–721.

Yubao, L., Xingdong, Z. and de Groot, K.: 1997, Hydrolysis and phase transition of alpha-tricalcium phosphate, *Biomaterials* **18**, 737–741.

Zhang, J. M., Lin, C. J., Feng, Z. D. and Tian, Z. W.: 1998, Mechanistic studies of electrodeposition for bioceramic coatings of calcium phosphates by an *in situ* *p*H - microsensor technique, *Journal of Electroanalytical Chemistry* **452**, 235–240.

Zhitomirsky, I.: 2002, Cathodic electrodeposition of ceramic and organoceramic materials. fundamental aspects, *Advances in Colloid and Interface Science* **97**, 279–317.

Zhitomirsky, I. and Gal-Or, L.: 1997, Electrophoretic deposition of hydroyxapatite, *Journal of Materials Science: Materials in Medicine* **8**, 213–219.

Appendix A

Calculation of Supersaturation

Further information will be given here on the practical calculation of supersaturation as carried out for this study. Theoretical definitions of supersaturation, solubility product, ionic activity product and ionic product have already been given in Section 2.4.1. Much of this information is based upon the work of Wong (1993).

A.1 Equilibria

In the coating solution there are a wide variety of charged entities present. The equilibria between these ions need to be taken into account in order to calculate the concentrations of ions and complexes respective to one another. The corresponding equilibria are listed in Equation A.1.

$$\mathrm{H_3PO_4} \Leftrightarrow \mathrm{H^+ + H_2PO_4^-} \quad \log \mathrm{K_0} = -\frac{799.31}{\mathrm{T}} + 4.5535 - 0.013386\,\mathrm{T} \text{ (Bates, 1951)}$$

$$\mathrm{H_2PO_4^-} \Leftrightarrow \mathrm{H^+ + HPO_4^{2-}} \quad \log \mathrm{K_1} = -\frac{1979.50}{\mathrm{T}} + 5.3541 - 0.019840\,\mathrm{T} \text{ (Bates and Acree, 1943)}$$

$$\mathrm{HPO_4^{2-}} \Leftrightarrow \mathrm{H^+ + PO_4^{3-}} \quad \log \mathrm{K_2} = -\frac{2017.76}{\mathrm{T}} - 1.5026 - 0.0136\,\mathrm{T} \text{ (Vanderzee and Quist, 1961)}$$

$$\mathrm{CaH_2PO_4^+} \Leftrightarrow \mathrm{Ca^{2+} + H_2PO_4^-} \quad \ln \mathrm{K_3} = -\frac{19373}{\mathrm{T}} + 122.81 - 0.1994\,\mathrm{T} \text{ (Gregory et al., 1970)}$$

$$\mathrm{CaHPO_4} \Leftrightarrow \mathrm{Ca^{2+} + HPO_4^{2-}} \quad \ln \mathrm{K_4} = -\frac{51090}{\mathrm{T}} + 341.14 - 0.5880\,\mathrm{T} \text{ (Gregory et al., 1970)}$$

$$\mathrm{CaPO_4^-} \Leftrightarrow \mathrm{Ca^{2+} + PO_4^{3-}} \quad \log \mathrm{K_5} = -\frac{1156}{\mathrm{T}} + 3.603 - 0.0208\,\mathrm{T} \text{ (Frèche and Heughebaert, 1989)}$$

$$\mathrm{CaOH^+} \Leftrightarrow \mathrm{Ca^{2+} + OH^-} \quad \log \mathrm{K_6} = -\frac{409.9}{\mathrm{T}} + 2.8235 - 0.0090\,\mathrm{T} \text{ (Frèche and Heughebaert, 1989)}$$

$$\mathrm{H_2O} \Leftrightarrow \mathrm{H^+ + OH^-} \quad \log \mathrm{K_W} = -\frac{4471}{\mathrm{T}} + 6.0875 - 0.01706\,\mathrm{T} \text{ (Harned and Owen, 1958)} \tag{A.1}$$

A.2 Electroneutrality

According to Harned and Owen (1958) the overall sum of all charges throughout the coating solution should be zero. This can be expressed as:

$$\sum_1^n n\left[X^{n+}\right] = 2[\mathrm{Ca^{2+}}] + [\mathrm{CaH_2PO_4^+}] + [\mathrm{CaOH^+}] + [\mathrm{H^+}] + [\mathrm{K^+}] \text{ and}$$

$$\sum_1^n n\left[X^{n-}\right] = 3[\mathrm{PO_4^{3-}}] + 2[\mathrm{HPO_4^{2-}}] + [\mathrm{H_2PO_4^-}] + [\mathrm{CaPO_4^-}] + [\mathrm{OH^-}] + [\mathrm{Cl^-}]$$

$$\text{where } \sum_1^n n\left[X^{n+}\right] = \sum_1^n n\left[X^{n-}\right] \tag{A.2}$$

A.3 Ionic concentration

As described previously in the Methods section (Section 3.1.1) the pH and pCa were monitored during coating. The free concentration of these two ions in solution can be calculated:

$$[H^+] = \frac{10^{-p\mathrm{H}}}{\chi_1}$$
$$[Ca^{2+}] = \frac{10^{-p\mathrm{Ca}}}{\chi_2} \tag{A.3}$$

Where χ_1 and χ_2 are the ion activity coefficients described previously (Section 2.4.1.2). These coefficients are dependent upon the ionic strength of the solution as calculated by Equation 2.15, Section 2.4.1.2 and here given by:

$$\mathrm{I} = \frac{1}{2}\{4[Ca^{2+}] + 9[PO_4^{3-}] + 4[HPO_4^{2-}] + [H_2PO_4^-] + [CaH_2PO_4^+] + [CaPO_4^-] + [CaOH^+] + [H^+] + [OH^-] + [K^+] + [Cl^-]\} \tag{A.4}$$

The initial ionic strength of the solution had been made up to be close to 0.1 mol/l by addition of KCl as a neutral electrolyte. This is the first approximation of the ionic strength and can be subsequently refined by using calculated values of ion concentrations.

This value of I can now be substituted into the Debye-Hückel law as modified by Davies (1962) (Equation 2.17, Section 2.4.1.2), giving the activity coefficients required for calculating the Ca^{2+} and H^+ concentrations in Equation A.3.

At this point, the concentration of PO_4^{3-} can be calculated by using the equilibrium values given in A.1 with the approximations already made and the electroneutrality ex-

pression (Equation A.2) to give:

$$[PO_4^{3-}] = \frac{C_1[Ca^{2+}] + C_2}{C_3[Ca^{2+}] + C_4} \tag{A.5}$$

$$\begin{aligned}
\text{where } C_1 &= K_1K_2K_3K_5(2K_6[H^+] + K_W) \\
C_2 &= K_1K_2K_3K_5K_6([H^+]^2 + [H^+][K^+] - [H^+][Cl^-] - K_W) \\
C_3 &= K_6[H^+](K_1K_2K_3 - K_5[H^+]^2) \\
C_4 &= K_3K_5K_6[H^+](3K_1K_2 + 2K_1[H^+] + [H^+]^2)
\end{aligned}$$

Now that the concentrations of H^+, Ca^{2+} and PO_4^{3-} ions are known, it is possible to calculate the concentrations of other species in solution:

$$\begin{aligned}
[HPO_4^{2-}] &= \frac{[H^+][PO_4^{3-}]}{K_2} \\
[H_2PO_4^-] &= \frac{[H^+]^2[PO_4^{3-}]}{K_1K_2} \\
[CaH_2PO_4^+] &= \frac{[Ca^{2+}][H^+]^2[PO_4^{3-}]}{K_1K_2K_3} \\
[CaHPO_4] &= \frac{[Ca^{2+}][H^+][PO_4^{3-}]}{K_2K_4} \\
[CaPO_4^-] &= \frac{[Ca^{2+}][PO_4^{3-}]}{K_5} \\
[CaOH^+] &= \frac{[Ca^{2+}]K_W}{[H^+]K_6} \\
[OH^-] &= \frac{K_W}{[H^+]}
\end{aligned} \tag{A.6}$$

These values are then used to recalculate the ionic strength of the coating solution.

A.4 Solubility Products

The solubility products described in Section 2.4.1.2, Equation 2.23 are equilibrium properties and only dependent on temperature. The relationships between K_{sp} and temperature are as follows:

$$\ln K_{sp(DCPD)} = -\frac{8403.50}{T} + 41.863 - 0.09678\,T \text{ (Gregory et al., 1970)}$$
$$\log K_{sp(OCP)} = -\frac{10.25}{T} + 40.098 - 0.031897\,T \text{ (Frèche and Heughebaert, 1989)}$$
$$\log K_{sp(HAp)} = -\frac{8219.41}{T} - 1.6657 - 0.098215\,T \text{ (McDowell et al., 1977)} \quad \text{(A.7)}$$

Appendix B

Materials Congress 2002 Abstract

Mechanical Properties of Novel Electrodeposited Hydroxyapatite coatings

Oliver N. F. King & Jan T. Czernuszka. Department of Materials, University of Oxford, Oxford, UK.

Hydroxyapatite coatings have been electrophoretically deposited on to a cathode, the anode was platinum.

This is a low temperature electrodeposition and it has a number of advantages over other techniques, such as plasma coating. Production of the coating under near-physiological pH and a temperature of 37°C is favourable to producing coatings which will be stable under physiological conditions. In addition, the composition of the hydroxyapatite can be closely matched to that found in bone.

The effect of standing time was investigated. After deposition, the coating was left to stand in the calcifying solution for up to 13 hours.

The interfacial shear strength was measured and found to initially increase with standing time, reaching a maximum after approximately 1 hour. Thereafter, the interfacial shear strength decreased to a value below the initial value. This behaviour has been correlated with microscopic examination and changes in crystallographic activities within the coatings.